Institut für Elektronik

Heinz Nixdorf-Lehrstuhl für Medizinische Elektronik

Univ.-Prof. Dr. rer. nat. habil. Bernhard Wolf

Evaluation of new bioelectronic cell based assays for diagnostic and therapeutic systems

Jochen Meyer

Vollständiger Abdruck der von der Fakultät für Elektrotechnik und Informationstechnik der Technischen Universität München zur Erlangung des akademischen Grades eines

Doktor-Ingenieurs

genehmigten Dissertation.

Vorsitzender: Univ.-Prof. Dr.-Ing. habil. Dr. h.c. Alexander W. Koch

Prüfer der Dissertation:

1. Univ.-Prof. Dr. rer. nat. habil. Bernhard Wolf
2. Univ.-Prof. Dr. rer. nat. Doris Schmitt-Landsiedel

Die Dissertation wurde am 01. 10. 2009 bei der Technischen Universität München eingereicht und durch die Fakultät für Elektrotechnik und Informationstechnik am 14. 10. 2009 angenommen.

Publications

- Papers

J. Meyer, B. Wolf, G. W. Gross, "Magnetic stimulation and depression of mammalian networks in primary neuronal cell cultures", IEEE transactions on biomedical engineering, vol. 56 (5), May 2009

F. Ilchmann, V. Lob, **J. Meyer**, H. Ressler, B. Wankerl, J. Wiest, B. Wolf, „Automated Cell Analytics, Application on Sensor Chips**"** Screening-trends in drug discovery, Volume 9, February 2008, 21-23

- Abstracts/Oral presentations/Poster presentations

J. F. Meyer, H. Schwark, G. W. Gross, "Magnetic stimulation and depression of non-homogeneous networks in primary neuronal cell cultures", Poster presentation, 35th Annual Meeting of the Society for Neuroscience, Washington D. C., 2005

J. F. Meyer, K. Wendicke, G. W. Gross, "Magnetic Stimulation and depression of non-homogeneous networks in primary neuronal cell cultures", Oral presentation, Proceedings 5th International Meeting on Substrate-Integrated Micro Electrode Arrays, Reutlingen, 2006

F. Ilchmann, J. Ressler, **J. F. Meyer**, H. Grothe, B. Wolf, „Recording chamber for glass sensor chips with MEA and integrated oxygen-, pH- and temperature", Poster presentation, Proceedings 5th International Meeting on Substrate-Integrated Micro Electrode Arrays, Reutlingen, 2006

J. F. Meyer, G. W. Gross, "Magnetic stimulation and depression of non-homogenous networks in primary neuronal cell culture", Poster presentation, BMT 2007 - 41. Jahrestagung der Deutschen Gesellschaft für Biomedizinische Technik im VDE - Proceedings, Aachen, 26.09-29.09 2007, Biomedizinische Technik Vol.52 (2007) Ergänzungsband ISSN 0939-4990

M. Nicoletti, **J. Meyer**, T. Weyh, T. Kinney, G. W. Gross, B. Wolf: "Analysis of optimal coil design for magnetic stimulation of neural tissue cultures on MEAs", Poster presentation, BMT 2007 - 41. Jahrestagung der Deutschen Gesellschaft für Biomedizinische Technik im VDE - Proceedings, Aachen, 26.09-29.09 2007, Biomedizinische Technik Vol.52 (2007) Ergänzungsband ISSN 0939-4990

M. Nicoletti, **J. F. Meyer**, T. Weyh, T. N. Kinney, F. Ilchmann, G. W. Gross, B. Wolf, "Coil design optimization for magnetic stimulation of neural tissue cultures on MEAs", Poster presentation, Proceedings 6th International Meeting on Substrate-Integrated Micro Electrode Arrays, Reutlingen, 2008

J. F. Meyer, T. N. Kinney, F. Ilchmann, B. Wolf, „Tissue-specific neurotoxicity of cytostatic and anaesthetic drugs", Oral presentation, Proceedings 6th International Meeting on Substrate-Integrated Micro Electrode Arrays, Reutlingen, 2008

J. F. Meyer, F. Kamp, T. Bartels, T. N. Kinney, F. Ilchmann, K. Beyer, B. Wolf, „MEA supported cortical cultures as a novel tool in Alzheimer's research", Poster presentation,

Proceedings 6th International Meeting on Substrate-Integrated Micro Electrode Arrays, Reutlingen, 2008

F. Ilchmann, **J. F. Meyer**, V. Lob, C. Zhang, H. Grothe, B. Wolf, „Automated multiparametric 24 Well Neuro Screening system", Poster presentation, Proceedings 6th International Meeting on Substrate-Integrated Micro Electrode Arrays, Reutlingen, 2008

F. Ilchmann, **J. F. Meyer**, J. Ressler, H. Grothe, B. Wolf, „Multiparametric NeuroLab recording chamber with MEA and integrated metabolic sensors", Poster presentation, Proceedings 6th International Meeting on Substrate-Integrated Micro Electrode Arrays, Reutlingen, 2008

J. F. Meyer, T. N. Kinney, F. Ilchmann, B. Wolf, "Tissue-specific, functional toxicity of cytostatic and anaesthetic drugs in primary neuronal cell cultures", Poster presentation, 38th Annual Meeting of the Society for Neuroscience, Washington D. C., November 2008

Acknowledgments

This doctoral thesis is the product of research conducted at the Heinz Nixdorf-Lehrstuhl für Medizinische Elektronik (LME) and the Zentralinstitut für Medizintechnik (IMETUM) of the Technische Universität München, and at the Center for Network Neuroscience (CNNS) of the University of North Texas, Denton, USA. At all three institutions, I was able to work in a laboratory environment that stimulated my scientific curiosity through excellent equipment and – more importantly – being part of a community of fantastic colleagues.

I wish to express my sincere thankfulness to my two main supervisors during the time of my thesis, Prof. Bernhard Wolf and Prof. Guenter W. Gross. Working, interacting and arguing with them has certainly been the source of invaluable enrichment of my personality, both academically and privately.

I am very thankful to all my colleagues and collaborators at the LME and the IMETUM who have always helped me tremendously with both the theoretical and practical aspects of the work behind this thesis. In particular, my cordial thanks go to R. Arbogast, Dr. M. Brischwein, Prof. G. Färber, I. Franz, Dr. B. Gleich, Dr. H. Grothe, L. Hafner, M.Sc., Prof. W. Hemmert, U. Hopfner, Dipl.-Ing. F. Ilchmann, A. Michelfelder, Dipl.-Ing. (FH) M. Nicoletti, M.Sc., Dr. Angela Otto, Dr. H. Oswald, M. Remm, W. Ruppert, S. Schnell-Witteczek, and U. Wanka.

My deepest gratitude I owe to the persons that matter the most to me: My parents, Ina Mählmann-Meyer and Wolfgang Meyer; my aunt, Annette Mählmann; my brother, Klaus-Martin Meyer; Tiffany Kinney, her parents, sister and grandmother, Carolyn, Alvin, Tinel and Wanda Kinney. I feel both humbled and honored by the boundless love and support I have received from all of them, and I know that my words could never express how much their presence in my life means to me. In addition, all my friends that have been accompanying me along this segment of my life deserve the same appreciation.

Financial support for this work was kindly provided by the Heinz Nixdorf-Stiftung (grant “Evopot”), and the Charles Bowen Memorial Endowment to the Center for Network Neuroscience (University of North Texas).

Chapter One: Introduction 9

1.1 MOTIVATION 9
1.1.1 Rationale 9
1.1.2 Search for alternative cancer treatment strategies 9
1.1.3 Novel strategies for in vitro neurological research 11
1.1.4 Chemotherapeutic drugs under investigation 12
1.1.5 Anesthetic substances used in this study 13
1.1.6 Alzheimer's disease research 13

1.2 MAMMALIAN CELLS 15
1.2.1 General organization of biological cells 15
1.2.2 Tissue types 17
1.2.3 The cell cycle 18

1.3 ION CHANNELS 19
1.3.1 A (r)evolutionary concept 19
1.3.2 Influence on proliferation and the cell cycle 19
1.3.3 Electric properties 20
1.3.4 Voltage-dependent ion channels 22
1.3.5 Potassium channels and proliferation 24
1.3.6 Cellular membrane potential 24
1.3.6.1 The transmembrane potential 24
1.3.6.2 Membrane impedance model 25

1.4 COMMUNICATION BETWEEN MAMMALIAN CELLS 27
1.4.1 Cell-cell contacts 27
1.4.1.1 Gap junctions ("cell-cell synapses") 27
1.4.1.2 Influence on the cell membrane and proliferation 27
1.4.2 Intracellular communication pathways 28
1.4.2.1 Calcium fluctuations and oscillations 28
1.4.2.2 Influence of calcium on proliferation 30
1.4.2.3 Ion channels and cancer 31

1.5 THE ELECTRICAL CELL 32
1.5.1 Membrane potential and proliferation 32
1.5.2 Influence of electrical and magnetic fields on biological cells 34
1.5.2.1 Non-excitable cells in electromagnetic fields 34
1.5.2.2 Electric/magnetic fields, currents and proliferation 36
1.5.2.3 Electric and magnetic fields interfere with calcium-oscillations 37
1.5.2.4 Electrical and magnetic fields: molecular and other effects 38

1.6 ELECTRICAL AND MAGNETIC STIMULATION METHODS 39
1.6.1 Advantages and disadvantages of electrical and magnetic cell manipulation 39
1.6.2 Application type and waveforms for electrical and magnetic manipulation 40

1.7 ELECTRICAL SIGNAL TRANSDUCTION IN NEURONS 41
1.7.1 Physiology of neurons 41

1.7.1.1 Overview 41
1.7.1.2 Conversion of electrical into chemical signals 43
1.7.1.3 Neurotransmitters and receptors 43
1.7.1.4 The Equilibrium potential 44
1.7.2 Neuronal communication 45
1.7.2.1 The action potential 45
1.7.2.2 Hodgkin-Huxley formalism 46
1.7.2.3 The cable model 47
1.7.2.3.1 History 47
1.7.2.3.2 Unmyelinated axons 48
1.7.2.3.3 Myelinated axons 51
1.7.2.4 Neural networks 53

1.8 ELECTROPHYSIOLOGICAL EXPERIMENTS WITH NEURONAL CELL CULTURES 55
1.8.1 Intracellular and extracellular recording methods 55
1.8.1.1 Measuring membrane potential in excitable cells 55
1.8.1.2 Cell-electrode coupling 56
1.8.2 Signal acquisition requirements 61
1.8.3 Signal amplification 62
1.8.4 MEA recording and equipment: State of the art 62

Chapter Two: Materials and Methods 65

2.1 LIST OF MATERIALS AND DEVICES USED IN THIS STUDY 65
2.1.1 Devices 65
2.1.1.1 Cell culture 65
2.1.1.1.1 Sterilization 65
2.1.1.1.2 Cell preparation and incubation 65
2.1.1.1.3 Centrifuges 65
2.1.1.1.4 Microscopes 65
2.1.1.1.5 Other 65
2.1.1.2 Experimental workstation 66
2.1.2 Consumables 67
2.1.3 Chemicals 67
2.1.4 Animal tissue 67
2.1.5 Software 68

2.2 ELECTRICAL STIMULATION USING GLASS CHIPS WITH DEINSULATED ELECTRODES 68
2.2.1 Cell culture 68
2.2.2 Glass chips 69
2.2.2.1 Design 69
2.2.2.2 Pre-treatment 69
2.2.2.3 Growing cells on the glass chips 71
2.2.3 Generation and application of electrical pulses 71
2.2.4 Assembly of experimental components 72
2.2.5 Simulating the field geometry numerically 73
2.2.6 Current density on the glass chip 74

2.2.7 Experimental schedule 76
2.2.8 Staining dead cells with Trypan blue 77
2.2.9 Temperature control on the glass chip during stimulation 77

2.3 CAPACITIVE STIMULATION USING 6-WELL PLATES 78
2.3.1 Stimulation device design 78
2.3.2 Seeding of the cells 78
2.3.3 Signal generation 79
2.3.4 Field simulation using the finite-elements method 79
2.3.5 Current density in the 6-well plate 79
2.3.6 Experimental setup and schedule 80
2.3.7 Electrical stimulation using a 6-well stimulator with IDES structures 82
2.3.8 Field simulation of the IDES structures 82

2.4 MAGNETIC STIMULATION 83
2.4.1 Comparison of different stimulation coil geometries 83
2.4.2 Magnetic field simulation of the miniaturized coil 85
2.4.3 Signal generation and application 85
2.4.4 Current density at the site of the cells 86
2.4.5 Seeding of the cells on the magnetic stimulation glass plates 87
2.4.6 Experimental setup 88
2.4.7 Experimental schedule 90

2.5 NEURONAL NETWORK EXPERIMENTS 91
2.5.1 Neuronal cell culture 91
2.5.1.1 Material preparation 91
2.5.1.2 Tissue isolation 92
2.5.1.2.1 Preparation 92
2.5.1.2.2 Animal dissection 94
2.5.2 Frontal cortex dissection 96
2.5.3 Midbrain dissection 97
2.5.4 Cell separation and seeding 98
2.5.5 Maturation of the neuronal cultures 99
2.5.6 Recording equipment 102
2.5.6.1 Multi-microelectrode plates 102
2.5.6.2 Plexon amplifier and signal acquisition system 103
2.5.7 Eight-network recording system 105
2.5.8 Experimental procedures 107
2.5.8.1 Conducting a compound titration 107
2.5.8.2 Interpretation of experimental data 108
2.5.8.3 Analysis approaches: Overview 110

Chapter Three: Electrical and magnetic manipulation of tumor cell growth 112

3.1 ELECTRICAL STIMULATION 112
3.1.1 Glass chips with deinsulated stimulation electrodes 112
3.1.1.1 Retardation of cell proliferation 112
3.1.1.2 Quantification of dead cells 114
3.1.1.3 Temperature control recording 115

3.1.2 Electrical stimulation in 6-well-plates 116
3.1.2.1 Effect on cell proliferation 116
3.1.2.2 Cell morphology 118

3.2 MAGNETIC STIMULATION 120

Chapter Four: Neuronal network experiments and data interpretation 122

4.1 RECORDINGS 122
4.1.1 Midbrain recordings 122
4.1.1.1 Characterizing typical midbrain activity patterns 122
4.1.1.2 Analysis of unit-specific responses: 125
4.1.1.3 Disinhibitory effects of bicuculline on midbrain tissue 127
4.1.2 Frontal cortex networks under bicuculline 132
4.1.2.1 Example 1: Low number of units 132
4.1.2.2 Example 2: High number of units 136

4.2 MIDBRAIN RESPONSES TO ETHANOL 139
4.2.1 Example recording 139
4.2.1.1 Summary of data from two networks 143

4.3 LIDOCAINE EXPERIMENTS 145
4.3.1 Frontal cortex 145
4.3.1.1 Sample recording I 145
4.3.1.2 Sample recording II 147
4.3.1.3 Summary of data from 11 networks 149
4.3.1.3.1 Dose response curve using network mean before normalization 149
4.3.1.3.2 Dose response curve using initial normalization with subsequent calculation of the network median activity 150
4.3.2 Midbrain 151
4.3.2.1 Sample recording I 151
4.3.2.2 Sample recording II 155
4.3.2.3 Summary of data from seven networks 157
4.3.2.3.1 Dose-response curves generated with standard calculation of average: 157
4.3.2.3.2 Dose-response curves generated with median of normalized data: 158

4.4 BARBITAL-SODIUM EXPERIMENTS 159
4.4.1 Frontal cortex, data from three networks 159
4.4.1.1 Network averages calculated before normalization 159
4.4.1.2 Network median after normalization 160
4.4.2 Midbrain, data from two networks: 161
4.4.2.1 Network averages before normalization 161
4.4.2.2 Network median after normalization 162

4.5 CISPLATIN EXPERIMENTS 163
4.5.1 Frontal cortex responses 163
4.5.1.1 Sample recording 163

4.5.1.2 Morphology of the neurons under CisPt 165
4.5.1.3 Summary data from six networks 167
4.5.2 Cisplatin responses after preincubation with 0.3 mM vitamin C 167
4.5.2.1 Data from 2 networks 167
4.5.3 Midbrain responses: 168

4.6 CHLOROACETALDEHYDE EXPERIMENTS 169
4.6.1 Frontal cortex responses 169
4.6.2 Midbrain responses 172

4.7 AMYLOID-BETA EXPERIMENTS 173
4.7.1.1 Analysis summary 173
4.7.2 PH-buffer tests 175
4.7.2.1 Effects on activity levels 175
4.7.2.2 Burst parameter analysis 176
4.7.2.2.1 Detailed analysis: Number of spikes per burst 179
4.7.2.2.2 Detailed analysis: Spike frequency inside bursts 184
4.7.3 A-beta monomers and oligomers 188
4.7.3.1 Example recording with monomers 188
4.7.3.2 Example recording with dimers 193

4.8 MULTI-NETWORK TITRATION OF MUSCIMOL WITH A LIQUID HANDLING ROBOT 199
4.8.1 Simultaneous recording of eight networks: 199
4.8.2 Analysis with initial normalization of individual units, using medians: 204
4.8.3 Calculation without initial normalization of individual units, network means: 205
4.8.4 Excluding networks 2 and 7: 206

4.9 MICROCHIPS FOR 24-NETWORK PLATFORM 208
4.9.1 Morphological assessment 208
4.9.2 First recording 210

Chapter Five: Discussion 213

5.1 ELECTRICAL AND MAGNETIC INHIBITION OF L929 CELL PROLIFERATION 213

5.2 NEURONAL NETWORK EXPERIMENTS 217

Chapter One: Introduction

1.1 Motivation

1.1.1 Rationale

The scope of this work spans novel systems designed to analyze and manipulate functional states of epithelial and neuronal cells. These cell types are of particular interest, because they are the medium of a plethora of diseases, some of which have always been around, but many others of which have been growing agonizingly fast over the past centuries, even decades. According to the World Health Organization (WHO), several kinds of cancer, which routinely affect many different kinds of epithelial tissue, are among the top 10 leading causes of death in "high-income countries". Dementia and Alzheimer's disease (AD), both neurodegenerative ailments, rank sixth [1]. The ongoing advances in general health care, nutrition, and prevention of premature death have led to increasing life-expectancies, and thus to a rapidly growing population of elderly persons who suffer from slowly progressing diseases, such as neurodegenerative diseases and cancer, for which modern medicine has not been able to develop any protective strategies.

1.1.2 Search for alternative cancer treatment strategies

Currently, treatment of cancer is still very difficult - unless caught very early on - one of the reasons being that there is a vast number of different cancer types. Each tumor theoretically requires its own, special treatment that is tailored around the specific diagnosis. Based on the currently available techniques, oncologists can only narrow down their choice of a chemotherapeutic drug for a given tumor to about 3 potential candidates, on average. This means that the chances of a successful treatment are 1/3, at best. Most chemotherapeutics are highly aggressive substances that are designed to preferentially destroy tumorous tissue, but healthy cells are always attacked, too, which usually leads to severe side effects. Recently, efforts have been made to bind antibiotic and chemotherapeutic substances to ferromagnetic nano-particles and hold them in the desired place using strong, externally applied, magnetic gradient fields [2, 119]. This approach certainly holds promise for future therapeutic strategies, but it requires sophisticated, expensive machinery that clinics in many countries will not be able to afford. Taking all these problems into account, one does not have to be a psychic to realize that new types of cancer treatment are needed. The new therapeutic approach should be effective for as many types of cancer as possible, easy to apply locally, non- or minimally invasive and as economic as possible. Based on previous studies that show that a common feature of all cancer cell types is a disturbance in the electrical properties of the cell membrane [10, 22, 28, 34], we have chosen to explore the possibilities of retardation of tumor cell proliferation utilizing electrical and electromagnetic fields and currents.

Electrical interactions have been defining and controlling the interactions of cellular and subcellular structures since life first came into existence on Earth. Miller

showed in 1953 that amino acids could be synthesized from H_2O, CH_4, NH_3, and H_2 using an electric discharge [139]. The next step toward cellular life was to create a separation of the inside from the outside. Several lines of evidence suggest that simple lipid layer membranes formed as spontaneously as the amino acids using the available molecular building blocks, and that membranes were actually necessary for the amino acids to polymerize [138] and for DNA and RNA to form [137]. Ion gradients that followed the inherent charge distributions of the polar membrane lipids drove dynamic reactions that gave rise to successive intracellular structures, including the incorporation of transmembrane proteins and the establishment of a potential difference between the inside and the outside. This potential difference became the driving force for numerous cellular processes and a means of communication with the outside world. In mammalian cells, lipid bilayer membranes are between 5 and 20 nm thick, which implies that small voltages across the membrane create enormous local field strengths: 1 mV would translate to ~10 kV/cm. These fields may be strong enough to interact with neighboring intracellular systems. In fact, several publications have shown that there is a strong, general correlation between the transmembrane potential (TMP) and the mitotic behavior of mammalian cells [10, 134]: Mitotically active cells – both regular and neoplastic ones - do not repolarize after a division. Their resting TMP remains less negative than approximately -40 mV, while cells that do not spontaneously divide have a more strongly polarized membrane with TMP values between -40 and -100 mV (fig. 1.1). This observation led to the question: Can the mitotic activity of tumor cells be manipulated using electromagnetic methods that interact with the TMP?

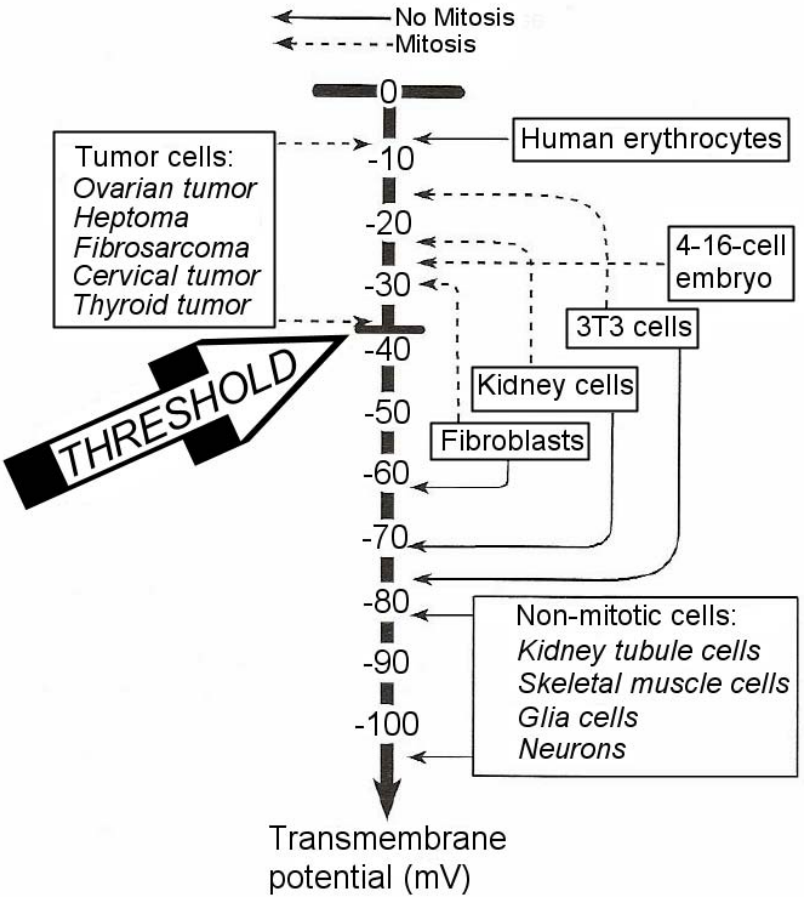

Fig. 1.1: Resting potentials of dividing and static normal versus neoplastic cells [redrawn from 15]

1.1.3 Novel strategies for in vitro neurological research

Another class of mammalian cells that depend strongly on their TMP in order to function properly are neurons. In fact, neurons are highly specialized in utilizing and manipulating their own and other cells' TMPs in a way so complex that researchers worldwide have not been able to unlock all the secrets of their inner workings. What has been observed in cortical neurons in vivo is a power-law relationship of the synaptic input, which influences the TMP, and the output firing rate: "The presence of membrane potential variances induces a nonlinear relationship between membrane potential and firing rate", as Haider et al. point out [135]. Other than synaptic input, a vast variety of chemical and physical influences can alter the neuronal membrane potential, and thus firing rates, as well. Since most of the information computed in the brain is in some way encoded in firing patterns, these influences consequently manipulate the functionality of the neuronal networks. Disturbances of neuronal function, such as memory loss, behavioral impairments, or life-threatening seizures, can be caused by many chemical substances: toxins, pollutants, heavy metals, altered proteins, or medical drugs (e.g. from an overdose or from side-effects). Depending on the substance, dose and exposure time, the symptoms may appear within minutes, hours, weeks, even decades. Chemical neurotoxicity has been studied using a range of methods, but none of them seems to hold as much potential as the emerging technology of recording electrical activity of neurons grown on multielectrode arrays (MEAs). The neuronal networks one can analyze with this methodology are very small (a few dozen to a few hundred neurons), yet large enough for basic intercellular communication and information processing to occur. Changes in the microenvironment of the neurons are sensitively and immediately translated into activity changes, which can be directly monitored.

Recording the electrical activity of large ensembles of neurons simultaneously over prolonged periods of time is an ability researchers have been attempting to achieve over the past several decades. Ideally, these recordings should be entirely non-invasive, long-term stable, economically and temporally efficient and highly reproducible. In vivo experiments using primates would obviously yield results with the highest certainty of being applicable to humans. However, many neuronal cell types appear to be less species-specific than one might expect. In fact, in vitro studies using planar, metal MEAs, have shown that pharmacological responses to a large variety of substances are comparable throughout many different mammalian species [3]. By bringing the neurons to the electrodes, rather than bringing the electrodes into the brain, a powerful tool for many applications in neurobiological research is now available. These applications range from neuro-developmental studies, neuro-informatics and network-neurophysiology to trauma and pathology, environmental toxicology, pharmacology and drug-development and tissue-based biosensors. The latter three application areas are especially important in the context of neurodegenerative disease research, development of respective drugs, and screening of other drugs for possible toxicity in the nervous system. Side effects on every part of the CNS can be quantified, as virtually any part of the embryonic, mammalian central nervous system can be cultured on the MEA plates. For efficient analysis and screening of these substances, a system is needed that can record from many cultures at once. The results of this study show that the present experimental setup is suitable for pharmacological and toxicological research, yielding reliable, significant results. However, large-scale

screening of potentially neurotoxic substances will not be achievable as long as an automated multi-network system is not available.

1.1.4 Chemotherapeutic drugs under investigation

Many cytostatic drugs as well as local and systemic anesthetics have been shown to exhibit neurological side effects. These rare but serious effects are difficult to diagnose. While complications involving parts of the peripheral nervous system are well recognized, the attention given to acute side effects to the central nervous system does not match the severity of the problem. A novel approach to quantifying the neurotoxicity of these drugs is needed. By measuring the changes in total action potential (AP) production as well as the internal activity pattern using MEAs, functional, reversible toxicity and cytotoxicity can be monitored with great accuracy and reliability.

Cisplatin (CisPt) is an anti-cancer drug widely used for bladder, testicular, ovarian, prostate and small cell lung cancers. Severe side effects are mainly concentrated on the kidneys, the inner ear and the peripheral and central nervous system. CisPt interferes with protein function, for example in mitochondria, and its cytotoxic activity is mediated by formation of Pt-DNA adducts that result in blockage of DNA transcription and replication. In the nervous system, cell bodied of peripheral sensory neurons and dorsal root ganglia have been identified as sites of major damage. Furthermore, blockage of sodium and potassium currents in myelinated axons has been reported [77]. Another publication claims that CisPt can cause a decrease of glutathione levels and inhibition of ATP synthesis. Glutathione is an important intracellular antioxidant. Also, clinically relevant doses of CisPt (1 – 100 μM) were shown to reduce currents of voltage-gated calcium channels of small dorsal root ganglion neurons by up to 76% within three to four minutes [78]. Searching for compounds that could serve for protection from cisplatin, ascorbic acid (vitamin C) was found to be able to scavenge reactive oxygen species (ROS) by rapid electron transfer. It has been shown to reduce lipid peroxidation in the liver and brain. Lipid peroxidation is one or the primary effects induced by oxidative stress [79].

Another chemotherapeutic drug under investigation in this study is Ifosfamide. Since Ifosfamide is metabolized into its active compounds in the liver, its most neurotoxic metabolite, chloroacetaldehyde (CAA) was used here. The clinically relevant concentrations of CAA can reach values as high as 20 μM. In experiments with hepatocytes, a 50% viability decrease after two hours under 300 μM CAA was observed. The mode of action, however, is not quite clear. CAA causes a number of physiological changes, such as reduction of ATP levels due to blockage of oxidative phosphorylation in mitochondria, DNA strand breaks, and inhibition of DNA synthesis. Like Cisplatin, it also causes depletion of glutathione from cells and induction of lipid peroxidation [80]. There are only a few clinical studies on the side effects of Ifosfamide, and they show that CAA serum concentrations were highly elevated in patients with Ifosfamide-induced encephalopathy. As treatment for these encephalopathies, methylene blue has been employed, which acts as an electron acceptor. Studies that show correlations between the pharmacokinetics of CAA and the neurotoxicity of Ifosfamide are needed. The lack of high-throughput bioanalytical methods has been the limiting factor in Ifosfamide research [81].

1.1.5 Anesthetic substances used in this study

The effects of two different classes of anesthetics were explored: Local and systemic. Substances like these, which specifically bind to or block neuronal receptors, are predestined to be explored by the MEA system. The local narcotic under investigation is lidocaine. This substance, first synthesized under the name xylocaine by Swedish chemist Nils Löfgren in 1943 [82], blocks voltage-gated sodium channels and is primarily used as a topical anesthetic, but also as an antiarrhythmic drug. Systemic toxicity of lidocaine resulting in central nervous and cardiovascular malfunction has been reported. The symptoms can be biphasic with an initial, selective blockage of inhibitory neurons, leading to seizure potentials. Then, at high concentrations, excitatory neurons are blocked, resulting in coma, apnoeic episodes and circulatory failure [83]. Another study [84] agrees that lidocaine can produce seizures when injected repeatedly. It can cause central excitation by suppression of inhibitory neurotransmission, specifically suppression of the gamma-aminobutyric acid (GABA) receptor. In the intact brain, epileptiform activity appears whenever the potency of GABAergic transmission is diminished. These side effects have not been studied systematically.

One of the groups of substances that have not been investigated extensively using MEA-based neuronal bioassay systems are non-opioid anesthetics, such as barbiturates, benzodiazepines, or ketamine. These substances are widely used, although they are not absolutely reliable and controllable. According to a 2004 study, 0.1 – 0.2% of all patients undergoing general anesthesia experience premature recovery from narcosis [105]. Barbital-sodium is the most basic and oldest member of the barbiturate systemic anesthetics. It is five to seven times less effective than pentobarbital, a modern barbiturate. Brain concentrations of 100 µM induce anesthesia reliably, which implies that the effective concentration of barbital-sodium should be 500 µM. There are a number of hypotheses on the mode of action of barbital-sodium [85]: It is capable of altering ion channels and membrane-bound enzymes, decreasing the surface charge of neuronal membranes and enhancing the fluidity of membrane lipids (which has also been observed in experiments with ethanol). It can also block calcium accumulation in autonomic ganglia and in brain synaptosomes (isolated synapses), and it reduces the calcium content of synaptic membranes. Another proposed mechanism is enhanced synthesis of GABA, attenuation of the effects of GABA antagonists and elevated activity of muscimol, a GABA agonist. In summary, inhibition of excitatory transmission through decrease of postsynaptic effects of excitatory neurotransmitters and inhibition of presynaptic transmitter release are likely mechanisms of action.

1.1.6 Alzheimer's disease research

AD is characterized by the appearance of neuritic plaque deposits comprised primarily of fibrillar and ß-sheet rich aggregates of the amyloid ß peptide, which is produced normally by the intramembrane proteolysis of APP, a protein of unknown function, throughout life. APP is cleaved by β–secretase, discarding its ectodomain. The remaining 99-amino acid long membrane-bound residue is then further cleaved by γ-secretase, producing different types of β-amyloid protein (Fig. 1.2). The most common form of Aβ is 40 amino acids long ($A\beta_{1\text{-}40}$), followed by $A\beta_{1\text{-}42}$. The latter

aggregation type is particularly associated with disease [86]. Different lines of evidence suggest that oligomer intermediates rather than the mature fibrillar deposits are responsible for the primary neurotoxic effects and memory loss in AD, possibly by membrane incorporation and pore formation in neuronal membranes. To date, there is no effective treatment that can prevent progression of AD. The drugs available can only delay the progression of the disease [87].

In low-density cortical cultures, beta-amyloid induced morphological changes (thickening and retraction of dendrites) have been observed after 12 hours incubation, perikaryal degeneration and neuronal loss after 24 hours [88]. Recent studies have shown that the beta-amyloid peptide may also interfere with several different cellular structures such as the NMDA receptor [89] and mitochondria [90]. These findings point towards a new understanding of how beta-amyloid peptides may induce memory malfunction in early stages of AD where robust diagnosis is presently almost impossible.

In the past, in vitro investigations of beta-amyloid neurotoxicity have yielded inconsistent results. Many different model culture systems have been employed, most of which had low neuronal survival periods. Another compromising variable is the nature of the A-beta peptide used. Even when provided from a single source, results obtained in different laboratories were irregular. Moreover, the choice of the solution the peptides are stored in seems to be of crucial importance, both in *in vitro* and *in vivo* studies [91].

It is possible that the aggregation state of the peptide is a decisive factor in the grade of neurotoxicity [92]. Aβ oligomers can inhibit hippocampal long-term potentiation [94, 95], impair complex learned behavior in the live rat [95], and reduce the density of dendritic spines in cultured hippocampal neurons [97, 98]. A recent study [98] found the dimer configuration to be particularly neuroactive and toxic. $A\beta_{1\text{-}42}$ has been shown to not be toxic by itself, but to promote excitotoxicity of glutamate at a concentration of 22 μM [99]: Brief exposure to glutamate, NMDA or kainite – at concentrations too low to be toxic on their own – caused significant neurodegeneration. Another study claims that beta-amyloid also destabilizes neuronal intracellular calcium levels [100].

The use of MEAs to characterize acute neurotoxicity of different species of amyloid beta peptide on primary cultures of frontal cortex neurons has been reported before [101], but it has not been carried out systematically. In particular, artifactual activity decrease due to the biochemistry of the pH-buffers the amyloid peptides are stored in, have not been taken into account. $A\beta_{25\text{-}35}$, $A\beta_{1\text{-}42}$ and $A\beta_{1\text{-}40}$ were applied at 50 μM, and they induced activity decreases of 90%, 60% and 40%, respectively. The use of MEAs as a research tool for neurodegenerative diseases has not been explored extensively enough. Employed properly, MEA-based electrophysiological analysis of neuronal activity can surely be of great value, especially since the application of neuroactive substances is well controllable. This, of course, also holds true for pre-treatment with protective substances. A number of compounds that may be able to protect neurons from amyloidogenic toxicity have been proposed, e.g. curcumin [102], Hematin, o-Vanillin and many histochemical dyes [103]. Moreover, recent studies have reported that antibodies specific to oligomer, but not monomer Aβ aggregates, are very effective in scavenging Aβ oligomers in soluble extracts of diseased brains. [104]

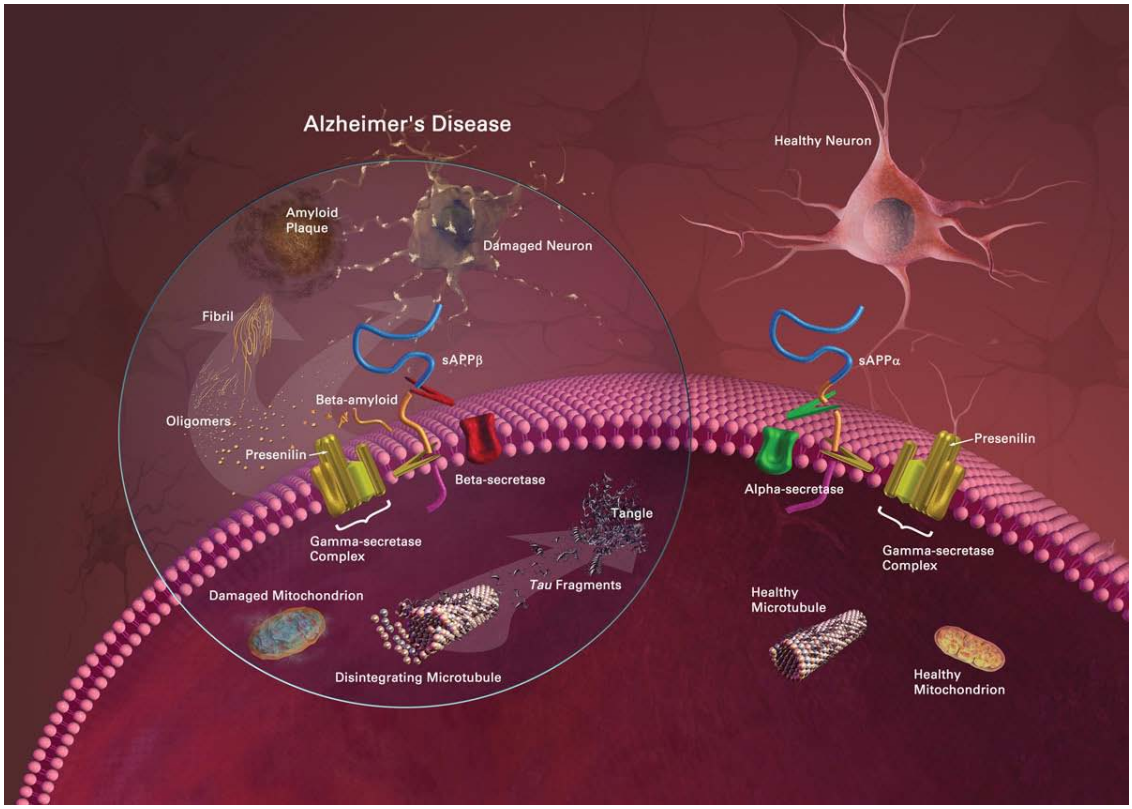

Fig. 1.2: Process of amyloid generation through cleavage of the beta-amyloid precursor protein APP leading to abnormal aggregations of fibrils and plaque (left) versus a healthy neuron (right) (illustration from US National Institutes of Health, National Institute on Aging: ADEAR Home > Publications > Progress Report on AD 2004-2005 > Part 3: 2004-2005 AD Research Advances. URL of the picture: http://www.nia.nih.gov/NR/rdonlyres/BF555973-D7E2-4C98-A81F-8E27B689A9BA/2659/03_players_big1.jpg)

1.2 Mammalian cells

1.2.1 General organization of biological cells

All mammalian cells share some common characteristics, despite sometimes extreme degrees of specialization for certain physiological functions. The most fundamental one is their ability to separate the extracellular space from the interior in a tightly controlled fashion: Cells are generally permeable to certain ionic particles, but - in healthy cells - the transmembrane traffic of these ions is never random and always serves some physiological purpose. Whenever the control of this ionic flow is disturbed, essential cellular mechanisms may lose their functional integrity. This may then lead to temporary or chronic cellular and organic malfunctions, which manifest in what is commonly referred to as diseases.

Another way nature has provided structure to all cells is compartmentation. In analogy with the distribution of physiological functions to organs in the body, single

cells possess organelles which carry out specific tasks. A typical animal cell contains the following organelles with their respective physiological functions (Fig. 1.3):

1. Nucleolus: Ribosome synthesis, transcription of messenger RNA.
2. Nucleus: “Control center”, maintenance of genetic integrity, regulation of cell activity and gene expression.
3. Ribosome: Translation of the genetic code into protein structure.
4. Vesicle: Storage, transport and digestion of cellular products and waste.
5. Rough endoplasmic reticulum: Production of lysosomal enzymes, secretion of proteins, glycosylation.
6. Golgi apparatus (or "Golgi body"): Modification of proteins delivered from the ER, creation of lysosomes, transport of lipids, creation of proteoglycans, carbohydrate synthesis, phosphorylation.
7. Mitochondrion: Generation of ATP, heat production, storage of calcium ions, regulation of membrane potential, apoptosis, proliferation regulation, steroid production.
8. Vacuole: Isolation of harmful substances, export of waste products.
9. Lipid bilayer membrane: Separation of inside of the cell from the outside, protection of organelles, substrate and backbone for cell-cell-contact and communication; contains transmembrane proteins such as ion channels and gap junctions.
10. Cytosol (in between other structures in figure 1.3): Substrate for cell processes such as signal transduction, cytokinesis, transport of metabolites, and maintenance of cell structure, osmolarity and pH.
11. Lysosome (not visible in figure 1.3): Digestion of excess organelles, food particles, viruses and bacteria.
12. Centriole (not visible in fig. 1.3): Organization of the mitotic spindle, cytokinesis, and spatial arrangement of organelles.
13. Cytoskeleton (in between other structures in fig. 1.3)
    a. Actin filaments for giving structural stability by resisting tension and maintaining cellular shape, forming cytoplasmic protuberances, cell-to-cell or cell-to-matrix junctions (signal transduction), and cytokinesis.
    b. Intermediate filaments for bearing tension, anchoring organelles, and supporting the nuclear lamina and sarcomers.
    c. Microtubules for providing structural stability by resisting compression, transporting organelles like mitochondria and vesicles, and assembly of the mitotic spindle.

14. Smooth endoplasmic reticulum (not visible in fig. 1.1): Synthesis of lipids and steroids, metabolism of carbohydrates, regulation of calcium concentration, drug detoxification, attachment of receptors on cell membrane proteins, and steroid metabolism.

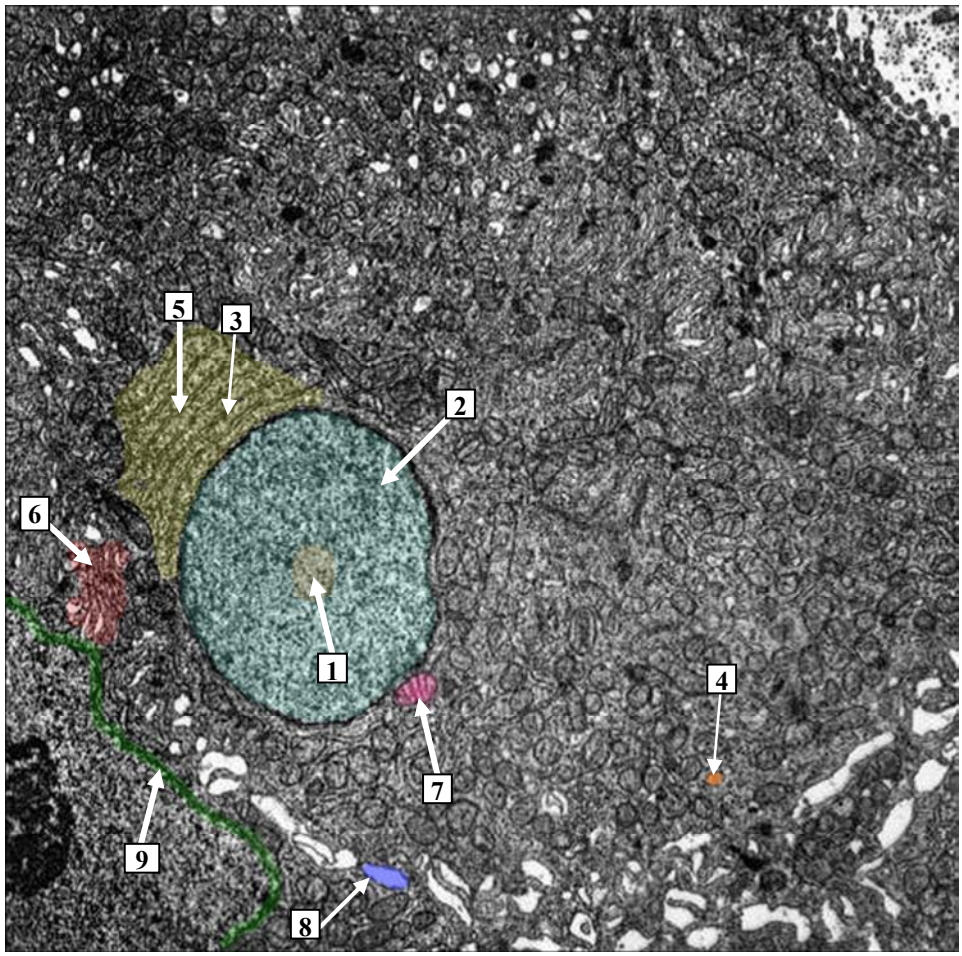

Fig. 1.3: Transmission electron micrograph: Cross-section of a biological cell. Artificially colored are some of the subcellular structures listed above [with permission of the publisher of 140].

1.2.2 Tissue types

Mammalian tissue is composed of four basic cell types: Epithelial, connective, muscle and nerve cells. Loose connective tissue, bones, blood, adipose tissue, tendons and cartilage are the different types of connective tissue. Muscle cells are highly specialized cells that are either controlled voluntarily (skeletal muscle) or unconsciously (smooth muscle of the internal organs, cardiac muscle). Muscle cells are usually organized in fibers in an orderly fashion. They contain myofibrils, which are responsible for their ability to contract and thus generate movement of the muscle tissue. Muscular cell-cell communication can take place via direct electrical coupling through special gap junctions, which consist of the so-called connexins (see section 1.4.1.1). Muscular electrical signaling creates membrane-potential fluctuations similar

to neural APs, except in the heart where AP durations are in the range of several hundred milliseconds due to relatively slow calcium channels being involved in the process. Epithelial cells make up most of the organs except the heart and the smooth muscle of the lungs and gut. This family of cell types is the most versatile one in terms of physiological function. Their shape is squamous, cuboidal or columnar, while their formation can be single-layered, stratified with several layers or pseudo-stratified, and some specialized epithelial cells can also be equipped with keratin or cilia. Neurons are the most fragile and sophisticated cells in the adult mammalian body. They are equipped with a multitude of ion channels and receptors that allow them to perform their extremely intricate and specialized functions in a highly controlled manner. Once fully differentiated, they cannot undergo mitosis, unless they become tumorous. They constitute the central and peripheral nervous systems and are specialized in processing and transferring information. Common to all neurons are three components: The cell body which internally converts the informational input signal(s) into an output signal, the dendrite(s) which receive the signal from another cell, and the axon which conducts the new signal to the next cell(s).

1.2.3 The cell cycle

Two main phases of the cell cycle can be distinguished easily: Mitosis (cell division) and interphase, the time between two divisions. During this period, the cell activity is higher than during mitosis, and the chromosomes which carry the DNA are unraveled. Interphase is composed of three sub-periods:

- The G_0 – phase, also called G_0 – arrest, is characterized by mitotic inactivity. During the G_1 – phase, synthesis of RNA takes place, which induces cell growth, and the chromosomes are diploid and consist of one chromatid each. The temporal progression of G_0 and G_1 can vary largely for cells that have not divided in a long time.
- The S – phase is usually seven to eight hours in duration and serves the purpose of replicating the DNA, so that a second chromatid is added to every chromosome.
- During the G_2 – phase, the DNA gets inspected for possible replication errors and repaired, if necessary.

Subsequently, the following four steps comprise the mitotic phase:

- During prophase, the chromosomes become condensed and are now visible in the light microscope. The centrioles move towards the poles of the cell and determine the position of the plane of cell division. Disintegration of the nuclear membrane and the nucleoli follow next.
- Metaphase is the period during which the spindle fibers connect to the kinetochores on the centromers, the central structures of the chromosomes. This way, the chromosomes are positioned in the plane of cell division.
- Following metaphase, the kinetochores split up, and the spindle fibers are shortened, separating the chromatids and pulling them towards the poles. Thus, there is now one diploid chromosome set with one chromatid each at each pole. This process is called anaphase.

- Finally, new nuclear membranes are generated during telophase. The cell divides (cytokinesis), new nucleoli are made and the chromosomes re-condense.

1.3 Ion channels

1.3.1 A (r)evolutionary concept

From an evolutionary point of view, the earliest self-replicating biological cells may not have had any active contact with the outside world, in particular with other cells. However, for life forms consisting of more than one cell to become a successful concept in nature, the need for communication with neighboring cells was certainly given. In order to exchange material or information with the outside world, openings in the cell membrane became a necessity. The concept nature has developed for this controlled exchange is both versatile and intricate: A combination of active transport mechanisms and passive valves maintains an electrochemical gradient, which stems from an uneven distribution of variously charged ions along the membrane. This allows the cell to activate and deactivate defined inbound or outbound ionic currents by opening or closing valves for short periods of time. The speed at which ions are exchanged via ion channels is eleven orders of magnitude higher than plain diffusion through the lipid bilayer membrane and three orders of magnitude higher than through active "pump" or carrier proteins [5].

Different types of ion channels are distinguished and categorized by their gating type, ionic conductance, ion selectivity, sensitivity to blocking agents and inactivation type. In terms of activation and inactivation control, there are two dominant categories of ion channels: ligand-gated and voltage-gated. This classification is not absolute, since some ligand-gated channels can also be voltage-sensitive. Ligands are molecules such as neurotransmitters and amino acids, or ions that can bond to a respective terminal on one of the ion channel segments and set off a reaction that causes the pore inside the channel to open or close.

1.3.2 Influence on proliferation and the cell cycle

Ion channels are transmembrane proteins accessible from the outside environment. Therefore, biological agents such as toxins or antibodies can be used to target and manipulate them. The fractional area of the cell membrane covered by channel pores is 0.01 – 0.1 % [6]. The role of ion channels in non-excitable cells is not completely understood. The best-researched role of voltage-gated ion channels is the maintenance of the TMP. A very important, active ion channel, especially in excitable cells, is the pump protein K^+- Na^+- ATPase. It exchanges internal Na^+ for external K^+. The pumping rate increases significantly with Na^+ - entry, which is paramount in the process of APs. Another active pump protein is the Na^+ - H^+ - exchanger, which is

believed to be involved in the regulation of pH as control of mitogenic activity [7]. Receptor-operated calcium channels are often non-selective, which means they can also be permeable to Na^+ and K^+ ions. Second-messenger operated calcium channels (SMOCs) open when external agonists bind to membrane receptors which release intracellular messengers that interact with the SMOCs [8].

The activity - or inactivity - of ion channels is clearly linked to many processes of cell proliferation. However, it is difficult to correlate proliferation with the activity of a particular ion channel. As an example of the cell's sensitivity to ion channel action, the activation rates of Cl^- — and K^+-channels must stay within a certain range to support proliferation; otherwise apoptosis is triggered [9]. Similarly, elevated sodium permeability and intracellular sodium concentrations are an indicator of proliferative activity, both in normal and tumorous cells. The sodium fluctuations measured in this context cannot be explained solely by the activity of the Na^+- H^+- antiporter. A possible explanation for the sodium-dependence is that DNA repressors strongly depend on Na^+ concentration [10].

1.3.3 Electric properties

The activity and conformation of channel proteins may largely be controlled by the TMP, because of their general nature of carrying charged molecular sub-groups. Membrane potential fluctuations as small as 5 – 10 mV can induce protein state transitions, for example changes in the conductance of Na^+ - and K^+ - channels in excitable cells. In small cells, the opening of one single channel can change the resting potential noticeably, for example in dendritic spines. Vice versa, charge movement from channel activity can also affect the membrane potential: Localized electric fields can arise from opening or closing of ion channels, which in turn affects the open/closed properties of neighboring cells [11]. The gating molecules of different channels in the same membrane experience varying local electric fields, which means that shifts in channel kinetics do not always translate to respective changes in TMP. Binding of divalent cations or charged molecules to the channel protein changes the local electric field and may disrupt the gating mechanism of the channel [12].

Ion channels are not singular structures but are composed of a number of sub-units: K^+-channels consist of four subunits, Na^+- and Ca^{2+}-channels of one protein with four homologous domains. Each one of the subunits or domains is made up of six transmembrane segments (S1-S6) and one pore loop. S5 and S6 and the pore loop are responsible for ion conduction. It is likely that in voltage-dependent potassium and sodium channels, the S4 segment, which is positively charged, functions as the voltage sensor. Membrane depolarization may open the channel by moving S4 outward, thus generating the gating current [13]. Some researchers hypothesize that S4 is generally the voltage sensor, others, that it can be anywhere in the S1 – S4 region [14]. The alpha-helix, a part of the S4 segment, has a very large dipole moment that acts like a half unit charge [11]. In order for the voltage sensor to transfer large amounts of charge, there is no need for a large movement, since the electric field is concentrated in a very narrow region of the protein. Voltage-gated channels consist of a voltage sensor, a pore (or conducting pathway), and a gate. The channel can be thought of as a field effect transistor, since the conduction is dependent on the transmembrane voltage. However,

gating of the channel is not produced by a change in space charge, but by mechanical obstruction to flow [14].

There are two types of electrical currents associated with the activity of voltage-gated ion channels: Ionic currents and gating currents. The gating currents result from the pore opening that follows the translocation of positive charges from the inside to the outside after membrane depolarization. They only occur in the potential range where the sensor responses to the electric field, and can be thought of as nonlinear capacitances. The driving force for a specific ion corresponds to the applied voltage minus the reversal potential (at which there is no ionic flow). If the channel is perfectly selective to one type of ion, then the reversal potential is the Nernst potential. For membrane potentials exceeding -40 mV, ionic currents are not activated significantly when a voltage is applied, whereas gating currents are always visible, which means that there is charge displacement at potentials where most of the channels are closed [14]. The estimated amount of charge per channel is 12 to 14 e_0, implying a very steep voltage dependence:

$$P_o \propto e^{\frac{c_T V}{kT}}, \qquad \textbf{1-1}$$

where c_T is the gating charge per channel (charge when open for traverse), and V is the applied voltage. At potentials more negative than -40 mV, there is no open probability: $P_o = 10^{-5}$ at -100 mV [14]. Assuming that the time constant τ_p of the channel is much larger than the relaxation time τ_{vs}, and that $1/\tau_p << \omega_0 << \tau_{vs}$, the fraction of the voltage sensors in the open state is given by:

$$\eta_o(\omega_0 t) = \frac{1}{1+\left(\frac{-Ze\left(V_0 - \overline{V} + V_m \cos\omega_0 t\right)}{kT}\right)}, \qquad \textbf{1-2}$$

where the DC membrane potential is V_0, the applied potential is $V_m \cdot \cos\omega_0 t$, $\overline{V}$ is the membrane potential at which the fraction of open channels is equal to the fraction of closed channels, Z is a positive integer, and e is the elementary charge. Knowing the voltage dependent conductance of the ionic pathway γ, the current flow through one open, conducting pore is

$$i = \gamma\left(V - \overline{V}\right), \qquad \textbf{1-3}$$

where V is the applied voltage and $\overline{V}$ is the voltage at which there is no flow. With the channel density N and the voltage- and time-dependent open probability P_o (V, t), the macroscopic current is

$$I = P_o(V,t) N\gamma\left(V - \overline{V}\right). \qquad \textbf{1-4}$$

1.3.4 Voltage-dependent ion channels

As stated earlier, the transport of ions across the cell membrane serves plenty of intracellular, physiological functions, be it regulation of pH or cell volume, Ca^{2+} - concentration, and many other processes that impact, for example, protein synthesis and proliferation control. Both passive and active ionic transport can take place in an electronically neutral fashion (ionic charges annihilate each other due to reciprocal flow of ions with equal, total amounts of opposite charges), or in a rheogenic way (an electric current is flowing). Table 1.1 summarizes the ionic transport systems in biological membranes known to date.

	Passive transport				**Active transport**	
	Diffusion		Co-transport		Transport – ATPase	
	Pore	Channel	Symport	Antiport		
Electroneutral			Na^+, K^+-$2Cl^-$ K^+-Cl^- Na^+-Cl^-	$Cl^-HCO_3^-$ Cl^-- Cl^- Na^+-H^+ K^+-H^+		Na^+-H^+-ATPase
Rheogenic	Na^+, K^+, Cl^-	Na^+, K^+, Cl^-		$3Na^+$-Ca^{2+} H^+-Ca^{2+}	H^+-ATPase Ca^{2+}-ATPase	$3Na^+$-$2K^+$-ATPase

Table 1-1: Ionic transport systems in biological membranes

An example for passive transport is the electrodiffusion through Na^+- und K^+- channels. The term co-transport implies the transfer of two or more ions by transmembrane-proteins or protein complexes in a fixed stoichiometric way. Symport denotes an equidirectional flux, while anti-port means that two coupled fluxes of equally charged ions in contrary directions are present. Active transport can only take place in combination with a metabolic process that delivers the energy required. Ionic diffusion due to the electrochemical gradient (electrodiffusion) always causes a shift in the TMP, which immediately unbalances the electrically driven fluxes [15].

Voltage-dependent ion channels such as sodium- potassium- and calcium-channels play a critical role in the development of tumors. A potassium channel consists of four identical subunits, a sodium channel of one inactivating and three activating subunits which operate on different time-scales. A calcium channel comprises four sub-units: α_1, $\alpha_2\delta$, $\beta_{1\text{-}4}$, and γ. L-, N-, P-, Q-, R- and T-type calcium channels are activated with strong or intermediate membrane depolarizations, while T-type calcium channels are activated by low membrane depolarizations. Channel type classification is assigned according to their physiological functions in the organism:

- L-type: long-lasting DHP receptor, high voltage-activated, found in skeletal muscle, bone, ventricular myocytes, cortical neurons
- N-type: neural, high voltage-activated, found throughout the brain
- P-type: Purkinje type, high voltage-activated, found in Purkinje neurons in the cerebellum
- Q-type: similar to P-type, found in cerebellar granule cells
- R-type: residual, intermediate voltage-activated, found in cerebellar and other neurons

- T-type: transient, low voltage-activated, found in neurons, pacemaker cells, bone.

Fig. 1.4 a) depicts a 3D model (side-by-side stereo display of a human $K_v1.1$ potassium channel generayed with the freeware molecule visualization program VMD 1.8.6 (http://www.ks.uiuc.edu/Research/vmd/, [128]). The central pore and the four protein chains are well visible. Voltage-gated ion channels can be thought of as a field effect transistor (FET): The voltage sensor corresponds to the gate of a p-channel FET. The p-channel itself can be thought of as the ionic conducting pathway, while the gate is modeled as the space charge of the p-channel. Although the specific mechanisms are rather different, the functions of a voltage-gated ion channel and a p-channel FET can be regarded quite similar. In tumor cells, sodium channels are involved in proliferation, migration and adhesion, while calcium channels have an impact on proliferation, migration and differentiation, and potassium channels are mainly limited to proliferation [16]. Fig. 1.4 b) describes how the enhanced expression of various ion channel proteins can have an influence over neoplastic cell growth.

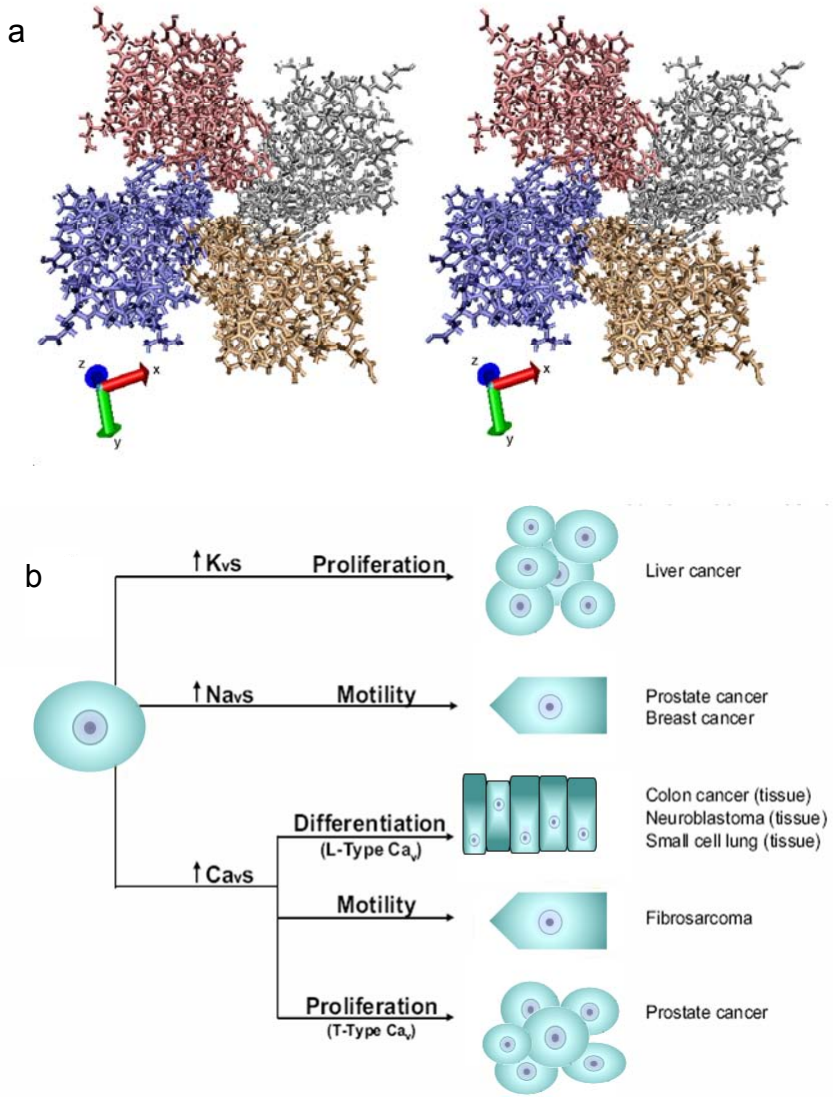

Fig. 1.4: a) Stereo-visual model of a human $K_v1.1$ voltage-gated potassium channel; b) Influence of voltage-dependent ion channels on cellular processes in neoplastic tissue [(b) redrawn from 16].

1.3.5 Potassium channels and proliferation

Voltage-gated potassium channels (K_v-channels or VGKCs) are the most important species of ion channels in the regulation of proliferative activity, because their activity is profoundly interwoven with many cellular characteristics, such as the TMP. For example, K_v-channels are activated via depolarized TMP of carcinoma cells. K^+-channels generally maintain the proper membrane voltage during the cell cycle [9]. Structurally, VGKCs are tetramers made of four identical subunits, each with six transmembrane segments (S1-6). S5 and S6 constitute the central pore at the interface between the subunits, and S1-4 are the voltage sensors, whose gating charges are four to seven positively charged amino acids, usually arginines. They undergo conformational changes when the pore gates open, coupling movement of the S4 gating charges within the membrane electric field to the open probabilities of the channel [17]. The sub-types $K_v1.3$, $K_v10.1$ (Ether-a-Gogo1, EAG1), $K_v11.1$ (HERG) and K2p9.1 are overexpressed in many cancer cell types. EAG1 overexpression generates increased proliferation in several cell lines, which makes these cells less dependent on growth factors in the medium [7].

Closing of K^+ - channels decreases K^+ - currents and depolarizes the cell membrane. This process inhibits proliferation in non-excitable cells and stimulates it in excitable cells like neurons and smooth muscle cells [18]. Cell proliferation is reduced by blockage of K^+-channels or inhibition of their expression [9]. K^+-channel blockers inhibit the cell cycle progression by membrane depolarization [19]. As shown above, voltage-gated K^+-channels are involved in cell proliferation. However, the causality is not clear, since the change in TMP, which activates the K^+-channels, and the hyperpolarization which results from the efflux of potassium ions, are the same. Activation of VGKCs alone does not affect proliferation, which would be expected if induction of proliferation was simply due to TMP changes induced by K^+ - ions. The specific molecular target for these blockers is unknown. Inhibiting cell proliferation with K^+-channel blockers does not always change the resting TMP [7].

In addition to regulation of the resting TMP, activity of K_v – channels may also modulate cell growth by regulating cytosolic Ca^{2+} [18]. K^+-channel activity may influence internal calcium levels by controlling membrane potential, and it might control the ion influx-efflux ratio [19]. Ca^{2+}-activated K^+-channels control proliferation of cancer cells during late G_1 and S phase [9]. They can also display spontaneous or agonist-induced cyclical activity, which induces calcium oscillations as a temporal signaling pattern [20]. Reduced K_v – channel activity (reduction of whole-cell $I_k(V)$) leads to elevated intracellular calcium concentrations by membrane depolarization which activate L-type voltage-gated C^{2+} - channels in pulmonary artery smooth muscle cells (PASMC) [18].

1.3.6 Cellular membrane potential

1.3.6.1 The transmembrane potential

The transmembrane potential V_m is the potential difference between the intracellular and the extracellular solutions:

$$V_m = V_i - V_e = \frac{RT}{z_e F} \ln \frac{[c_e]}{[c_i]} \qquad \textbf{1-5}$$

, where V_i: intracellular potential;

V_e: extracellular potential;

R : universal gas constant, R = 8.31447 [J $mol^{-1}K^{-1}$];

T : absolute temperature [K];

z_e: valence;

F : Faraday – constant, F = 96485.34 [C mol^{-1}];

c_e, c_i: external and internal ionic concentrations.

The TMP can be replaced by a DC potential and a superimposed alternating component:

$$V(t) = V_o + V_m \cos \omega_0 t \qquad \textbf{1-6}$$

The TMP does not always stay absolutely constant, even within one phase of the cell cycle. For a cell with diameter 14 μm and resting potential = -5 mV, the TMP fluctuations can be 10-20 mV [11]. Asymmetric surface potentials in cell membranes can generate an electric field within the membrane which mimics a decrease in intramembrane potential or a hyperpolarization [12]. When the membrane is electropermeabilized, the specific conductivity can rise from 10^{-3} S/m^2 to 10^4 S/m^2 [6]. Very rapid perturbations of the membrane potential can cause very small relaxation times of the ion channel opening or closing velocities, because before the conductive state, the channel enters an excited state at a rate constant proportional to the first temporal derivative of the membrane potential state [23]. A large depolarization (30 mV) of the membrane can increase the open times and decrease the closed times of an ion channel significantly. Depolarization also increases the magnitude of the ionic current by raising the driving force for the ion [14]. The standard mathematical description of the membrane potential in non-excitable cells is the Goldman-Hodgkin-Katz equation, which takes into account potassium, sodium and chloride currents:

$$V_m = \frac{RT}{F} \ln \frac{[P_K(K_o) + P_{Na}(Na_o) + P_{Cl}(Cl_i)]}{[P_K(K_i) + P_{Na}(Na_i) + P_{Cl}(Cl_o)]} \qquad \textbf{1-7}$$

1.3.6.2 Membrane impedance model

Bilayer lipid membranes are good insulators to low-frequency currents. Nevertheless, they are permeable to charged ions. This permeability is a complex operation that can be affected by exogenous electric and magnetic fields. The fraction of the current passing through the cell grows with increasing frequency. The membrane can be modeled as a parallel circuit of a capacitor (lipid membrane) and a resistor (ion channels). It is a hydrophobic insulator sheet with a central, non-polar layer (2-3 nm thick, permittivity: ε = 2). Because of the large differences in permittivities (ε_{H_2O} = 80), a large amount of electrostatic energy is needed to move a charge across the membrane

[6]. The charge density at the membrane surface is approximately 10 μC/cm^2, which is enough to orient the H_2O dipoles [11]. The stationary charges on the outside of the membrane are the carboxylic groups of the glycoproteins as well as polar heads of some of the phospholipids. Fig. 1.5 shows a schematic circuit diagram of a cell membrane.

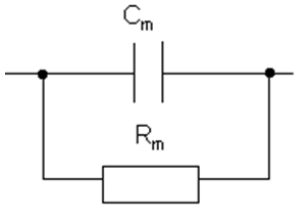

Fig. 1.5: Equivalent circuit diagram of a cell membrane

The conductivity of the extracellular medium and the cytosol is larger than the membrane's by a factor of 10^7. As a result, direct currents will circumvent the cell almost entirely through the medium. If an alternating current is applied, a displacement current will flow through the capacitance of the membrane X_C:

$$X_C = \frac{1}{\omega C} \qquad \textbf{1-8}$$

The capacitive part of the impedance drops with increasing frequency, and the current grows. The impedance Z of the membrane can now be calculated as the parallel connection of the resistance and the capacitance:

$$Z = \frac{R}{1+\omega^2 C^2 R^2} - i\frac{\omega C R^2}{1+\omega^2 C^2 R^2} \qquad \textbf{1-9}$$

The real part and the imaginary part of the impedance are functions of the angular frequency ω. Fig. 1.6 shows the circular RC-curve on the Gaussian number plane: At ω = 0, direct current will only pass the Ohm resistance, while at ω = ∞, there will be a short-circuit in the membrane capacitance.

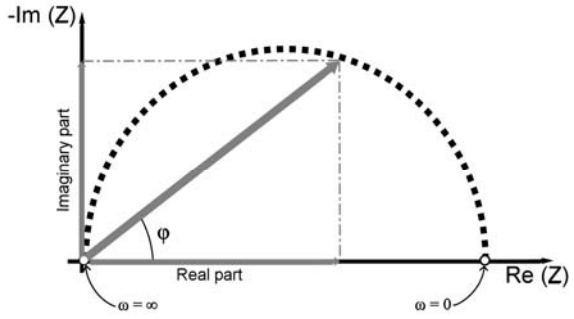

Fig. 1.6: Transfer locus of the impedance $\underline{Z}$, frequency 0→∞

1.4 Communication between mammalian cells

1.4.1 Cell-cell contacts

1.4.1.1 Gap junctions ("cell-cell synapses")

Gap junctions are a specialized version of ion channels that serve as connectors for a variety of cell types (fig. 1.7). They are 15 Å in diameter, allow transmission of a wide range of cellular molecules, and are fundamental in cell differentiation, e. g. through transmission of growth-regulating signals [21]. Recent work has shown that gap junctions may be significantly diverse in structure, number and distribution among different tissues. Several studies indicate that the subunits of gap junctions (connexins) and sodium channels are the same entity: Since gap junctions are assembled within 3 to 30 minutes, they must be made of pre-existing pore elements, as it takes longer than 30 minutes to synthesize complex proteins. Formation of gap junctions is accompanied by a decrease in intracellular sodium and an increase in TMP, both of which are probably a result of decreased sodium permeability. This indicates that the connexins may be sodium channels [10].

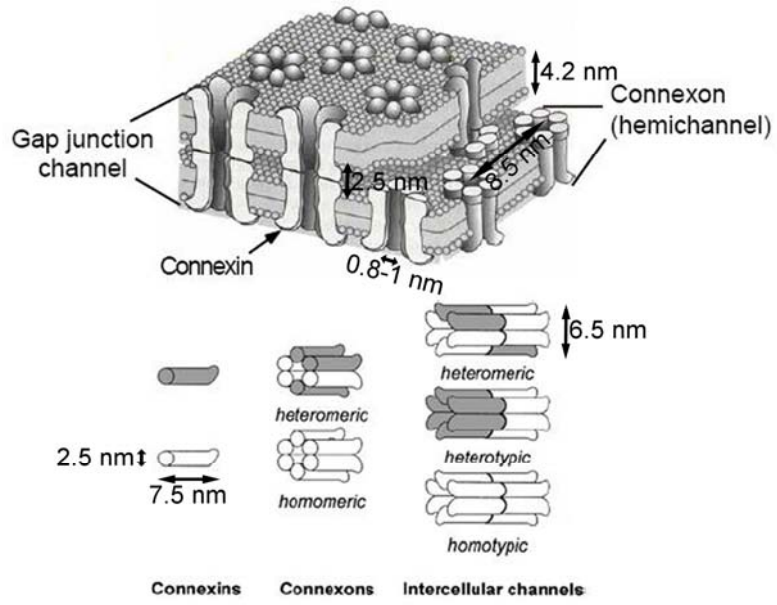

Fig. 1.7: Different types of connexins forming connexons and gap junctions [redrawn from 122]

1.4.1.2 Influence on the cell membrane and proliferation

Changes in the number, distribution or function of gap junctions can result in significant alterations of the cellular physiology: For example, changes in cell-cell junctions may alter the TMP; contact inhibition in vitro is established when TMP levels are mediated through cell surface contacts [22]. Proliferation can be started or enhanced in several kinds of tissue when cell-cell connections are broken, e. g. in wounds or after cell death. In normal, proliferating cells, gap junctions seem to be removed after the

cells were in a resting state. Electrical communication and gap junctions are also lost after damage or wounding, leading to a drop in TMP, enhanced DNA synthesis and augmented proliferation. Cell junctions seem to play a role in normal cell growth control and in uncontrolled proliferation of cancer cells when they are modified, which has been demonstrated [10]. According to [21] and [22], many cancer cell types do not produce gap junctions and are electrically isolated from each other. The structural modification of the connexins causes a lack of cell-cell bonding and leaves a surplus of sodium channels and therefore an elevated sodium permeability which leads to excess intracellular sodium [10]. Human stomach carcinoma cells have been shown to have no intrinsic electrical coupling [21].

The lack of specific connexins may be a prerequisite for tumor formation. Gap junction genes Cx32 and Cx43 have been shown to be underexpressed in hepatic and lung cancer. The connexins seem to control a large variety of processes which may lead to cancer if they do not function properly. Connexins are expressed in lower quantities than usual, and they are located in the wrong cellular compartments at different tumor progression stages. Gap junctions seem to have lost their function in the invasion stage of cancer, and gain function in the metastasis stage. There is evidence that the loss of gap junctional intercellular communication (GJIC) correlates with the metastatic potential [21]. Furthermore, gap junctions in tumor cells are eliminated within 24 hours after application of the tumor promoter 12-O-tetradecanoylphorbol-13-acetate (TPA) [10].

1.4.2 Intracellular communication pathways

1.4.2.1 Calcium fluctuations and oscillations

Calcium ions are used by the organism as a chemical carrier of information. Unlike neurotransmitters, which usually bear specific and unique functions, Ca^{2+} is a universal key molecule that can activate a large variety of intracellular signaling processes. There are numerous cytosolic proteins that alter their activity after binding to Ca^{2+}. It may regulate motility, proliferation, differentiation and secretion of cells. Following an injury, timing, duration, frequency and amplitude of Ca^{2+}-oscillations play an important role in determining which specific signaling pathways are activated (besides the cell type and the surrounding environment). For example, initial contact of corneal epithelial cells with a substrate is accompanied by Ca^{2+} oscillations [24]. Ca^{2+} pumps in the endoplasmic reticulum (ER) and the plasma membrane keep the internal calcium concentration at 100 nM in resting conditions. Ca^{2+} concentrations in the ER are 5,000-20,000 times higher than elsewhere, allowing completely passive Ca^{2+} influx and release [19]. Signal transduction proteins in the cytosol and transcription factors in the nucleus, which are essential for the progression of the cell cycle, are activated by increased levels of cytosolic calcium. For example, a constant Ca^{2+} - influx through sarcolemmal (muscle cell membrane) Ca^{2+} - channels is involved in pulmonary artery smooth muscle cell (PASMC) proliferation [18]. Ca^{2+} store depletion causes inhibition of DNA synthesis, protein synthesis and nuclear transport. Ca^{2+} acts both as a ubiquitous allosteric protein activator and inhibitor of intracellular enzymes in the cytosol, organelles and the nucleus [19].

Internal Ca^{2+} is always heterogeneously distributed. Oscillatory Ca^{2+} - gradients can originate from one cell pole, where the sarcoplasmic reticulum (SR) is located, and spread along the longitudinal axis of the cell. However, oscillations may not always originate from overloading of the SR. The type of calcium response depends on the stimulus [20]. Non-excitable cells do not express voltage-gated Ca^{2+} - channels, which explains the results of studies showing that membrane depolarization with concomitant Ca^{2+} - influx increases PASMC (excitable) proliferation, but inhibits lymphocyte (non-excitable) proliferation [18]. Intracellular calcium release usually has a delay of several seconds. There are four types of internal calcium release: single spikes from intracellular stores, mostly the ER, a slow but persistent calcium signal depending on extracellular calcium entry, a biphasic spike from combination of the two, and calcium oscillations [8].

To date, several research laboratories have collected evidence for spontaneous calcium oscillations in a variety of cell types. For example, in HeLa cells, Ca^{2+} oscillations are primarily due to Ca^{2+} mobilization from intracellular stores, but extracellular Ca^{2+} supply is also necessary to maintain the oscillations [25]. In neurons, Ca^{2+} can induce both long-term potentiation and long-term depression in the same synaptic connection. This versatility is mainly due to the way the Ca^{2+} signal is temporally and spatially organized [26]. In cardiac cells, small calcium bursts ("sparks") are released at the junctional zones by local groups of ryanodine receptors. Ca^{2+} diffuses into myofibrils and activates contraction [19]. The mean frequency of spontaneous calcium oscillations in colonic smooth muscle cells is 12.6 ± 1.1 per min. Calcium oscillation frequency was shown not to be influenced by K^{+} - induced membrane depolarization, only the baseline calcium concentration was affected by that. The mean speed of calcium propagation was 23 μm per sec. The oscillations appear to originate from recycling across the SR membrane and less from plasma membrane entry. In jejunal (middle part of the small intestine) myocytes, the mean Ca^{2+} - oscillation frequency at a holding potential of -40 mV is 13.2 per min. The frequency decreases with hyperpolarization, but is independent of the internal calcium concentration [20].

It is not quite clear what sets off spontaneous calcium oscillations. Plasma membrane oscillators and cytoplasmic oscillators are the two proposed explanations for periodic calcium oscillations to date [27]. Spontaneous oscillatory activity might also be due to overload of internal stores. Frequency might be decoded through protein phosphorylation [26]. There is substantial evidence that propagation of calcium waves between cells takes place via gap junctions. In excitable cells, calcium oscillations can be brought about by a membrane oscillator which results in intermittent influx of extracellular Ca^{2+} - ions through voltage-gated Ca^{2+} - channels. By contrast, intracellular mechanisms are responsible for oscillations in non-excitable cells. Another possible cause for calcium oscillations are Ca^{2+} - activated K^{+} - channels, which can display spontaneous or agonist-induced cyclical activity, causing calcium oscillations as a temporal signaling pattern [20]. The intracellular initiation of Ca^{2+} spikes is governed by the sensitivity of the Inositol phosphate 3 (IP3) receptor, which in turn is set by the loading of the internal stores. Oscillation frequencies are also limited by the rate at which extracellular calcium enters across the membrane, which in turn may be governed by extracellular agonist concentration [26]. Calcium release induced by IP3 causes a very fast and short cytosolic calcium spike. Some excitable cells express ryanodine receptors, multimeric calcium channels that are modulated by calcium itself. This way, they can sustain intracellular calcium oscillations through calcium induced

calcium release [8]. Ca^{2+}-induced Ca^{2+}-release provides positive feedback and renders a rapid regeneration of the Ca^{2+}-signal possible. Generally, calcium oscillations are frequency modulated and not amplitude modulated [26].

1.4.2.2 Influence of calcium on proliferation

Ca^{2+}-fluctuations and oscillations are major hallmarks of proliferating cells and have not been seen during apoptosis [9]. In general, lower calcium concentrations may lead to higher proliferation rates [28]. Ca^{2+} - influx is predominantly regulated by the permeability of the membrane towards calcium ions and by the TMP, since the chemical gradient is always very high (Extracellular Ca^{2+} is 20,000 times higher than intracellular Ca^{2+}). When cells are hyperpolarized, the driving force for Ca^{2+} - ions rises; when cells are depolarized, it drops [18]. In non-excitable cells, the membrane is hyperpolarized by activation of K^{+}-channels, increasing the driving force for Ca^{2+} entry. Membrane depolarization of melanoma cells by voltage-clamp decreased and hyperpolarization increased internal calcium levels, indicating a transmembrane Ca^{2+} flux according to its electrochemical gradient [19]. Hyperpolarization can be a result of increased extracellular calcium, both in normal and cancer cells. Doubling an initial calcium concentration of 1.6 mM raised the membrane potential by 5.6 mV, which means that the membrane channels were altered. Increased intracellular calcium has been observed to decrease the permeability of gap junctions [28]. Voltage-operated Ca^{2+} - channels (VOCs) are activated by depolarization in excitable cells (neurons, muscles, secretory cells) [19]. TMP potential oscillations depend on changes in resistance which is controlled by Ca^{2+}, so they may be caused by underlying Ca^{2+} oscillations [26]. One of the most strongly TMP-sensitive biological processes is Ca^{2+}-release through voltage-sensitive channels in the sarcoplasmic reticulum of muscle cells [23]. Spontaneous membrane depolarization may be dependent on Ca^{2+} influx [20]. TMP is involved in the regulation of cytosolic calcium since the sarcolemmal Ca^{2+} - channels are voltage-gated. Sustained TMP depolarization increases both cytosolic and SR calcium concentrations and may therefore be the cause for the increased resting value of cytosolic calcium in PASMC during proliferation [18].

As cells progress through the cell cycle, increased free cytosolic calcium concentrations have been observed, which might indicate that a low calcium content is only necessary before or during the initiation of mitosis [8]. A rise in the cytosolic calcium can increase nuclear calcium within 200 ms. Ca^{2+} in the nucleoplasm promotes cell proliferation by moving quiescent cells into the cell cycle and moving proliferating cells through mitosis. Ca^{2+} can also influence expression of many transcription factors that propel the cell cycle and stimulate division [18]. Calcium can directly or indirectly regulate the activation of transcription factors essential for neural differentiation and may also release neurotransmitters that guide neuronal migration. In radial glia cells, spontaneous calcium waves propagate upon a trigger ATP signal that results from opening of connexin hemichannels. Disruption of these ATP-mediated calcium waves significantly decreases cell proliferation [29]. Growth hormone secreting pituitary cells have been shown to generate APs spontaneously. APs coincide with changes in the resting level of intracellular calcium: Calcium oscillation amplitude and duration increases result from elevated AP frequencies. In gonadotrophs, as well as other non-excitable cells, TMP oscillations depend on the rise in internal calcium, which shows in the similarity in the Ca^{2+}- and TMP oscillatory patterns which are synchronized through

the activity of a Ca^{2+}- and apamin-sensitive K^{+}-current. The TMP and Ca^{2+} patterns are intermediate between those of typically excitable and non-excitable cells, and similar to non-excitable pancreatic cells. The initiation of Ca^{2+}-spiking in gonadotrophs is independent of TMP, while maintenance of these oscillations is highly dependent on extracellular Ca^{2+} and TMP [27].

1.4.2.3 Ion channels and cancer

One specific trait that the vast majority of malignant tumors share is the inability of its constituent cells to stop dividing when they are fully surrounded by cells of the same type [30]. This lack of contact inhibition may have reasons that are not entirely understood, but it certainly happens at the interface of the cells, where a defined and controlled interaction with the extracellular space is no longer present.

Most tumors have a higher rate of glycolysis than normal cells, and their cell surface is altered in some way. They often have smaller (meaning more positive) resting TMPs than their healthy counterparts [10]. Their cell division process – oncogenesis -, like mitogenesis in healthy cells, is regulated in the nucleus, the cytoplasm (through fluctuations in the ionic concentrations) and the cell membrane [10, 30]. Certain active transmembrane proteins, such as the Na^{+}/H^{+} - exchanger, HCO_3— transporters and monocarboxylate transporters are enhanced in cancer cells, because these cells need a basic intracellular pH to proliferate [9]. Formation of metastases involves cell dissociation that leads to invasion and recognition between tumor and endothelial cells leading to secondary tumors. Thus, the metastatic potential is greatly influenced by gap junctions and cell adhesion molecules [21]. Figure 1.8 a) provides an overview of some of the processes distinguishing normal cell cycle activity from tumorous mitosis, while b) focuses on those aspects leading to cancerous growth in more detail.

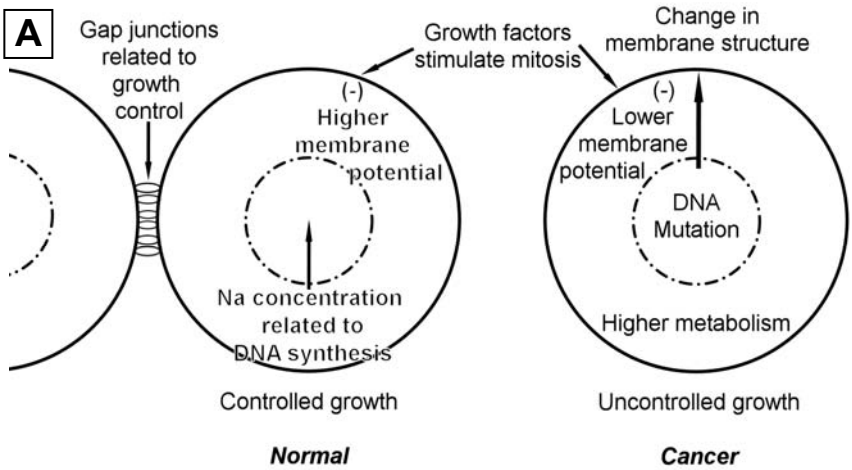

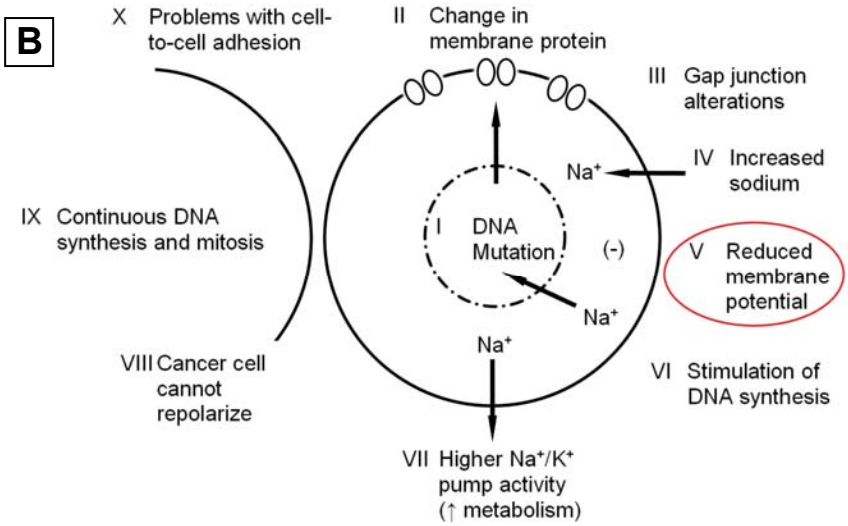

Fig. 1.8: a) Overview of some of the processes distinguishing normal cell cycle activity from tumorous mitosis, b) Influence of several parameters leading to neoplastic growth [redrawn from 10]

1.5 The electrical cell

1.5.1 Membrane potential and proliferation

When reflecting upon biological cell membranes, it is important to keep in mind that the lipid bilayer is not a static construct, but a semi-stable sheet of dynamically interacting molecular elements. Membrane lipids can move about 1 nm every µs [31]. What makes the membrane an electrically active cellular component is the TMP. It reflects the ionic selectivity of the membrane and the transmembrane ionic concentrations [32]. The conductance of the membrane is entirely due to that of the pores, because the bilayer conductance is very poor in comparison [6]. In normal, excitable cells, sodium permeability is much lower than potassium permeability, which means that the resting TMP basically depends on potassium diffusion [10]. The resting TMP of both excitable and non-excitable cells is close to the K^+ - equilibrium potential and has been shown to control electrical excitability, muscle contraction, secretion, apoptosis and gene expression [18]. In fact, the TMP of non-excitable cells may play a role as an intermediary of diverse cellular signaling processes: It is used by the cell to drive the transport of nutrients, which makes it very important for rapidly proliferating cells [33]. Calcium entry through Ca^{2+} - channels is required for cell division and is facilitated by a negative intracellular potential [7]. The membrane surface potential generally has a great impact on cell adhesion, cell spreading, chemotaxis, endo- and exocytosis and binding of biologically active molecules, such as ion channel agonists, anesthetics and enzymes. The negative extramembrane surface potential determines the local ion concentrations around the ion channels and thereby affects the steady-state conductance of the channels [12]. Specific capacitance of neuronal membranes was shown to be 9 mF/m^2 and independent of membrane protein densities [6]. R_{mem} is 0.1

$\Omega \cdot m^2$, relaxation frequency for proteins and lipids is between 100 kHz and 1 MHz. The interior of the cell is shielded by the membrane below 1 MHz [6]. Cells with low membrane potential are likely to be more sensitive to TMP changes than cells with higher TMPs [34].

There exists a wide range of cellular processes which the TMP has been shown to be involved in, for example regulation of mitosis control (DNA synthesis and proliferation), both in tumorous and normal tissue [10, 30, 32]. However, there is still no definite proof of TMP being the cause for proliferation changes, although it responds rapidly to changes in the extracellular K^+ concentration. Varying the external Na^+- and K^+ - concentrations alone also alters the kinetics of proliferation [32]. There is, however, strong evidence in favor of a decisive dependence of the cell cycle on TMP: During proliferation, the TMP of normal cells is below -36 mV, and above that when they stop dividing. Tumor cells seem to be trapped below that threshold and are unable to repolarize to levels above the threshold [10]. In proliferating cells, an early, significant plasma membrane potential drop in the transition from resting state to mitotic activity has been reported [22]. TMP is lowest immediately after division, and it increases during the G_1 - phase. It rises abruptly at the beginning of DNA synthesis, stays constant during S- and G_2-phase and declines during mitosis [32]. Hyperpolarization during G_1 phase has been reported essential for proliferation, while constant hyperpolarization was detrimental to proliferation [9]. Most cell types exhibit a transient hyperpolarization at the end of G_1 – phase, and tumor cells are generally depolarized compared to normal cells [7]. TMP rises during the transition to S-phase, and then decreases again in the next G_1-phase [30].

TMP depolarization also occurs in other, aberrant situations, such as wounded tissue, where it gradually extends from the leading edge of the wound inward to neighboring cells through an increase in epithelial Na^+-channel-mediated Na^+-permeability. The depolarization may be necessary for cytoskeletal reorganization. As a possible mechanism, it has been suggested that a wound-induced increase in growth factors and intracellular Ca^{2+} activates epithelial Na^+-channel (ENaC) expression genes and their membrane insertion. This intracellular Ca^{2+} does not seem to be propagated by gap junctions [33].

Other observations were made that give rise to a new perspective on electrically controlled mechanisms possibly leading to and maintaining malignant tumor growth: TMP elevation, which is absent in cancer cells, leads to an increase in contact inhibition. Specifically, it was shown that in normal 3T3 cells that TMP increases simultaneously with formation of intercellular contacts and cell density dependent growth inhibition up to the point of contact inhibition [22]. Cancer cells also appear to have lower membrane potentials with progressing differentiation [28]. After neoplastic transformation, the surface charge density changes and the TMP drop [30]. In an experiment with normal 3T3 cells, no TMP changes were observed during the first mitosis, then a drastic increase shortly before the second mitosis was recorded. After that, the proliferative activity came to a halt. This does not prove that high TMP inhibits mitosis per se, but it seems to be necessary and might inhibit DNA synthesis, which is why there is no third cell cycle. The experiment was repeated with tumor cells: The TMP rose from -10 to -31 mV, and then stayed at that level throughout the following mitoses. Cell division was not inhibited (Fig. 1.9, [22]). In another study using normal Chinese hamster lung cells, the TMP was at -20 mV in the late G_1 phase, before rising abruptly to -29 mV in early S-phase. It remained steady through S- and G_2-phase. 11 hours later, the next mitotic division occurred. The cells in metaphase displayed a wide

range of TMPs, the average value being -22 mV. TMP increased significantly between the end of mitosis and late G_1 phase [32].

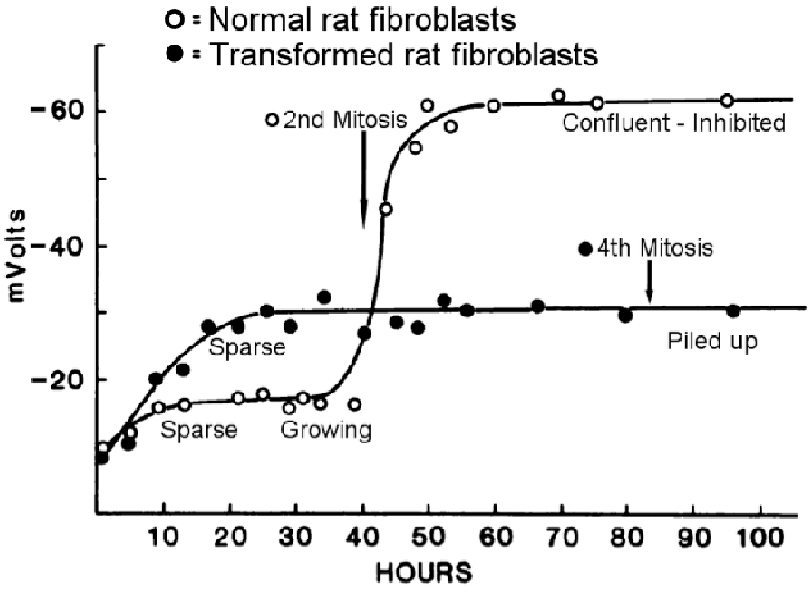

Fig. 1.9: Membrane potential during cell cycles in normal (hollow dots) and malignant cells (solid dots) [redrawn from 22].

1.5.2 Influence of electrical and magnetic fields on biological cells

1.5.2.1 Non-excitable cells in electromagnetic fields

Electrical, magnetic and electromagnetic (high frequency) fields can be used to manipulate biological cells. The conductivity of an intact, spherical cell in an electrostatic field is very low. An external field does, however, have the ability change certain characteristics of the cell. It causes a charge accumulation on the membrane surface perpendicular to the field vector, and therefore polarizes the cell (fig. 1.10). The spontaneously induced opposite electric field inside the cell attenuates the outside field. For DC fields, polarization effects are low and can be considered insignificant. In the case of AC fields, the polarization of the membrane surface affects the TMP of the cell and renders it dependent on a specific position. An external, sinusoidal field of the amplitude E and frequency f induces the following potential deviation in the membrane of a cell with the radius r (see Fig. 1.10):

$$\Delta\Psi_{ind.} = \frac{1{,}5Er\cos\alpha}{\sqrt{1+(2\pi f\tau)^2}} \qquad \textbf{1-10}$$

, where α is the angle between a point on the membrane and the field vector [6, 15]. The time constant of the membrane can then be expressed as

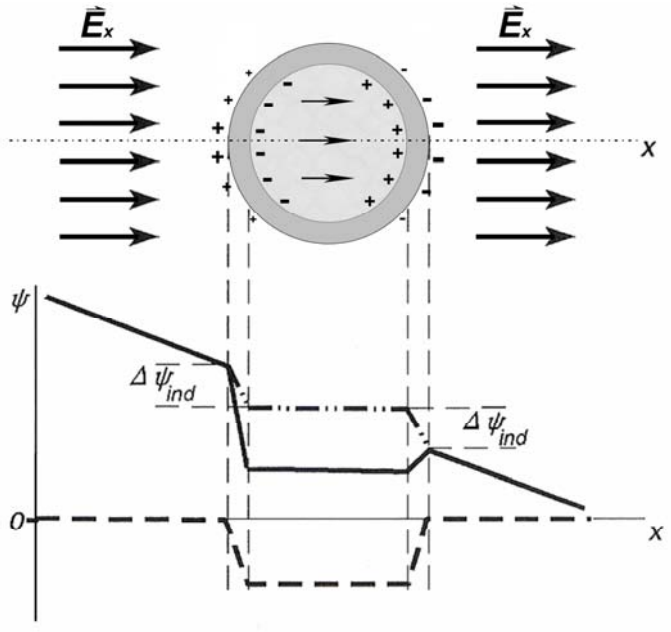

Fig. 1.10: Schematic distribution of the charge, potential and induced field geometry of a spherical cell in a static electric field. The arrows denote field lines. Charges on the membrane are generated through polarization. The bottom curves illustrate the membrane potentials through the center of the cell: ----- potential course without external field; --··--··-- potential induced by the external field without consideration of the innate cellular potential; — actual potential (sum of both functions). $\Delta\Psi_{ind}$ = induced membrane potential. Redrawn from [15].

$$\tau = r_{mem} c_{mem} \left(\frac{1}{\sigma_{\text{int}}} + \frac{1}{2\sigma_{med}} \right), \qquad \textbf{1-11}$$

with r_{mem} and c_{mem} the specific resistances and capacitances, respectively, and σ_{int} and σ_{med} the conductivities of the cytoplasm and the medium, respectively. Equation 1-10 can be simplified for DC fields and AC fields below a frequency of 10^5 Hz [15]:

$$\Delta\Psi_{ind.} = 1{,}5 E r \cos\alpha \qquad \textbf{1-12}$$

The membrane potential of a spherical cell with a radius of *10 μm* will experience an increase in membrane potential of 15 mV after application of an $E = 10^3 \frac{V}{m}$ field at the point of perpendicular field vector lines ($\alpha = 0^0$). The induced membrane potential will always increase with growing cell radius [6, 15].

Phez et. al. propose a more general equation for the induced membrane potential, since they postulate that the field effect depends on the position on the cell surface, which is backed up by their observations:

$$\Delta\Psi_{ind.} = \Psi_{in} - \Psi_{out} = F \cdot g \cdot r \cdot E \cos\alpha(M), \qquad \textbf{1-13}$$

where *F* is a function of the cell shape, *g* depends on the conductivities of the medium, cytoplasm and membrane conductivities, *r* is the cell radius, *E* the electric field strength, and α(*M)* the angle between the normal to the membrane at the position M and the direction of the field [35]. For detailed descriptions of these parameters, see [122].

In Fig. 1.11, the field lines of a homogenous, alternating electric field inside and around a spherical cell are shown schematically. The membrane is bridged above a frequency of approximately 1 MHz, so that the external field can pass through the cell. At frequencies above that level, membrane potential changes do not have any significant effects. Electrical currents around and through cells can also be induced by applying alternating magnetic fields that induce circular eddy currents in biological tissue.

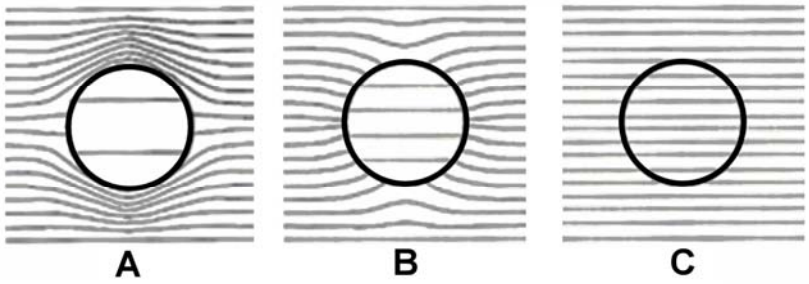

Fig. 1.11: Schematic field lines of a homogenous, alternating electric field around and inside a spherical cell. a) low-frequency field lines, b) higher frequency: intracellular conductivity begins to increase, c) high frequency field, intracellular conductivity equals extracellular conductivity. [redrawn from 15]

1.5.2.2 Electric/magnetic fields, currents and proliferation

Electric fields and currents have been employed to manipulate cell growth and division in a number of studies. Electric currents might accelerate cell growth and division when the rate is too low, and might inhibit them when it becomes too high [30]. Controversially, electrical fields have been shown to induce growth stimulation of tumor cells and to support bone growth and wound healing [36]. Several studies report improved wound healing after DC electrical therapy. An experiment using in vivo fibrosarcoma showed significant tumor growth retardation of up to 3 days growth difference after a 0.6 mA current was applied for 1 hour [30].

From a mechanistic point of view, TMP can be raised from -65 mV to -25 mV by a sequence of nine electrical stimulation pulses (4 ms, 400 mV) with a time interval of 30 sec [37]. In general, electric fields cause joule heating, electromechanical effects and electrically induced potential differences in biological tissue. For an overview of cellular responses to electrical fields described in the literature, see fig. 1.12. There is some controversy regarding the minimum amplitude of electric fields required to induce significant alterations. In voltage gated ion channels, the peak of charge movement currents and the total amount of moved charged particles were shown to decrease only above a pulse magnitude of -400 mV [37]. When dimensioning field strengths for potentially therapeutic applications, certain limits should not be exceeded, which holds true for both negative and positive voltages. The critical potential value for membrane permeabilization is between ± (200-500 mV). The threshold for the cells facing the anode is lower than for the ones facing the cathode. For elongated cells, only

those parallel to the field lines can be permeabilized [35]. Neurons were shown to collapse at an induced TMP of 400 mV at 100 kHz, 500 mV at 250 kHz, 1.1 V at 800 kHz and between 0.6 V and 2.7 V at 1 MHz [6].

In an experiment investigating the effects of very low intensity magnetic fields, normal human neuronal progenitor (NHNP) cells were subjected to 10 Hz, 0.1 – 20 µT alternating fields for 17 days [38]. Growth rates were significantly increased after the treatment. This effect was reversible, and the cells grew more uniformly in one direction than in the control groups. Oxygen-, glucose or lactate metabolism was not altered. A mechanism underlying these results was not found. Another publication agrees with the observation of magnetically induced directional cell growth: Schwann cells were treated with an 8 Tesla static magnetic field for sixty hours and adjusted their direction of growth according to the field lines [39]. When mixed with collagen, the cells oriented themselves in the field after only two hours. Neuronal axons mixed with collagen, however, were shown to grow perpendicularly to the field lines.

A publication from the University of Tokyo reports trials in which murine melanoma were reduced in weight by up to 50% after 17 days of treatment with pulsed magnetic fields (peak field strength: 0.25 T, pulse width = 238 µs, 25 pulses/sec, duty cycle 50%, 1000 pulses/day, induced current density: 0,79-1,54 A/m²) [40]. Besides tumor reduction, enhanced immune system function (tumor necrosis factor (TNF-α) production was significantly elevated) was measured. In concomitant *in vitro* trials, no reduction in cell viability was seen. However, cell cultures were merely given a total of 1000 pulses. Therefore, a definite conclusion on the cause of the anti-tumor effect could not be drawn.

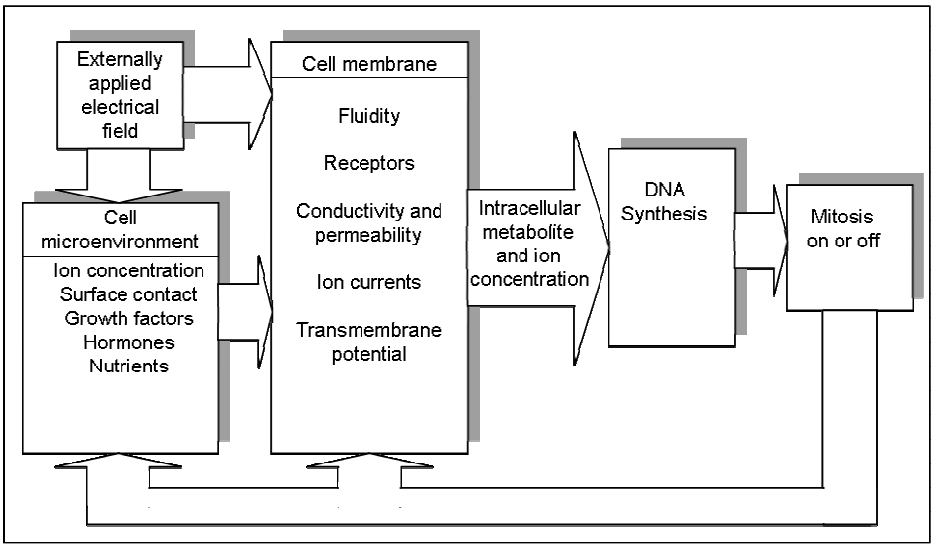

Fig. 1.12: Effects of electrical fields on proliferation proposed in the literature [redrawn from 2]

1.5.2.3 Electric and magnetic fields interfere with calcium-oscillations

In a recent study, a 13 – 114 µT AC magnetic field (7 – 72 Hz) and a 27 – 37 µT static field were applied to plant membrane vesicles [41]. Ca^{2+} - inflow and outflow were affected, depending both on the ratio of the AC amplitude and the DC amplitude

as well as the stimulation frequency. The proposed mechanism was a direct opening or blocking of calcium channels at the respective resonance frequencies.

Cultured lymphocytes and adrenal gland cells exhibited marked differences in Ca^{2+} - inflow and –flux after stimulation with a low intensity magnetic field [42]. The authors reason that the induced eddy currents cause these shifts in Ca^{2+} - flow directly. They estimate the strength of the eddy currents inside the cells to be three times lower than in the surrounding culture medium as a result of the high impedance of the cell membranes [42, 43]. Exposure of the adrenal gland cells to a 1.5 Tesla, 0.3 Hz field inhibited bradykinin-induced increase of intracellular Ca^{2+} as well as ionomycin- and caffeine-induced Ca^{2+} - release from internal stores. The inhibitory action was reversible. However, no influence on the transmembrane flux of Ca^{2+} was observed. In the same studies, K^+ uptake and activation of intracellular Ca^{2+} in HeLa cells was shown to be affected by magnetic fields. Since magnetic fields can have entirely opposite effects on calcium-related cellular phenomena, even with very similar experimental setups, there is no agreement as to which mechanisms are responsible for the observed effects. The field amplitude is believed to be a decisive factor for the type of response evoked.

1.5.2.4 Electrical and magnetic fields: molecular and other effects

Because so many cellular structures carry charges and therefore are susceptible to interaction with external electric and electromagnetic fields, a variety of intracellular events and sequences have been shown to be manipulated by such fields. Biological systems can respond to exogenous electromagnetic fields with cytoskeletal reorganization, cell surface receptor redistribution, changes in intracellular Ca^{2+} and intracellular levels of reactive oxygen species (ROS) [36]. Electric fields can induce structural and functional changes by exerting a force on charges within a protein. Proteins have high densities of fixed ionic groups and large dipoles, which makes them prone to electrical field interference [11]. If an alternating field causes a shift in the position of charged voltage sensors, the change in channel conductance might follow with a certain delay, since voltage sensing is assumed to be much faster than the process of channel-gating. The rectifying effect would not operate on ions crossing the channel directly. Oscillating electric fields can only directly interact with voltage-sensors or dipoles above a frequency of $1/(2\pi\tau_p)$, with τ_p being the time constant of the channel opening or closing. When the voltage sensor goes from state closed to state open, 5 elementary charges cross the membrane. Then, applying a DC potential 10 mV more positive than the average resting potential will cause the open probability of the sensor to be 0.88. However, a 10 mV AC potential will decrease the probability of the sensor open state. It was shown that a 4 mV depolarization will cause an *e*-fold increase in g_{Na}. For some channels, the interaction energy between the dipole and the applied field is greater than kT for TMP perturbations of the order of 1 mV [23].

Electric fields can also enhance chemical processes such as ATP synthesis by changing the conformation of the membrane-bound ATPase [11]. Electric field pulses have been shown to increase ATP bioluminescence by 324% in multicellular tumor spheroids, causing a Ca^{2+} - response. ATP has a mitogenic effect on several different kinds of cancer cells. In previous studies, intracellular calcium elevations in response to EM fields have been described and attributed to transmembrane influx of calcium through voltage-gated Ca^{2+} - channels, or simulation of membrane receptors with

subsequent activation of phospholipase C, generation of inositol triphosphate and Ca^{2+} - release from intracellular stores. DC electrical fields have been shown to elevate intracellular ROS, which in turn raised intracellular Ca^{2+} - concentrations. A 60 s, 750 V/m electric field "pulse" released intracellular calcium at the anode-facing side spreading through the cell at 12 μm/s [36]. 6 – 75 Hz electric fields and RF radiation modulated at these frequencies have been shown to significantly change efflux of calcium ions from brain cells at field strengths below thermal artifacts [23]. DC electrical fields can accelerate tumor growth by as much as 38-fold through a mechanism involving a transient Ca^{2+} elevation. Growth stimulation was inhibited by a 60 min pre-incubation with the anion channel inhibitor niflumic acid and with the purigenic receptor antagonist suramin. The DC fields also caused a release of c-Fos protein [36].

Culture medium does not sustain electric fields because of its conductivity, which makes the membrane a privileged site for them [11]. Pulse-modulated RF fields (0.1 – 1.5 MHz) were shown to affect the membrane potential in giant cells of Nitella flexilis significantly [23].

1.6 Electrical and magnetic stimulation methods

1.6.1 Advantages and disadvantages of electrical and magnetic cell manipulation

Both variants of external stimulation, electrical and magnetic, have their advantages and their drawbacks [61]. It is obviously easier to stimulate tissue directly by applying the stimulation energy through electrodes that are in immediate contact with the biological tissue. Electrical stimulation devices are smaller, cheaper and more energy efficient than magnetic stimulators. Moreover, it is much easier to control the exact amounts of energy, waveforms and frequencies that the stimulated cells experience. A great disadvantage is certainly the fact that the electrical current always chooses the least resistant path, which means that the current distribution is never homogenous, and there are often irreversible electrochemical reactions around the electrodes. There can be substantial heating of the tissue, and pain receptors are often stimulated, which limits the field strength and duration that can be applied in one session. The main advantage of magnetic stimulation is its non-invasiveness. It is also largely pain-free. The stimulation coil is simply held over the tissue at an appropriate distance and acts as the primary coil of a transformer, while the stimulated cells are the secondary coil. Since the coupling of the two coils is considerably worse than in a standard transformer with an iron core, the energy is transmitted approximately six to seven times less efficiently than with electrical stimulation. Therefore, magnetic stimulators must be capable of producing and delivering large currents (several kA), at high voltages (several kV) and high frequencies, which makes their design and construction difficult and expensive. Another disadvantage is the relatively poor focality of the stimulation (10 – 20 mm as opposed to 1 mm area diameter). Great care

has to be taken to avoid the recording of artifacts when effects of stimulation are recorded during or right after magnetic stimulation, e. g. in fMRI studies.

1.6.2 Application type and waveforms for electrical and magnetic manipulation

In order for electrical stimulation to work – at least for supra-threshold stimulation of excitable tissue – ionic charges need to flow between and inside the cells, and inside the cell medium for in vitro settings, respectively. Two methods for the delivery of electrical energy can be employed. When coupled directly, electric currents are delivered through metal electrodes in immediate contact with the cells. These electrodes generate charges mainly through faradaic processes necessary for a physiological reaction. For application in biological tissue, inert and biocompatible electrode materials such as iridium or platinum must be chosen [62]. Temporal and amplitude characteristics of the applied fields in the vicinity of the cells can be controlled well when working with electrodes. However, there has to be a compromise between the desired strength of the stimulation and the electrochemical reactions that increase proportionally with the field strength. In *in-vitro* experimental setups, part of the stimulation voltage drops over the cell medium. This is a result of the ohmic resistance of the electrolyte solution and of polarization effects on interface surfaces. The resulting time-varying electrical currents are attenuated and resemble the charging and discharging currents of an RC-circuit [63].

Electrical fields are coupled capacitively, when charge distributions alternate in an electrical double layer depending on the charge on the electrode surface. There is no direct transfer of electrons at the interface between the electrode and the electrolyte. This way, only the amount of charge that is stored in the double layer is injected. By coupling the electric field capacitively, there are no significant chemical reactions in the cell medium and the charge densities induced are very low. At very high charge densities, a dielectric breach might occur [62].

Another approach for the induction of electrical fields is the application of alternating magnetic fields that induce eddy currents in biological tissue. The currents' distribution depends on the geometry and the position of the coil and on the conductivity and homogeneity of the tissue. An estimation of the induced electric field strength requires the knowledge of the amplitude of the magnetic flux as well as the temporal course of the magnetic field. Generally, the higher the slope of the stimulation pulse, the higher the induced field strength. Since the time course of the field is differentiated by the inductive transmission, harmonic waveforms, such as sine or cosine, are ideal. This way, distortions of the applied waveform are kept at a minimum.

1.7 Electrical signal transduction in neurons

1.7.1 Physiology of neurons

1.7.1.1 Overview

The central part of the neuron, the soma, contains the nucleus, which is the site of most of the protein synthesis in the cell. Depending on the type of neuron, it can be between 5 and 100 μm in diameter. The central computational unit of the nervous system, the neuronal soma processes the incoming signals via a direct spatial and temporal integration of the membrane potential shifts. As a result of the integration, an AP is elicited at the axon hillock when the threshold potential is exceeded. This process is often circumscribed as the "all-or-nothing law": Either there is an AP or there is none, but there cannot be a little bit of an AP.

The postsynaptic branches that originate from the soma are called dendrites (Greek: δένδρον, tree) and are responsible for reception of excitatory or inhibitory input in the form of APs through the synapses on the axons of other neurons (afferent). The dendritic arbor of a human nerve cell can hold contact with 100,000 to 200,000 fibers of other neurons. Dendrites can be regarded the information collector of the nervous system. Recent research has also found that dendrites can support APs and release neurotransmitters. This property was originally believed to be specific to axons.

The axon hillock is part of the soma and constitutes the interface between the soma and the axon. It contains the highest concentration of ion channels anywhere in the neuron, which reduces the threshold potential on the axon hillock strongly and renders it a trigger for APs. The APs are then transferred to the axon, but there is also some passive rebound transduction of the AP to the dendrite according to the cable equations. This phenomenon has been termed neural backpropagation [44]. Recently, some researchers have suggested that active dendritic signal propagation is possible, too.

Growing outward from the axon hillock, the axon (Greek: άξον, axis) is a long extension of the neuron, the "active cable" that carries information to the next cells. Depending on the neuronal cell type, it is more or less branched, with a high density of synapses at the tips of the branches. The length of an axon can vary between 1 μm and 1 m, depending on the type of the nerve. The axons of mammalian nerve cells are between 0.5 and 10 μm thick. The axon can be coated by several sequential myelin sheaths. The myelin sheaths are formed in the central nervous system (CNS) by oligodendrocytes, in the peripheral nervous system (PNS) by Schwann cells [45]. Small gaps are located between these myelin sheaths, called nodes of Ranvier [46]. In myelinated axons of the same diameter, the nerve impulse conducts about ten times faster than in axons without myelin sheaths. The axon terminal is a specialized structure at the end of the axon that is used to release neurotransmitters and to communicate with target neurons.

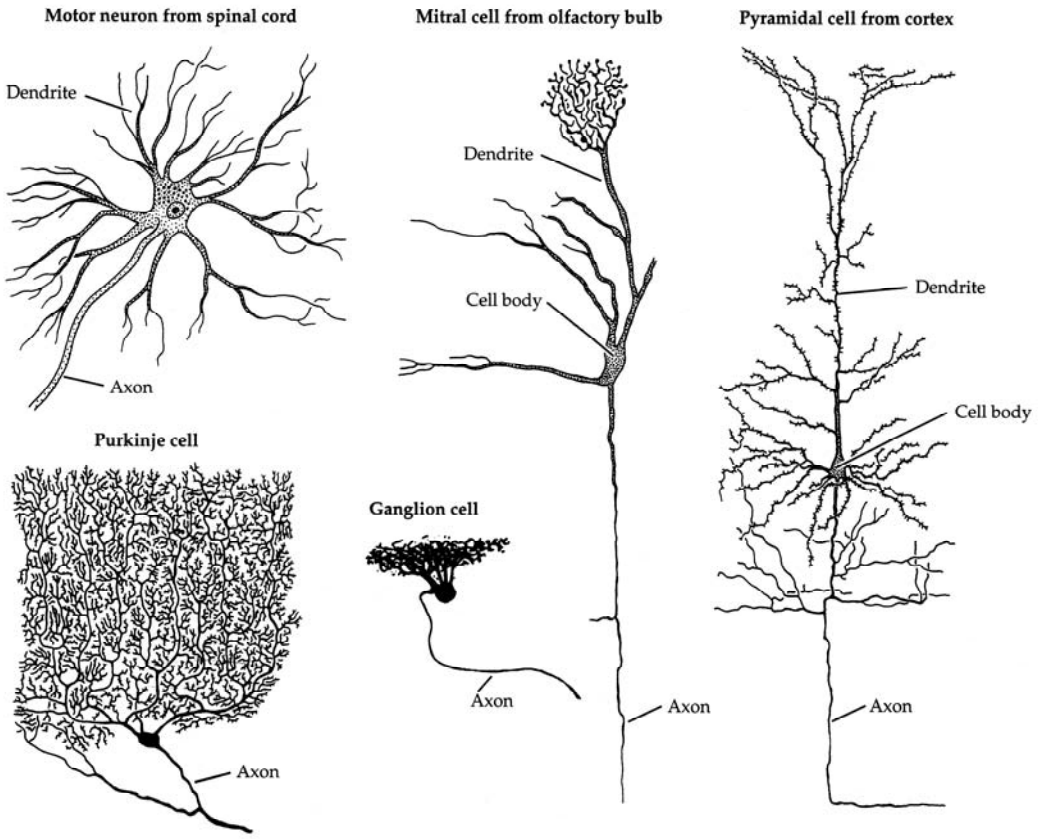

Fig. 1.13: Different types of neuronal cells found in mammalian organisms [with permission from the publisher of 124]

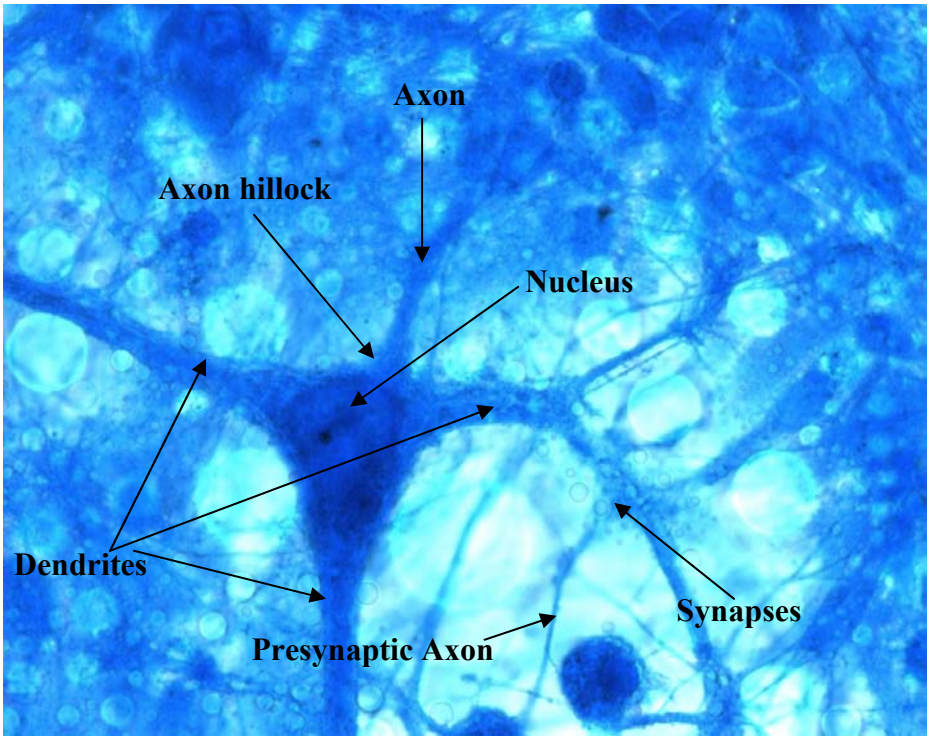

Fig. 1.14: Cortical neuron and processes from other neurons stained with Luxol fast blue. Light blue structures in the background: glia cells.

1.7.1.2 Conversion of electrical into chemical signals

A neuron receives its incoming signals in the form of neurotransmitters that originate in the preceding cell. The neurotransmitters bind to the receptors of the postsynaptic membrane of the dendrite or soma and cause a depolarization of the equilibrium resting potential, given a certain threshold is exceeded. If the excitation is transferred this way, it is passed on over the dendrites to the soma and from there to the axon hill. Every one of the incoming depolarizations from the different synapses changes the postsynaptic membrane potential. If a synapse is closer to the soma it has more influence on the nerve cell; if this distance is increased, the influence tends to get weaker. Simultaneously entering excitations summarize their effect, which means that an excitation potential is generated on the axon hillock.

For transmission of an excitatory or inhibitory signal from the neuron or a sensory cell to the next neuron in line, that signal always has to cross a synapse. The synapse represents an interface in form of a synaptic gap, in which it can transmit information chemically to another cell. It consists of a presynaptic membrane which contains the neurotransmitters and is part of the transmitting cell, the synaptic cleft, and the postsynaptic membrane. The postsynaptic membrane is equipped with receptors that fit the neurotransmitter molecules which have been discharged by the presynaptic cell. Once these transmitter substances have bound to the receptors, they cause a variety of biochemical reactions, e. g. ion channels to open, which initiates the electrical excitation of the postsynaptic cell. The synaptic cleft of chemical synapses is a gap filled with plasmatic solution, ca. 30 nm wide. Within that small gap, the concentrations of the different neurotransmitters can be adjusted very quickly. A neuron can have up to 10,000 synapses.

1.7.1.3 Neurotransmitters and receptors

Whether a neuron interacts in an inhibitory or excitatory way is determined by the synapses and depends on the type of the neurotransmitters it exchanges with the postsynaptic cells. The transmitter exchange through the synaptic cleft happens only through diffusion. The receptors that accumulate the neurotransmitters are divided into two broad categories: ionotropic and metabotropic [47]. The ionotropic receptors open and close ion channels depending on the transmitter docking to them. The time constant of these receptors lies in the range of a few ms. The metabotropic receptors do not have ion channels; they release intracellular, so-called second messenger cascades. This process then triggers ion channel activities that are spatially separated. In this type of process, the time constant is much longer, ranging from seconds to minutes. The metabotropic receptors play an important role in synaptic plasticity and are responsible for learning and adaptation behavior of neural circuits. Examples of inhibitory transmitters are glycine and $GABA_A$. They produce so-called inhibitory postsynaptic potentials (IPSP). Examples of excitatory transmitters are glutamate and acetylcholine, which generate so-called excitatory postsynaptic potentials (EPSP).

1.7.1.4 The Equilibrium potential

For analytical convenience, electrical circuit diagrams can be used to represent the basic properties of membrane and channels (Fig. 1.15). Here, the membrane is electrically equivalent to a capacitor C_m, and the channel to a conductor g_c. The electrochemical gradient between the extracellular and the intracellular space can be thought of as a battery with an electromotive force (emf) E_c in series with the conductor. The energy stored in the battery is given by the Nernst potential (or equilibrium potential), which in turn arises from the semi-permeable membrane separating solutions with different ionic concentrations from each other. Since the natural progression of all dynamic systems is to move towards an equilibrium (or maximal entropy), there are driving forces for each type of ion, which results in the transmembrane potential V_m across the porous membrane. A membrane separating a small amount of charge can still produce a large potential difference, since the energy required to overcome the lipid bilayer with closed channels is very high. Therefore, units need to be defined that are independent of the membrane area, because the resistance decreases as the access area increases: the membrane specific resistance R_m [cm^2] and the specific conductance G_m [S/cm^2]. According to the discussion above, the Nernst equation can be used to describe the membrane potential:

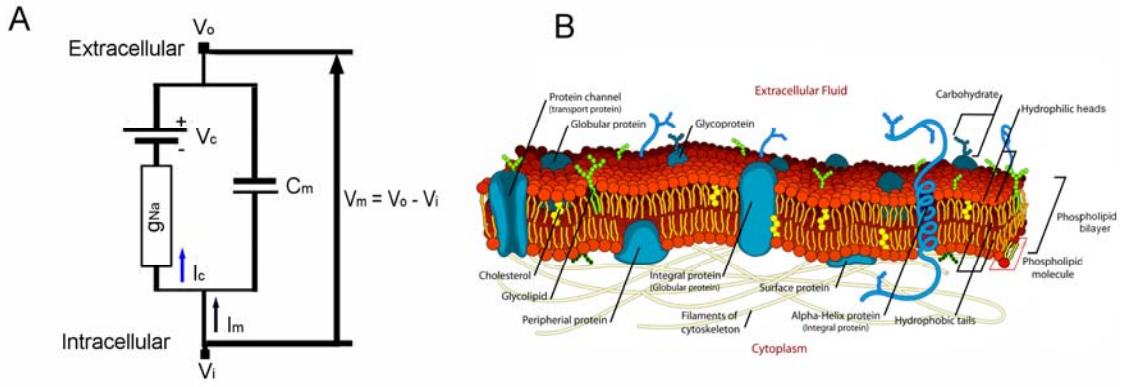

Fig. 1.15: Equivalent electrical circuit (a) and drawing (b) of a cell membrane (picture: license-free)

$$V_m = V_e - V_i = \frac{RT}{z_e F} \ln \frac{[c]_o}{[c]_i}, \qquad \textbf{1-14}$$

where V_m is the equilibrium potential of a channel, V_i is the intracellular potential, V_e is the outside potential, $[c]_i$ and $[c]_e$ are the intra- and extracellular ionic concentrations, respectively, R is the gas constant, T is the absolute temperature in [K], F is Faraday's constant and z_e is the valence, or charge, of the ion [48].

1.7.2 Neuronal communication

1.7.2.1 The action potential

Prior to the initiation of an AP, the inside of the cell is charged negatively in comparison with the outside. This is due to the ionic gradients and the specific neuronal membrane characteristics. A depolarization occurs when the charge on the inside of the cell becomes less negative (fig. 1.17). A more positive inner potential denotes a hyperpolarization. As soon as positive ions, e. g. Na^+, cross the membrane and enter the intracellular space, the TMP experiences a positive shift, a depolarization. An outflow of positive ions, in this case K^+, causes a hyperpolarization by pushing the membrane potential into a more negative direction. As the membrane around the axon hillock receives excitatory input which reduces the membrane potential, the voltage – gated Na^+ - channels start to open. With more of these channels letting Na^+ - ions pass, the membrane potential decreases even further until a threshold potential is reached which leads to the majority of the remaining Na^+ - channels to open, releasing a large quantity of Na^+ - ions into the cell and reversing the membrane potential to approximately 50 mV. Following the depolarization, K^+ - channels release potassium ions into the extracellular space, which repolarizes the membrane. The membrane potential is now even more negative than it was before the AP started. In order to regain the equilibrium potential, Na^+ - K^+ - exchange proteins re-introduce K^+ - ions that are lacking inside the cell and expel excess Na^+ - ions, until the resting potential is reached. This active pumping process is relatively slow, compared with the fast, passive movement through the Na^+ - and K^+ - channels during the depolarization and repolarization phases of the AP.

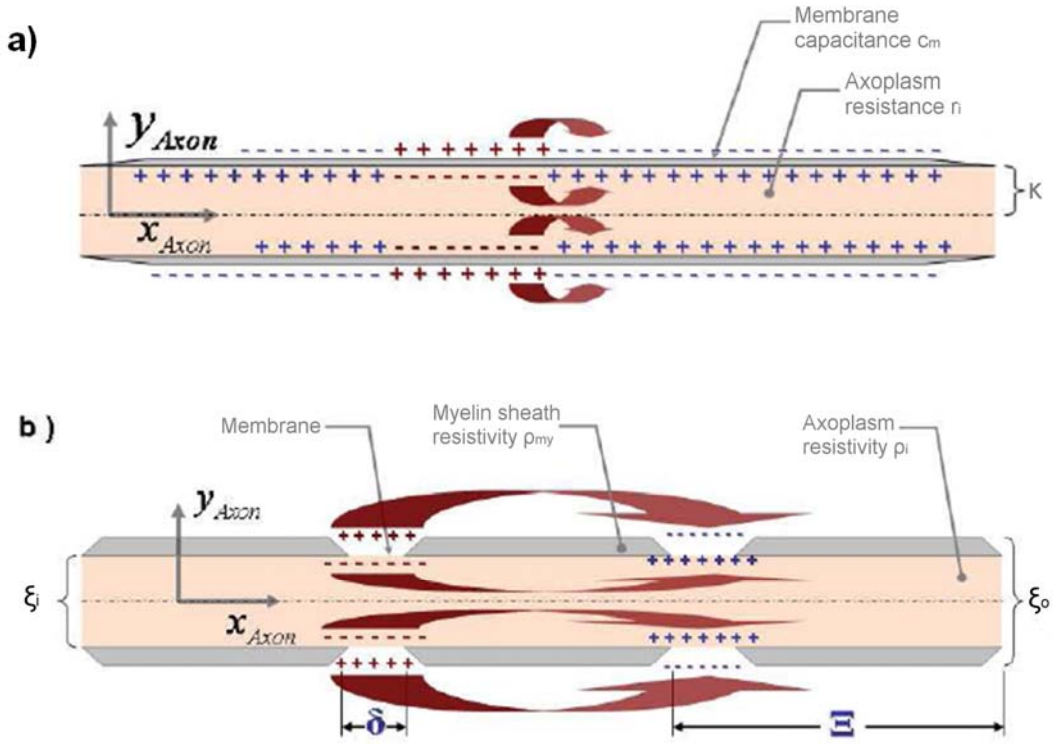

Fig. 1.16: Continuous (a) versus saltatory (b) action potential propagation. Source: [125]

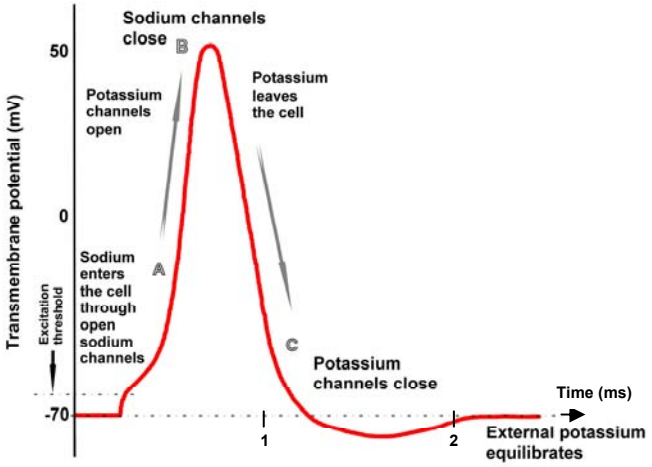

Fig. 1.17: Temporal and biochemical evolution of a typical action potential in an axon [redrawn from 125]

1.7.2.2 Hodgkin-Huxley formalism

In the excitable membrane, the transmembrane current per unit area i_m consists of a capacitive part and the ion currents i_m^k for sodium, potassium and other ions, which is reflected in the following equation [49]:

$$i_m = c_m \frac{dV_m}{dt} + \sum_k i_m^k, k \in \{Na, K, L\} \qquad \textbf{1-15}$$

The ionic current i_m^k can be approximated using Ohm's voltage-current law. Knowing the conductance g_m^k and the equilibrium potential V_0^k of the respective ionic driving force, the ion currents are given by:

$$i_m^k = g_m^k \left(V_m - V_0^k\right) \qquad \textbf{1-16}$$

Implementing this relation, the equivalent circuit diagram of the membrane is extended as shown in Fig. 1.18.

From these equations, one can deduct that the resting membrane voltage always lies between the equilibrium potentials of sodium and potassium. The equilibrium membrane potential is, for the most part, determined by the largest channel conductivity. Following membrane potential changes, the kinetics of the sodium and potassium currents can be approximated using the dimensionless and statistically independent gating variables n, m, and h. These variables are functions of time and voltage and vary between zero and one. Each one of them follows a first-order differential equation:

$$\frac{d\Gamma}{dt}\alpha_\Gamma(1-\Gamma)-\beta_\Gamma\Gamma,\Gamma\in\{n,m,h\} \qquad \textbf{1-17}$$

where α and β are the voltage-dependent rate constants in [ms^{-1}], determined empirically from voltage-clamp experiments (see [126] for detailed calculations and values).

The non-linear potassium conductivity can now be computed as:

$$g^K = n^4 g^K_{\max} \ , \qquad \textbf{1-18}$$

and the sodium conductivity as

$$g^{Na} = m^3 h g^{Na}_{\max} \qquad \textbf{1-19}$$

Even though this model cannot be applied to human tissue quantitatively, most of the qualities of nerve conduction in humans can be represented by it.

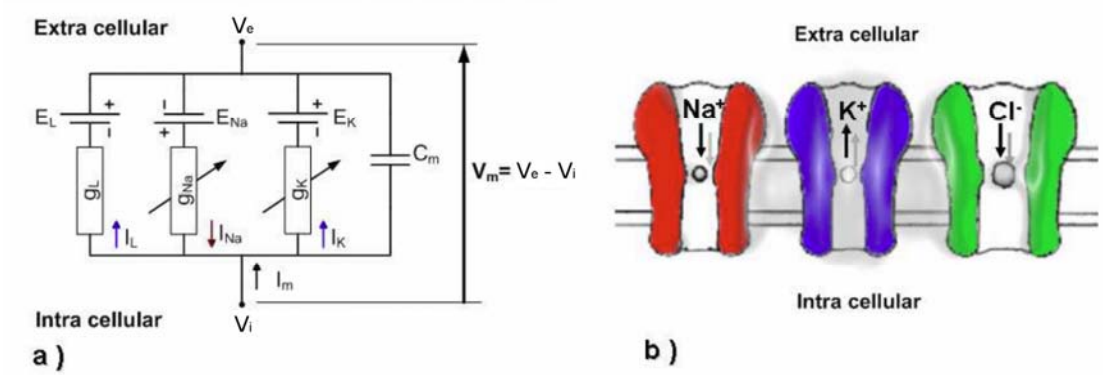

Fig. 1.18: Hodgkin-Huxley model of the excitable membrane (a); Schematic drawing of selective ion channels (b, source: [125])

1.7.2.3 The cable model

1.7.2.3.1 History

A milestone in neuro-electrophysiological research were the studies conducted by Hodgkin and Huxley in 1952, which opened up a new understanding of how APs are initiated and propagated [49, 51, 52]. The giant squid axon, which was used in their experiments, has a diameter of 0.5 mm, allowing the introduction of electrodes into the axon and the exchange of solutions with the internal axoplasm. These studies have general relevance because the properties of the squid axon are very similar to non-myelinated nerves in vertebrates, including mice.

1.7.2.3.2 Unmyelinated axons

In order to better understand how APs are propagated along the axon (fig. 1.16), and for modeling of the interaction between electromagnetic pulses and an axon, the cable equations were derived. For this model to work, it is assumed that the intracellular potential is constant in angular direction, i. e. it is only a function of the axial distance. Furthermore, the axoplasm is a linear, ohmic conductor, and the extracellular potential generated by the fiber's own electrical activity is so small that it can be neglected. The latter assumption means that the intracellular potential equals the transmembrane potential V_m. Applying Kirchhoff's law of current conservation, the membrane current (per unit length) i_m is

$$i_m = -\frac{\partial I_i}{\partial x}, \qquad \textbf{1-20}$$

where I_i is the intra-axonal current. The axial current I_i through the fiber is calculated according to Ohm's law:

$$r_i I_i = -\frac{\partial V}{\partial x}, \qquad \textbf{1-21}$$

r_i being the internal resistance of the axoplasm per unit length. The membrane current per unit length can now be calculated using eqs. 1-15, 1-20 and 1-21:

$$i_m = c_m \frac{\partial V}{\partial t} + \frac{V}{r_m} = \frac{1}{r_i}\frac{\partial^2 V}{\partial x^2}, \qquad \textbf{1-22}$$

where c_m is the passive membrane capacitance per unit length, and r_m is the resistance times unit length. By defining a length constant λ and a time constant τ of the membrane,

$$\lambda = \sqrt{\frac{r_m}{r_i}}, \tau = c_m r_m, \qquad \textbf{1-23}$$

the combination of the equations for the membrane current and the axial current yields the cable equation:

$$\lambda^2 \frac{\partial V^2}{\partial x^2} - V = \tau \frac{\partial V}{\partial t}. \qquad \textbf{1-24}$$

The following figure illustrates the passive cable model.

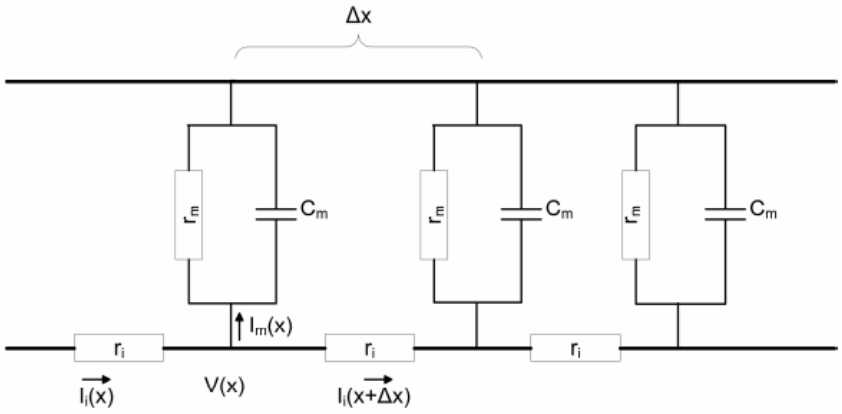

Fig. 1.19: Equivalent circuit diagram of a passive cable [source: 125]

The model above only applies to the intracellular electric field. The axial component of that field inside the axon equals the negative gradient of the intracellular potential:

$$E_i = -\frac{\partial V}{\partial x} \qquad \textbf{1-25}$$

Once there is an additional source of an electric field, such as through temporally varying electromagnetic induction, another axial field component must be added to the intracellular electric field:

$$E_i = -\frac{\partial V}{\partial x} + E_x \qquad \textbf{1-26}$$

A magnetically induced field would be calculated using the magnetic vector potential, because the induced electric field cannot be calculated from the gradient of the voltage alone. Only the electric field component in axial direction results in significant modulation of the membrane potential [53]. Thus, the induced electric field is

$$E_x = -\frac{\partial A}{\partial t} \qquad \textbf{1-27}$$

with

$$\vec{A} = \frac{\mu_0}{4\pi}\int \frac{j(r')}{|r-r'|} d^3 r\,, \qquad \textbf{1-28}$$

where μ_0 is the vacuum permeability, r' is distance to the source, j is the current density in the conductor, and r is the distance between the coil element and the site of the calculated electric field. The vector potential and the induced electric field are determined by the geometry and the current of the coil. The magnetic vector potential theory serves as the basis for numerical computations in electromagnetic finite-element method programs [54, 55].

The equation for the intracellular axial current can now be computed:

$$r_i I_i = -\frac{\partial V}{\partial x} + E_x(x,t) \qquad \textbf{1-29}$$

The surface charges on the cell membrane create an electric field of the order of 10^7 V/m, while the field induced by a stimulating coil is generally less than 10^3 V/m [56, 57]. Consequently, the radial component of the electric field can be neglected. Hence, the modified cable equation reads as

$$\lambda^2 \frac{\partial V^2}{\partial x^2} - V - \lambda^2 \frac{\partial E_x}{\partial x} = \tau \frac{\partial V}{\partial t} \qquad \textbf{1-30}$$

The passive cable model is capable of describing the interaction between the nerve fiber and the induced electric field. However, a comprehensive model for the dynamics of AP propagation and nerve stimulation requires an active membrane model. The equivalent circuit diagram of the membrane is now extended by the Hodgkin-Huxley model. For its implementation, the passive cable model is divided into unit lengths of cable with a fixed diameter. Thus, the resistance per unit length of the fiber can be calculated using the fiber radius κ and the axoplasmic resistivity R_i:

$$r_i = \frac{R_i}{\pi \kappa^2} \qquad \textbf{1-31}$$

Analogously, the membrane current per unit length i_m and the membrane capacitance per unit length c_m can be expressed in terms of its current density J_m and the capacitance per unit area C_m:

$$i_m = 2\pi\kappa J_m \qquad \textbf{1-32}$$

$$c_m = 2\pi\kappa C_m \qquad \textbf{1-33}$$

As shown in Fig. (1.20), the passive membrane resistances are now replaced with active elements representing the time- and voltage dependent ion channels. The equation that follows this operation, along with incorporation of the discretized resistivities, currents and capacities, is the cable equation for excitable axons:

$$\frac{\kappa}{2R_i}\frac{\partial^2 V}{\partial x} - \left(g_{Na} m^3 h (V - E_{Na}) + g_K n^4 (V - E_K) + g_L (V - E_L)\right) = C_m \frac{\partial V}{\partial t} + \frac{\kappa}{2R_i}\frac{\partial E_x}{\partial x} \qquad \textbf{1-34}$$

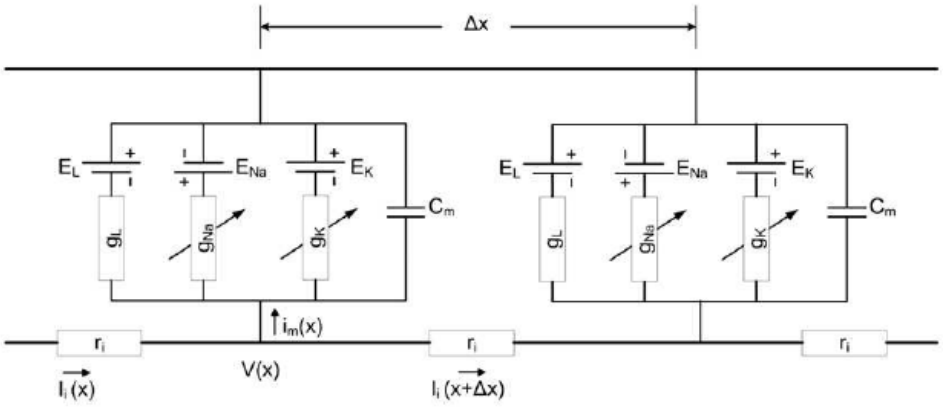

Fig. 1.20: Equivalent schematic of the Hodgkin-Huxley-implemented active membrane model [source: 125]

1.7.2.3.3 Myelinated axons

As mentioned earlier, there are two primary types of mammalian axons: myelinated and unmyelinated. Unmyelinated axons transmit their APs continuously, while myelinated axons make use of an insulating layer around them that is regularly interrupted by small gaps. These active gaps in the otherwise passive membrane, the nodes of Ranvier, act like repeaters broadcasting the signal down the insulated cable to the next node in line (see Fig. 1.16b). In the nodes, the membrane current per unit length i_m flows through the nodal capacitance C_n and the sodium and leakage channels, but not through the potassium channels [50, 58]. The voltage sources V_m represent active pump proteins beneath the myelin that maintain the resting potential of the membrane. Each node is modeled as a discrete current source contributing the following part to the membrane current:

$$\pi\xi_i\delta\left(g_{Na}m^3h(V-E_{Na})+g_L(V-E_L)+C_n\frac{\partial V}{\partial t}\right), \qquad \textbf{1-35}$$

where ξ_i is the internal diameter of the axon and δ is the width of each node. The gating variables m and h are the same as before. However, the rate constants they contain are adjusted to values from mammalian, myelinated axon recordings [50, 58]:

$$\alpha_m(V)=\frac{126+0.363V}{1+e^{-\frac{V+49}{5.3}}} \qquad \textbf{1-36}$$

$$\beta_m(V)=\frac{\alpha_m}{e^{\frac{V+56.2}{4.17}}} \qquad \textbf{1-37}$$

$$\alpha_h(V) = \frac{\beta_h}{e^{\frac{V+74.5}{5}}} \qquad \textbf{1-38}$$

$$\beta_h(V) = \frac{15.6}{1+e^{-\frac{V+56}{10}}} \qquad \textbf{1-39}$$

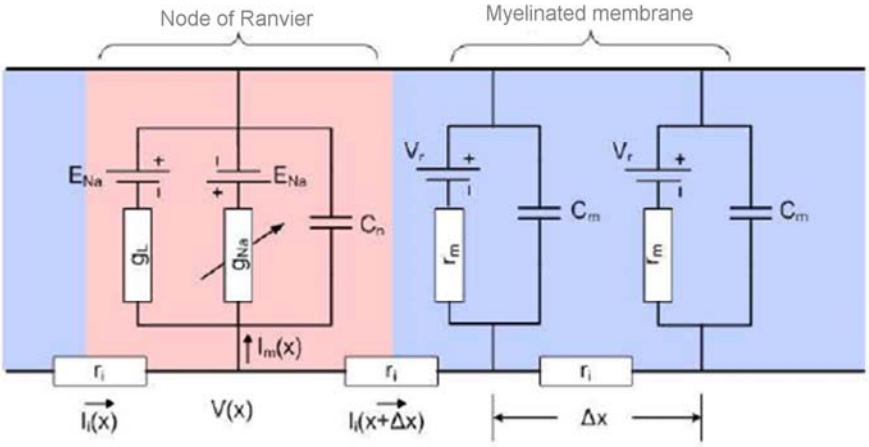

Fig. 1.21: Equivalent schematic of a myelinated axonal membrane [source: 125]

The TMP in the myelinated internodal regions follows the cable equation (1-36). The length constant of the internodal spaces is defined as

$$\lambda_{my} = \xi_i \sqrt{\frac{\rho_{my}}{8\rho_a} \ln \frac{\xi_o}{\xi_i}}, \qquad \textbf{1-40}$$

ξ_o being the outer diameter of the axon, ρ_{my} the resistivity of the myelin sheath, and ρ_a the resistivity of the axoplasm. The time constant of the myelinated membrane follows as

$$\tau_{my} = \mu_0 \varepsilon_{my} \rho_{my}, \qquad \textbf{1-41}$$

where ε_{my} is the permittivity of the myelin. The resting membrane potential was shown to be uniform throughout the internodal segments (V_r=-80 mV), due to the activity of potassium channels [59].

According to the cable equations, the induced electric field is proportional to the square of the length constant λ. Keeping this correlation in mind, the conductivity or susceptibility to external fields of myelinated versus unmyelinated axons can now be compared. Assuming that the myelinated and the unmyelinated axons have the same internal diameter ξ_i=2κ, and that the membrane resistance times unit length is

$$r_m = \frac{r_m}{\Delta x} = \frac{\rho m}{\pi \xi_i \Delta x}, \qquad \textbf{1-42}$$

the squares of the length constants are

$$\lambda^2 = \frac{\xi_i}{4}\frac{\rho_m}{\rho_i} \qquad \textbf{1-43}$$

and

$$\lambda_{my}^2 = \xi_i^2 \frac{\rho_{my}}{8\rho_i}\ln\left(\frac{\xi_o}{\xi_i}\right), \qquad \textbf{1-44}$$

which means that

$$\frac{\lambda_{my}^2}{\lambda^2} = \frac{\xi_i}{2}\frac{\rho_{my}}{\rho_m}\ln\left(\frac{\xi_o}{\xi_i}\right). \qquad \textbf{1-45}$$

Assuming an axoplasmic resistivity of 5.47 x 10^{-2} kΩ*cm, and a myelin resistivity of 7.4x10^5 kΩ*cm [50], the ratio of the myelinated axon follows the curves in figure 1.22, depending on the inner axonal diameter (number adjacent to each curve), and the outer diameter.

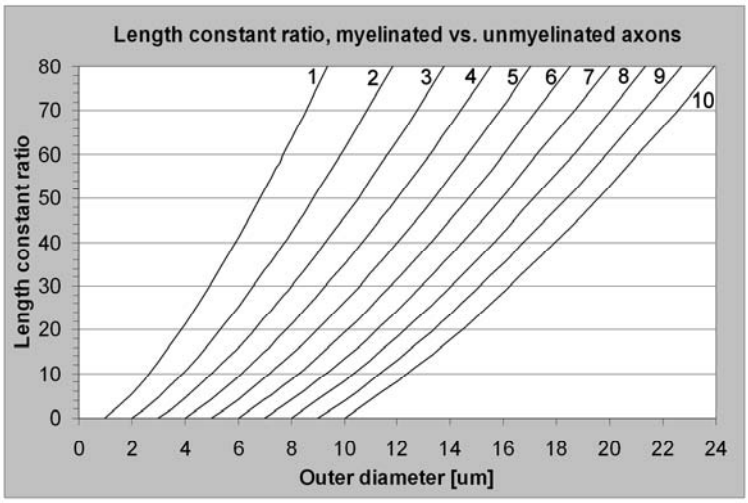

Fig. 1.22: Length constant ratio of myelinated versus unmyelinated axons. For example, the length constant of a 6 μm diameter axon with a myelin sheath of 2 um is 20 times greater than an equally wide, unmyelinated axon.

1.7.2.4 Neural networks

Besides the molecular computation of signals taking place inside each neuron, there is also information processing on the network level, much like a computer processor whose single transistors communicate with each other using ones and zeros. The enormous computational power of the whole brain has not been entirely understood or explained, but small networks of a few dozen - up to a few hundred - neurons can

nowadays be studied in great detail using the available electrophysiological and/or optical techniques. One factor that seems decisive for the efficiency of the brain's massively parallel processing capabilities is the vast number of interconnections between excitatory and inhibitory neurons. The so-called interneurons, which are usually of inhibitory character, are of crucial importance to the control of complex procedures. Fig. 1.23 exemplifies the interaction between inhibitory and excitatory neurons in a very simple neural network that controls a pair of extensor and flexor muscles. The axon "1a" comes from an upper motoneuron and controls the lower motoneuron "1" as well as an inhibitory interneuron "2", both of which it has excitatory, acetylcholine (Ach)-mediated influence over. Interneuron 2 inhibits another motoneuron, "4", which controls the flexor. The flexor must be limp while the extensor is active. If only one pattern of APs, namely a burst that dies out gradually due to refractory processes, were needed for the control of this particular muscle, this combination of cells would be enough. However, the Renshaw neuron "3", which receives positive feedback from the axon of motoneuron 1 and is capable of inhibiting both motoneuron 1 and interneuron 2, can shape, and particularly shorten, the activity bursts innervating the extensor and silencing the flexor. That way, more individual movements can be performed in a short period of time. This simple illustration does not apply to most other neural networks, but it is a neat model for the way bursting activity is controlled in small networks of neurons. In the brain, input-output relations in neural networks are, of course, far more complicated and they involve neurons expressing several different kinds of inhibitory and excitatory receptors, such as GABA, AMPA, glycine, NMDA, acetylcholine and glutamine, which also depends highly on the respective part of the CNS. For a detailed description of bursting activity in spinal networks in vitro, see [60].

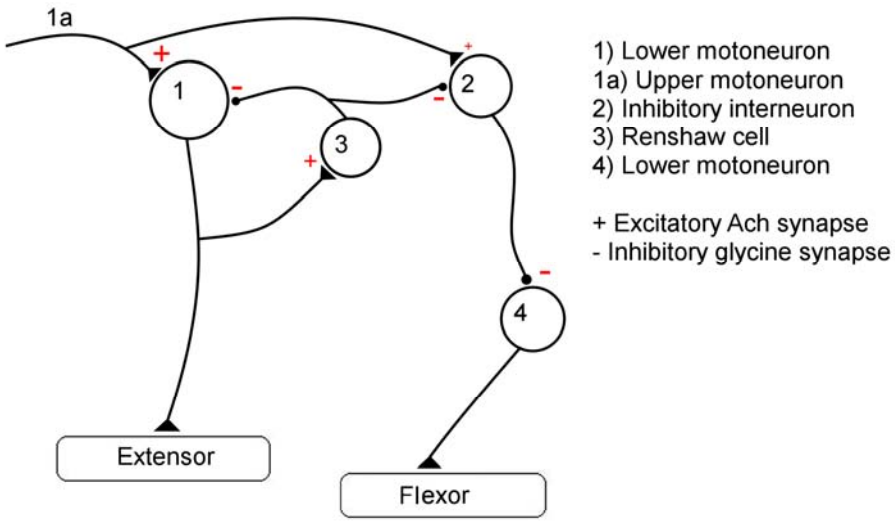

Fig. 1.23: Minimal neural network: Two lower motoneurons controlling extensor and flexor muscle fibers. The motoneurons are intricately controlled through excitatory transmission from an upper motoneuron and inhibitory input from an interneuron (2) and a Renshaw neuron (3).

1.8 Electrophysiological experiments with neuronal cell cultures

1.8.1 Intracellular and extracellular recording methods

1.8.1.1 Measuring membrane potential in excitable cells

Neurological research employing electrophysiological techniques has been one of the most quickly developing areas of medical studies in the past 50-60 years. A neuron's primary function is to receive, compute and transmit information via production of APs which can be thought of as binary on/off signals. Thus, information is transmitted by either giving the next cell in line a signal or not. This communication principle gives electrophysiological analysis its great power, enabling it to detect changes in a neuron's functional state immediately and accurately by simply counting the number of produced APs and monitoring their temporal and spatial distributions. If the experimental setup is sensitive and sophisticated enough, details of the AP wave shapes can also be measured. Since the different temporal phases of an AP can often be attributed to movements of certain types of ions, analysis of these phase shifts can be translated into changes in ion channel functions. The most straightforward way of recording membrane potential changes in detail, is the patch-clamp technique, invented in the late 1970's by Neher & Sakmann [67]. Micropipettes are used to penetrate the cell membrane and contact the cytosol, while the extracellular solution is electrically separated from the recording electrode due to a tight seal that forms between the membrane and the glass pipette. This way, ionic currents in the pA range, and thus the activity of ion channels of a single cell can be measured (Fig. 1.24). While single cells can be analyzed very precisely with this technique, it is a highly invasive method, and it is limited to a few neurons in a small network at the same time. Non-invasive, extracellular, multi-site recordings of entire networks comprised of a few dozen to a few thousand neurons require a different approach: Neurons can be electrically contacted extracellularly with substrate-integrated electrode arrays. These arrays generally consist of a suitable substrate (e. g. glass, for concomitant light microscopy), covered with an array of conductive paths, which, in turn, are covered with a biocompatible insulation layer. Only the very tips of the conductors, which merge into an array in a small region on the substrate (typically ≈ 1 mm^2), are de-insulated for recording of potential fluctuations. Since implanting these electrode arrays in live animals is problematic and has only been achieved reliably during the past decade, the groups of Thomas and Gross independently developed *in vitro* recording systems that allow for recording from neuronal cell cultures residing on MEA plates [68, 69]. Both primary, embryonic tissue and slices from adult brain areas can be used with this technique.

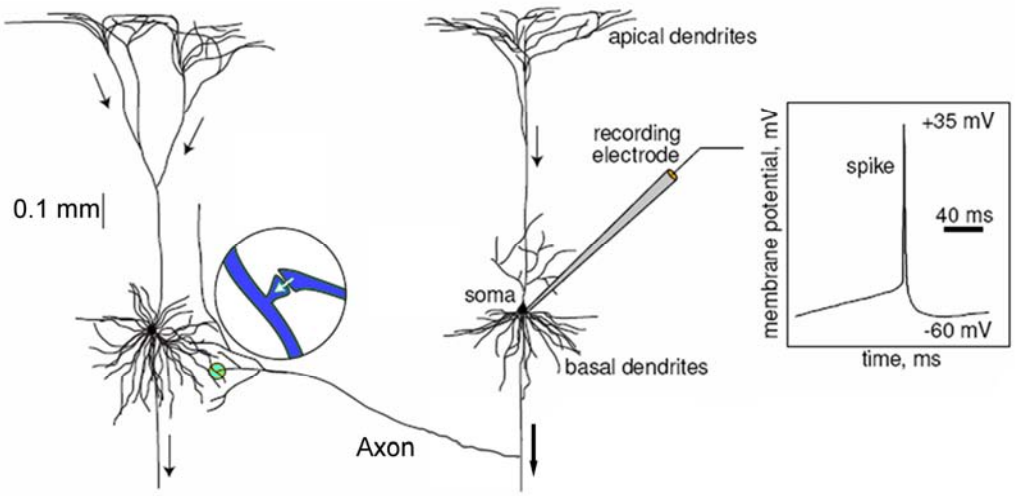

Fig. 1.24: Intracellular recording of an action potential from two synaptically interconnected cortical pyramidal neurons [redrawn from 70]

1.8.1.2 Cell-electrode coupling

Recording electrical signals from outside a biological cell is only possible when the charge distribution on the membrane surface changes quickly, since the transduction is a capacitive process. In case of the neural cultures used here, the capacitor between the electrically active cell and the electrode is the coating of the multi-microelectrode plate (MMEP), a combination of the adhesion molecules poly-d-lysine and laminin, and a thin monolayer of glia cells (and/or fibroblasts) that serves as a feeding and support layer for the neurons. The absolute electric field created by the dipoles that consist of charged and uncharged membrane parts can be detected with the planar electrodes, depends on the distance z and follows the equation

$$\left|\vec{E}\right|(z) = V_{DP} d^2 \frac{\cos\gamma}{z^3}, \qquad \textbf{1-46}$$

where V_{DP} is the voltage between the dipole parts, d is the distance between them and γ is the angle between the dipole axis and the electrode point [71]. We can deduct form this equation that the dipoles parallel to the electrode induce the largest fields, that large dipoles are more effective than small ones, and that the field dissipates proportionally with the third power of the distance to the cell membrane. Hence, the closer the cell is to the electrode, the better the signal transduction.

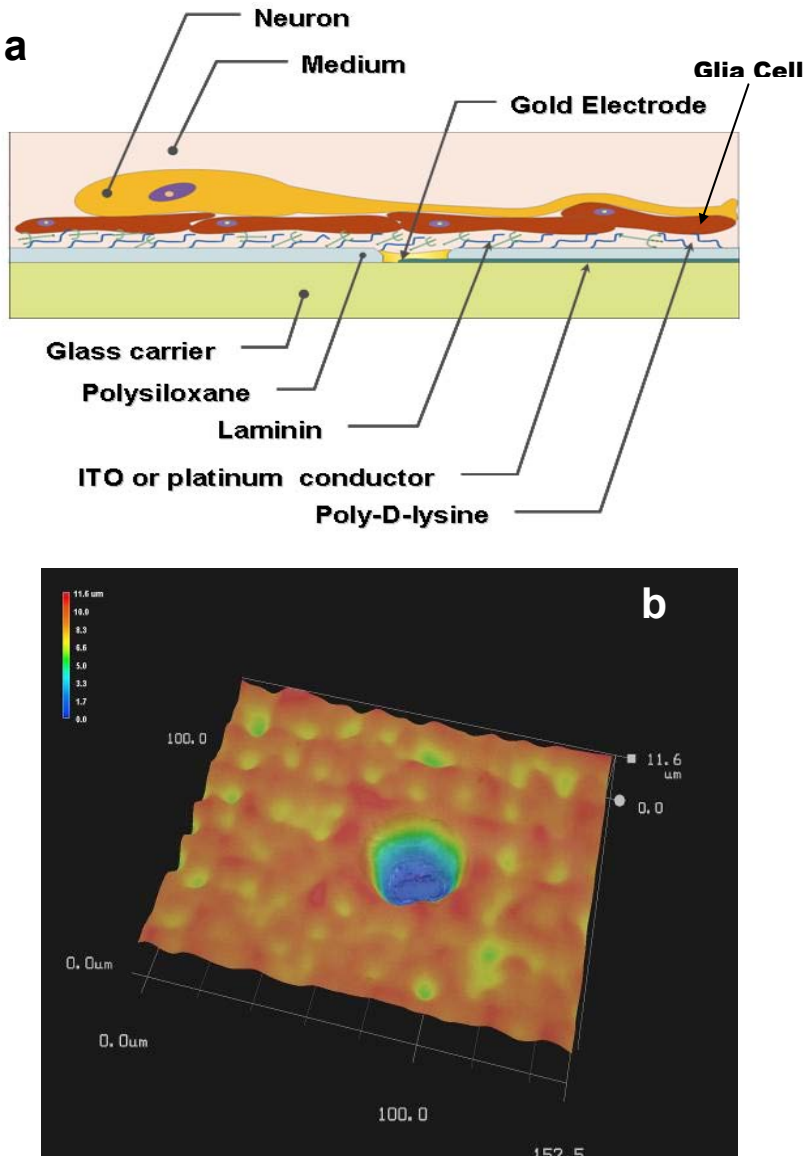

Fig. 1.25: a) Simplified drawing (cross-section) of a neuron, glia cells and extracellular proteins on an MEA glass plate; b) 3D digital micrograph (taken at the IMETUM) of a laser-deinsulated electrode crater on a Center for Network Neuroscience (CNNS)-multi microelectode plate.

This postulation is also apparent from simulations conducted in the laboratory of S. Martinoia [72]: Fig. 1.26 shows an equivalent circuit diagram mimicking the sealing impedance (corresponding to the cell-electrode connection minus the electrode impedance), and simulations of APs computed with the electric circuit simulation program SPICE using varying values for the seal resistance, which is a measure of the degree of electrode coverage by the cell. In the circuit diagram, R_i denotes the cytoplasmic resistance connecting two adjacent compartments; R_{Cl} and V_{Cl} are the chloride resistance and the chloride equilibrium potential. I_{act} represents the sum of all active ionic currents, C_{me} the membrane – medium capacitance. R_{seal} and R_{spread} are the seal resistance modeling the resistive component of the thin layer of solution between the cell membrane and the microelectrode, and the spreading resistance of the extracellular matrix. C_m is the membrane capacitance, C_h the Helmholtz capacitance,

and C_d the capacitance of the diffuse layer of ions in the solution. The parameters for the potential simulations were (a) C_{me} = 0.7 pF, R_{seal} = 0.2 MΩ, (b) C_{me} = 1 pF, R_{seal} = 1 MΩ, (c) C_{me} = 1.4 pF, R_{seal} = 4 MΩ.

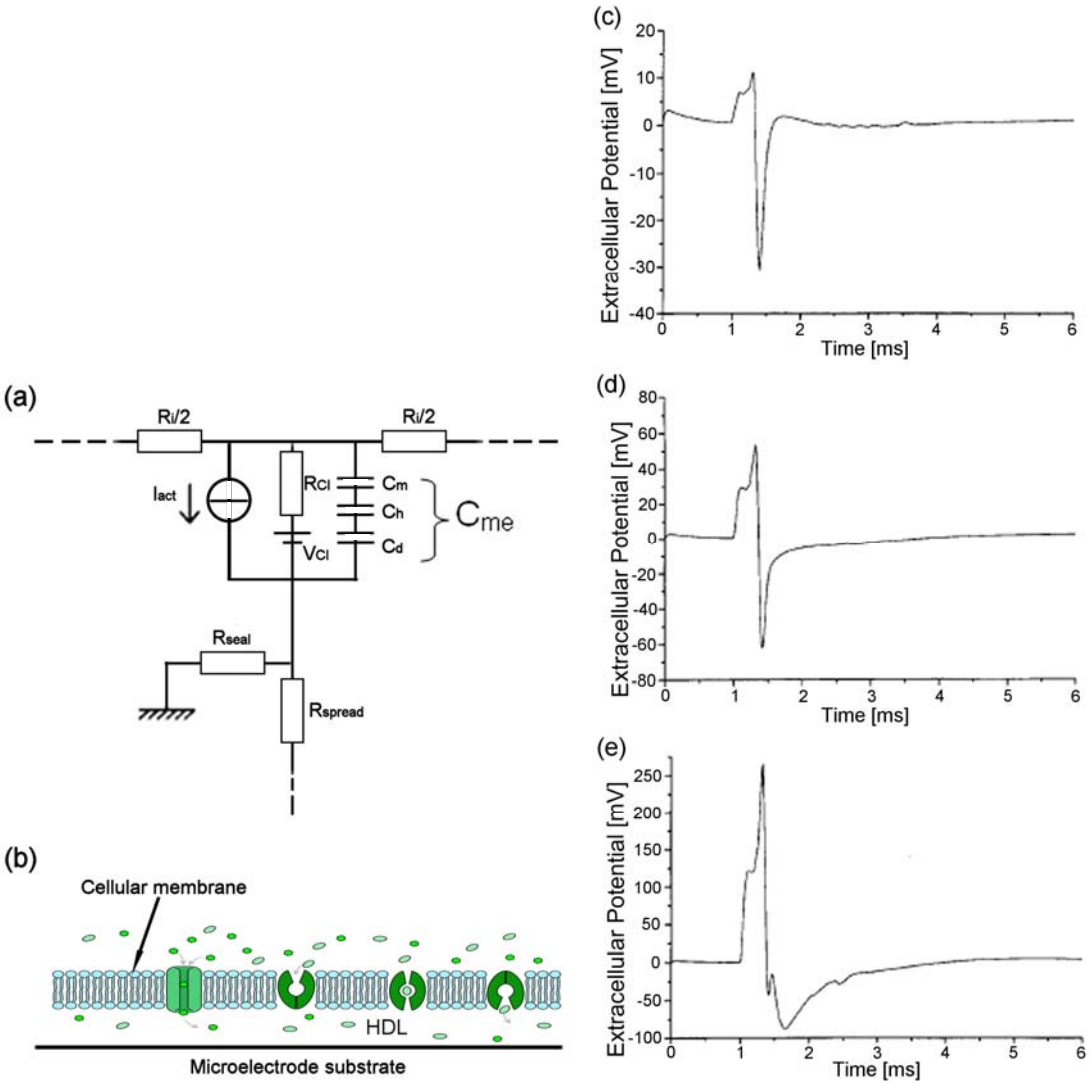

Fig. 1.26: a) Equivalent circuit of the active and passive electrical elements constituting the cell-electrode contact, b) Schematic drawing of the membrane – surface interface showing the Helmholtz double layer (HDL); Action potential simulations generated with *SPICE*, using different seal impedance values. [a) redrawn from 72, b) with permission of the publisher of 72]

The simulations show that with increasing coverage of the electrode area, the overall amplitude of the transferred signals increases dramatically. The sodium current, represented by the first peak, increases, while the second peak, representing the potassium outflow during repolarization, is reduced.

A precise explanation of the electrical processes leading to the possibility of extracellular electric recording requires the following considerations and assumptions [73-75]. The specific membrane capacity c_m is assumed to be constant. The ionic

concentration gradient inside the gap between the cell and the electrode (membrane area A_{JM}) is different from the rest of the cell membrane (A_{FM}). Hence, the gradient-dependent Nernst potential for every ionic species V_{J0}^{i} is different in this region. The ion channel specific factor

$$\mu_J^i = \frac{g_{JM}^i}{g_{FM}^i} \qquad \textbf{1-47}$$

describes the ratio of the conductances of the junction part, g_{JM}^i, and of the free part, g_{FM}^i, of the membrane. The voltage inside the gap is different from the voltage between the free membrane and the extracellular medium. For a cell with no contact to a substrate, the conductivity of all ion channels for a specific sort of ions g_{FM}^{i} is equal over the entire surface. The time course of the intracellular potential V_m depends on the injected current I_{inj} and the ionic currents through the membrane channels only:

$$\frac{I_{inj}}{A_M} = \sum_i g_{FM}^i \left(V_m - V_0^i\right) + c_M \frac{dV_m}{dt}, \qquad \textbf{1-48}$$

Where c_M is the membrane capacitance. Now, we consider a cell that is in contact with a substrate, the ratio of the area in contact, A_{JM}, and the entire area A_M

$$\beta = \frac{A_{JM}}{A_M}, \qquad \textbf{1-49}$$

so that

$$A_{JM} = \beta A_M \text{ and } A_{FM} = (1-\beta)A_M, \qquad \textbf{1-50}$$

Where A_{FM} is the free membrane area that is not in contact with the substrate. Thus,

$$\frac{I_{inj}}{(1-\beta)A_M} = \sum_i g_{FM}^i \left(V_m - V_0^i\right) + \frac{\beta}{1-\beta}\sum_i g_{JM}^i \left(V_M - V_J - V_{J0}^i\right) + c_M \frac{dV_M}{dt} + \frac{\beta}{1-\beta} c_M \frac{d\left(V_M - V_J\right)}{dt}$$

1-51

Since the membrane conductivity is much smaller than the conductivity of the medium in the gap, V_M-V_J equals V_J. It can be assumed that the ionic concentrations in the gap are negligibly different from the medium surrounding the cell. Therefore, the Nernst potential in the gap is equal to the Nernst potential of the free surface. The capacitive currents in the gap area can also be neglected, since the time constant is of the order of 1 µs. The current through the gap, $g_J \cdot V_J$, depends on the charging current of the membrane and the bulk capacitance, and the current through the ion channels in this area:

$$g_J V_J = \sum_i g_{JM}^i \left(V_M - V_0^i\right) + c_M \frac{dV_M}{dt} \qquad \textbf{1-52}$$

Applying these simplifications and introducing the conductance ratio μ_j^i, the local extracellular voltage in the gap depends on the injection current, the conductivity of the free membrane area, and the intracellular voltage:

$$V_J = \frac{1-\beta}{g_J}\left[\frac{I_{inj}}{(1-\beta)A_M} - \sum_i g_{FM}^i \left(1-\mu_J^i\right)\left(V_M - V_0^i\right)\right] \qquad \textbf{1-53}$$

The ion channels can be distributed in five different ways (percent depletion/enrichment as examples): homogenous ($\mu_J = 1$), no channels or only ohmic resistance in the gap area ($\mu_J = 0$), homogenous depletion/enrichment of channels in the contact area, or inhomogeneous ion channel distribution changes. In case of homogenous ion channel depletion/enrichment, the extracellular voltage becomes proportional with the first temporal derivative of the intracellular potential:

$$V_J = \frac{1-\frac{1}{1-\beta}\mu_J}{1+\frac{\beta}{1-\beta}\mu_J}\frac{c_M}{g_J}\frac{dV_M}{dt} \qquad \textbf{1-54}$$

In case of non-homogenous depletion or enrichment of the channels in the gap region (i. e. Na^+ channels may be less expressed while K^+ channels are more expressed compared with the free membrane area) the first derivative is still a major part of the equation, but the induced voltage is not merely the first derivative of the intracellular potential multiplied by a scaling factor:

$$V_J = \frac{\mu_J^{Na} g_{FM}^{Na}\left(V_M - V_0^{Na}\right) + \mu_J^K g_{FM}^K \left(V_M - V_0^K\right) + \mu_J^L g_{FM}^L \left(V_M - V_0^L\right)}{g_J} + \frac{c_M}{g_J}\frac{dV_M}{dt} \qquad \textbf{1-55}$$

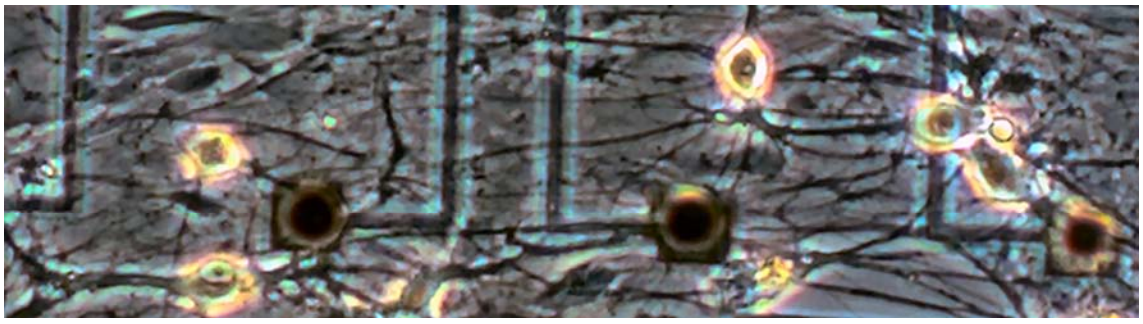

Fig. 1.27: Living neurons on a multielectrode array, showing various parts of the cells (bright elliptical bodies and dark dendritic and axonal processes) partially covering recording electrode craters (black spots).

1.8.2 Signal acquisition requirements

The requirements for electrophysiological recording electronics depend strongly on the type of analysis that is desired to be performed with the acquired data. For purely quantitative data providing an overall measurement of the network activity, the system must be capable of detecting each AP reliably. However, this is only sufficient for applications where only the overall network activity is of interest. As soon as single APs from an overlapping group of recorded waveshapes need to be separated and studied in detail – whether in real-time or offline – their exact time courses must be recorded. Since the neurons are grown with minimal external influence, i. e. to a great extent randomly, a large portion of the electrodes usually receive signals from several cell parts, thus constantly creating superposition of signals. A wide range of applications, including analysis of subgroups of neurons, studies of ion channel blockers, network information processing, etc., require this detailed recording of APs. The Nyquist theorem states that for an exact reconstruction of any given signal, the sampling frequency of the reconstructing system must me at least higher than twice the bandwidth of the original signal:

$$f_s \succ 2B \qquad \textbf{1-56}$$

Fig. 1.28 shows an example of a series of neuronal APs recorded using an MEA, at a bandwidth of 100 kHz. Most neuronal APs are roughly 0.5-2 ms long (hence the maximum frequency response between 0.5 and 2 kHz), but the exact waveform frequencies and shapes can vary quite drastically, depending on the cell-electrode coupling conditions, the type of neuron firing, which part of the neuron the signal is coming from, and whether the firing cell is under any chemically or physically induced altered condition that causes a change in receptor or ion channel kinetics. Empirically, the highest spectral components of a neuronal AP do not exceed 10,000 Hz. Therefore, the digitizing system should sample the neuronal signals at a frequency equal to or exceeding 20 kHz.

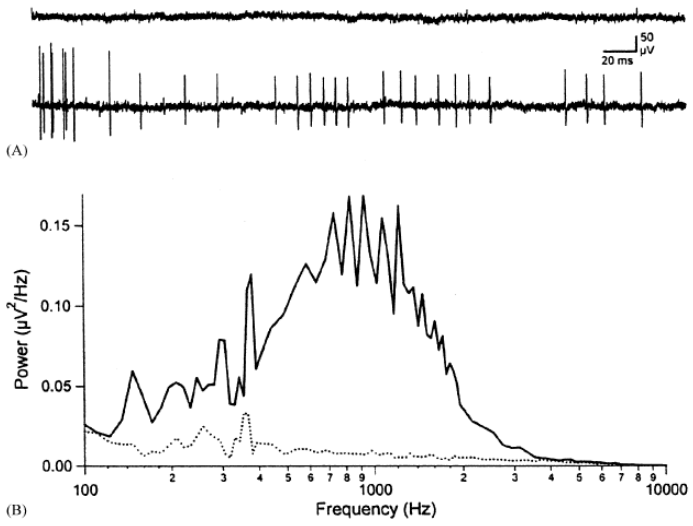

Fig. 1.28: Noise line without spikes (top), Spike series (middle), frequency response of the analog recording of spike activity (bottom) [from 76 with permission of the publisher]

1.8.3 Signal amplification

Unless the information desired from an MEA recording is purely about the time points at which an AP occurred, the amplitudes and time courses of the signals need to be reliably described by the cell-electrode-electronics system. For most planar metal electrode MEA designs, the signal cannot be amplified directly at the site of origin, as opposed to systems that consist of field-effect transistors the cells grow on. Consequently, the signal has to travel a certain distance to where it can be picked up by the first amplification stage. This distance must be kept at a minimum. Usually, the first amplification stage is an operational amplifier with a gain of ten to 100, followed by a high-pass or band-pass filter cutting off unwanted noise components. A second amplification stage can then further process the signal before it is digitized. Different input impedances of the headstage amplifier have been shown to affect the recorded potentials significantly, especially when the APs contain low-frequency components, such as cardiac potentials. These signals can only be obtained reliably by using high input impedances. Great care should also be taken in terms of shielding and induced noise, since the signal to noise ratio of the cellular signals varies greatly depending on the quality of the cell-electrode coupling.

1.8.4 MEA recording and equipment: State of the art

In electrophysiology, patch-clamp recording has long been established as the reference method for measuring electrical activity in the form of APs on the cellular level, despite its invasiveness. On the other end of the spectrum, field potentials, which represent the activity of large groups of neurons, are routinely recorded using Electroencephalogram (EEG) technology, whether the recording electrodes are applied externally or subdurally. For recordings of APs and field potentials on the local network level (up to a few hundred neurons), the use of MEAs has been constantly gaining popularity over the past 3 decades. As discussed earlier, there are many factors that determine the quality and stability of neuronal recordings. A variety of electrode geometries and materials have been proposed, manufactured and tested. Most of the designs now available are centered around square or hexagonal arrays of 30-256 electrodes with diameters of 10-40 µm. The arrays cover areas between 0.5 mm^2 and 10 mm^2. Electrode surface materials have been subject to extensive experimentation. Most commonly, they are made of, or coated with, gold or platinum (black), although other materials that offer a much higher total surface area, such as titanium nitrite or carbon nanotubes, have been introduced as well. From long-term experience gathered at the CNNS, plain gold provides impedance values that are sufficiently low to generate good signal-to-noise ratios. The electrode material is merely one of many parameters that influence the quality of the cell-electrode coupling. Another factor is the grade of adhesion between the surface of the MMEP and the neurons. Nanoporous materials are especially popular when the cells are to be electrically stimulated through the recording electrodes, as their high capacitance values limit the faradaic currents applied to the neurons [136].

The MEA substrate, usually glass (for simultaneous light microscopy), ceramic or silicon, is covered with a dielectric insulation material in order to exclusively expose the electrode spots to the cells and to shield the conductors from the culture medium.

Insulation materials such as several different siloxane derivatives, SU-8 epoxy, silicon nitrite and polyacrylamide are used nowadays. Each one of these materials has its advantages and pitfalls in biocompatibility, long-term stability in a saline environment, high dielectric constant, ease of handling, cost efficiency and sterilizability.

The first amplification stage for the bioelectric signals from the active tissue is typically positioned as closely to the MMEP as physically possible. That way, noise levels can be kept at about 20-40 µV. The AlphaMed Sciences MMEPs have a nominal impedance of 10 kΩ at 1 kHz, which is 10-100 times less than most other manufacturers' MMEPs. Therefore, they do not require a headstage amplifier. The total required gain of the amplification stage varies strongly with the cell-electrode coupling. While a gain of 1,000 may suffice for cases where a neuron is in direct contact with an electrode and covered by glial cells, we find that a gain of 10,000 is enough to amplify even such signals that are barely strong enough to be recognized as APs. Signal acquisition and spike detection programs have been evolving rapidly over the past years, and providing a comprehensive description of the available programs is beyond the scope of this work. Many laboratories have been tailoring individual programs using Matlab- or Labview-based platforms around their special needs. From our perspective, the data acquisition and real-time spike detection software provided by Plexon Inc., and the online and offline data analysis program Neuroexplorer offer outstanding quality and flexibility.

What other components does an MEA workstation need? The answer to this question depends entirely on the specific application aimed at. The encapsulation of the MMEP can be designed in one, user-friendly piece (e.g. Multichannel Systems), bearing the advantage of short assembly times and portability. For short-term recordings, as is often the case with brain slices, this approach is certainly useful. However, for recordings that last days or weeks, a reliable, sterile life-support system is required. The AlphaMed Sciences setup can be kept in a humidified, CO_2-controlled incubator, as there are no electronic parts in the enclosure holding the MMEP. However, this approach does not allow for simultaneous optical inspection of the cells. The design developed by Prof. Gross (CNNS, Denton) is capable of keeping cell cultures alive under in vivo-like conditions on the microscope stage for up to 14 days (7 days routinely). Using a modified, closed chamber setup with constant, slow medium circulation, recordings of 4-6 weeks in duration have been achieved. The CNNS MMEPs feature translucent ITO conductor lines that enable the user to monitor the morphology of the cells over the entire course of an experiment.

Currently, complete MEA systems for neuronal recordings, i.e. MMEPs, an enclosure, amplifiers, A/D-conversion, and signal acquisition software, are available from four individual companies. A brief overview is provided below.

- Multichannel Systems, Tübingen, Germany
    - MEAs and amplifiers with up to 6 wells and 256 electrodes, largest variety of MEA geometries, conductor materials, and electrode surfaces. Insulation material: Silicon nitrite
    - Sampling frequency of amplifiers: 40 kHz, gain: up to 5,000
    - Data transmission: USB 2.0
    - Real-time data acquisition software, limited real-time spike sorting
    - Stimulation pulse generators
    - No integrated life-support system with CO_2- and water supply

- Ayanda Biosystems, Lausanne, Switzerland
    - MEAs and amplifiers with up to 9 wells and 256 electrodes, 3D MEAs with 1 or 4 wells. Insulation material: SU-8 epoxy, conductors: platinum
    - Sampling frequency: 13 kHz, max. gain: 750
    - Data transmission: USB 2.0
    - Real-time data acquisition, no real-time spike sorting
    - No integrated life-support system with CO_2- and water supply
- BioCell Interface, Morteau, France
    - MEAs with up to 40 electrodes. Only for brain slices
    - Amplifier can handle 8 of the 40 input signals, gain: 500 or 5,000
    - Limited real-time data acquisition software
    - Perfusion system for life support of slices
- AlphaMed Sciences, Osaka, Japan
    - MEA with 64 or 2x32 electrodes, ITO conductors, platinum black coated for 10 kΩ impedance at 1 kHz, therefore no pre-amplifiers. Insulation material: polyacrylamide
    - Amplifier: gain 1,000, sampling frequency: 20 kHz, integrated stimulation pulse generator
    - Real-time spike sorting and data analysis software
    - No integrated life-support system with CO_2- and water supply

In addition to these companies, Plexon Inc., Dallas, USA and the Center for Network Neuroscience (CNNS), University of North Texas, Denton, USA, offer complementary amplification and MEA systems, respectively:

- Plexon Inc., Dallas, USA
    - Amplifiers with up to 128 channels at a sampling frequency of 40 kHz, gain: up to 14,000
    - Real-time and offline data acquisition, spike sorting and data analysis software
- CNNS, Denton, USA
    - MEAs with up to 256 electrodes and 8 wells
    - Electrodes: gold-plated, conductors: ITO, insulation: polydimethylsiloxane
    - Complete life-support system with sterile CO_2- and water supply for long-term recordings on the microscope stage. Closed-chamber setup for recordings of up to 6 weeks available.

Chapter Two: Materials and Methods

2.1 List of materials and devices used in this study

2.1.1 Devices

2.1.1.1 Cell culture

2.1.1.1.1 Sterilization

- Steam autoclave, “Autoklav 23”, MELAG, Germany
- Dry sterilization oven, Memmert, Germany

2.1.1.1.2 Cell preparation and incubation

- CO_2-incubator, Binder, Germany
- CO_2-incubator, Advantage-Lab, Belgium,
- Laminar flow safety workbench, vertical flow, BDK, Germany
- Laminar flow safety workbench, horizontal, BDK, Germany

2.1.1.1.3 Centrifuges

- Centrifuge, for 15 ml vials: “Universal 320”, Hettich, Germany
- Centrifuge, for Eppendorf cups, “Mini spin plus”, Eppendorf, Germany

2.1.1.1.4 Microscopes

- Inverted phase contrast microscope, “Axiovert 40 CFL”, Zeiss, Germany
- Inverted phase contrast microscope, “Axiovert 200”, Zeiss, Germany
- Inverted fluorescence/phase contrast microscope, “Eclipse TE 2000-W”, Nikon, Japan

2.1.1.1.5 Other

- pH meter, “inolab level 3”, WTW, Germany
- Vapor pressure osmometer, “Vapro 5520”, Wescor, USA
- Water bath, “K20”, Haake, Germany

- Haemocytometer, “Neubauer improved 0.1 mm depth, 0.0025 cm^2”, Assistant, Germany
- Automated cell counter, “Casy® 1”, Schärfe System GmbH, Germany
- Single channel pipettors, “Series 2100 Research Pipettors”, 0.5-10 µl, 2-100 µl, 100-1000 µl, Eppendorf, Germany
- Pipetting aid, “Pipetus®”, Eppendorf, Germany
- Gas flaming torch, “Microflam Brenner”, Proxxon, Germany
- Stereo microscope, Zeiss, Germany
- Digital Camera, “Digital Power shot A650IS”, Canon, Japan

2.1.1.2 Experimental workstation

- Neuronal signal acquisition system, “MEA-Workstation” (including 64 channel headstage amplifier, 64 channel computer-controlled variable gain main amplifier, 64 channel BNC-bypass board, A/D conversion adapter, Desktop PC), Plexon, USA
- Fluorescence imaging system, including monochromator “Polychrome IV”, air-cooled CCD camera, controller box, Till Photonics, Germany
- External USB audio adapter, “SB0270”, Creative, USA
- Impedance/Gain-phase analyzer, “SI 1260”, Solartron Analytical, United Kingdom
- DC power supply, “63G32RU30 32V/32A”, Gossen Konstanter, Germany
- Digital/analog oscilloscope, “HM 507”, Hameg Instruments, Germany
- Mono Hifi amplifier, “K 4007”, Velleman, USA
- DC power supply, “PS152A”, Voltcraft, Germany
- DC power supply, “VLP 1405 pro”, Voltcraft, Germany
- Stereo PA amplifier, “TA 3200”, the t.amp, USA
- Magnetic stimulator, “MagPro”, Medtronic, Denmark
- Magnetic stimulation coil, “S100”, Medtronic, Denmark
- Peristaltic tubing pump, “IPC-N 8”, Ismatec, Switzerland
- Peristaltic tubing pump, “MS-CA 2/820”, Ismatec, Switzerland
- Syringe pump, Harvard apparatus, USA
- pH-meter, “950”, Fisher Accumet, USA

- Vapor pressure osmometer, “Vapro 5500“, Wescor, USA
- Dry heating thermostat, VWR, USA
- Temperature controller, “ETC 742”, Suran Enda, Germany
- HEPA Laminar flow module, ”FMS 24”, Spetec, Germany
- HEPA Laminar flow module, ”FMS 56”, Spetec, Germany

2.1.2 Consumables

- Dulbecco’s Modified Eagle Medium, Gibco Invitrogen, USA
- Minimal Essential Medium, Gibco Invitrogen, USA
- Heat inactivated horse serum, Gibco Invitrogen, USA
- Fetal calf serum, Gibco Invitrogen, USA
- B-27 supplement, Gibco Invitrogen, USA
- PBS, Biochrom, Germany
- Sodium hypochlorite, Merck, Germany
- Ethanol, VWR, Germany
- Trypsin-EDTA solution, Biochrom, Germany

2.1.3 Chemicals

- HEPES, Sigma-Aldrich, USA
- Sodium Chloride, Sigma-Aldrich, USA
- Poly-D-Lysine, Sigma-Aldrich, USA
- Sucrose, Sigma-Aldrich, USA
- D-Glucose, Sigma-Aldrich, USA
- Sodium bicarbonate, Sigma-Aldrich, USA
- Laminin, Gibco Invitrogen, USA
- DNAse I, Gibco Invitrogen, USA
- Papain, Gibco Invitrogen, USA

2.1.4 Animal tissue

- Timed-pregnancy Balb/C mice, E 15, Harlan-Winkelmann, Borchen, Germany

2.1.5 Software

- Plexon Workstation software package, Plexon, USA
- Neuroexplorer, Nex Technologies, USA
- Impedance measurement: ZPlot 1.0, Solartron Analytical, United Kingdom
- SMaRT impedance software, Solartron Analytical, United Kingdom
- Remote control software for magnetic stimulator, "MagTrig", Medtronic, Denmark
- Statistical analysis program, "Origin 8.0", Microcal, USA
- Statistical analysis program, "SigmaPlot 8.0", SPSS Inc., USA
- Statistical analysis program, "SigmaStat 3.0", SPSS Inc., USA
- Statistical analysis program, "Prism 5" (demo version), Graphpad, USA

2.2 Electrical stimulation using glass chips with deinsulated electrodes

2.2.1 Cell culture

For the growth manipulation experiments, an L929 cell line was used. These cells were derived from normal subcutaneous connective tissue of an adult C3H strain mouse. The cells were treated with 20 μM methylcholanthrene and produced sarcomas when injected into C3H strain mice. Their proliferation kinetics therefore resemble the ones of many tumorous cell lines well with a doubling time of approximately 21 hours and very limited contact inhibition. However, their cellular shape is more regular and smooth than many other cancer cell lines', and while they do continue to divide after the monolayer is confluent, they do so at a reduced proliferation rate, and they do not grow over each other excessively. Since the doubling time was determined to be 21 hours, this was also the length of the stimulation period chosen for the experiments. That way, every cell should be stimulated at least once during every part of the cell cycle.

The cells were kept in an incubator at a temperature of 37 °C, 95 ±5% humidity and 8 % CO_2. The CO_2 concentration had to be adjusted to that value because the ratio of cell number on the stimulation chips to the medium volume was very low, and thus the buffer capacity of the medium, which came with a $NaHCO_3$ concentration of 3.7 g/l, would have been too high. Cells were split once every week at a ratio of 1:15. The stock cultures were kept in 25-cm^2 polystyrol culture flasks with 6 ml of DMEM supplemented with 5 % fetal calf serum (FCS). The following protocol was used for every round of cell splitting:

- Aspirate old medium from culture flask.
- Wash cells once with 6 ml pre-warmed PBS.
- Add 2 ml trypsin solution; incubate at 37 °C for 7 – 10 minutes.
- Check under microscope whether cells are completely detached.
- Add fresh DMEM + 5% FCS to the trypsinated cells.
- Shake and transfer cell suspension to a centrifuge vial, spin down at 800 RPM for four minutes and discard supernatant.
- Resuspend the cells in 6 ml fresh DMEM + 5% FCS carefully using a transfer pipette.
- Adjust the final cell density to 0.8 * 10^5 cells/ml and seed a total suspension volume of 6 ml.

2.2.2 Glass chips

2.2.2.1 Design

A number of cell carrier plates with thin-film biohybrid sensors on glass or ceramic substrates have been developed at the Heinz Nixdorf-Lehrstuhl für Medizinische Elektronik (LME). For the electrical stimulation experiments, a design was chosen that featured two pH-sensor spots with ruthenium oxide, two clark-electrodes for the monitoring of oxygen consumption, a Pt1000 temperature sensor and two rod shaped stimulation electrodes (fig. 2.1). The plate, referred to as "glass chip" below, is 30 x 40 x 0.5 mm in size, all conductors and structures were made using sputtered and photo-etched platinum, and the insulation layer was made of SU-8 photoresist, a material that can withstand high temperatures (<200 °C) and that is chemically inert and thus biocompatible. A thin layer of titanium was deposited between the glass and the platinum as an adhesion promoter. These chips were in part supplied by Heraeus Sensor Technology, Germany, and in part provided by the Heinz Nixdorf Lehrstuhl f. Med. Elektronik, TU München, Germany.

2.2.2.2 Pre-treatment

Several coatings and procedures for improved cell adhesion on the glass chip were evaluated:

1. Coating with Poly-D-Lysine (PDL)
2. Coating with Poly-L-Lysine (PLL)
3. Flaming of the surface

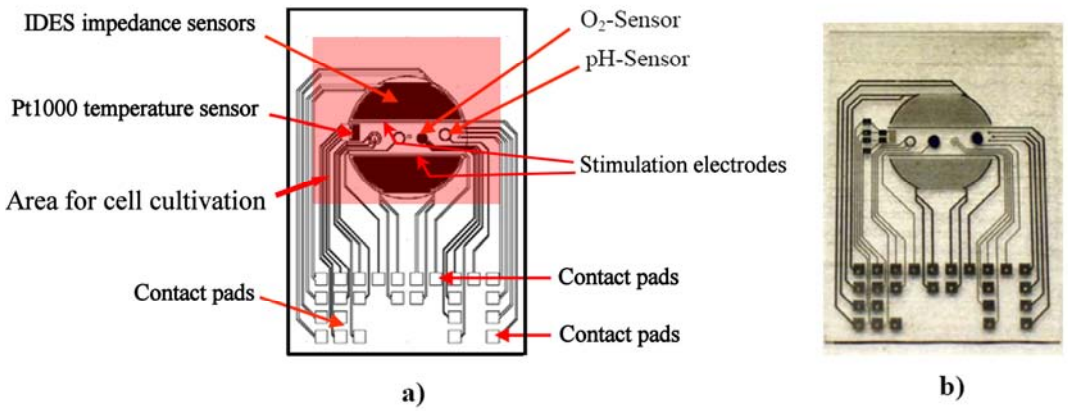

Fig. 2.1: Biohybrid analytic chip with glass substrate, platinum conductors and SU-8 insulation: a) schematic, b) photograph (taken by the author).

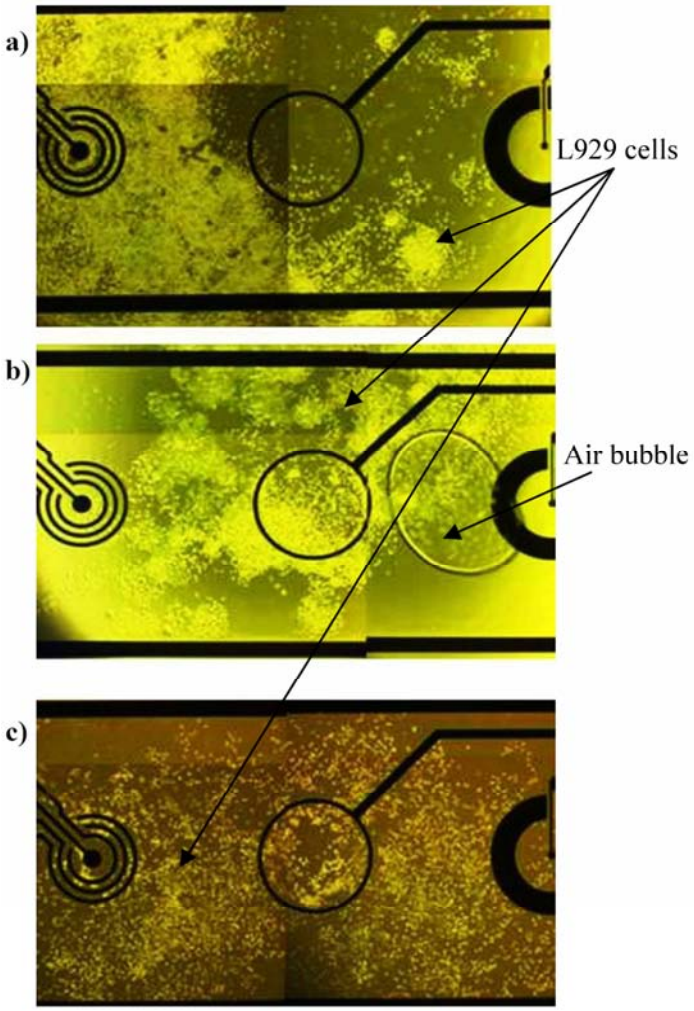

Fig. 2.2: L929 cells on glass chips with different kinds of coatings: a) PDL, b) PLL, c) flamed [taken from 127].

It is well known that positively charged polymers, such as PDL and PLL, can improve the adhesion of cells to synthetics or glass. In addition, poly-lysine enhances the adsorption of serum proteins that are contained in the extracellular matrix to the substrate. Flaming utilizes the fact that the insulation material contains methyl groups that oxidize when briefly exposed to strong heat. This process turns the hydrophobic surface hydrophilic, which is essential for good cell adhesion. Flaming proved to generate the most even distribution of cells, as fig. 2.2 demonstrates.

2.2.2.3 Growing cells on the glass chips

Preparation of the chips and seeding of the cells were carried out subject to the following process:

- Clean the chips using cotton swabs and a 10 % solution of Deconex® 12PA, inspect chips for cleanliness and intact insulation under the phase contrast microscope.
- Sterilize chips in the dry oven for four hours at 130 °C, allow 2 – 3 hours for cooling.
- One by one, put chips on an autoclaved aluminum block with a droplet of autoclaved water between the chip and the aluminum. Flame the area between the stimulation electrodes using a gas torch for 1 second, pause for 2 seconds, and flame once more for 1 second, both at a distance of 1 cm above the chip.
- Transfer chip to a polystyrol Petri dish and stick a square silicone gasket onto the glass chip using a small amount of autoclaved silicone grease.
- After splitting the cells, collect a portion of the fresh cell suspension and dilute to a density of $4.5 * 10^5$ cells /ml.
- Seed 1 ml of the final cell solution onto the 1.5 cm^2 growth area on the chip, generating a plating density of $3 * 10^4$ cells/cm^2.
- Place 2 ml of sterile ultra-pure water into the Petri dish around the chip for evaporation control. Keep in incubator for 48 hours. By that time, the cells have entered the exponential growth phase and can be used for the experiments.

2.2.3 Generation and application of electrical pulses

The signal shape chosen to stimulate was a positive monophasic square 10 ms pulse, at 5 Hz and 750 mV amplitude (similar to the parameters used by Wang et. al. [111]). The signal was generated and replayed by a sound-editing program, transmitted through an external USB sound adapter (Creative labs, USA) for reduced noise levels, and amplified using a mono Hifi-amplifier (Velleman, USA) driven by a 28 V power supply (Gossen Konstanter). Fig. 2.3 a) shows the generated pulse shape, while b) reveals that the pulse the cells receive is somewhat distorted. This is partially due to the capacitive characteristics of the cell layer covering the electrodes. However, the main reason for the distortion is that the Hifi-amplifier was not capable of reproducing the high-frequency components of the rectangular input signal that exceeded its bandwidth.

However, this did not impair the experimental protocol, since the decisive factor for polarizing the cells was the plateau of the pulse, but not the time course of the slope.

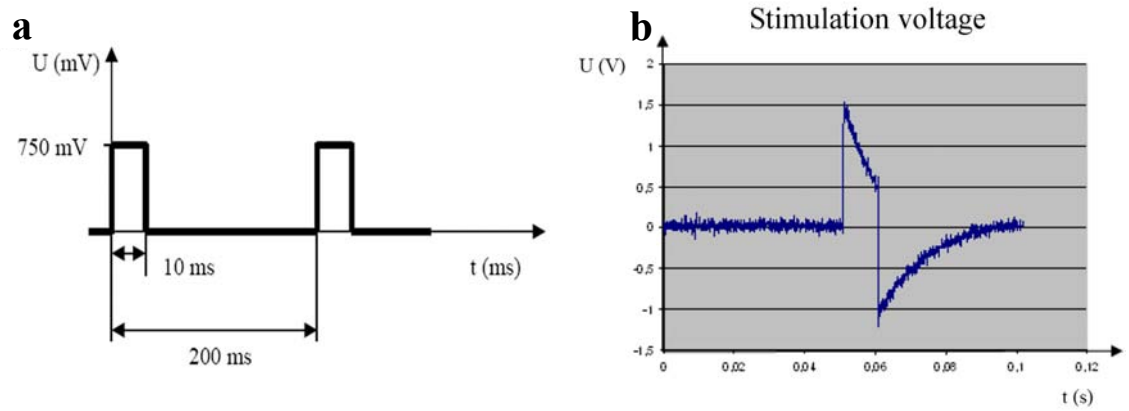

Fig. 2.3: Stimulation pulse shapes. a) Generated shape, b) Stimulation pulse with connected cell chip [taken from 127].

2.2.4 Assembly of experimental components

For fixation of the glass chips holding the cells, they were installed in custom made culture chambers made of poly-ether-ether-ketone (PEEK), a thermoplastic that is widely used for medical implants and other applications that require high chemical inertness and biocompatibility (fig. 2.4 a). Before each experiment, two chambers were sonicated it a 10% Deconex solution for 15 minutes, and twice in ultra-pure water. After autoclaving the chambers at 2 bar steam pressure and 130 °C for 20 minutes, they were allowed to cool down, and sterile o-rings were placed in the circular groove in the top part of the chamber. The culture medium and the silicone ring were removed from the chip, it was mounted in the chamber, and the medium was returned to the open well in the chamber block, covering the cells.

The chambers were then mounted in an aluminum plate with holes in the bottom for microscopic inspection of the cells. These base plates also provided slots for insertion of the connectors that constituted the interface between the contact pads on the glass chips and the stimulation/recording electronics. The aluminum base plate with the glass chips was placed inside a CO_2 incubator at 37 °C and 95 % humidity, providing exactly the same conditions for the treated cultures as for the control ones.

Before each stimulation cycle, the Solartron impedance analyzer was used to verify the contacts between the glass chips and the cable. The actual connectors attaching the chip to the cable were gold-plated spring contact pins which are fragile in nature. Fig. 2.5 shows a typical impedance curve of an intact contact ranging from 1 Hz to 1 MHz. If the impedance values were in this range, the stimulation was started and kept going for 21 hours.

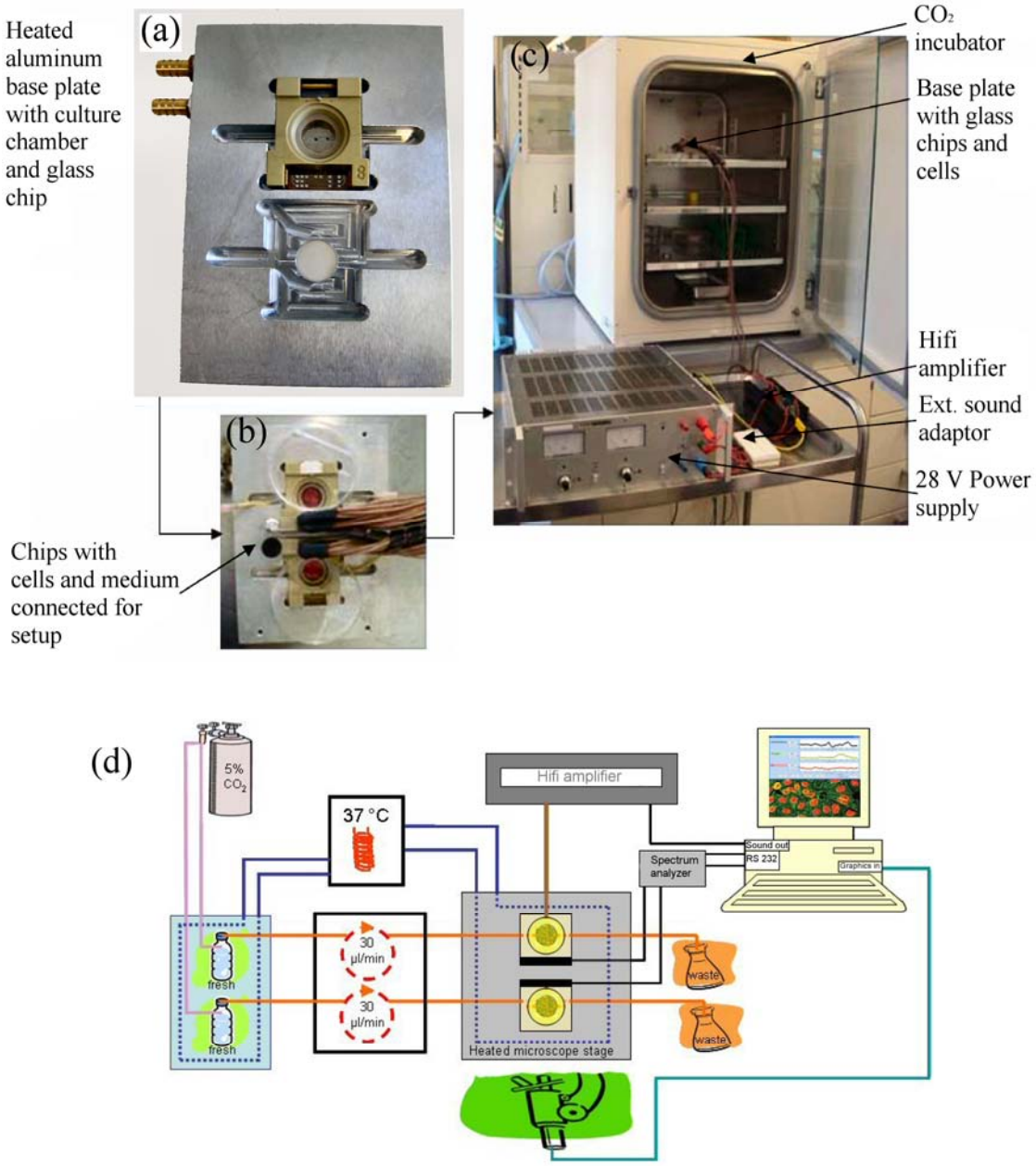

Fig. 2.4: a) Base plate with PEEK culture chamber; b) culture chambers mounted in base plate with connectors; c) complete setup in front of incubator with stimulation electronics; d) schematic of setup.

2.2.5 Simulating the field geometry numerically

Using the program package COMSOL, the two-dimensional field geometry on the glass chip with culture medium was simulated. COMSOL solves the Maxwell-equations in a discretized geometry using the finite-element method (FEM). The simulation indicates that a very strong spatial field gradient is present near the electrodes. The relatively constant field strength between the electrodes is between 120 and 200 V/m at a stimulation voltage of 750 mV.

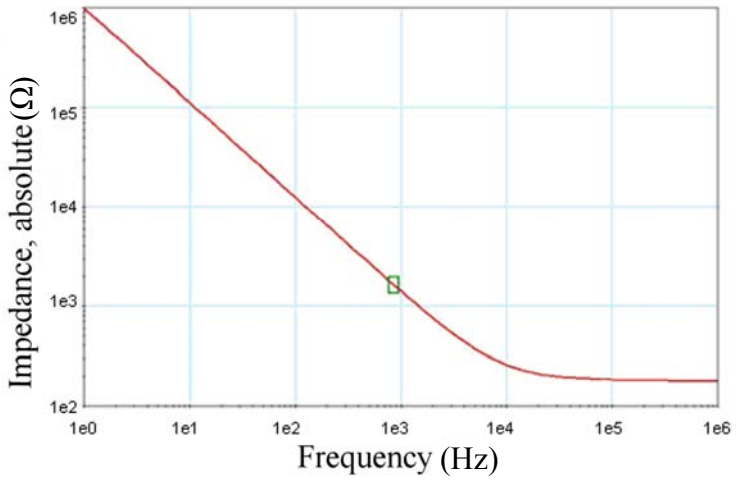

Fig. 2.5: Graph showing the absolute impedance value |Z| (Ω) of the glass chip with cells measured using the Solartron impedance analyzer

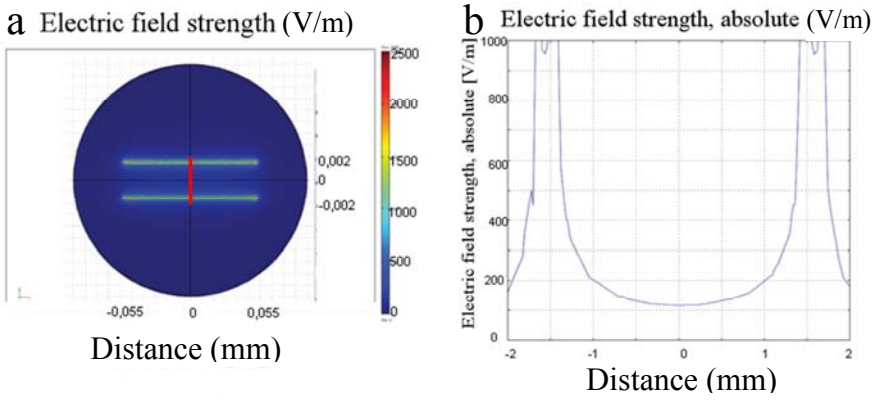

Fig. 2.6: a) Spatial distribution of the electrical field on the glass chip. b) One-dimensional field distribution between the stimulation electrodes (following the red line in a) [adapted from 127].

2.2.6 Current density on the glass chip

In order to determine the current density that the cells are experiencing on the glass chip, an equivalent schematic diagram of the components is needed (fig. 2.7). Assuming the specific conductivity *g* of the culture medium to be homogenous and on the order of 1.25 $\Omega^{-1}m^{-1}$ [20], the medium resistance is

$$R_a = \frac{1}{g} \cdot \frac{l}{A_{st}} = 69\Omega \quad , \qquad \textbf{2-1}$$

where A_{st} = 0.35 cm^2 is the area between the stimulation electrodes, and l = 3 mm is the distance between the electrodes.

The membrane capacitance is the product of the specific capacitance of the membrane and the surface area A_c:

$$C_m = c_m \cdot A_c = c_m \cdot 4\pi r_z^2 = 6pF \quad , \qquad \textbf{2-2}$$

assuming $c_m = 0.01$ F/m^2, and $r_z = 7$ µm.

The impedance of the cell Z equals the membrane impedance parallel to the membrane capacitance. Therefore, the complex impedance of the entire cell-medium-cell arrangement Z^* computes as

$$\underline{Z}^* = R_a + \frac{2R_m}{1+\omega^2 C_m^2 R_m^2} - i\frac{2\omega C_m R_m^2}{1+\omega^2 C_m^2 R_m^2} \quad . \qquad \textbf{2-3}$$

The absolute value of the impedance is thus

$$\left|Z^*\right| = \sqrt{2(Z)^2 + R_a^2} = 3.7 * 10^8\,\Omega\,, \qquad \textbf{2-4}$$

assuming $R_m = 26 * 10^7\ \Omega$ [112], and f = 5 Hz.

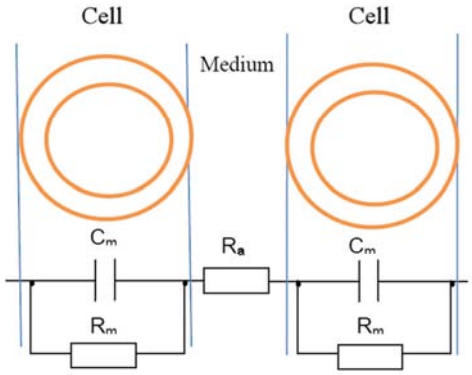

Fig. 2.7: Equivalent schematic of the cell-chip arrangement assuming homogenous medium distribution [adapted from 127]

With a stimulation voltage of U = 750 mV, the total amount of current flowing through the system is

$$I_{tot} = \frac{U}{Z^*} = 2nA \ . \qquad \textbf{2-5}$$

Since the stimulation electrodes are 11.5 mm long, 0.3 mm wide and 0.5 µm tall, the front surface can be neglected, and the surface area per electrode is

$$A_{stim} = 3.5 \cdot 10^{-6} m^2 \quad , \qquad \textbf{2-6}$$

which leads to the current density at the electrode:

$$j_{stim} = \frac{I_{tot}}{A_{stim}} = 600 \frac{\mu A}{m^2} \qquad \textbf{2-7}$$

Thus, assuming a cell surface area of 200 μm^2, the current density at each cell is

$$j_c = \frac{I_{tot}}{A_c} = 10 \frac{A}{m^2} . \qquad \textbf{2-8}$$

2.2.7 Experimental schedule

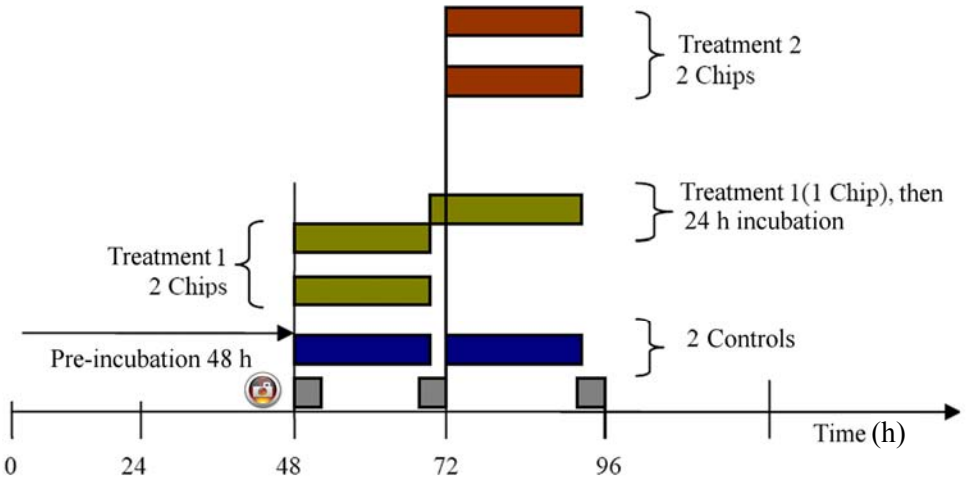

Fig. 2.8: Time course of the glass chip experiments: incubation time of controls (blue), treatment 1 (green), and treatment 2 (red). Grey: times during which cells were counted and photographs of the cells were taken [adapted from 127].

At the beginning of each experimental cycle, cells were seeded on seven glass chips. After the initial 48 hours of incubation, two chips were stimulated for 21 hours ("treatment 1", fig. 2.8). Treatment 2 started 72 hours after the seeding. After the end of treatment period 1, one control and on treated chip were disassembled, and the cells were counted. The other treated chip remained inside the incubator until 24 hours later, when it was finally evaluated, along with both chips of treatment 2, and another control.

Since only the cells between the stimulation electrodes were treated, the rest was carefully removed under the stereo microscope using a cell scraper. The cells were detached from the glass substrate according to the protocol described above. However,

they were centrifuged in a 0.5 ml Eppendorf cup at 3500 RPM and resuspended because of the considerably lower total cell count. The number of cells was determined using a dual Neubauer-counting chamber. The values from all eight 1-mm^2-squares were averaged, and the cell density θ was calculated according to the formula

$$\vartheta = \frac{\sum_{i=1}^{8} x_i \cdot 10 \cdot V}{A_{st} \cdot i} (cells / cm^2) \quad , \qquad \textbf{2-9}$$

where x_i is the number of cells per square, i is the number of squares, V is the volume of the cell suspension, and A_{st} = 0.35 cm^2 is the area between the stimulation electrodes.

2.2.8 Staining dead cells with Trypan blue

The Neubauer counting chamber was also used to quantify the percentage of dead cells after each treatment, both in the supernatant and the trypsinated cells that had been part of the monolayer. Trypan blue is a dye that cannot pass the membrane of intact cells and can therefore be used to selectively stain cells that underwent necrosis, apoptosis or lysis. A 64 µL sample of the cell suspension was mixed with 36 µL of a 0.5 % Trypan blue solution, and the dead cells were counted. This procedure was carried out quickly, since the Trypan blue becomes cytotoxic after a while and might induce cell death itself, which would then distort the results of the counting.

2.2.9 Temperature control on the glass chip during stimulation

When applying currents over a prolonged period of time to electrolytic solutions, Joule heating of that medium is a process that cannot be avoided. Despite the very low amplitude of current generated in these trials, we utilized the temperature sensors embedded on the glass chips to investigate whether there were any significant temperature changes during the stimulation period. A Pt1000 temperature sensor is made of a thin, meandering film of platinum which exhibits temperature-induced resistance changes. For calibration of the absolute values and the slopes of each sensor, the resistances at 37 and 40 °C were measured. The slope of 3.7 Ω/°K was the same for every Pt1000 used.

2.3 Capacitive stimulation using 6-well plates

2.3.1 Stimulation device design

The direct electrical stimulation with deinsulated stimulation electrodes did prove effective in reducing the cell count in comparison with the control cultures. In order to explore whether the plain electric field is capable of inducing the same sort of effects through purely non-galvanic, capacitive coupling, a new stimulation device was designed. Coupling the electric field capacitively with the cells means that the charges in the double layer fluctuate according to the charges at the electrode surface, without actual transfer of any electrons. That way, only the amount of charge is transmitted that is stored in the double layer. In this case, the double layer is the bottom of the 6-well plate. Whereas the glass chip stimulation setup was limited to the simultaneous treatment of two cell cultures, the new stimulation board is capable of stimulation the wells of a standard format 6-well culture plate (fig. 2.9). This approach offers two major advantages: A higher number of cultures can be stimulated using different stimulation parameters, attaining statistically valid results within a shorter period of time. Additionally, the number of treated cells per well is much higher, which lessens the statistical error made when counting and calculating cell densities.

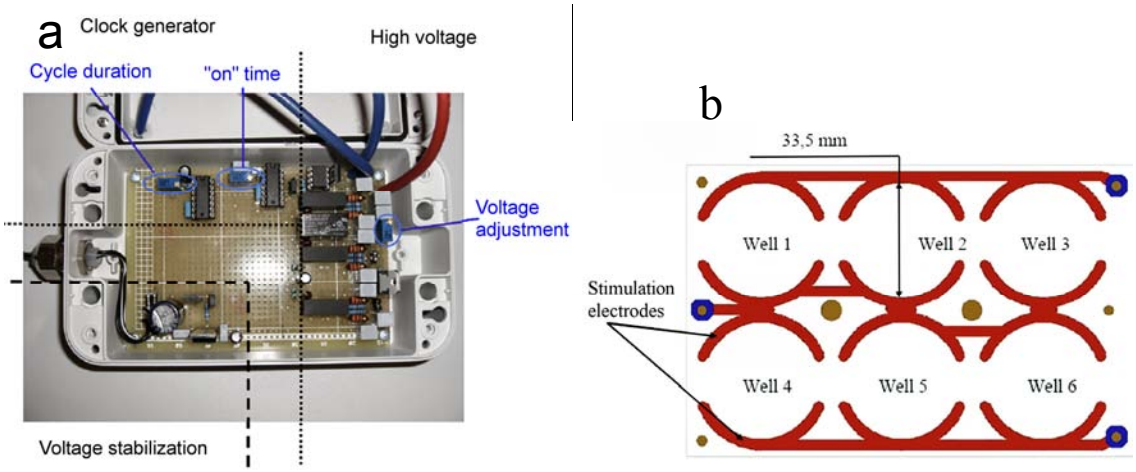

Fig. 2.9: a) Electronic circuit board controlling electrical stimulation of cultures in 6-well plates with voltage supply block, clock generator, voltage stabilization and adjustments for cycle duration, duty cycle and voltage amplitude; b) Layout of the stimulation board. The 6-well plates with the cells were set on top of this board for stimulation.

2.3.2 Seeding of the cells

0.45 * 10^5/ml L929 cells were seeded 48 hours before every trial, which corresponds to a cell density of 2.64 * 10^5 cells per well. The interspaces between the wells were then filled with 4 ml sterile water each, in order to minimize evaporation. Prior to each treatment, the cultures were pre-incubated for 48 hours.

2.3.3 Signal generation

The new stimulation circuit can produce voltages between 24 and 96 V continuously. The voltages are generated by three DC/DC transformers. The stepless control is performed by an LM317 – voltage converter. The circuit generates square wave signals with a variable duty cycle. 13 V AC voltage is transferred to the voltage stabilizer using an external power-switching adapter. The voltage is converted to and stabilized at 12 V and passed on to a clock generator which produces a cycle duration of 200 ms (corresponding to 5 Hz) and an "on-time" of 10 ms, before amplifying the signal to its final amplitude by using another DC/DC transformer.

2.3.4 Field simulation using the finite-elements method

In order to reach the electric field strengths needed for the experiments, several simulations were plotted to quantify the amplitudes needed (fig. 2.10). Independently of the applied voltage, the spatial field distribution remained the same, as expected. The field strength needed to achieve 150 – 300 V/m (resembling the stimulation parameters on the glass chips) was 9 V. Field strengths resulting from 24, 60 and 90 V were evaluated, as well, resulting in field amplitudes of 0.6 – 1.1 kV/m, 1.5 – 3 kV/m, and 2.2 – 4.5 kV/m, respectively. Approximately 70 % of the well area is covered uniformly by the same field strength. At the perimeter, the field becomes drastically stronger. However, the percentage of cells that experience a high field gradient is very low in comparison with the glass chips.

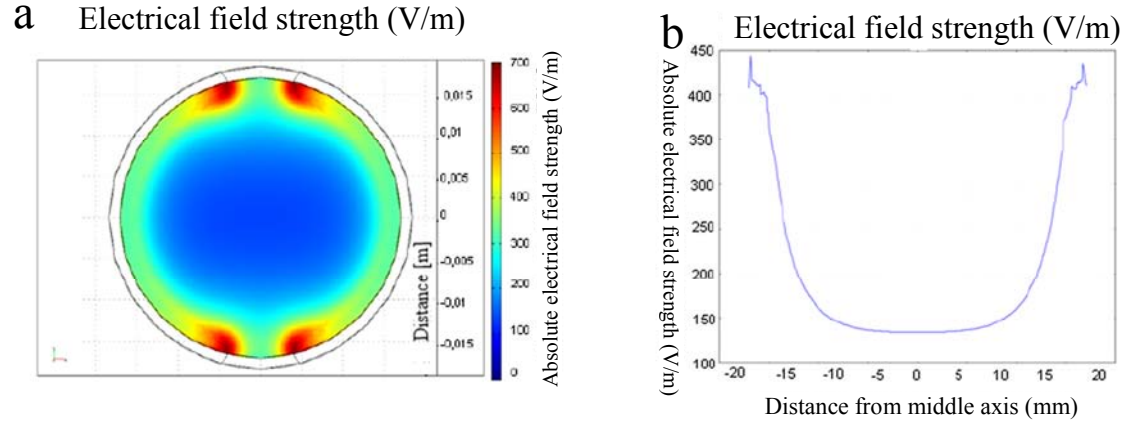

Fig. 2.10: FEM-simulation of the spatial distribution of the electric field strength, excitation voltage: 9 V, area in well: 9 cm^2, a) top view of a well, b) field line following cut through well. Field strength throughout well: 150-300 V/m. [taken from 127]

2.3.5 Current density in the 6-well plate

The equivalent schematic in fig. 2.11 shows how the cells are interconnected with their surroundings during the stimulation. The current densities present the various

stimulation voltages and 5 Hz stimulation frequency are summarized in table 2.1. The detailed calculation of these currents can be found in appendix A.

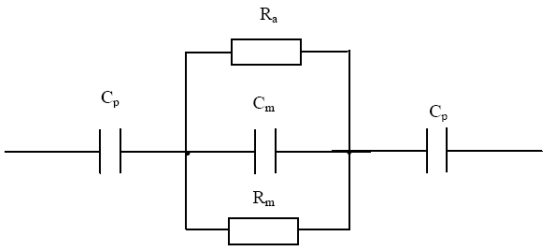

Fig. 2.11: Equivalent schematic of a spherical cell grown inside a 6-well plate in homogeneous medium: C_p = Capacitance of the well-plate bottom, C_m = membrane capacitance, R_m = membrane resistance, R_a = medium resistance.

Stimulation voltage (V)	**9**	**24**	**60**	**90**
Current density at cells (A/m^2)	**10^{-6}**	**$2.7*10^{-6}$**	**$6.7*10^{-6}$**	**$9*10^{-6}$**

Table 2.1: Current densities at different excitation voltages inside a well of the 6-well plate

2.3.6 Experimental setup and schedule

48 hours after seeding, one plate was placed on top of the stimulation device inside a CO_2-controlled incubator that was kept at 37 °C and 95 % humidity for 21 hours. In fig. 2.12, the stimulation device and its placement inside the incubator is demonstrated. Fig. 2.13 verifies the shape and amplitude of the voltage pulses applied by showing a respective oscilloscope screenshot.

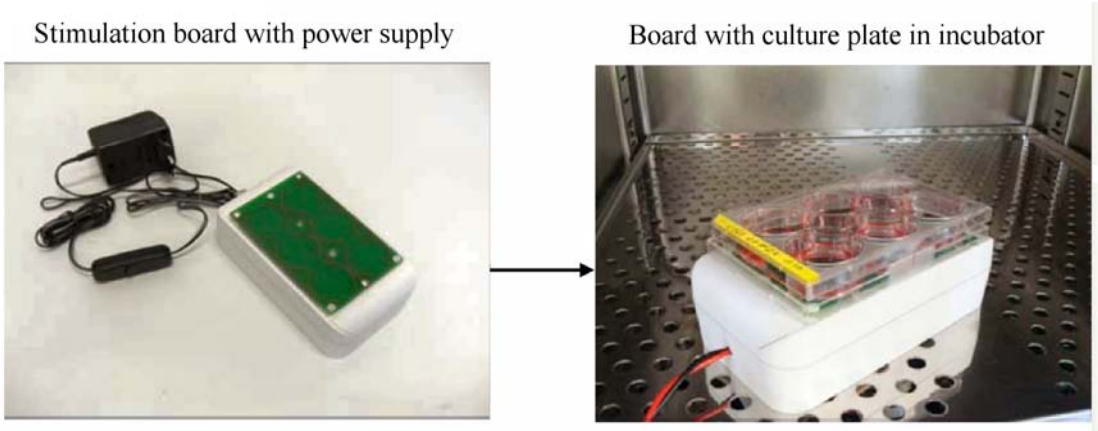

Fig. 2.12: Experimental setup of the 6-well plates on the newly developed stimulation device (left), stimulation board with 6-well plate containing cells and medium inside the incubator. [source: 127]

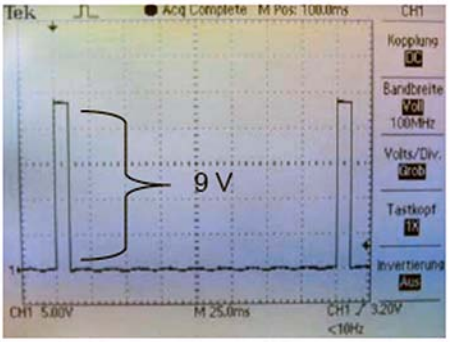

Fig. 2.13: Shape of the stimulation pulse as applied to the 6-well plate stimulation board. Amplitude: 9 V, pulse duration: 10 ms, period between two pulses: 200 ms. [taken from 127]

Four 6-well plates each were prepared at the beginning of each experimental cycle. Plates one and two were used as controls, plate three for treatment 1 (between 48 and 69 hours after seeding), and plate four treatment 2 (72 – 93 hours after seeding). For a detailed explanation of the experimental time course, see fig. 2.14. The grey boxes at the bottom of the diagram denote the times at which photographs of the controls and the stimulated cultures were taken. With the area inside each well amounting to A = 9 cm^2, the cell count x, determined using the Casy automated cell counter, could be easily converted into the cell density

$$Z = \frac{x \cdot V}{A} Cells / cm^2 . \qquad \textbf{2-10}$$

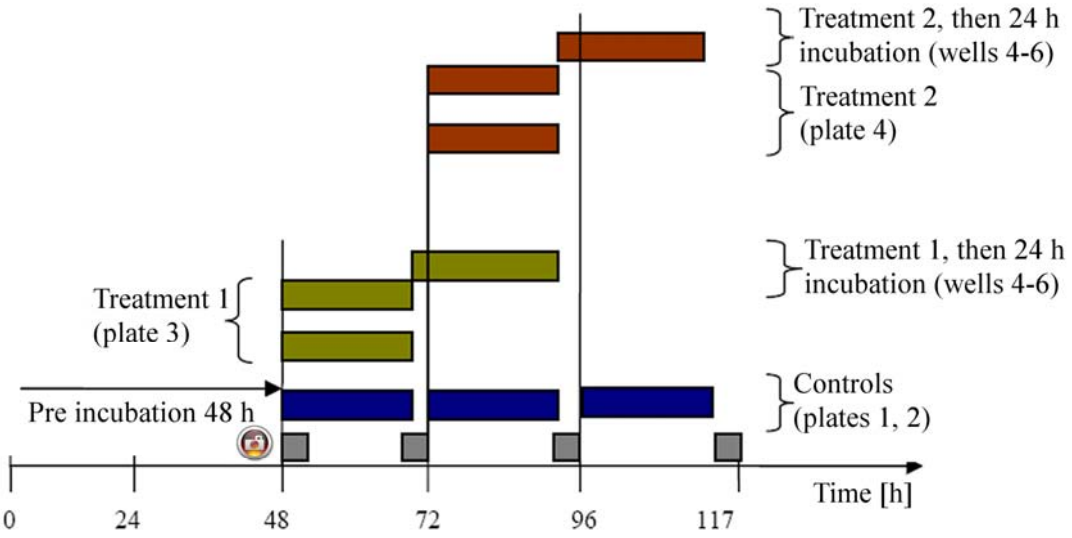

Fig. 2.14: Time course of one experimental cycle (5 days) for the electrical stimulation using 6-well plates. [adapted from 127]

2.3.7 Electrical stimulation using a 6-well stimulator with IDES structures

Contrary to what was expected, purely capacitive stimulation did not cause any significant inhibition in cell growth as observed after direct stimulation using the glass chips. Therefore, one hypothesis that was explored was whether the high spatial field gradient on the glass chip was responsible for its effectiveness. The fraction of cells experiencing a high gradient was much larger on the glass chip than inside the 6-well plates. Therefore, a new stimulation board was designed with the directive to generate gradient fields, one with a relatively coarse structure, one with a finer one. Three of the interdigital electrode structures (IDES) on the board had a 3 mm pitch, while the fingers of the other three were spaced 1 mm apart from each other. This approach is depicted in fig. 2.15 which shows the respective layout.

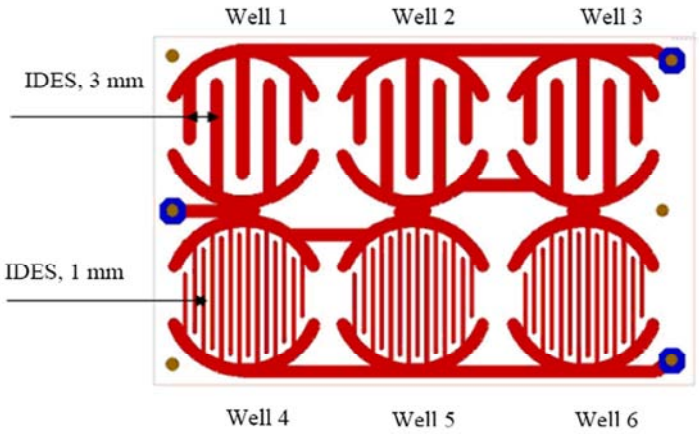

Fig. 2.15: Layout of the 6-well stimulation board featuring 3 mm- and 1 mm-IDES structures for two levels of spatial field heterogeneity [taken from 127].

2.3.8 Field simulation of the IDES structures

The two-dimensional field geometry obtained from both 1 mm and 3mm IDES structures was simulated using an FEM program. At 90 V, the electric field strength at the level of the cells is between 0.72 – 1.05 kV/m and 1.12 – 1.35 kV/m (IDES 1 mm and 3mm, respectively. The cells are located 2 mm above the top of the stimulation board. As fig. 2.16 shows, the field distribution is highly heterogeneous. The gradient near the electrodes is rather strong, and in the middle of the well, it becomes attenuated.

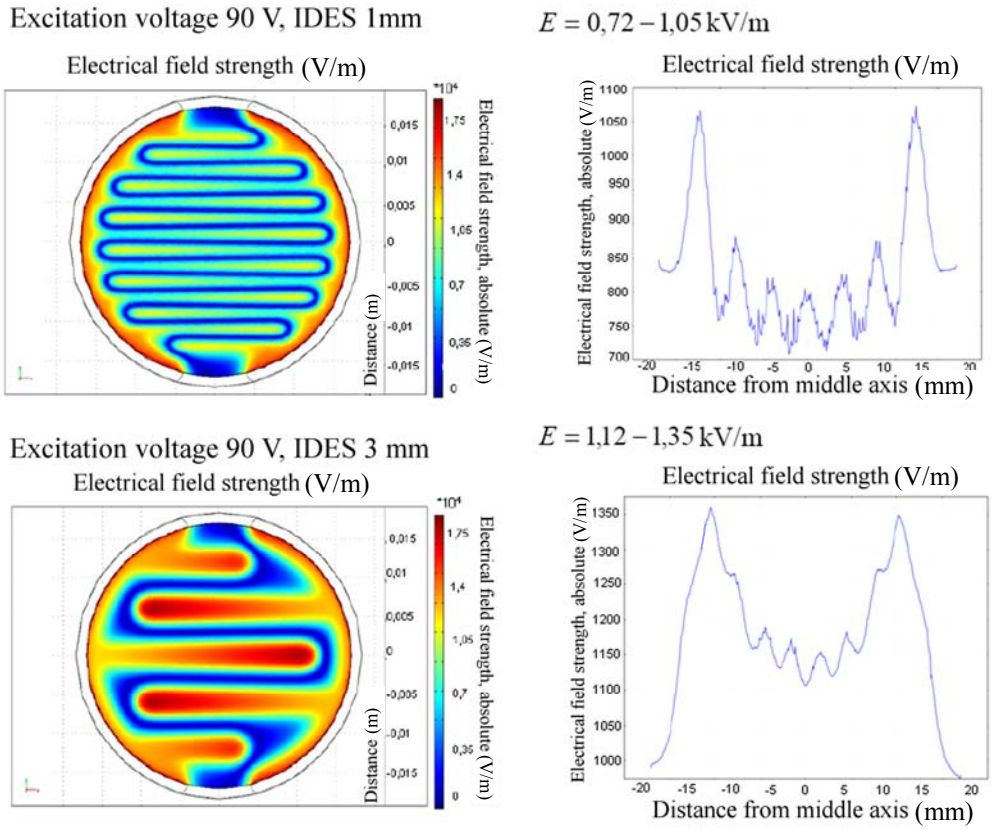

Fig. 2.16: Left: Spatial distribution of the electric field using 1 mm (top) and 3 mm (bottom) IDES structures as stimulation electrodes. Right: Traces of the electric field strength along a cut from back to front through the well [adapted from 127].

2.4 Magnetic stimulation

2.4.1 Comparison of different stimulation coil geometries

For transcranial and peripheral, therapeutic magnetic stimulation, there are two preferred types of coil geometries that are commercially available:

- Circular coil: Induces eddy currents in biological tissue which run parallel to the plane of the coil turns. The trough-shaped field distribution complicates stimulating certain areas of a few mm or cm in diameter in a focused manner. Used to stimulate motor cortex areas. Fig. 2.17 shows the schematic mechanism of TMS (a) and the E-field vector generated by a circular coil.
- Butterfly coil: Side-by-side combination of two circular coils driven by currents flowing in opposite directions. Electrical field components add up in the middle of the coil and enhance focality drastically (fig. 2.18).

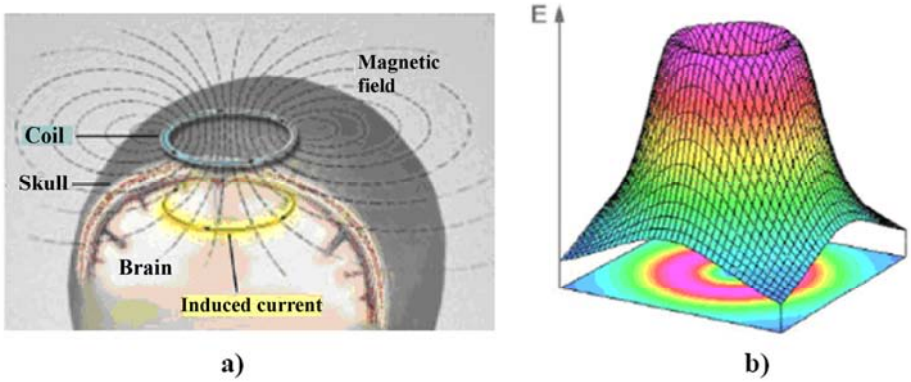

Fig. 2.17: a) Model of a circular coil stimulating the cortex of the brain. b) E-field vector of a circular coil [adapted from 61]

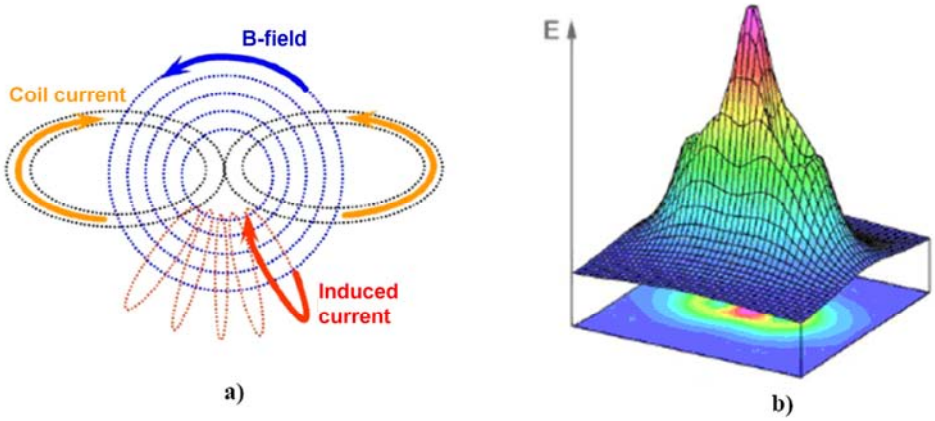

Fig. 2.18: a) Simulation of the field lines created by a butterfly coil; b) the respective E-field vector [adapted from 61]

Initially, a miniaturized stimulation coil had been developed for the trials in this study. It was supposed to be positioned in very close proximity of the cells, thus requiring only a fraction of the energy needed to drive the commercially available TMS coils. That way, an ordinary HiFi amplifier could be used to drive the coil, providing the possibility of using an infinite variety of different waveforms and frequencies for stimulation. In order to achieve a good focality of the field, the miniaturized coil was evaluated in a butterfly configuration (fig. 2.19).

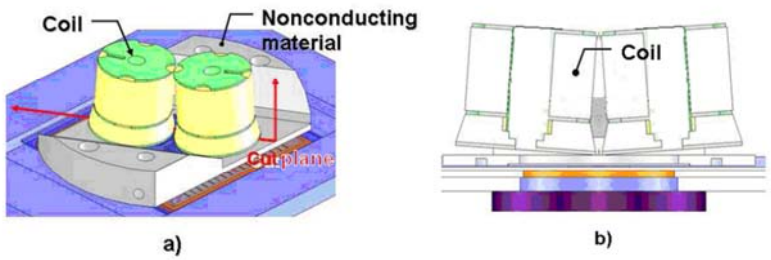

Fig. 2.19: Drawing of the miniaturized coil in "butterfly" configuration: a) plan view, b) cut through plane indicated in a), red line [source: 125].

2.4.2 Magnetic field simulation of the miniaturized coil

The magnetic flux generated by the miniaturized coil was simulated at 5 mm distance from its bottom (fig. 2.20). In the simulation, the coil was fed a biphasic cosine pulse, amplitude 21 A, wavelength 238 µs. It shows that the maximum magnetic flux generated by the coil was 45 mT. However, there is no focusing of the field in the middle of the structure, as was expected. Between the coils, the flux is 35 mT. In addition to the poor focusing of the magnetic field, problems with the cooling of the coils arose, because they had to be positioned very close to the cells, making an efficient removal of heat impractical. Larger circular coils that are routinely used in TMS applications can be positioned at a greater distance to the cells due to their very high amounts of energy transferred. In addition, they can be cooled very easily using a standard PC cooling fan. For these reasons, a commercially available stimulator by Dantec was finally chosen as the pulse source. The coil chosen was a Dantec circular coil S100, diameter: 10 cm.

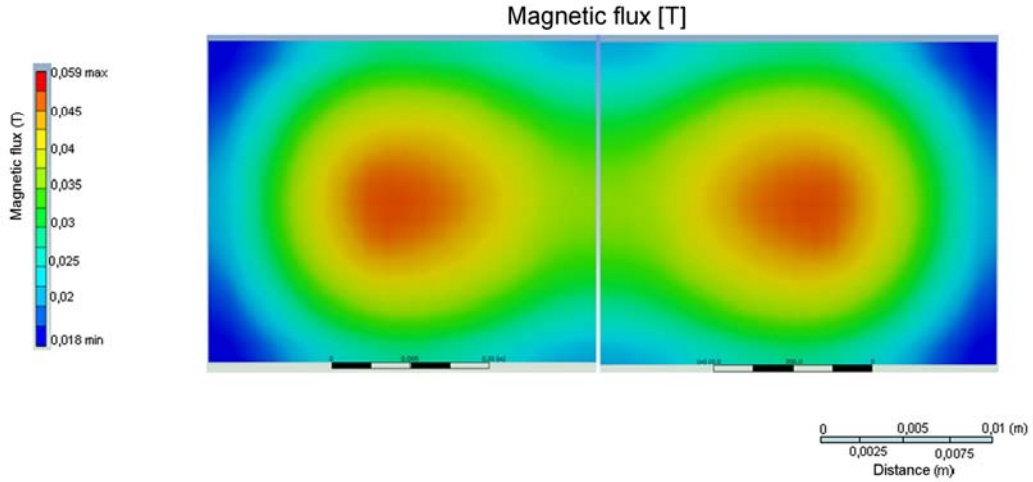

Fig. 2.20: FEM simulation of the spatial distribution of the magnetic flux generated by a miniature butterfly coil. Simulated at 5 mm distance from the coil's bottom [adapted from 127].

2.4.3 Signal generation and application

Based on the study by Yamaguchi et. al. [40], stimulation parameters were chosen that allowed for a continuous treatment with single 350 µs pulses, and repetition rate 1 Hz. Stimuli were spread out temporally as much as possible using the control software of the Dantec stimulator: The cycle "500 pulses, 120 s silence" was repeated for 17 hours. Fig. 2.21 shows the stimulation device with the laptop control computer (a), and the waveform chosen for application (b).

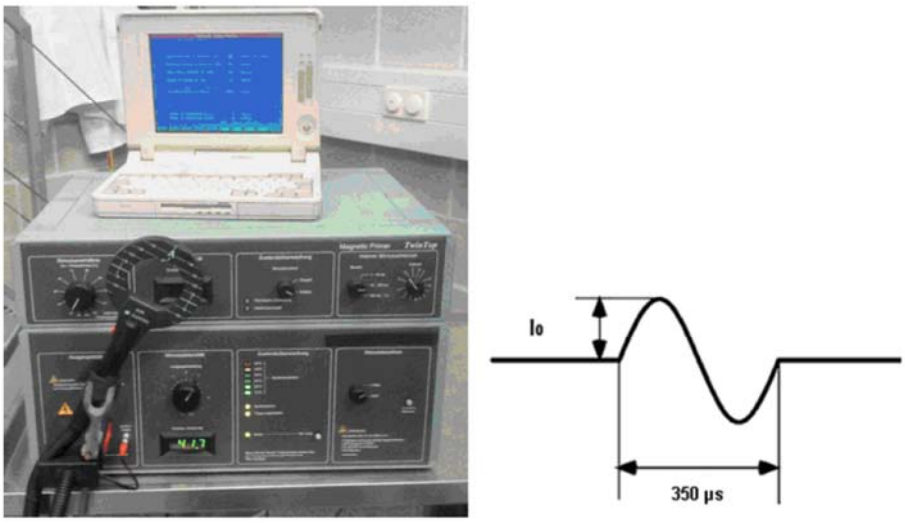

Fig. 2.21: a) Magnetic stimulator Dantec MagPro, b) stimulation pulse shape

2.4.4 Current density at the site of the cells

Assuming a frequency of f = 2.9 kHz, the current density at the site of the cells can be calculated as follows. A coil probe (diameter: 4.5 mm, n = 25) measured the voltage induced by the stimulation coil:

$$U_m = n \cdot U_0 \cdot \sin(\omega t) \quad , \qquad \textbf{2-11}$$

$$U_0 = 16mV \, .$$

Therefore, the current flowing through the cells amounts to

$$I_Z = \frac{U_0}{Z_Z} \quad , \qquad \textbf{2-12}$$

where I_Z is the current through the cell, and Z_Z is the impedance of the cell. The impedance of the cell Z^* at f = 2.9 kHz is

$$\underline{Z^*} = \frac{R_m}{1+\omega^2 C_m^2 R_m^2} - i\frac{\omega C_m R_m^2}{1+\omega^2 C_m^2 R_m^2} \quad . \qquad \textbf{2-13}$$

The voltage induced has the signal shape of a biphasic cosine at f = 2.9 kHz, which results in the impedance

$$\left|\underline{Z}\right|^* = \sqrt{R_m^2 + X_c^2} = 0.9 \cdot 10^7 \, \Omega \quad , \qquad \textbf{2-14}$$

Where R_m is the membrane resistance and X_c is the reactance of the membrane. The maximum current at the site of the cell is $I_Z = 2$ nA. Therefore, the current density at the cell is

$$j_Z = \frac{I_Z}{A_Z} = 11\frac{A}{m^2} \quad , \qquad \textbf{2-15}$$

where $A_Z = 1.54 * 10^{-10}$ m^2 is the cross sectional area of the cell.

2.4.5 Seeding of the cells on the magnetic stimulation glass plates

In order to be able to always position the cell cultures the same way using the culture chambers at hand, they were grown in a 0.8 cm^2, circular area on a 5 x 5 cm glass plate ("mag-stim chip"). This way, the cells were located in a relatively small area that the peak of the magnetic field could be focused on.

Cleaning and sterilization of the mag-stim chips is a critical step to ensure a growth behavior of the cells that is highly repeatable. After each run, the chips were sonicated in a 10% solution of the special laboratory cleaner Deconex 12 PA for 15 minutes at 70 °C. Subsequently, the chips were rinsed with ultra-pure water, sonicated twice in ultra-pure water for 15 minutes each, and rinsed again. Under the phase-contrast microscope, they were thoroughly inspected for cleanliness. The chips were then autoclaved in a steam pressure sterilizer at 120 °C for 15 minutes.

The surface preparation was performed under the sterile safety workbench. Flaming was performed in accordance with the procedures used for the electrical stimulation glass chips. The only difference was that we used a custom made stainless steel flaming mask to limit the area that was hydrophilized.

The seeding area on the mag-stim chips was defined using a self-adhering gasket made of silicone. These gaskets were manufactured according to the following protocol. The 2-component silicone elastomer kit Sylgaard 184 was mixed according to the user manual, de-gassed in a vacuum desiccator, and dispensed onto planar, cleaned glass plates. Pre-cut silicone rings were put down onto the Sylgaard material, and it was cured in the drying oven at 125 °C for 20 minutes. During this process, the silicone rings were bonded permanently to the Sylgaard elastomer. The final product was then carefully removed from the glass plate, and excess Sylgaard was removed carefully using a medical scalpel. The bottom surface of the rings was then smooth enough to stick to the smooth surface of the mag-stim chips without the aid of silicone grease.

The cell suspension was diluted to a final density of $3*10^4$ cells/cm^2, which corresponds to $0.75*10^5$ cells/ml. 200 µl of the cell suspension were dispensed onto the chip and incubated for 2 hours to allow adhesion of the cells to the flamed surface. After that time, adhesion was confirmed under the microscope and a large gasket was attached to the chip around the small seeding gaskets, so that an additional 2 ml of culture medium could be added. 8 ml autoclaved, ultra pure water were added to the Petri dish around the mag-stim chip for compensation of water evaporation.

2.4.6 Experimental setup

For the proper connection to the life-support systems and the stimulation equipment (figs. 2.22, 2.23), the following protocol was developed:

- Add 100 ml pre-heated and pH-adjusted culture medium (DMEM + 5% fetal calf serum (FCS)) to a 75 cm^2 culture flask. Block the opening of the flask with a silicone cork which was pierced with four sterile needles. These needles serve as ports for the tubing supplying CO_2, ultra-pure water, for transporting the medium to the culture chamber, and the fourth one remains open as an exhaust.
- A custom made, closed culture chamber made of PEEK is used to mount the chip into place the chip onto the aluminum base plate. The cover glass on the bottom of the culture chamber seals the cells against external influences. Before placing the chip onto the base plate, it must be dried using sterile filter paper.
- Remove ¾ of the culture medium from the chip, then remove the silicone gasket that was holding the medium. Carefully place the closed chamber over the chip, making sure not to introduce any air bubbles that might harm the cells.
- Prime the tube that connects the medium reservoir with the culture chamber, so that it is devoid of air, then connect it to the chamber. Connect the outflow tubing to the other side of the chamber, holding the base plate vertically, so that remaining air bubbles can escape into the outflow tubing. During this procedure, the medium reservoir flask must rest at an elevated level, so that no medium can flow backwards into the flask.
- Attach a syringe to the end of the outflow tubing and gently prime the rest of the culture chamber that had not been filled with medium. Close both the inflow and the outflow tubing off using a clamp.
- Transfer the base plate with the culture chamber, the tubing and the medium reservoir to the microscope stage, attach it firmly using the Plexon pre-amplifier as a spacer and custom made brackets, and put medium tank inside the heated holder.

The physiological life-support parameters were maintained by continuously pumping fresh DMEM through the culture chamber at a speed of 21 µl/min, using a peristaltic pump the outflow tubing was attached to. The pH in the culture chamber was kept constant at 7.4 by maintaining a 10% CO_2 atmosphere inside the medium reservoir. This way, the pH inside the reservoir was at 7.2, and on the way to the chamber, a fraction of the CO_2 in the medium evaporated, so that the pH was empirically determined to be 7.4 at the site of the cells. The inflow tubing was wrapped with a tungsten heating wire that kept the temperature of the medium moving through the tubing at a constant temperature of 35 °C. The temperature of the medium reservoir was maintained at 38 °C, while the culture chamber itself was heated to 33 °C. This procedure proved necessary, since it was the only way to reliably keep gas bubbles from forming inside the culture chamber. These bubbles appear when the medium is

heated up; therefore we made sure that the temperature of the medium constantly declined on the way from the reservoir to the cell chamber.

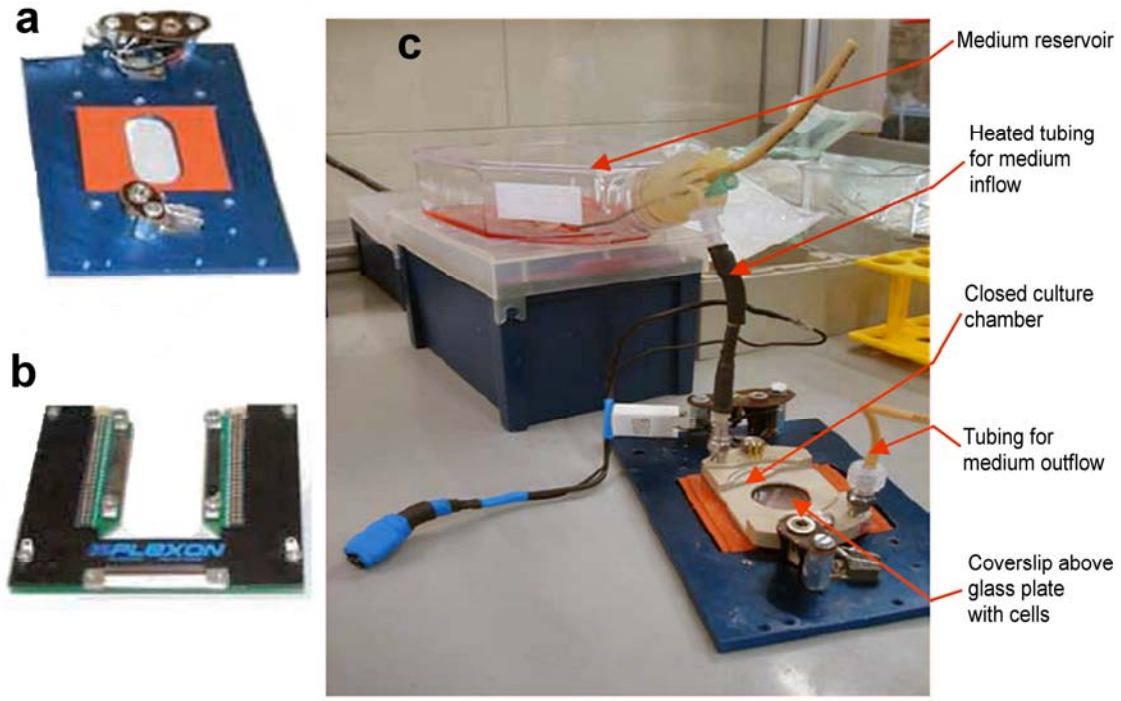

Fig. 2.22: Experimental setup for magnetic stimulation trials: a) heated aluminum base plate, b) Plexon pre-amplifier, used as spacer for attachment on microscope stage, c) Base plate with cell chip and closed chamber attached to medium reservoir.

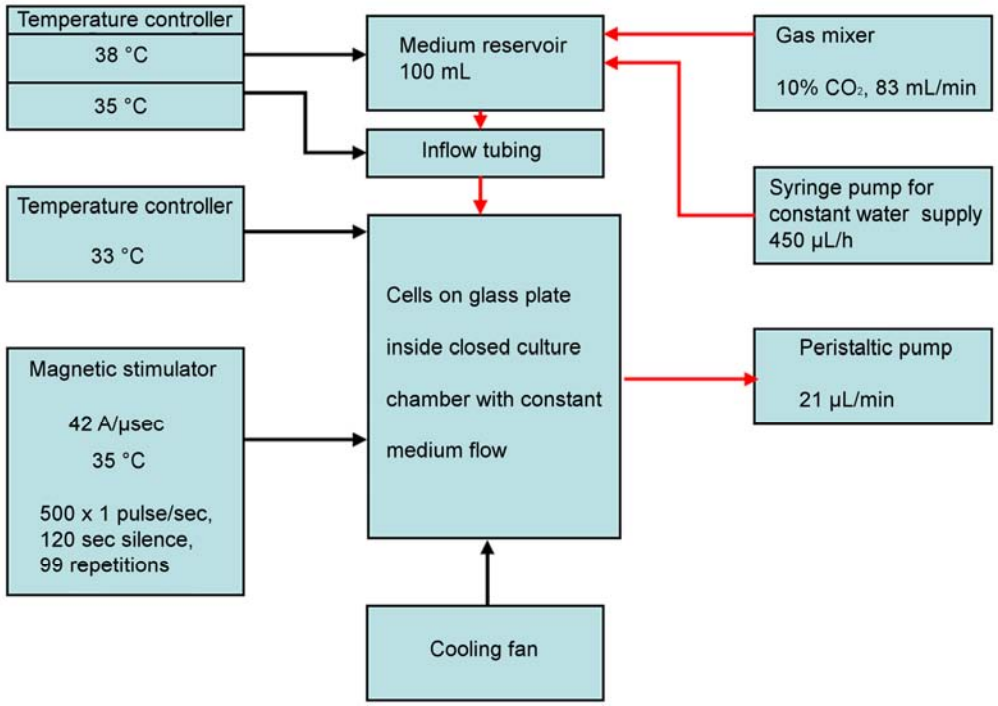

Fig. 2.23: Schematic flow-chart illustrating the components of the experimental setup, showing all life-support and stimulation components.

The chamber temperature had to be set to 33 °C for another reason as well. While mounted above the culture plate on the microscope, the stimulation coil had to be cooled to maintain a temperature of 35 °C, which a cooling fan was employed for. This fan, however, did not only cool the coil, but the culture chamber as well. The culture chamber was heated indirectly through heating resistors that were attached the base plate the culture chamber was mounted to. Due to the resistors' limited heating capacities, 33 °C at the site was near the maximum temperature achievable while being cooled by the fan.

For each treated culture, two controls were set up the exact same way, and then kept inside a 33 °C, CO_2-controlled incubator for the entire stimulation period of 17 hours.

2.4.7 Experimental schedule

After a pre-incubation time of 48 hours, one culture was set up for treatment, along with two control chips. The cells were treated for 17 hours ("treatment 1", fig. 2.24) and then counted. Treatment 2 began 72 hours after seeding, again accompanied by two control cultures. After another 17 hours, these cultures were counted as well. The cells were detached and counted according to the procedure described previously. Microscopic photographs of the treated and control cultures were taken at the time points marked with grey squares.

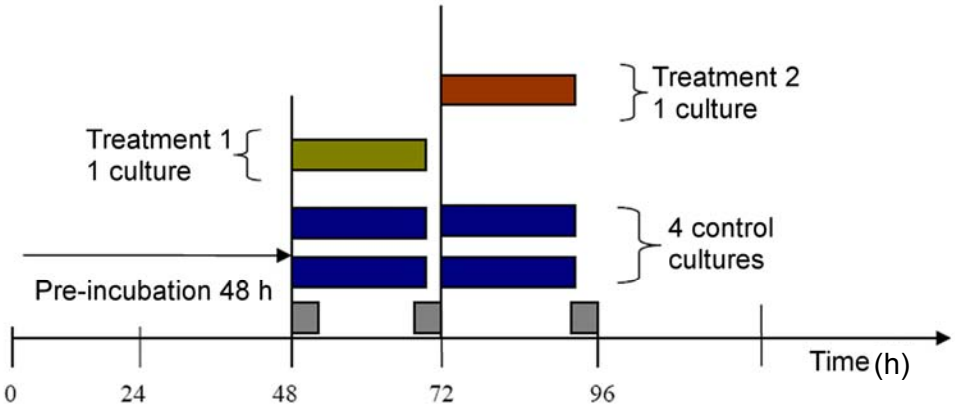

Fig. 2.24: Time line of the magnetic stimulation experiments [adapted from 127].

2.5 Neuronal network experiments

2.5.1 Neuronal cell culture

2.5.1.1 Material preparation

A few days in advance of the dissection day, the necessary tools and materials need to be cleaned. The MMEPs were cleaned using the laboratory detergent Deconex 12 PA. Remaining organic material and silicone grease was removed gently with a cotton swab. The plates were rinsed with ultra-pure water and soaked in it for at least one day, so that any remaining detergent would be completely removed. On the day before dissection, they were autoclaved. In order to protect the insulation layer from cracking, the plates were cooled down as slowly as possible. Since the materials the plates are composed of – glass, ITO, gold and polysiloxane – all have different heat dissipation coefficients, they expand and contract differently when heated or cooled, which increases the probability of cracks induced by shear forces. This is especially problematic at the corners of the conductors.

For the same reason, the plates were placed inside an aluminum block (fig. 2.25) when flamed. A droplet of autoclaved water was placed between the flaming block and the plate. Flaming is necessary in order to hydrophilize the surface of the MMEPs which are naturally hydrophobic. A hydrophobic surface would not allow the cells to adhere firmly. In order to only flame the area in the middle of the MMEP where the neuronal network was actually supposed to grow, a planar, stainless steel flaming mask was used to coverall of the MMEP except a 5 mm diameter hole in the middle.

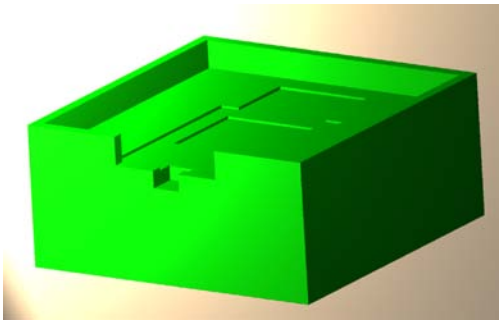

Fig. 2.25: Schematic drawing of the aluminum flaming block

After the flaming, 20 µl of a Poly-D-Lysine solution was applied carefully to the center of each MMEP. PDL serves as a nonspecific attachment factor for in vitro cell culture preparations. It is a positively charged polymer of the amino acid lysine and works by promoting the favorable ionic interaction between the negatively charged cellular membranes and the cell culture surface. The negatively charged carbonyl oxygen can interact with the cations of the flamed surface, while the positively charged side chains are free to attach to the neuronal cell membranes. The PDL was left to settle down on the MMEPs over night.

2.5.1.2 Tissue isolation

2.5.1.2.1 Preparation

Before beginning dissection, all the necessary materials must be in place, and the first part of surface preparation must have taken place the day before dissection. That means that MMEPs and coverslips are appropriately hydrophilized and coated with PDL. The second part of surface preparation includes coating the culture area additionally with laminin, and labeling the petri dishes. The laminin should be applied at least 45 minutes prior to the beginning of the dissection procedure. The following list contains the materials needed for dissection.

- 2 pairs sterile dissection scissors
- 2 pairs sterile large forceps
- 2 pairs sterile long, fine surgical forceps
- 1 dissection mat
- 70% Ethanol
- 4% NaOCl (sodium hypochlorite)
- Several sterile petri dishes
- 3-5 sterile 40 – 50 ml conical tubes
- 1-3 sterile 15 ml tubes
- Several sterile small fine surgical forceps
- Small bore, sterile transfer pipettes
- 2 – 6 sterile scalpels (2 per tissue type)
- 300 ml sterile D1SGH
- 3 to 10 ml papain (depending on number of tissues to be isolated)
- 200 to 600 µl DNAse
- ~50 ml DMEM 5/5 and/or MEM 10/10, depending on tissues to be isolated (MEM needed for spinal cord, though DMEM may be used in its place, but not vice versa)
- Chloroform (or other volatile anesthetic, such as isoflurane)
- 1 desiccation chamber for anesthetization
- 3 sterile laminar flow workbenches
- 1 fume hood
- 1 stereo microscope for dissection
- 1 haemocytometer

Ideally, the animal to be dissected has arrived one to two days prior to the dissection date and has been housed in a calm, non-stressful environment. The desiccation chamber (fig. 2.26 a) is prepared by adding a small amount of chloroform and closing it tightly under the fume hood. Five minutes should be allowed for the chloroform to diffuse throughout the chamber. During this time the dissection hood (fig. 2.26 b) should be prepared. The photo below depicts an ideal example of how to prepare the hood for removal of the embryos from the mother. A tube of cold, sterile D1SGH is needed to transport the embryos to the second dissection area. The second dissection hood should also be prepared in advance to minimize the time between

removal of the embryos and cell isolation. This ensures the best possible tissue culture health. Under this hood, one will need a dissecting microscope, several petri dishes, half way filled with cold D1SGH, and large and small fine surgical forceps. See figure 2.27.

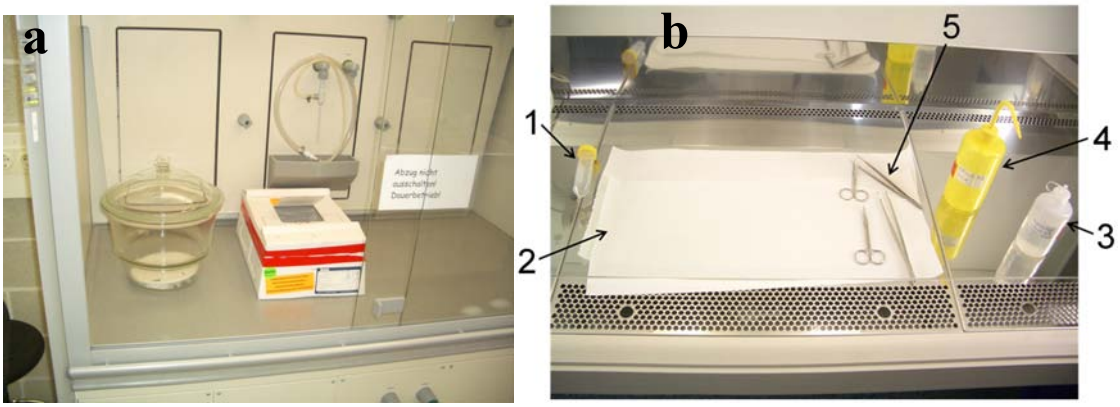

Fig.2.26: a) Desiccation chamber with chloroform inside and animal shipping container under fume hood; b) Initial dissection hood preparation. 1) 50 ml conical tube half full of cold D1SGH, 2) Dissection mat, 3) large forceps and scissors, 4) 70% Ethanol, 5) 4% sodium hypochlorite solution.

Fig. 2.27: Dissection hood 2. Here dissecting microscope and other dissecting supplies can be seen. All supplies and surfaces should be thoroughly sterilized prior to preparation and dissection.

After dissection of the embryos, supplies for preparing the cells from the isolated tissue for seeding are needed. Once again, these should be ready in advance to avoid any delays which might lead to poor cell/culture quality. These can be set up in an additional hood. See figure 2.28.

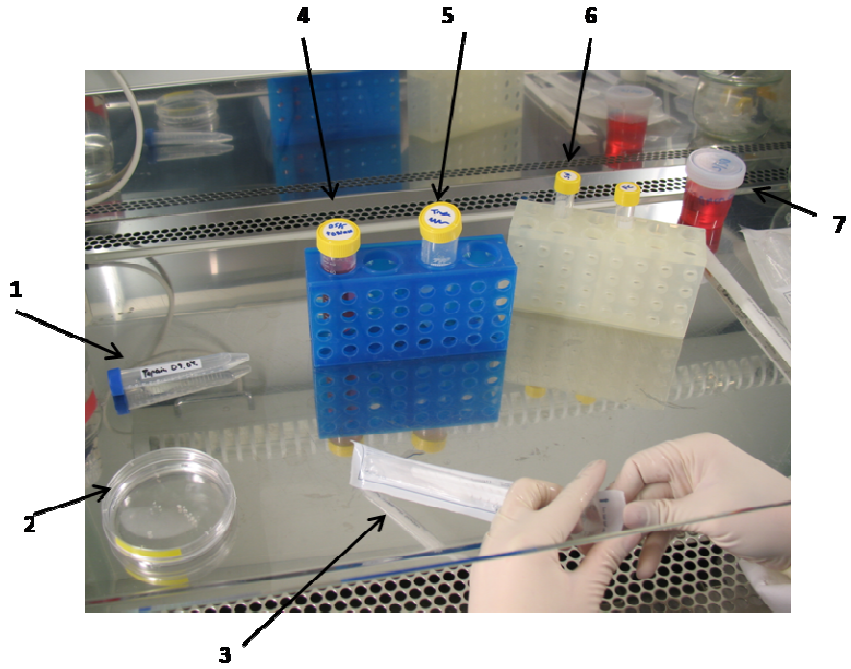

Fig. 2.28: Workbench prepared for cell trituration and seeding. 1) Papain. 2) Isolated tissue. 3) Scalpel (at least 2 needed). 4) Seeding media with DNAse. 5) Tube for liquid waste. 6) Labeled tubes for cell suspensions. 7) Seeding media.

2.5.1.2.2 Animal dissection

Once all preparation is complete dissection may begin. The animal is removed from the shipping container as gently as possible and placed into the chamber with the chloroform. After a short time (several seconds) the animal will be still breathing but have stopped moving. The animal should be left in the chamber until it ceases breathing. Whether the animal is thoroughly anesthetized can be checked by touching its whiskers and eyes.

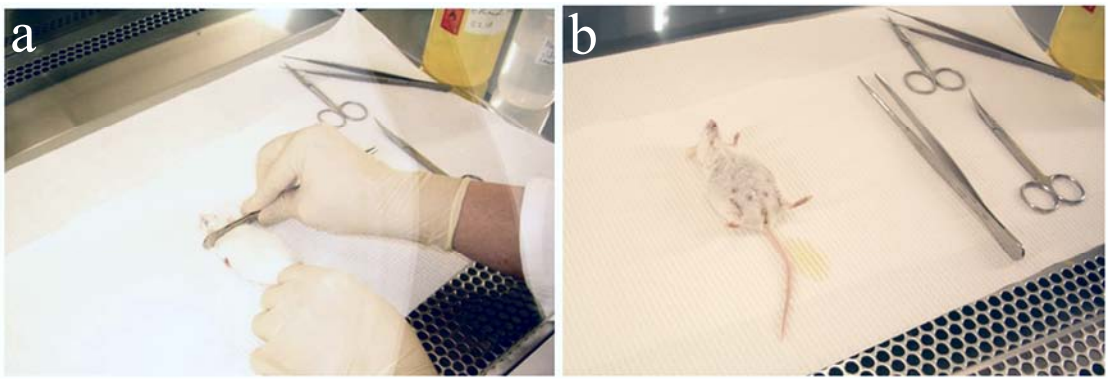

Fig. 2.29: a), b) Termination of the animal

The animal is laid prone (belly down) with its limbs outstretched onto the surgical mat. To kill the animal, the blunt end (handle) of the large forceps is placed caudal to its

head and held firmly in place. (fig. 2.29) The base of the tail is grasped and pulled caudally until one feels the popping of the cervical spine column. At this time, the animal may urinate or defecate as its sphincter muscles relax. Now, the animal is laid supine (belly up, see fig. 2.29 b). The abdomen and lower body are rinsed with bleach and alcohol, going against the hair. Using the forceps, the skin of the lower abdomen is lifted and carefully cut with the scissors to penetrate the skin. The incision is extended towards the sternum making a 'Y' shape. (fig. 2.30 a) At this point the uterus enclosing the fetuses should be visible. The cranial end of one horn of the uterus is lifted carefully with the forceps. The connective tissue and blood vessels along the dorsal side are cut, gradually freeing the horn from the abdominal cavity. The body of the uterus is transected at the base, and continuing cutting the connective tissue along the other horn, the entire uterus is freed from the abdomen (fig. 2.30 b).

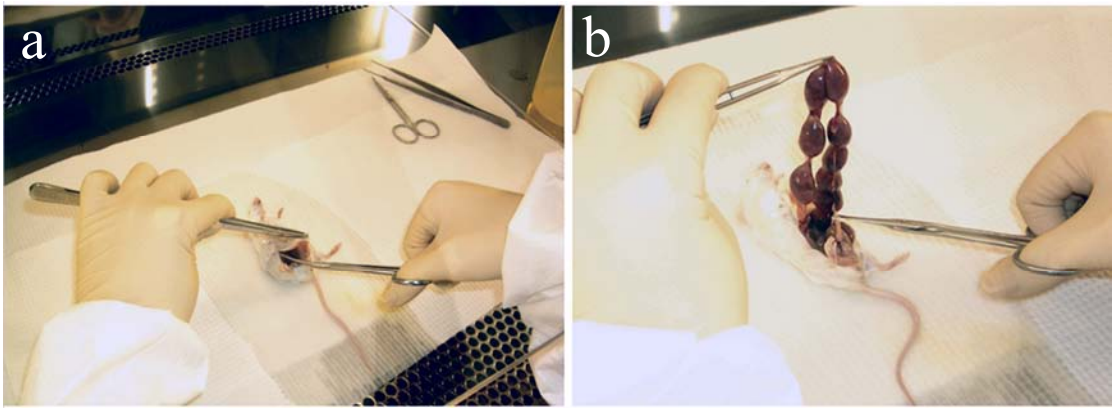

Fig. 2.30: a) Making the 'Y' incision to expose the internal organs and uterus. b) Removing the uterus and embryos from the abdominal cavity.

The uterus is rinsed with alcohol and placed into the conical tube of cold D1SGH. The tube containing the embryos is transferred to the other prepared dissection hood. Under the hood, the embryos are transferred to a Petri dish, and using the long fine tipped forceps they are delivered from the uterus to a Petri dish containing D1SGH (See fig. 2.31 a). To do this, the placenta is exposed by gently tearing through the uterus. The placenta is removed from the uterus, and the amniotic sac is worked away from the embryo (see fig. 2.31 b). Once the embryo is free from the placenta and amnion, it is transferred to a new petri dish containing D1SGH. This procedure is repeated for the remaining embryos. At this point, the embryos are counted and checked for abnormalities. Any abnormal embryos are discarded of before proceeding. The embryos are decapitated by grasping the neck, between the shoulder and base of the skull, with both pairs of fine forceps and then squeezing those closest to the base of the skull tightly shut. (see fig. 2.32). The head is transferred to a fresh petri of D1SGH. From here, the procedures for isolating the different tissues diverge.

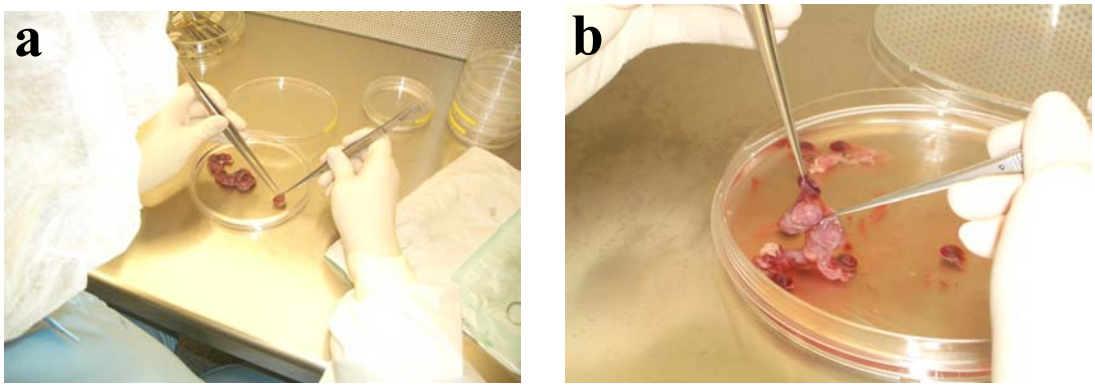

Fig. 2.31: a) Removing the placenta and the amniotic sac, b) removing the embryos from the uterus

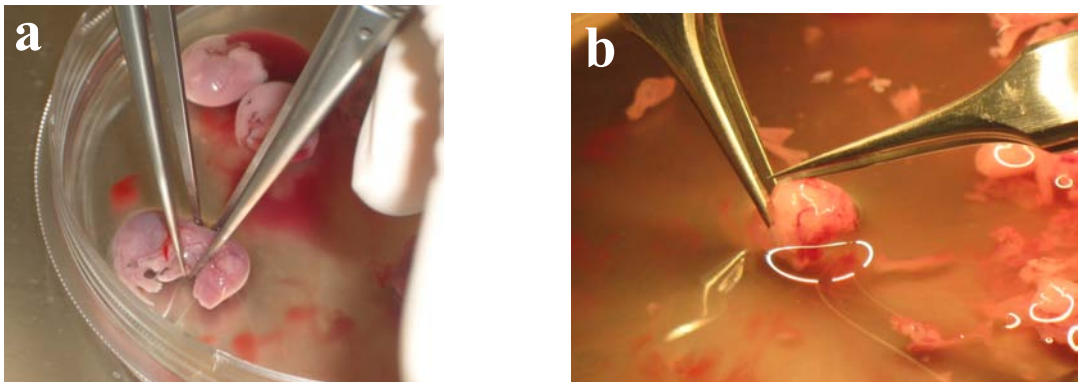

Fig. 2.32: a) Decapitating the embryos, b) Removing the skin and skull to reach the brain.

2.5.2 Frontal cortex dissection

Using two fresh pairs of fine tipped forceps and working under the dissecting microscope, the head is placed right-side up and grasped by inserting the tips of one pair of forceps into the eye sockets and gently squeezing the cartilage located between the eyes. With the tips of the second set of forceps, an incision in the skin is made stretching from between the eyes to the base of the skull. The skin is peeled away to the sides of the head; however, it is not necessary to completely remove the skin. The thin skull is now visible. Using the tip of the second pair of forceps, a small incision just above the base of the skull is made, not poking too far inward so as not to damage the brain. Carefully, one tip of the forceps is slid between the skull and the brain, gently pulling up to make an incision matching the one made in the skin. The skull is peeled away to the sides. To remove the brain from the skull, the tips of the second pair of forceps are closed together and slid under the olfactory bulbs at the front of the brain. Slowly and gently lifting and pushing back, the brain comes wholly out of the skull. The brain is transferred to the next petri dish of D1SGH. This routine is, again, repeated for the remaining embryos. The olfactory bulbs are removed from the front of the brain. The meninges are removed by grasping the membrane at the hole left by the olfactory bulbs. To isolate the frontal cortex, one tip of the forceps is inserted into this hole. A cut

is made extending about a third of the way back in the cortex on both the dorsal and medial sides of the hemisphere. By making a snip, these two cuts are joined. The circumscribed tissue is the frontal cortex. This new tissue is transferred to a new petri dish containing D1SGH.

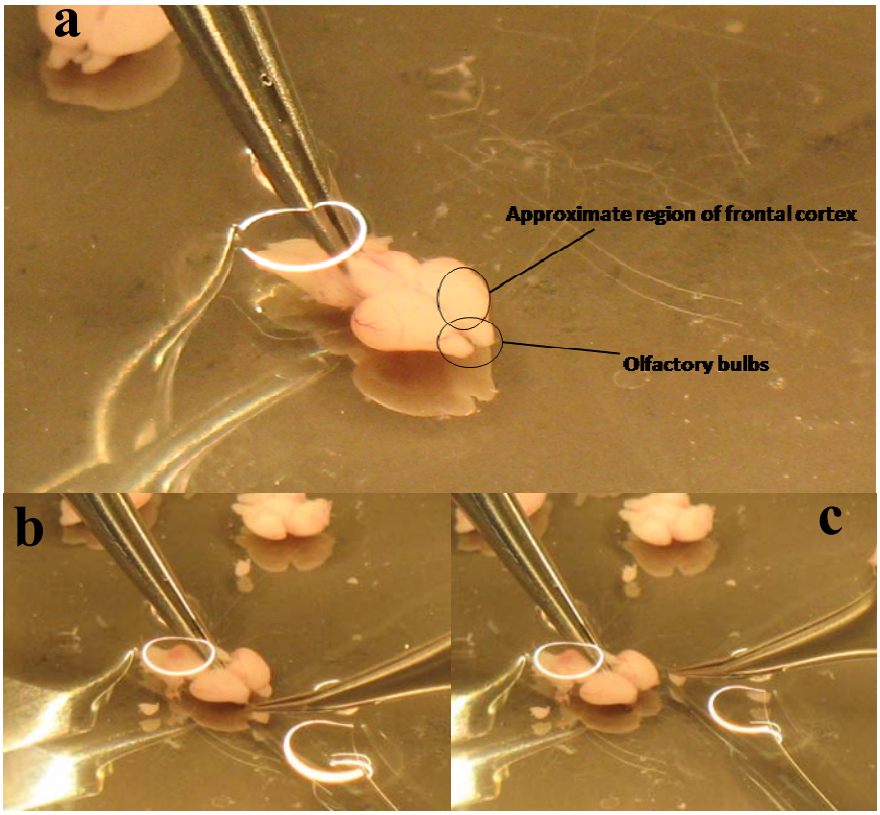

Fig. 2.33: a) The whole brain, b) removing the olfactory bulbs, c) removing the meninges

2.5.3 Midbrain dissection

Isolating the midbrain tissue is more difficult than removing the frontal cortex. The substantia nigra is a part of the midbrain, which lies partly between the cortex and the brainstem, partly underneath the cortex. The dopaminergic cell density is particularly high in the substantia nigra pars compacta, which is depicted in Fig. 2.35 b. In the live tissue, the substantia nigra does not actually appear darker than the rest of the brain. This will only occur if the tissue is fixed. Fig. 2.34 shows how the midbrain slice containing the substantia nigra is cut out using a sterile scalpel (a). The outside parts of the slice are part of the cortex and have to be removed (b). The remaining piece is cut in half, and the bottom half is kept.

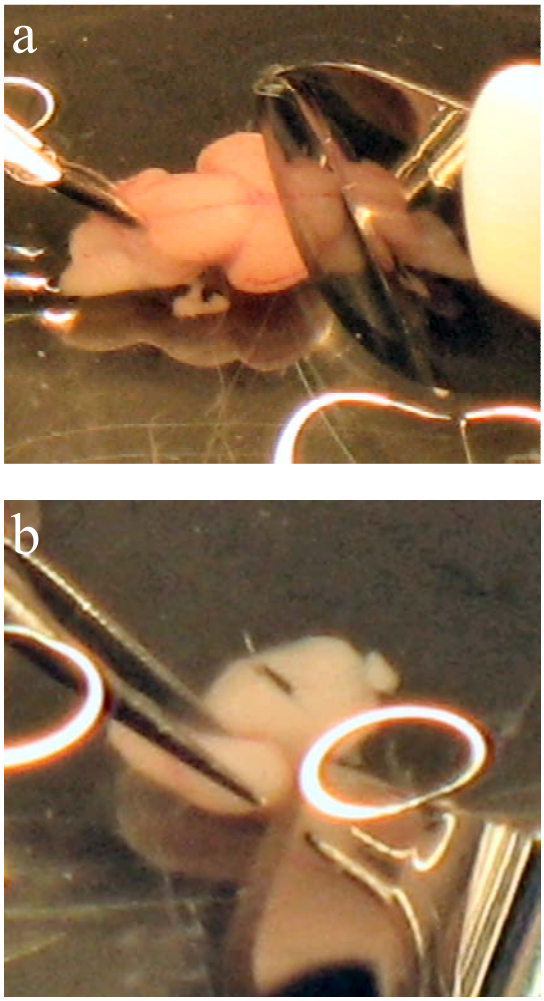

Fig. 2.34: a) Cutting the midbrain slice, b) Removing parts of the cortex

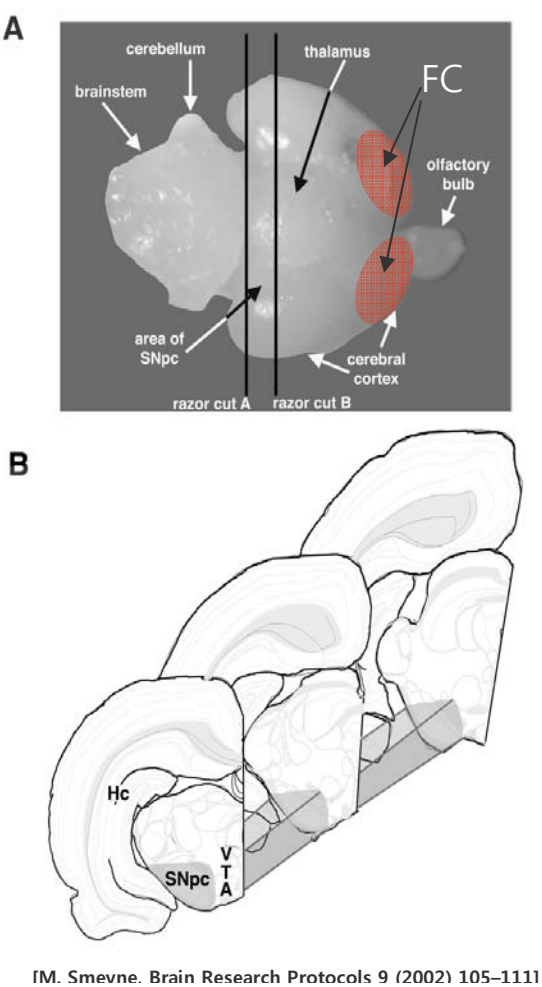

Fig. 2.35: a) Location of the midbrain slice, b) Location of the substantia nigra pars compacta

2.5.4 Cell separation and seeding

Right after the respective tissue is isolated, the cells need to be dissociated for seeding, since the new networks will only form properly if the cells are completely separate from each other. The dissociation is a two-step process. Firstly, they are mechanically minced using two sterile scalpels (fig. 2.36 a), then incubated at 37 °C with papain (b). The incubation times vary for the different tissue types. Papain has been established as the digestion enzyme of choice, since it is powerful enough to break up the remaining cell-cell connections, yet gentle enough not to injure the cells significantly. The final steps in the seeding process are re-suspending them in DMEM containing DNAse, diluting them to their final concentration and plating them on the prepared MMEPs. The DNAse is needed because some cells are of course destroyed during the mincing/digestion process, thus leaking DNA, which is sticky and causes clumping of the cells. The cells are counted using a haemocytometer, and the density of the suspension is adjusted to 300,000 – 500,000 cells per ml, depending on the culture

density desired. 100 µl of this suspension are finally pipetted onto the MMEP (fig. 2.37) and then incubated for 2 hours, before more medium is added. This time is required for the cells to settle down and achieve adhesion to the surface.

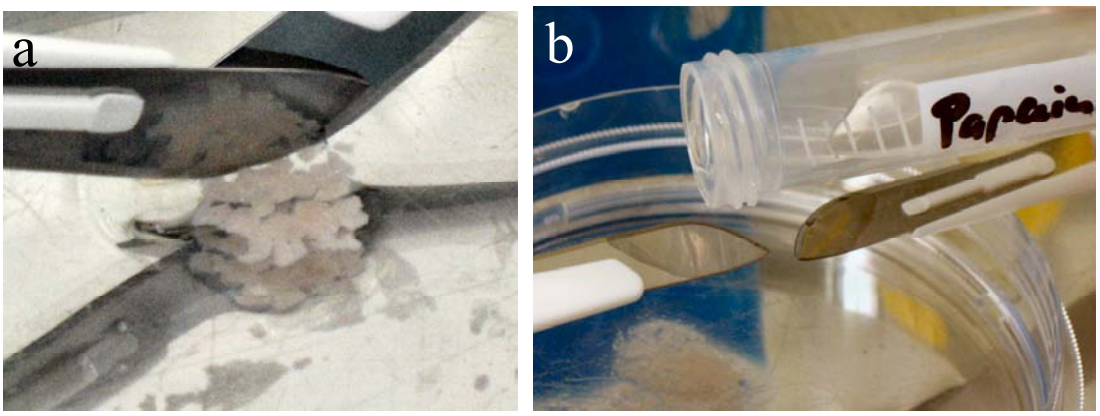

Fig. 2.36: a) Mechanical mincing of the cells using sterile surgical scalpels, b) Digestion of the cellular connections using papain.

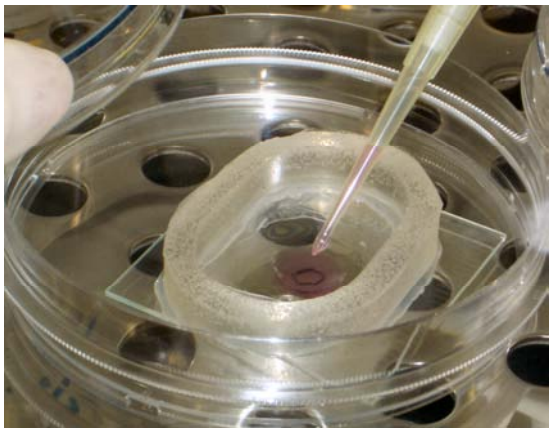

Fig. 2.37: Plating of 100 µL cell suspension on a laminin-coated MMEP with a Sylgard gasket

2.5.5 Maturation of the neuronal cultures

Observing the neuronal cell cultures grow over the first two weeks of their existence reveals major morphological transformations that are best described by showing phase contrast photographs. Since the morphology of the neurons changes from relatively small, elliptical objects to larger, taller, branched-out structures with a vast number of interconnections, the phase contrast is ideally suited to monitor these changes in the live cultures, since it visualizes the three-dimensionality of the cells. The further a structure sticks out from the surface, the brighter it will appear in the phase contrast. In fig. 2.38, we see that the freshly isolated and dissociated cells appear round and small, and no distinction between neurons and glia cells can be made. The cells are

taken from the embryo within a time frame during which they are not pluripotent anymore, but not fully differentiated either, which means that they can fully recover from being separated and grow back together. Figures 2.39 through 2.43 show both FC and midbrain cultures at different developmental stages as denoted in the respective legends.

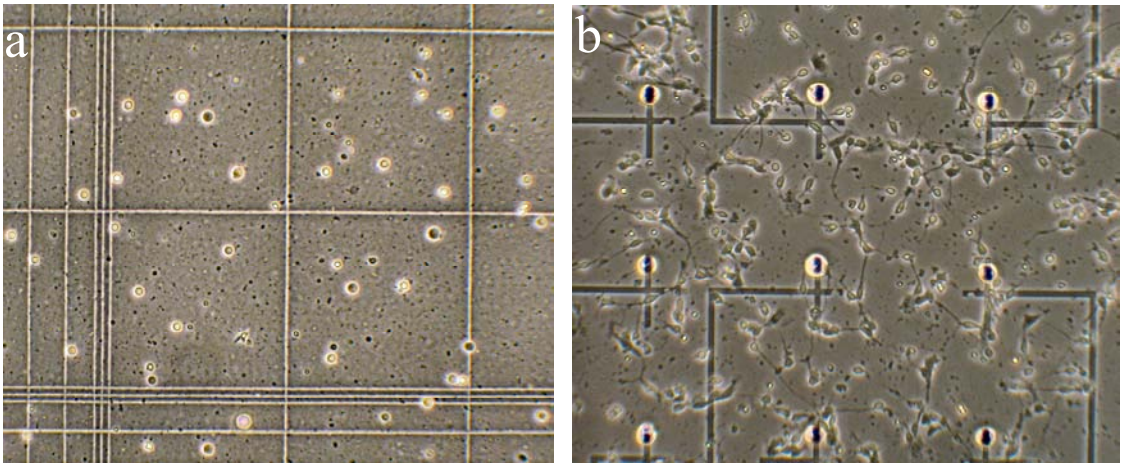

Fig. 2.38: a) Frontal cortex, seeding day, in counting chamber, b) Frontal cortex, day 1 after seeding, on a dual-matrix MMEP

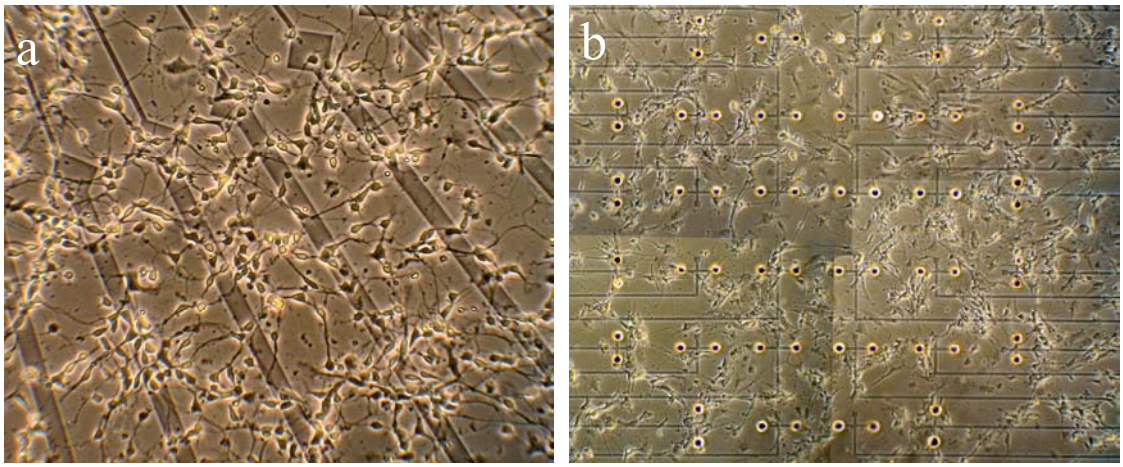

Fig. 2.39: a) Frontal cortex, day 3 after seeding, on a single-matrix MMEP; b) midbrain cells, day 3, on a dual-matrix MMEP

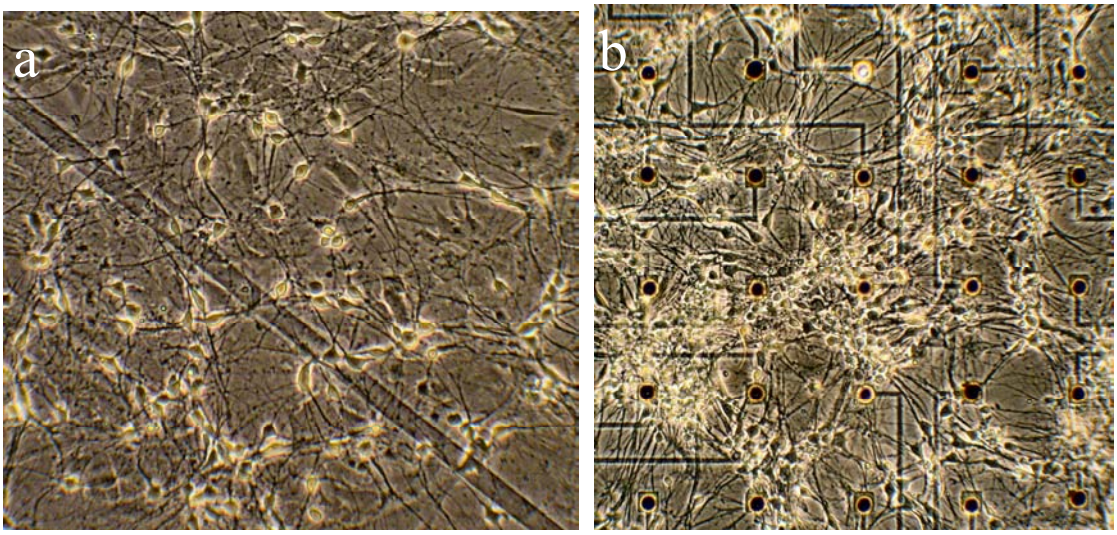

Fig. 2.40: a) Midbrain, day 9, on a single-matrix MMEP; b) Frontal cortex, day 9, single-matrix MMEP

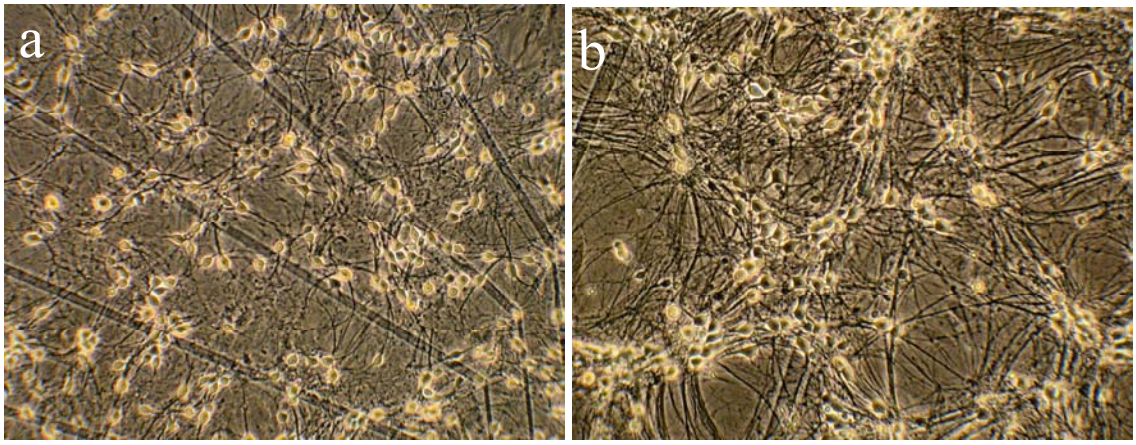

Fig. 2.41: a) Midbrain, day 11, on dual-matrix MMEP; Frontal cortex, day 11, on single-matrix MMEP

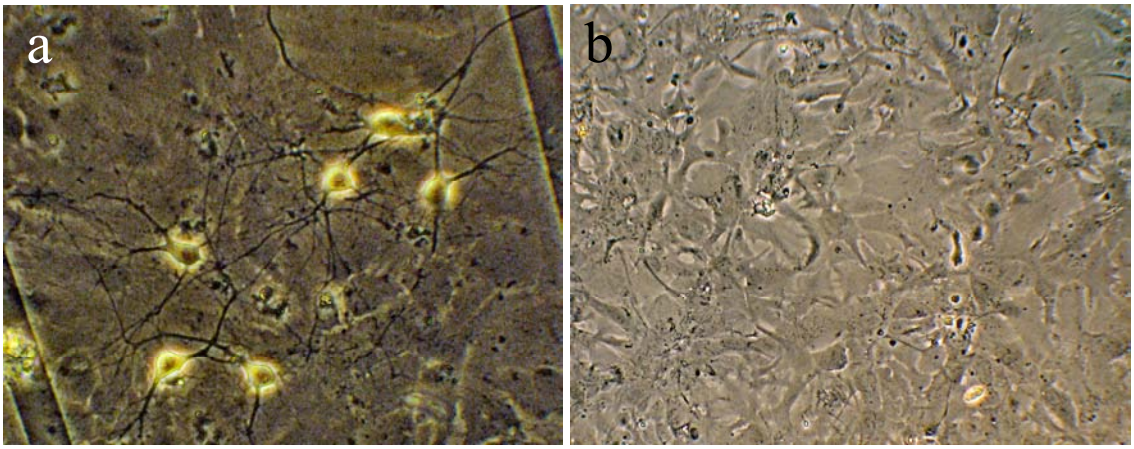

Fig. 2.42: a) Frontal cortex, day 14, single-matrix MMEP; glia carpet without neurons.

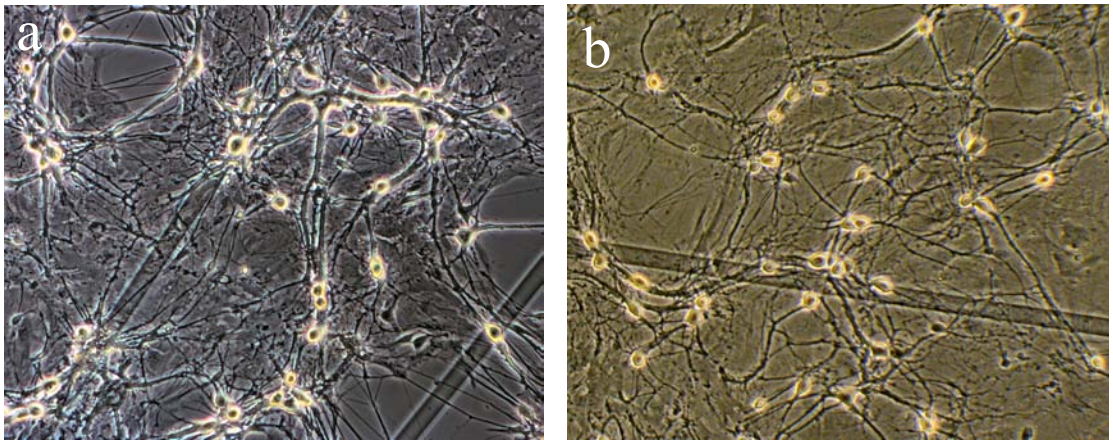

Fig. 2.43: a) Mature frontal cortex culture, 25 days in culture, on a single-matrix MMEP; b) Mature midbrain culture, 29 day in vitro, on a single-matrix MMEP

2.5.6 Recording equipment

2.5.6.1 Multi-microelectrode plates

MMEPs are 1 mm thick glass plates that contain a multi electrode array (MEA) with 64 electrodes on an area of approximately 1 mm^2 in their middle (fig. 2.44 a). There are also dual MMEPs that have two 32-electrode matrices (fig. 2.44 b). Both designs were designed and fabricated at the Center for Network Neuroscience (CNNS), University of North Texas, USA, and used in this study. Except for the different geometry, they share most of their characteristics. The conductors (black structures in fig. 2.44) are made of indium tin oxide (ITO), which was sputtered and photo etched before an insulation layer was deposited onto the whole area of the MMEP except for the contacts on the sides. The insulation material is a custom composed Methyldimethylpolysiloxane with optimized balance of durability (hard bake) and minimal brittleness (soft bake), which is a tightly balanced procedure. Finally, the electrode spots in the middle of the MMEP are deinsulated using a Laser that is coupled into an inverted microscope. The laser-induced craters are electrochemically filled with gold which lowers the resistance of the electrode considerably to about 1 MΩ at 1 kHz. The dielectric properties of the polysiloxane allow for a 10 µm thick layer to have an impedance of >10 MΩ at 1 kHz. This ratio of the electrode-to-shunt impedance has to be in the order of 10, so that the majority of the signals will be detectable. The shunt impedance is the impedance of the insulation layer that covers the conductors outside of the de-insulated electrode points.

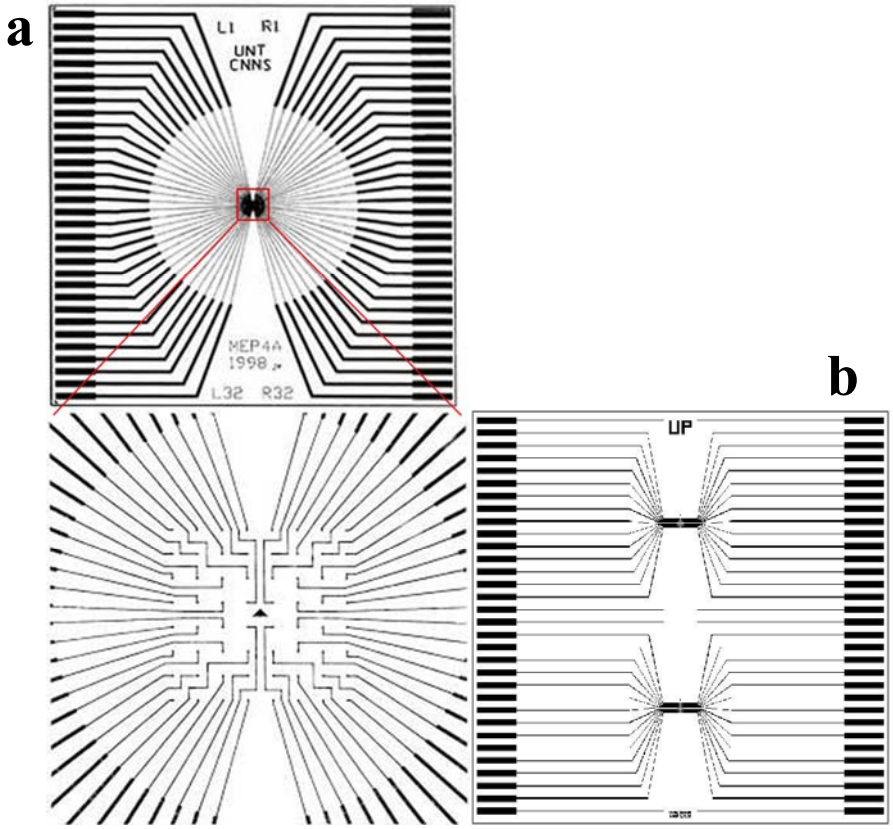

Fig. 2.44: a) Single multi-microelectrode plate layouts with 64 recording electrodes ("MMEP4"), b) Dual CNNS MMEP with 2 x 32 electrodes ("MMEP5"), designed at the Center for Network Neuroscience.

2.5.6.2 Plexon amplifier and signal acquisition system

The recording system used to acquire the neuronal APs was provided by Plexon, Dallas, USA. The MEA workstation consists of a headstage amplifier with a fixed gain of 50, a variable gain (40 – 350) computer controlled main amplifier, a workstation PC containing the 64-channel A/D converter card, the data acquisition software, a BNC output panel, and a digital/analog oscilloscope. The headstage is required to amplify and bandpass-filter the neuronal signals as close to where they are generated as possible, because the voltages detected by the gold-plated electrodes are usually on the order of 50 – 500 μV, while the noise amplitude is around 30 μV. Without immediate amplification, external fields would add to the noise and make it impossible to reconstruct the actual signals. After full amplification, usually at a total gain of 10,000, the signals are digitized at a sampling rate of 40 kHz. The waveshapes of the APs are initially displayed as raw, unsorted waveforms in a fixed-width, single-triggered window. The trigger threshold can be adjusted individually for each channel, as the signal characteristics vary from one electrode to the next. In order for the software to recognize and record the waveshapes, they need to be sorted. For that purpose, a template set of waveforms is collected and then assigned as one or several AP shapes. The software can discriminate up to four different waveforms per channel. There are

different ways to have the program recognize a waveshape, but the preferred one is the following: Active units are discriminated by template matching. A template is an average of a group of waveforms selected from the APs of one class, or unit. Incoming waveforms are compared to the template, or templates if more than one unit is recorded by a specific electrode, using a sum of squared differences calculation (SSQD) over the points of the waveform and template. The SSQD is compared to a tolerance or tightness of fit value. If it is less than that value, the waveform is assigned to the class (unit) represented by that template. The tolerance value is manually adjusted by observation during the selection of units. Waveforms are accepted or rejected on this basis. Artifacts have a very large SSQD compared with waveforms of the unit classes and are rejected as an active unit. This sorting algorithm is performed in real-time by the Plexon software. Activity windows (fig. 2.45, #18) showed both the discriminated waveforms of the currently chosen unit AP, all the active waveforms recorded from the current MMEP, and a real-time raster window of adjustable time scale showing all the recorded APs as timestamps.

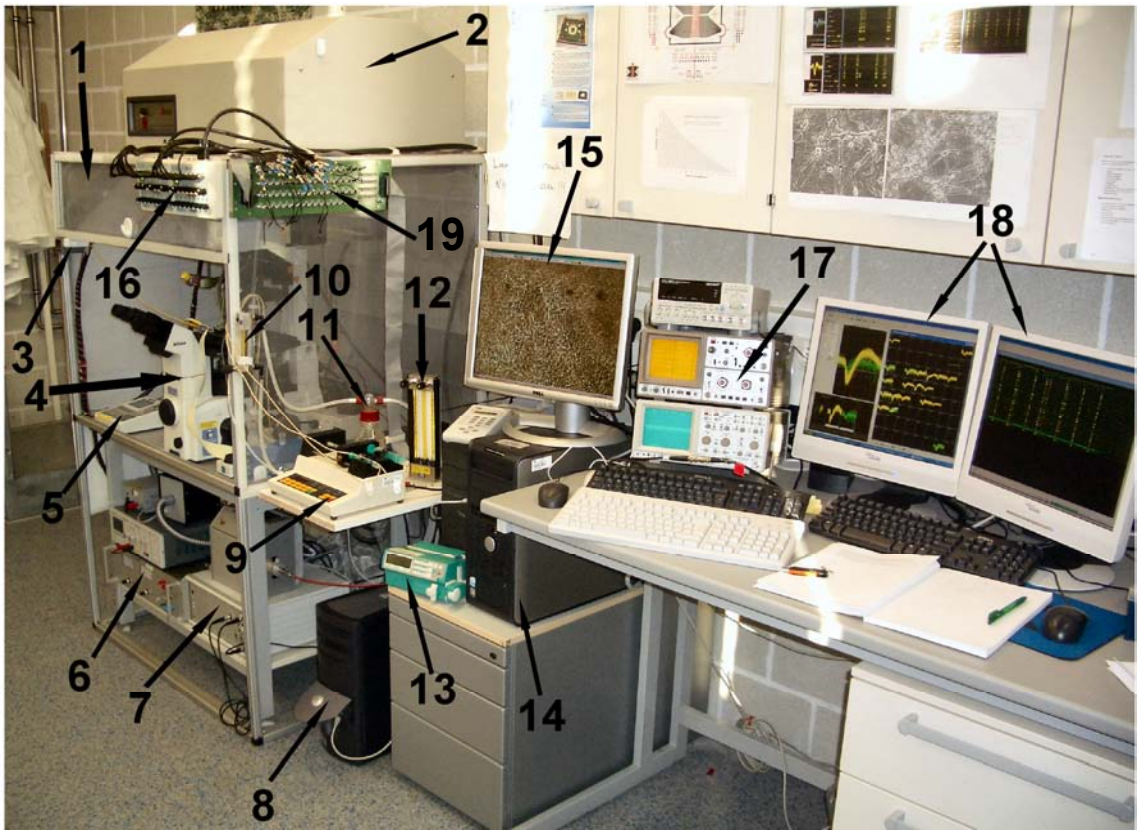

Fig. 2.45: Workstation for neuro-electrophysiological experiments showing all the necessary life-support and data acquisition equipment: 1) Faraday cage, 2) HEPA air filter unit, 3) Temperature controller for cell culture chamber, 4) Inverted phase contrast/fluorescence microscope, 5) Manual control pad for microscope, 6) Power supplies for heating and stimulation devices, 7) Control unit and monochromator for fluorescence microscopy, 8) Microscope control PC, 9) Precision syringe pump for osmolarity maintenance, 10) Low-volume gas flow meter, 11) Gas humidification bottle, 12) CO_2/air mixing controller, 13) Infusion pump, 14) Plexon data acquisition PC, 15) Live cell culture display, 16) 16-channel pre-amplifier/filter system for audio output of electrical activity, 17) Analog/digital storage oscilloscopes for variable-resolution (temporal) activity display, 18) Activity display, 19) 64-channel Plexon BNC board for connection of analog signals to audio amplifiers.

2.5.7 Eight-network recording system

For the muscimol experiment using eight networks, grown on a single MMEP (layout shown in fig. 2.46 a, photograph with chamber block and eight headstage amplifiers (black): b), a robotic pipetting machine was used (Biotek Precision 2000, fig. 2.46 c). This apparatus can pick up eight pipette tips simultaneously and perform complex liquid handling tasks that are programmed by the user before each experimental run. The liquid aspirating/dispensing head moves in x- and z-direction, while the y-direction is covered by the base tray (5). Before each experiment, the MMEP8 is carefully positioned on the base plate. The contacts are cleaned and dried and the circuit board holding the 8 headstage pre-amplifiers is connected using carbon-zebra strips which are held in place between the MMEP8 plate and the circuit board by a custom made plastic holder. This setup provides good electrical coupling between the amplifiers and the MMEP8, but poses some difficulties during assembly. For example, it is almost impossible to guarantee perfect alignment of the circuit board with the MMEP8. This means that the numbering of the channels on the MMEP8 plate might not be accurately reflected in the numbering of the digitized channels. This downfall was addressed in the design under development and will be amended.

One of the most challenging aspects using the robot for liquid supply of the neuronal cultures is the sensitivity of the neurons to mechanical stress and to overdoses of compounds. An overdose occurs when a compound is added without extensive mixing with medium. However, an "underdose" might occur just as well, depending on the exact position of the pipette tip while dispending the compound. If one adds a compound using a standard pipette tip and it is positioned right above the cells, they will experience almost the concentration of the stock solution. One possible way around this problem is to mix the medium beforehand, which is the standard approach when applying a compound to the cultures on single- or dual MMEPs. However, the pipetting robot can only aspirate and dispense up to 120 µl, which means it would have to remove the medium in 10 steps, if the majority of the medium was to be mixed with the compound before applying it. The total volume per well required for the neurons to be active in a stable manner is 1.5 ml. Therefore, a more efficient mixing method was needed.

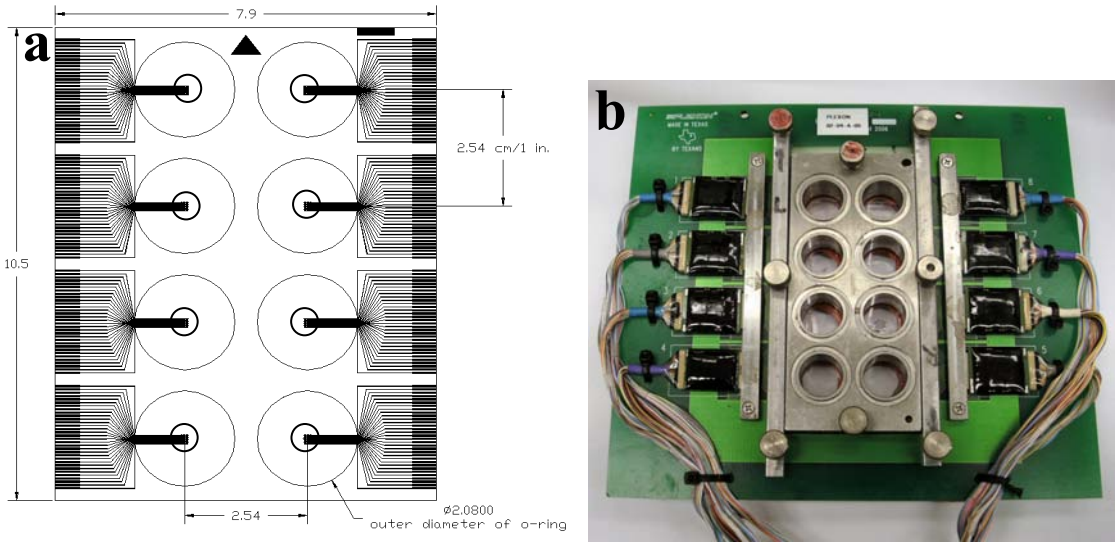

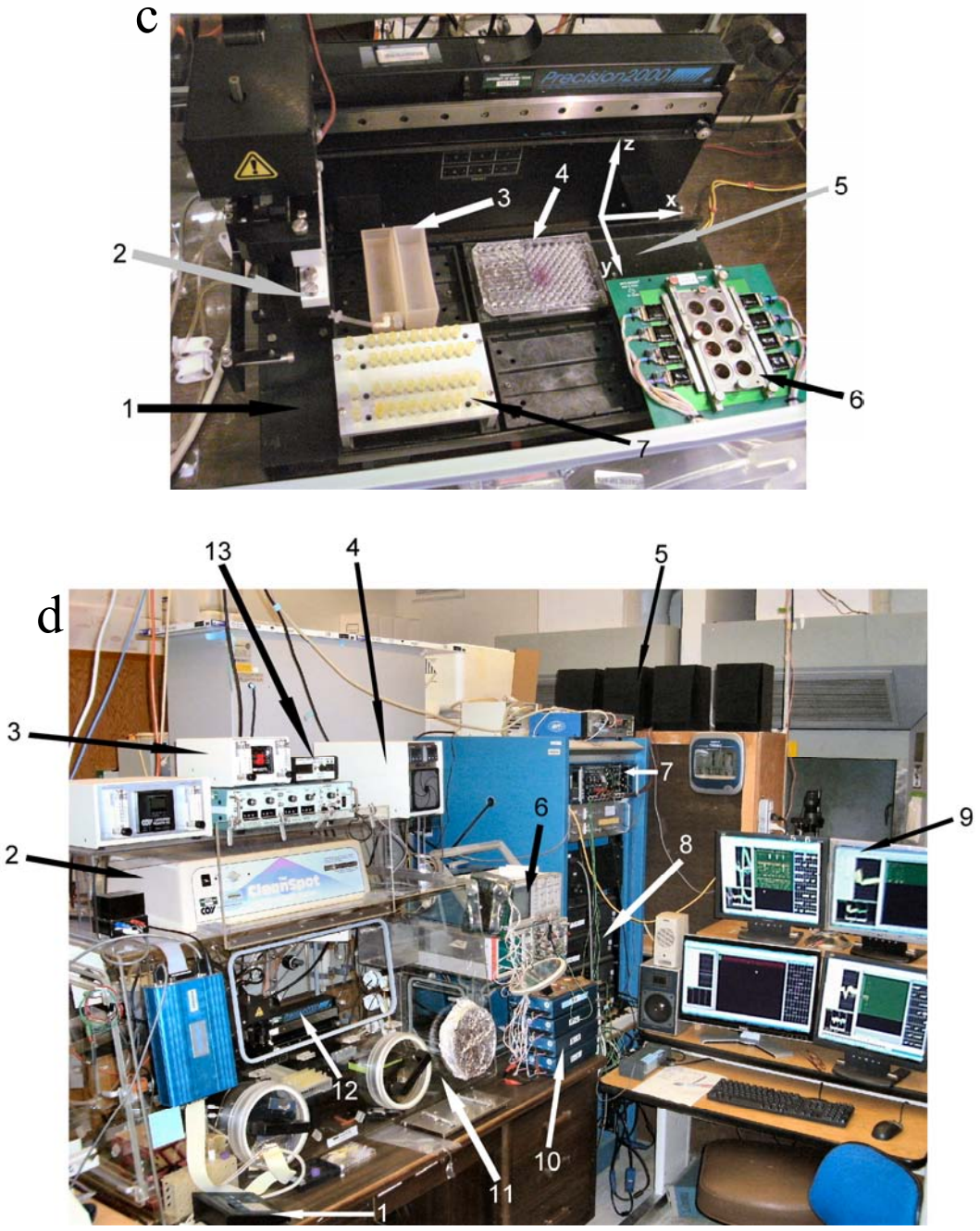

Fig. 2.46: a) Layout of the eight-network MMEP ("MMEP8"), designed and manufactured at the Center for Network Neuroscience, Prof. Gross; b) complete assembly with culture chamber block for eight separate networks and the eight headstage pre-amplifiers; c) Pipetting robot at the Center for Network Neuroscience (CNNS): 1: Anodized steel base, 2: Pipetting head, 3: Water reservoirs, 4: 96-well plate for fresh medium supply and waste disposal, 5: Base tray for movement in y-direction, 6: MMEP8 with chamber block and pre-amplifiers, 7: Aluminum pipette tip holder; d) Robot workstation: 1: manual control pad for pipetting robot, 2: UV sterilization lamp housing, 3: CO_2-control unit, 4: Temperature controller, 5: Loudspeaker array, 6: Analog/digital oscilloscopes, 7: Audio amplifier/filter system, 8: Plexon system computers, 9: Flatscreen real-time activity displays, 10: Plexon computer-controlled analog amplifiers, 11: Sterile acrylic Glovebox, 12: Pipetting robot inside glovebox, 12: Humidity controller

Using a concentrated dye, we could show that the standard pipette tips with one hole pointing vertically downwards did not mix the fluids in the wells appropriately. Instead, the dye was merely pushed outwards to form a circle at the perimeter of the well. In an attempt to improve the mixing efficiency of the pipette tips, we modified them using a biocompatible silicone sealant to close off the vertical hole, and we introduced four horizontal holes just above the very tip of the pipette (fig. 2.47). This procedure was performed under the stereo microscope using 28.5 gauge needles. The new design did improve the mixing efficiency, which was verified by another dye test. In addition, the artifactual spikes in activity were diminished. These horizontal ejection tips were used for all MMEP8 experiments shown in this study.

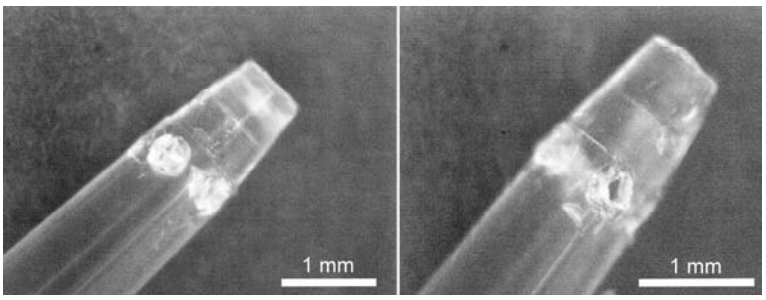

Fig. 2.47: Stereo microscope photographs of the horizontal ejection pipette tip prototypes. Magnification: 25x

2.5.8 Experimental procedures

2.5.8.1 Conducting a compound titration

The major group of applications the MEA system is tailored to are pharmacological and toxicological experiments with one or several substances with unknown or partially known inhibitory or excitatory – or a combination of both - characteristics, thus generating a dose-response correlation. In these types of tests, a substance of a potentially neuroactive power is dissolved in a suitable carrier solution and then added to the culture medium. The carrier solution should be formulated in such a way that does not interfere with the chemical composition and configuration of the active ingredient, and that does not affect the neuronal activity by its own properties. If it does, it should do so in a highly repeatable, linear fashion, so that its effects can be easily subtracted from – or added to – the gross effect of the solution with the compound under investigation in it. This is often the case when complex molecules, such as proteins or enzymes, are to be evaluated. These molecules often require certain storage conditions, such as a particular pH value, in order to remain intact and at their desired activity. In these cases, the carrier solution must be tested first, so that its own neuroactivity can later be taken into account when analyzing the data. Additionally, the solution should be well soluble in water, isotonic, pH-neutral and similar in temperature to the culture medium. Ideally, the initial stock solution should be highly concentrated, so that a very small amount α of that solution can be mixed with a certain amount of pre-conditioned culture medium β (i. e. the medium that the cells have been in since the start of the respective recording) to yield a

concentration that can then be further diluted to yield the final working concentration in the culture medium. Since the researcher will always wish to test a range of concentrations, amount β should be calculated based on the range of molarities desired for testing and the minimal step size of fluid volume that can be reliably measured with the equipment at hand. The amount α will also depend on the minimal step size, as well as on the maximum solubility of the compound in the carrier solution chosen. For example, if compound x has a maximal solubility of 100 mM in water, the minimal step size is 0.5 µl and the amount of culture medium is 2 ml, the desired concentrations for testing are 0.1, 0.2, 0.5, 1 and 2 µM, amount β will be 3.8 µl. The concentration of solution β is 0.4 mM, and the concentration of solution α is 3.04 mM. Assuming a maximum solubility of 100 mM, solution α could be adjusted so that final concentrations up to 33-fold greater could be achieved.

Once the solutions are made and ready for application, great care has to be taken about the way they are added to the culture medium. It is critical that all cells experience the correct working concentration at the same time without subjecting them to excessive mechanical stress that would be reflected in an artifactual distortion of the electrical activity. It is advisable to aspirate a certain amount of medium (usually about 0.5 – 1 ml) from the culture chamber using a small syringe, add solution β into the syringe using a microliter-pipette, shake it until mixed well and then dispense it back into the culture chamber. Pulling some medium out and pushing it back in 2-3 times facilitates the mixing process. As mentioned earlier, there has to be a balance between the thoroughness of mixing and the care taken not to stress the cells mechanically. Not all cultures react the same way to a mechanical stimulus. If a short-term upward or downward spike in activity is observed immediately after the addition of a compound, it should be ignored in the analysis of the data.

2.5.8.2 Interpretation of experimental data

The electrode spots detect APs from both axons, somas, and dendrites. For convenience, a neuronal cell part is referred to as a unit. The number of units recorded from depends on the cell density, the grade of interconnectedness, the percentage of healthy, active cells in the population, and the quality of the MMEP. Every recorded AP that is recognized as a valid waveshape assigned by the experimenter or the software is accounted for as a single event by the data acquisition software. For convenient visualization of the activity, a histogram of the average number of APs per time period of the recording can be plotted in real time using either Neuroexplorer (Nex Technologies, USA), or CNNS custom designed program VernAC (based on Labview, National Instruments, USA). For practical reasons, the time base for each data point of the histogram is usually chosen to be one minute. Before each drug addition, a reference activity plateau with a minimal slope has to be achieved. This slope refers to fluctuations in the 10 – 30 minutes range. Short-term fluctuations from one minute to the next often cannot be avoided since they are due to intrinsic properties of the neuronal network or the culture medium. They usually result from the complex mechanisms governing the spontaneous neuronal activity. Without any external input, e. g. from sensory neurons, the neuronal networks are in an idle state of activity. This means that the cells are trying to keep the amount of APs produced as low as possible in order to save energy, while being forced to expend enough energy to keep the synaptic connections that make up the structure of the network from degenerating.

Certain pacemaker cells that are the primary source of excitatory input are present in every network, but their influence depends on the degree of their interconnectedness with the other cells in the network. This is particularly obvious in frontal cortex networks, which always express a highly coordinated activity structure: Either all the cells in the network fire simultaneously in a short sequence (burst) of APs, or they are silent, except for the pacemaker cell(s) which often fire tonically, providing a stimulatory input to the cells they are connected with. Since the activity is quantized in this case, fluctuations in the time periods between activity bursts are reflected in relatively big fluctuations in the activity histograms, especially if the average period between two bursts is on the order of several tens of seconds. Other tissue types display different spontaneous activity structures. For example, spinal cord networks always contain several subgroups that have coordinated activity whose dynamics vary from one group of neurons to the next. Midbrain cultures display spontaneous activity with a high degree of apparent randomness with embedded waves or bursts of coordinated firing of all or some of the neurons. All of these different activity dynamics are due to the distribution and expression of the different types of excitatory and inhibitory receptors in the different types of neurons, and on the developmental stage of the networks. Activity generated by midbrain or spinal cord tissue usually does not display such large minute-by- minute deviations, so that the zero-slope reference activity plateau might be reached earlier than in cortical cultures. Once the plateau has been stable for at least 15 minutes, the first dose should be added. For a proper dose-response curve, another stable activity plateau for each drug concentration is required. The time required to reach the next plateau can vary significantly from substance to substance and depends highly on the chemical kinetics of both the binding reaction to the cellular structure it affects, and on the speed of the intracellular signaling cascade that ultimately modulates the firing rate. Substances that affect the membrane potential or that block sodium or potassium channels directly certainly have a more immediate effect on the activity than those that interact with the cell through more complex mechanisms. After the endpoint of a substance titration has been reached, one usually attempts to determine whether the effects observed are reversible by exchanging the culture medium with a fresh compound-free solution. Depending on the binding affinity of the substance under investigation, this procedure may have to be repeated several times.

When quantifying changes in network activity, it is crucial to investigate the single units that the network consists of first. The activity rates are never the same for every neuron in one network. In fact, they can vary by as much as several orders of magnitude, especially between pacemaker cells and “normal” neurons. The most convenient and quickest way of determining a measure for the network activity is of course calculating the average of the firing rates of all the cells in the network. However, this approach does not treat every member of the network equally, but gives more weight to those units with higher firing rates than the rest. It also ignores the fact that the activity rates of the network population usually follow a bell-shaped distribution. In many pharmacological experiments, the response of the whole network is the significant, dependent variable. Therefore, every member of the network should be treated equally. In addition, since a dose-response curve consists of single values for each data point, one single value that represents the network activity has to be determined for every drug concentration that is evaluated. Analysis of the activity distribution across all recorded units shows that in most cases this distribution is approximately normal during the initial reference period, and then becomes skewed

after the addition of a compound. In a perfectly normal distribution, the mean equals the median, whereas this is not the case in a skewed distribution: Here, the average still represents the value that would be needed to achieve the same sum if all the values were the same, but the median is a more robust indicator of the value that is surrounded by the majority of the data points. It also ignores the values of outliers which can affect the mean significantly. Hence, the median is a more accurate and reliable indicator of the behavior of the majority in the network.

2.5.8.3 Analysis approaches: Overview

In order to fully grasp the complexity of the data analysis procedure preceding the generation of a meaningful dose-response curve, one must consider the different ways in which the data can be analyzed. Fig. 2.48 summarizes all possible approaches that can lead to a dose-response curve derived from recordings from several different networks. The input variables ("raw data") are the numbers of spikes binned in one-minute steps from all individual units. The first decision that needs to be made is whether every unit's spikes/min values are to be normalized with respect to their respective average values during the initial reference period of the recording. If so, every unit's values will have the same weight on the overall network behavior that is calculated during the next steps. If not, either the median or the mean values for each minute are calculated directly, thereby yielding a single network activity value for each minute in the first step of the analysis procedure. Subsequently, one value for each titration step's activity plateau must be calculated, either using the median or the mean of these values. In order to combine the values from several recordings in one dose-response curve, a normalization of the values with respect to the reference network activity must be performed, either before or after the calculation of the plateau values. Finally, the activity values from the different recordings must be combined, which, again, can be accomplished by either calculating the mean or the median of these values. If a unit-wise normalization is performed in the first step, it is advisable to continue with the median as the network activity value. Normalizing every unit's activity means that the absolute spikes/min values are transformed into values reflecting only the change in activity with respect to each unit's own native reference activity. If, for example, the average activity rate in a network (without normalization) is 300 spikes/min, but there is one unit that changes from 20 spikes/min in its reference state to 600 spikes/min in an excited state, e. g. after the addition of a disinhibitory substance, this change will not be considerably apparent when calculating a network activity value before normalizing, whereas it will be immediately visible within the normalized data with a jump from 100% to 3000% activity rate. Therefore, it is advisable to use the median of the distribution and not the mean, since outliers will always have a considerable influence on the mean, but far less so on the median.

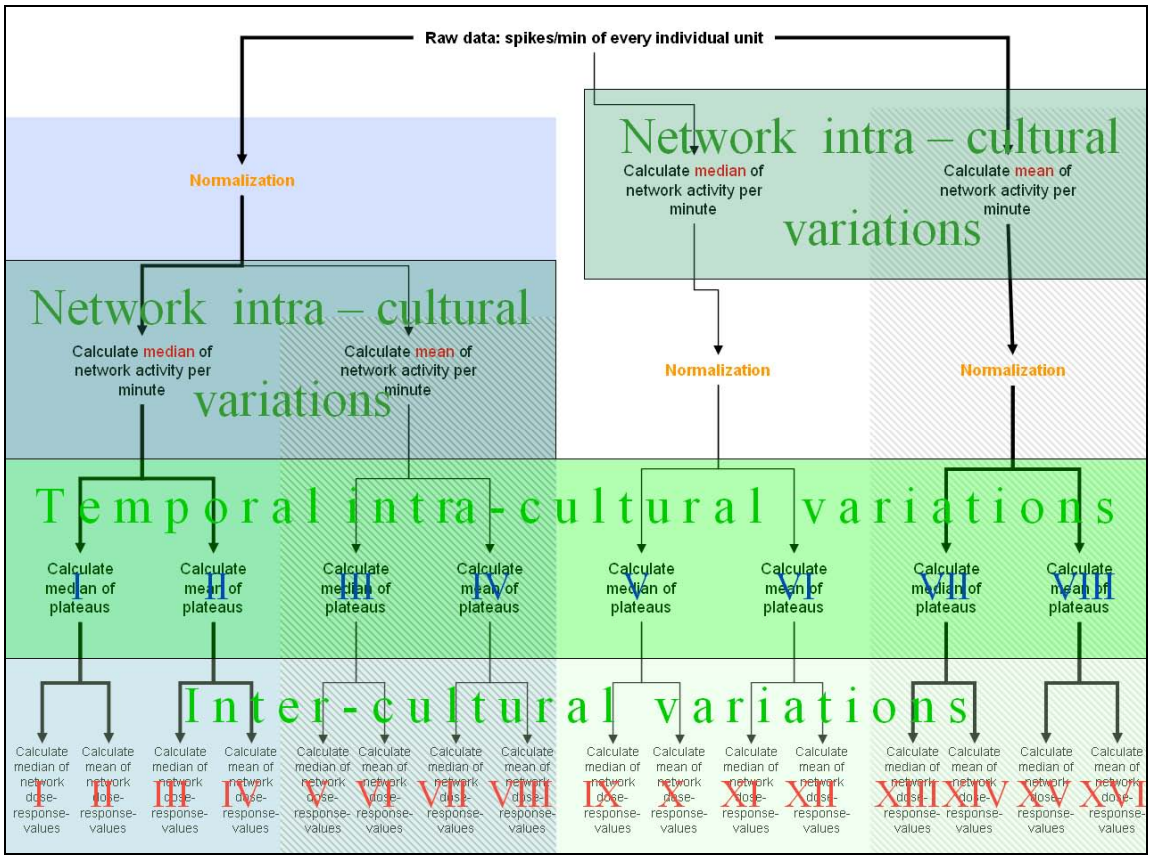

Fig. 2.48: Theoretical number of different ways to analyze MEA-derived network activity data

Chapter Three: Electrical and magnetic manipulation of tumor cell growth

3.1 Electrical stimulation

3.1.1 Glass chips with deinsulated stimulation electrodes

3.1.1.1 Retardation of cell proliferation

After the L929 cell cultures were treated in accordance with the procedures described in chapter 2.2, they were counted at the respective points in time. A comparison between the treated and untreated cells reveals a reduction in the number of cells by 29% after being treated between 48 and 70 hours after seeding, 33% after treatment from hour 72 until 93, and 51% after the first round of treatment plus an additional 24 hour incubation period (Fig. 3.1). The three groups of treated and untreated data points were evaluated for statistically significant divergence using a one-way ANOVA with a multiple post-test (Sidak-Holm test). For both analysis times, hour 71 and 95, the treated groups differed significantly from the control. These results indicate that the treatment using electrical stimuli delivered through deinsulated platinum electrodes did significantly reduce the number of cells compared with the controls, and therefore the growth rate of L929 cells.

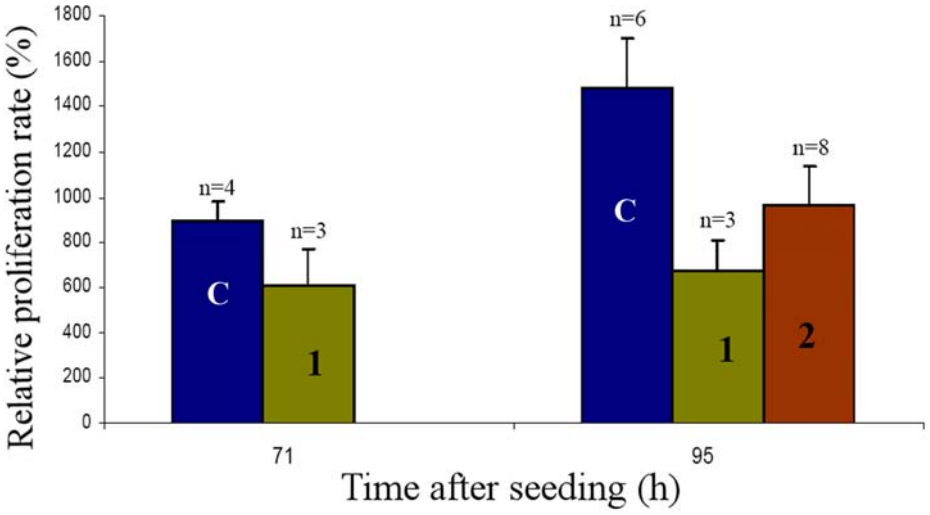

Fig. 3.1: Electrical growth retardation: C: control groups, 1: treated between hour 48 and 70, then either counted at hour 71, or incubated for an additional 24 hours. 2: Treated from hour 73 until 94, then counted.

In order to determine whether drastic cytoskeletal changes induced by the electrical pulses may account for the growth retardation, cells from both the treatment and control groups were photographed at every significant point in time during the experimental procedure (fig. 3.2) No obvious morphological differences between the control groups and the treated groups were recognized. The black structures in the pictures are parts of a platinum Clark-electrode (sensor for dissolved oxygen) that was located on each chip.

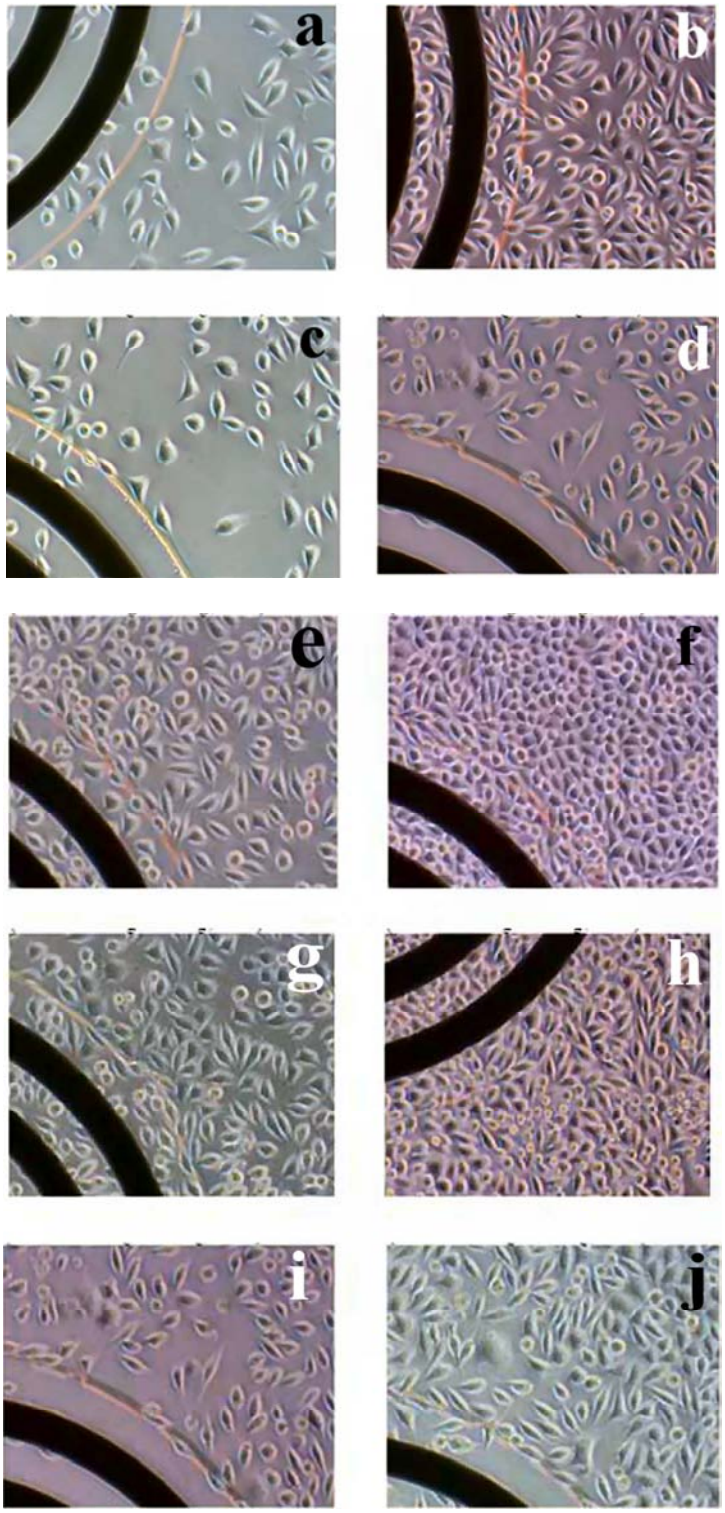

Fig. 3.2: L929 cells: a) control, 48 h; b) control, 70 h; c) before treatment 1, 48 h; d) the same culture after treatment, 70 h; e) control, 70 h; f) control, 94 h; g) before treatment 2, 70 h; h) after treatment 2, 94 h; i) after treatment 1, 70 h; j) after treatment 1 and 24 hours of additional incubation. Magnification: 200 x

3.1.1.2 Quantification of dead cells

It is critical to show whether the reduced cell count was due to a highly aggressive process that actually killed a portion of the cells, or whether the proliferation was slowed down through a more complex mechanism that is based on the alteration of the membrane potential. If a large percentage of dead cells were detected in the treated groups, one might suspect that excessive thermal energy or toxic byproducts of the electrochemical processes were released at the electrodes. Both scenarios would pose serious problems if a therapeutic device based on the technology presented here were to be used as an implant. Hence, we show in figure 3.3a that the number of dead cells in the supernatant alone was either lower (treatment 1) or insignificantly higher (treatment 2) than in the control cultures. 3.3b demonstrates that when combining the counts from both the supernatant and the cell culture layer, the percentage of dead cells does not differ significantly between the treated and untreated groups. Dead cells were identified using Trypan blue staining technique. These results indicate that cells were not mortified directly by the application of the electrical pulses applied in the experiments.

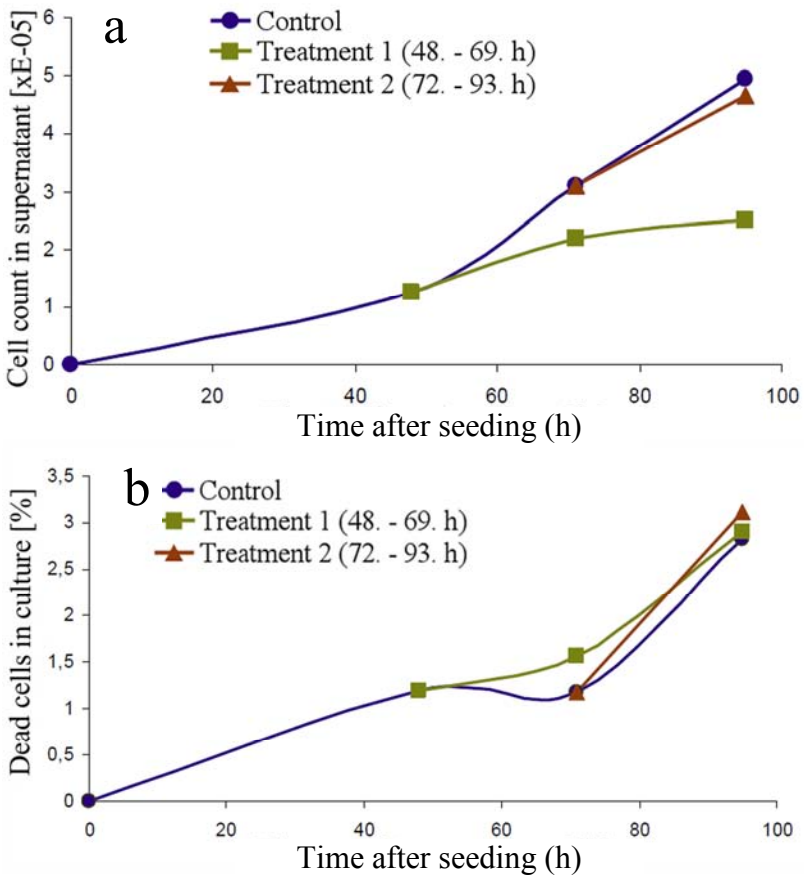

Fig. 3.3: a) Number of dead cells in the supernatant before and after treatments and in control cultures; b) Percentage of dead cells in the supernatant and culture layer combined

3.1.1.3 Temperature control recording

Since the electrical voltage pulses are applied to an electrolytic solution, there will be certain currents flowing through that solution, a process that releases thermal energy. Whether this thermal effect is large enough to cause damage to the cells and therefore contribute to the proliferation decrease is explored in fig. 3.4. It shows that in two independent control recordings during stimulation, the resistance measured from the Pt1000 sensors on the chip increased by only a few Ohm, which translates to 0.8 °K, within 21 hours. This extremely slow temperature increase cannot be held accountable for the growth retarding effects that were measured.

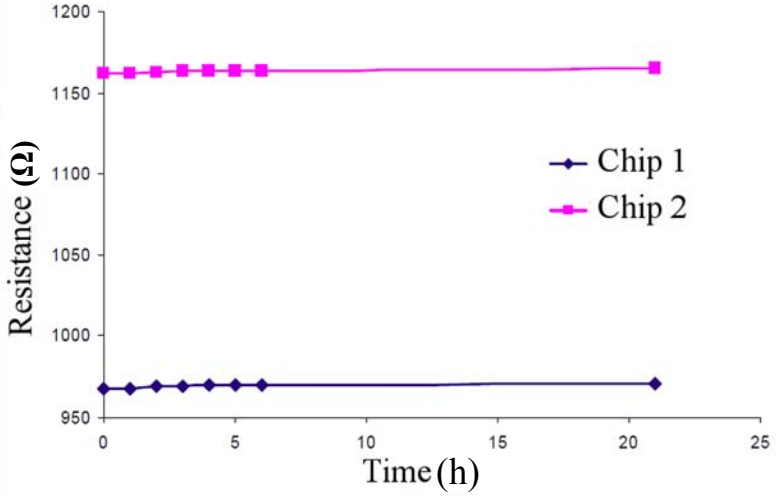

Fig. 3.4: Temperature recording using on-chip Pt1000 sensors, during stimulation over 21 hours. Pt1000 sensors were not matched in the manufacturing process and had to be individually calibrated.

3.1.2 Electrical stimulation in 6-well-plates

3.1.2.1 Effect on cell proliferation

After the proliferation rate of L929 cells had been shown to be manipulable through direct stimulation with deinsulated electrodes, the question consequently following this recognition was whether the same effect could be achievable using electrodes that are galvanically separated from the cells and the culture medium. This approach, relying on purely capacitive coupling of the electric field with the cells, would have big implications for possible new cancer treatment approaches, since it would circumvent the electrochemical complications mentioned earlier. Therefore, a stimulation device was used that was designed to apply electric fields to cells grown in 6-well culture plates of industrial standard dimensions. The 6-well plates offer three main advantages over the glass chips: Their surface is pre-treated and does not need any hydrophilization or coating with adhesion proteins. There is no need for cleaning, since it is a disposable product, and the area the cells can grow on inside each well is 20 times larger than the area on the glass chips. A higher number of cells for the treatment and control groups generally results in lower standard error values.

Based on recreating the same electric field strengths that were generated on the glass chips, the voltages applied to the stimulation board were 9, 24, 60 and 90 V, according to the simulations shown above. The greater availability of 6-well plates and the fact that the seeding cell density could be lowered because of the larger area enabled us to extend the total period of one experiment to 117 h. That way, half of the cultures that underwent the second treatment could be incubated for an additional 24 hours, just like the ones from treatment 1. Figure 3.5 summarizes the measurements in terms of proliferation rates: The results from the 9 V stimulation are shown in a), the 24 V ones in b), 60 V in c), and 90 V in d). None of the stimulations were as effective as the ones performed using the glass chips. All the data groups were positively tested for normal distribution. Subsequently, a one-way ANOVA revealed that none of the differences measured between the control groups and the respective treatment groups were statistically significant.

The geometries of the electric fields simulated in figs. 2.6 and 2.10 showed that the percentage of cells experiencing a high degree of spatial field gradient were much larger for the cultures grown on the glass chips than in the 6-well plates. Therefore, a new design incorporating IDES structures was implemented in the second version of the stimulation plate. Since no effects had been observed using the standard plate even at stimulation voltages as high as 90 V, this voltage was the first one to be evaluated on the IDES plate, both with 3 mm and 1 mm structures. However, fig. 3.6 confirms that even at 90 V stimulation voltage, both types of IDES structures did not improve the effectiveness of the stimulation. In fact, a spatial gradient of the geometries used here can be ruled out to modulate the proliferation rate of L929 cells.

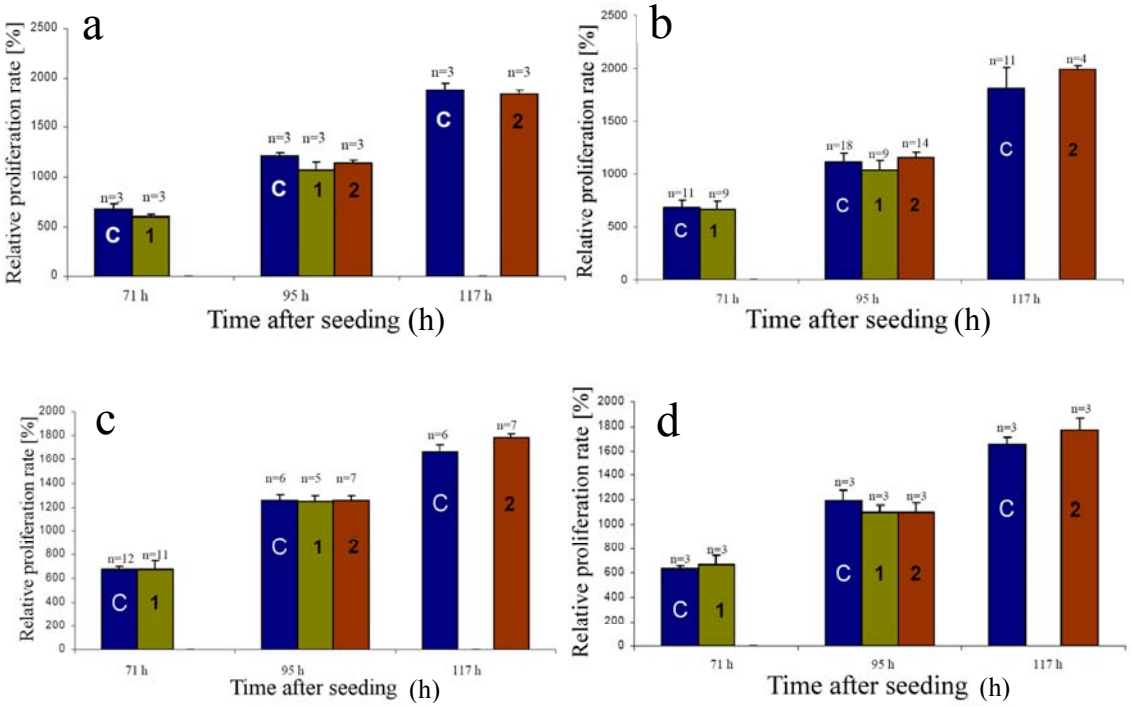

Fig. 3.5: Proliferation rates after electrical stimulation on 6-well plates. Stimulation field strengths: a) 150-300 V/m, b) 400-800 V/m, c) 1-2 kV/m, d) 1.5-3 kV/m.

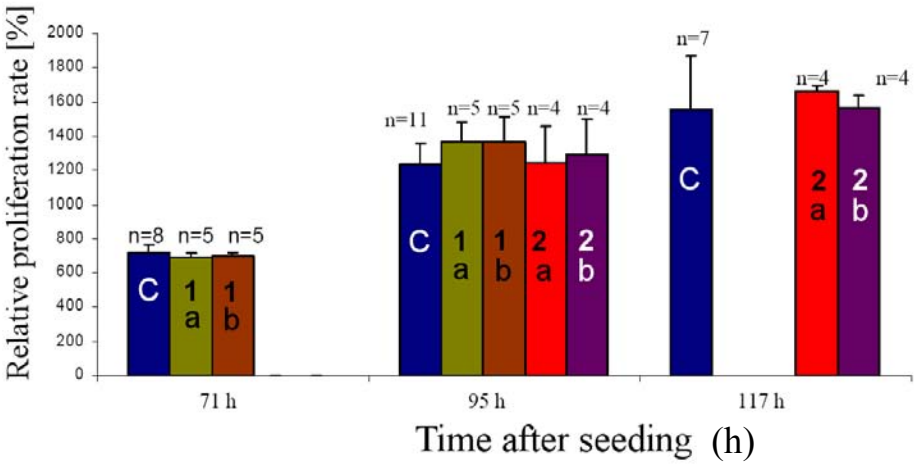

Fig. 3.6: Proliferation rates with IDES electrical stimulation: a) IDES 1 mm pitch, b) IDES 3 mm pitch, C: control cultures

3.1.2.2 Cell morphology

In order to rule out any major effects on the cell morphology, pictures of the cells were taken before and after each experiment. Fig. 3.7 shows a selection of these micrographs: a) control culture at 48 hours after seeding; b) control 70 h after seeding; c) culture before treatment 1 at 48 h; d) the same culture after treatment 1, at 70 h after seeding; e) control culture at 70h; f) control at 94 h; g) culture before treatment 2 at 70 h; h) the same culture after treatment 2 at 94 h; i) culture after treatment 1, 70 h; j) the same culture after an additional 24 h incubation time; k) culture after treatment 2; l) the same culture after an additional 24 hours in the incubator.

Figure 3.7 provides phase-contrast micrographs of the L929 cell monolayers at the specific analysis time points mentioned above. We could not recognize any major differences between the control cells and the respective treatment groups at the same time. The only obvious observation is the relatively high density of phase-bright cells in the culture shown in j), which might indicate a higher density of cells undergoing mitosis at that particular point in time.

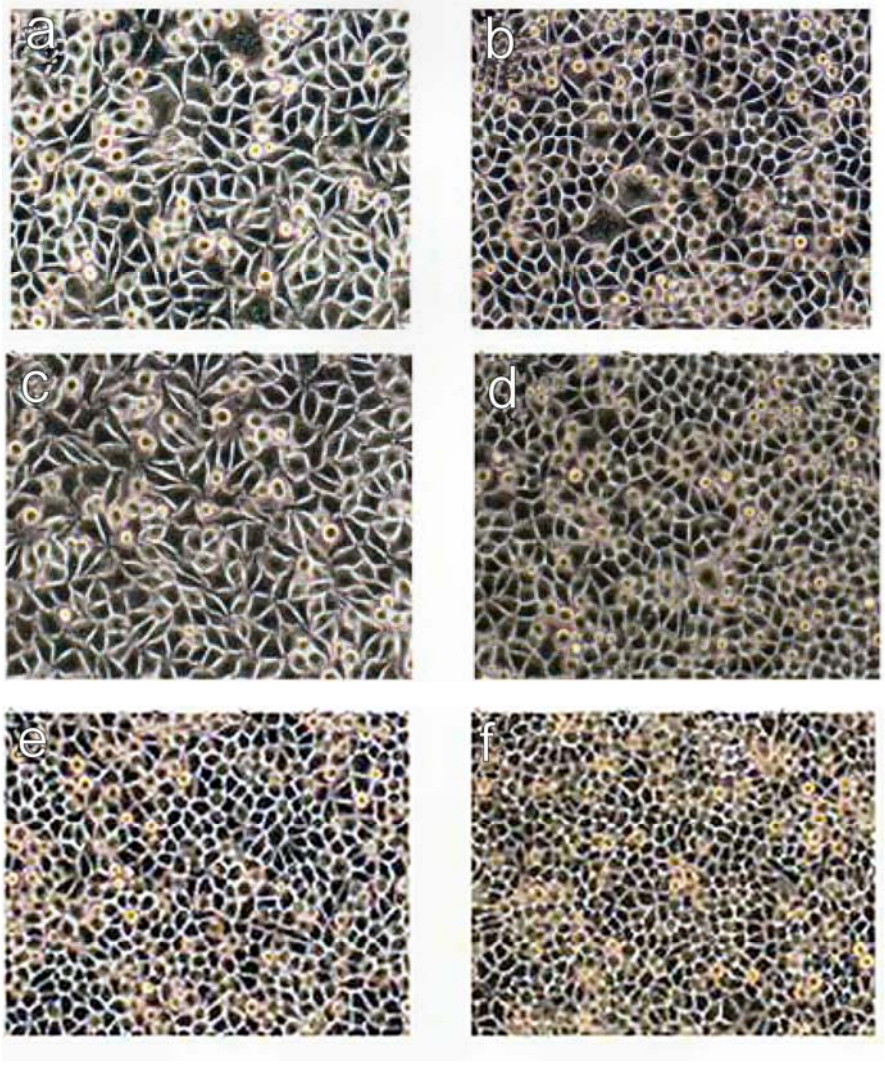

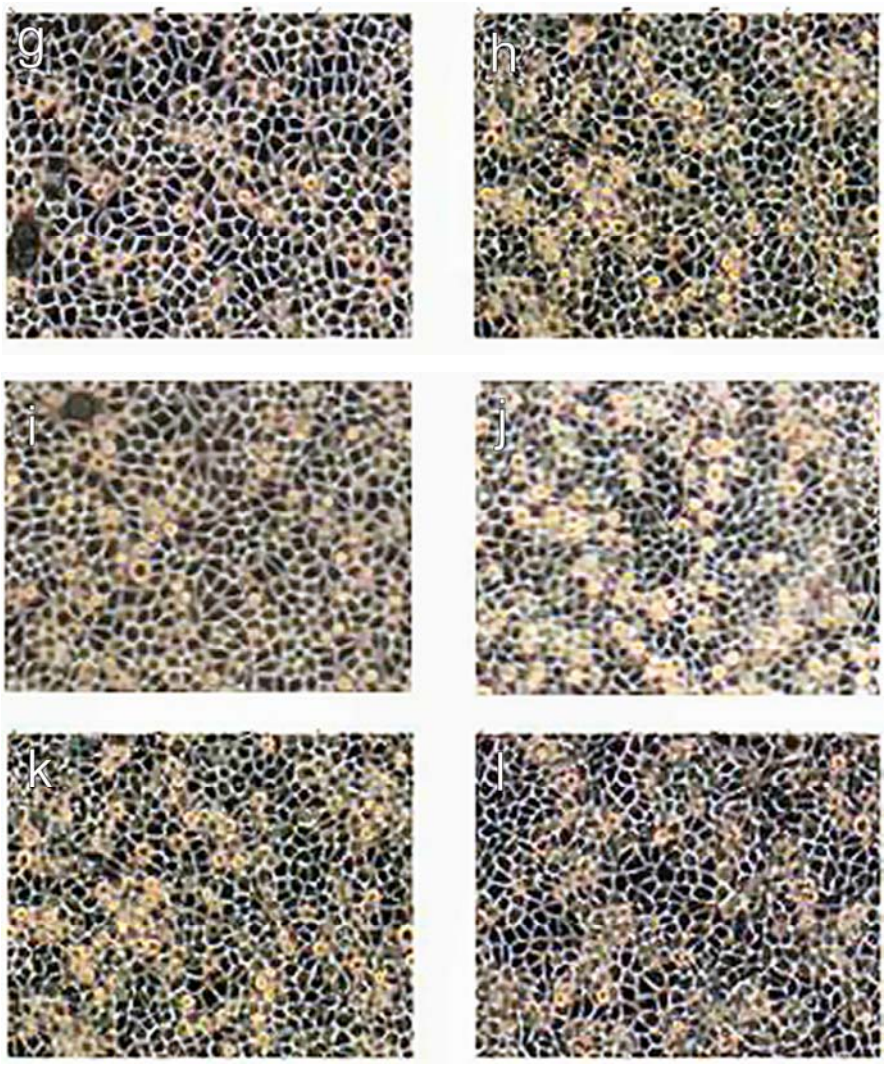

Fig. 3.7: Treated and untreated cells grown on 6-well plates. Magnification: 200 x. a) control culture at 48 hours after seeding; b) control 70 h after seeding; c) culture before treatment 1 at 48 h; d) the same culture after treatment 1, at 70 h after seeding; e) control culture at 70h; f) control at 94 h; g) culture before treatment 2 at 70; h) the same culture after treatment 2 at 94 h; i) culture after treatment 1, 70 h; j) the same culture after an additional 24 h incubation time; k) culture after treatment 2; l) the same culture after an additional 24 hours in the incubator.

3.2 Magnetic stimulation

Imposing a circular, transient magnetic field onto an electrolytic solution creates eddy currents inside that solution, which, in this case, is the culture medium surrounding and containing the L929 cells. The result of this inductive coupling of electrical energy, in terms of current applied, is more similar to what was achieved using the deinsulated electrodes on the glass chips than the stimulation board and the 6-well plates, as the calculations have shown. Since the electrical field alone was shown not to be able to slow down the cell proliferation, both with and without a gradient geometry, one might suspect that the application of a certain current strength is required. Therefore, the effects resulting from magnetic stimulation are expected to be higher than the ones from the capacitive electrical stimulation. Fig. 3.8 supports this hypothesis by showing that treated cultures had 30 ±9 (SD) % (n = 4, control cultures: n = 8) less cells than the control cultures after applying the magnetic pulses between the 48th and 67th hour after seeding. Treatment between hour 72 and 91 after seeding had an even stronger effect with 49 ±18.6 % (n = 3, controls: n = 6) reduction in cell number. In addition to the control cultures that were kept under the same conditions as the stimulated cultures during each experiment, sham stimulations with the lowest possible stimulator setting of ca. 5 % of the maximum field strength (regular stimulations were carried out at 65 % of the maximum field strength) are also shown in figure 3.8 (black bars). These were repeated twice with two control cultures each and showed no significant differences over the controls (3.6 ±4.8 %; 1.7 ±14 %).

The morphological analysis in figure 3.9 indicates that no obvious changes in cell shape were caused by the magnetic stimuli: a) control at 48 h after seeding; b) control 70 hours after seeding; c) before treatment, 48 h; d) the same culture after treatment, 70 h; e) control at 70 h; f) control, 94 h; g) culture prior to treatment, 70 h; h) the same culture after treatment, 94 h.

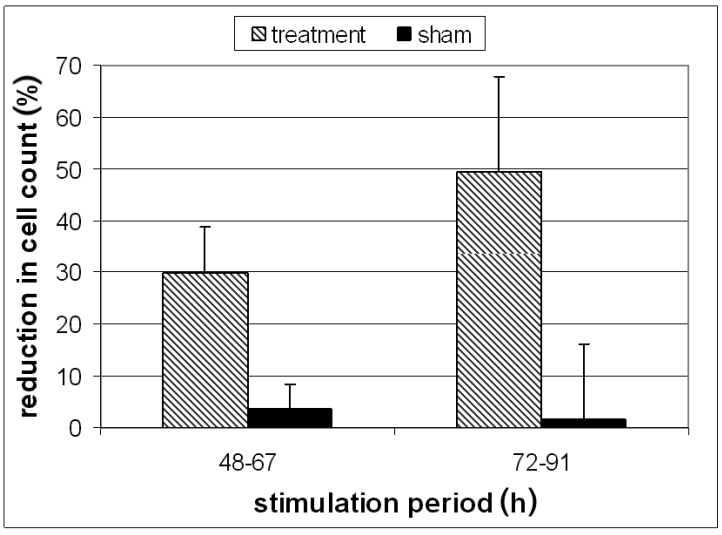

Fig. 3.8: Cell count reduction in comparison with the respective control cultures. Error bars: standard deviation

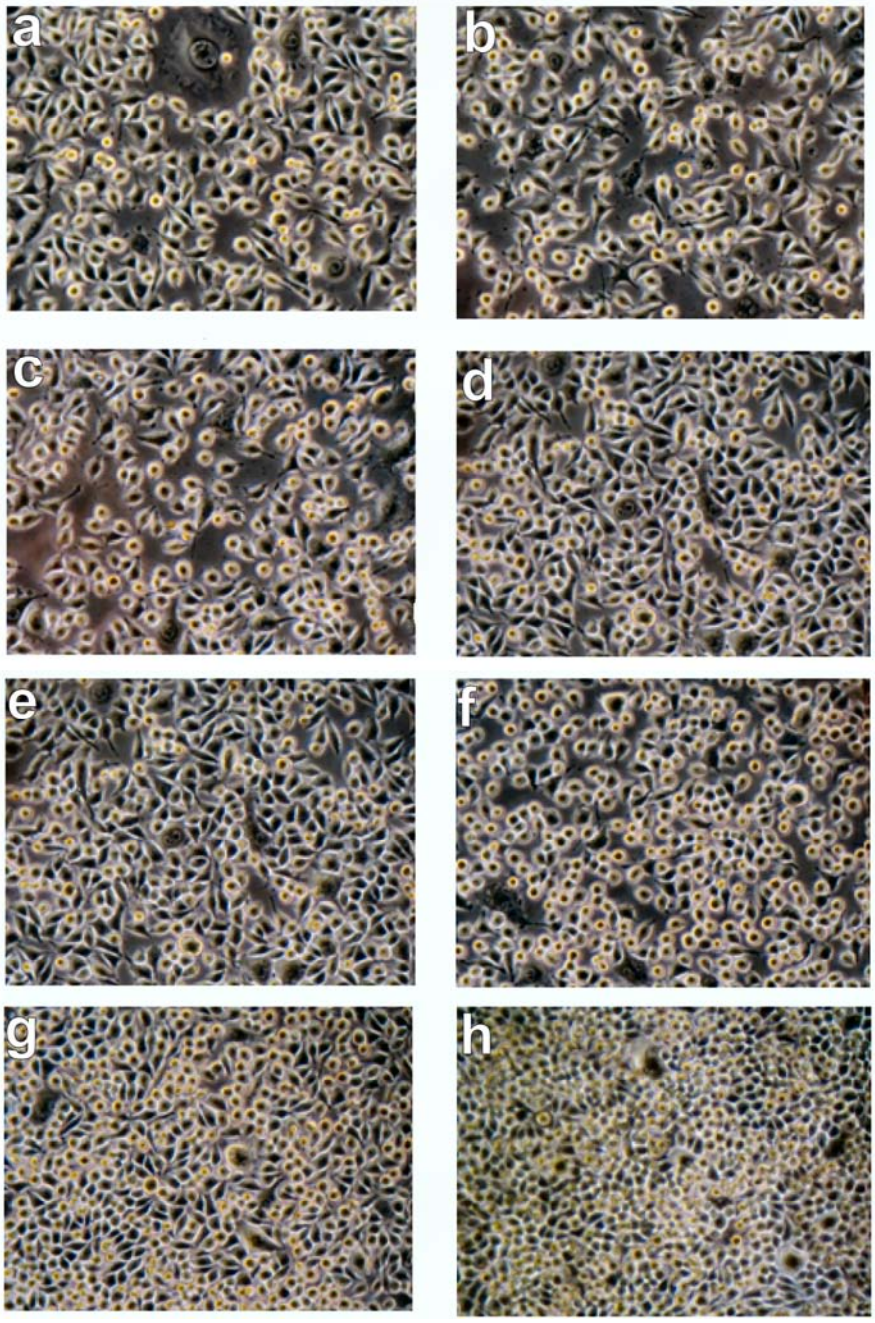

Fig. 3.9: Cell morphology prior to and after magnetic stimulation experiments. Magnification: 200 x.

Chapter Four: Neuronal network experiments and data interpretation

4.1 Recordings

4.1.1 Midbrain recordings

4.1.1.1 Characterizing typical midbrain activity patterns

To date, most pharmacological and toxicological studies using primary neuronal cell cultures on MEAs have used cortical or spinal tissue. The midbrain is an extremely old structure in terms of mammalian evolution and contains the superior and inferior colliculi (visual and auditory pathways), the cranial nerve nuclei, the reticular system, the red nucleus, and the substantia nigra, which is primarily associated with motivation and motor control. The substantia nigra is the region of the brain that accommodates the highest density of dopaminergic neurons in the brain and is implicated in neurodegenerative ailments, such as Parkinson's disease. The evaluation of potentially neurotoxic substances on this area and the comparison with recordings from other parts of the brain is therefore of great interest.

The following figure exemplifies the correlation of a healthy, low-density midbrain culture and the activity characteristics recorded from it. It shows all 64 electrode recording sites (black dots, 20 µm in diameter) on a 1.25-mm^2 square.

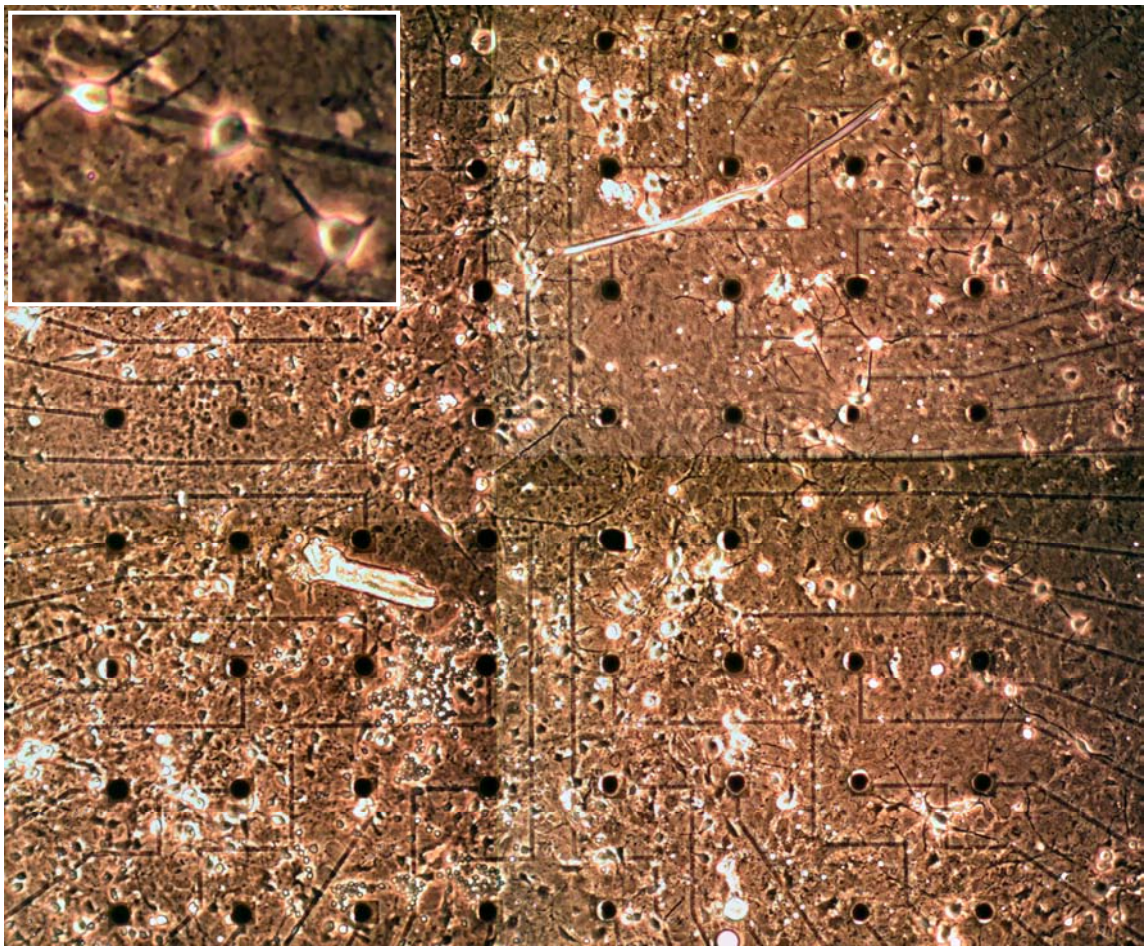

Fig. 4.1: Photo-micrograph of a living low-density midbrain culture on a multielectrode array, 44 days in vitro, magnification: 100x. Insert: Three healthy neuronal cell bodies with partially overgrown processes.

In the background, glia cells are visible that appear grey and low in contrast in the phase-contrast micrograph. The neuronal cell bodies, which are 10-15 µm in diameter, appear as the brightest structures in this picture, since they have a very strong cytoskeleton and are rather thick compared to the other cell types present in the culture.

With approximately 84 neurons on the electrode matrix area plus an undetermined number of cells outside the matrix whose processes overlap onto the matrix, 62 units (73.8 %) could be recorded from. However, only 2.6 % of the area is covered by the electrode spots. If every unit represents a distinct cell, there must be a high number of interconnections, even though the majority of them cannot be seen clearly in this photograph. This is often the case and can be explained by the interaction of the neuronal processes with the glia cells and their tendency to be overgrown by them.

A screenshot of the initial activity pattern of this particular culture (fig. 4.2) reveals a number of observations: The active cells display an even spatial distribution, according to the multichannel window in the Plexon software. The cell-electrode coupling is decent but rather irregular, which is reflected in the varying waveshape amplitudes. The tick marks in the raster display on the right side of the image represent temporal occurrences (time stamps) of single APs.

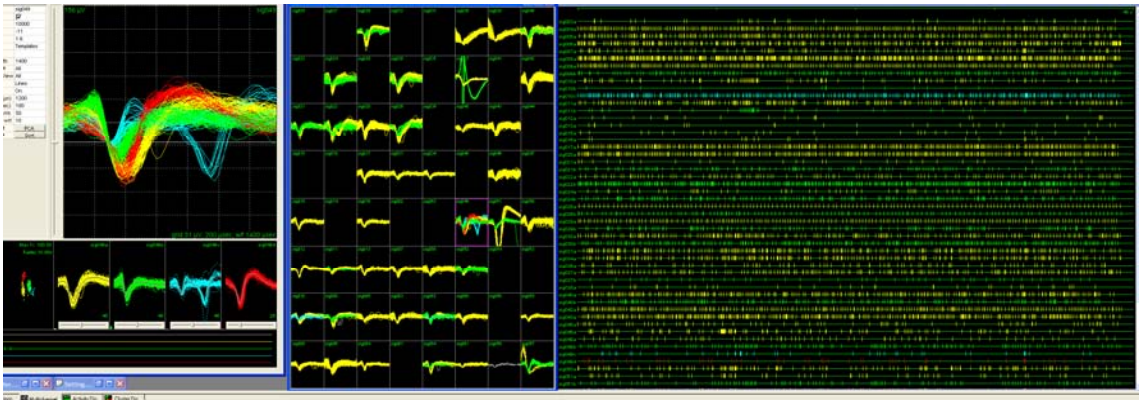

Fig. 4.2: Typical activity pattern of midbrain tissue: little obvious coordination of firing, hardly any bursts visible. 40 seconds of activity shown.

Looking at the activity from the same culture (Fig. 4.3) after addition of 10 µM barbital-sodium, the pattern has changed with groups of neurons now firing in synchrony. Wave-like fluctuations of periods with high and low activity rates with time constants of 10-15 seconds are visible. Interestingly, the amount of spikes per minute did not change significantly during this period (Fig. 4.4, black curve) despite the obvious changes in pattern dynamics. At 400 µM, the activity did decrease substantially, but the number of active units remained constant (red curve). At 650 µM, the activity level finally dropped by 50 %. This relation between the activity and the number of active units may often be an important factor when determining mechanisms and analyzing the data in depth. The amount of spikes/min is a good indicator of the overall health and functionality of the network and serves as the most important parameter when generating a dose-response curve. However, it does not describe the

changes in pattern dynamics as shown in figures 4.2 and 4.3. These effects may be subtle but nonetheless significant.

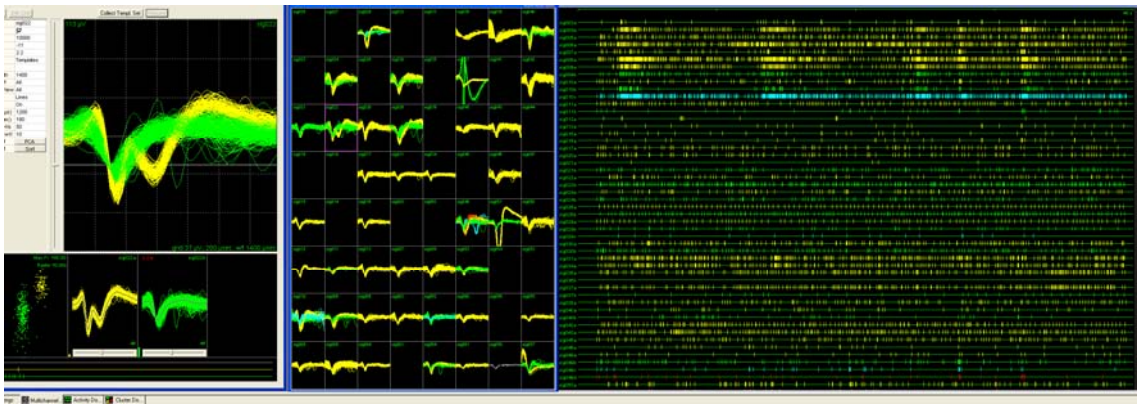

Fig. 4.3: Activity pattern of the same culture as in fig. 4.1 under the influence of 10 µM barbital-sodium.

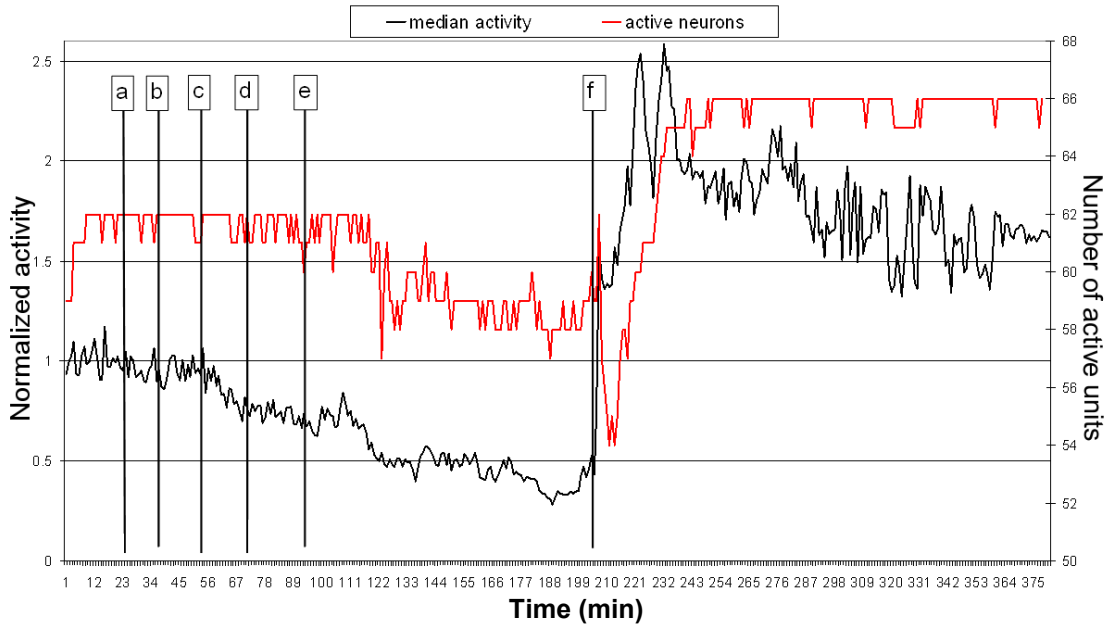

Fig. 4.4: Standardized median activity values (black curve, left y-axis) and number of active units (red curve, right axis) from the midbrain culture discussed above. Duration of recording episode: 381 minutes. Letters denote the following cumulative concentrations of barbital sodium: a: 10 µM, b: 50 µM, c: 150 µM, d: 400 µM, e: 650 µM. F: full medium change.

4.1.1.2 Analysis of unit-specific responses:

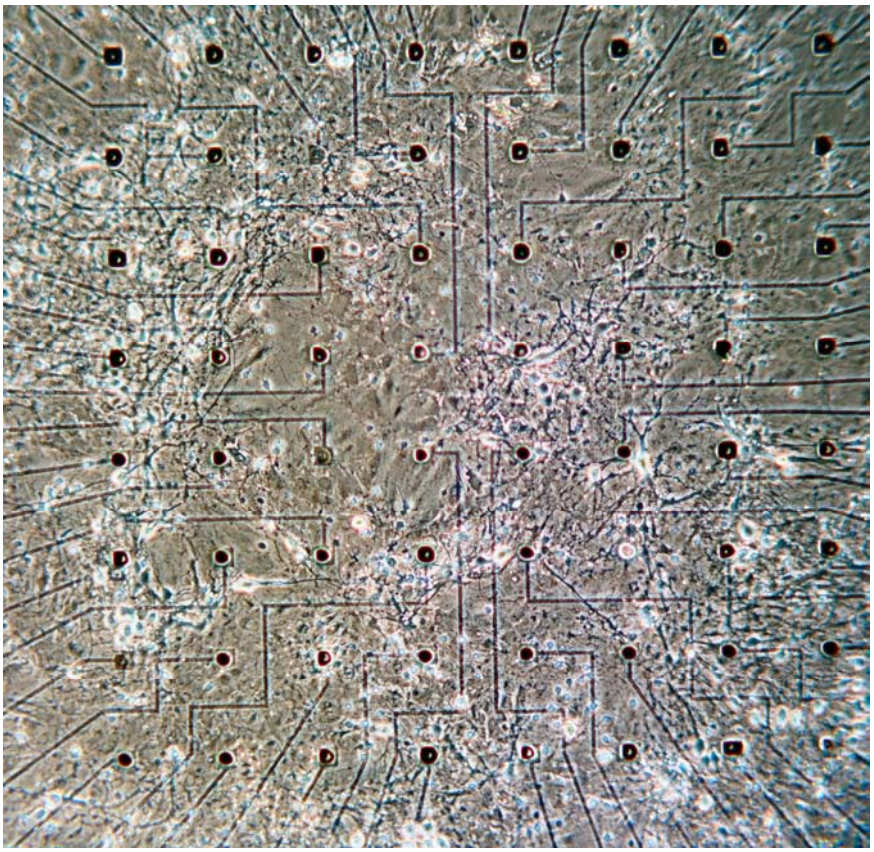

Fig. 4.5: Cultured midbrain neurons on multielectrode array (electrodes: black dots), spacing between electrodes: 125 µm, 69 cells on matrix, 45 days in vitro.

Fig. 4.6 shows an offline analysis graph, the raster plot, as generated using the program Neuroexplorer. The heterogeneous distribution of activity, generated by the cells shown in Fig. 4.5, across the units makes it impossible to visualize all the timestamps for every unit on one screen, if the time period depicted exceeds a few seconds. In this case, 410 seconds of activity are shown. Black timestamps are single events. Where the density of timestamps is too high to plot them separately, they are shown in red, and as the density becomes even higher, in yellow. This approach makes a quick assessment of the heterogeneity of the network in terms of activity possible. The program Neuroexplorer also enables the user to examine the development of the activity over the entire span of an experiment for each unit separately. Fig. 4.7 shows how this approach may be used to investigate unit-specific responses to a particular event. In this example, 200 µl of fresh medium were added 102 minutes into the recording (green bars, figure 4.7). Eleven units responded to the medium addition with a >10% increase in activity, 15 with a >10% decrease, and 13 with no significant change. In addition to the variations in the spikes/min values, one can see that the temporal evolution, or onset time, of these changes is not uniform, either. The degree of unit-specific responsiveness and the onset time dynamics constitute two more

parameters that may be used in the data analysis, particularly regarding possible interaction mechanisms of the respective compounds.

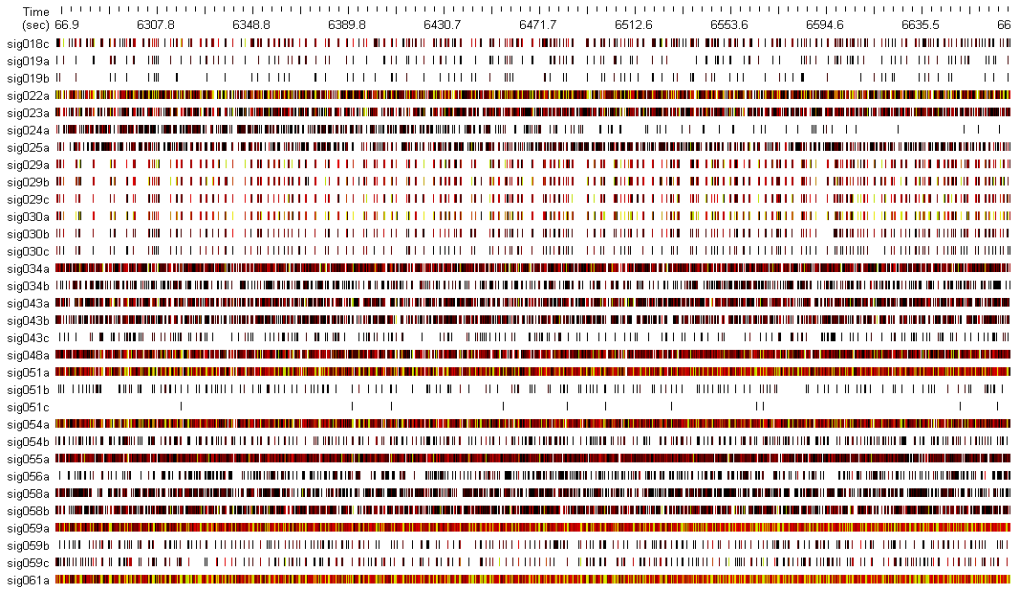

Fig. 4.6: Raster plot of spontaneous midbrain activity. Each row represents one unit.

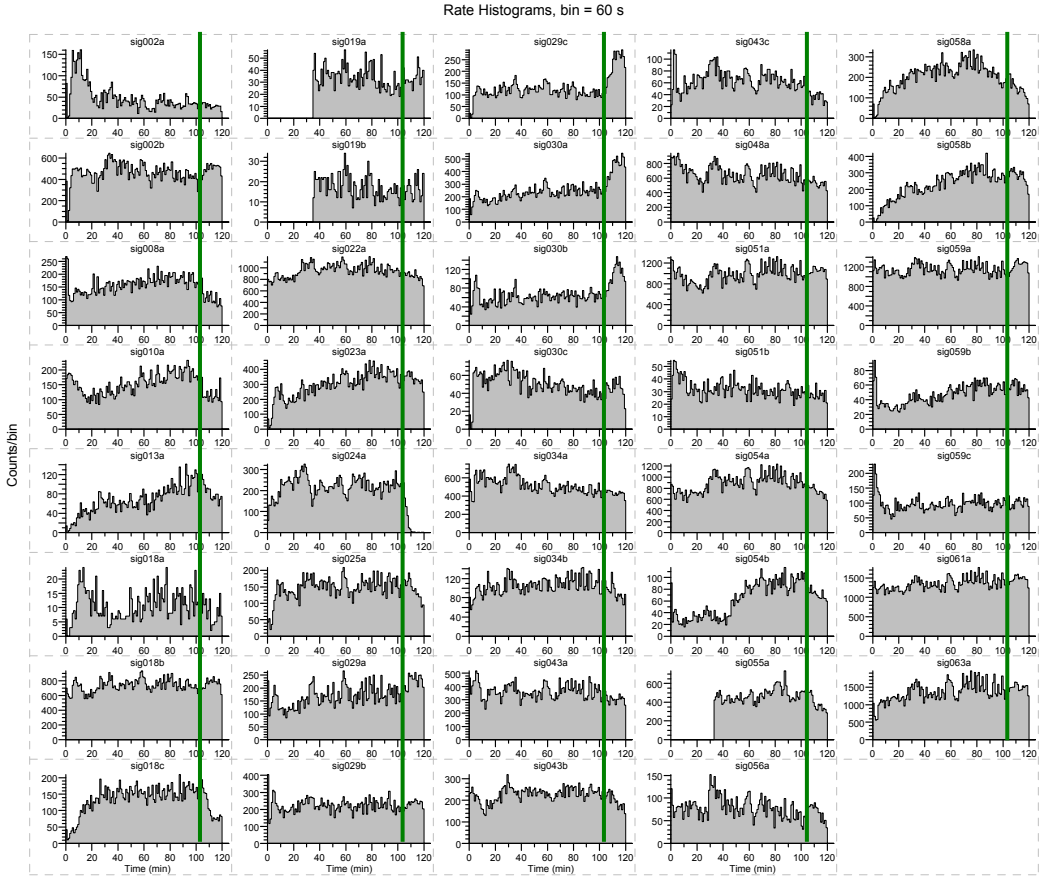

Fig. 4.7: Activity rate histograms of individual units. Time period shown: 120 minutes. Green bars: time of 200 µl medium addition.

4.1.1.3 Disinhibitory effects of bicuculline on midbrain tissue

Contrary to the relatively subtle activity pattern modulations shown in Fig. 4.3, a major transformation occurs when midbrain tissue is subjected to bicuculline. Bicuculline is an antagonist of $GABA_A$, whose influence on frontal cortex and spinal cord networks in culture has been studied. However, this is not the case for midbrain tissue. The activity pattern resulting from 20 µM bicuculline displays long, rhythmic bursts and is shown in figure 4.8. After washing the bicuculline out with two consecutive medium changes, the pattern returns to its native, apparently random state (Fig. 4.9). The culture in this example was 42 days old, and 60 units were recorded.

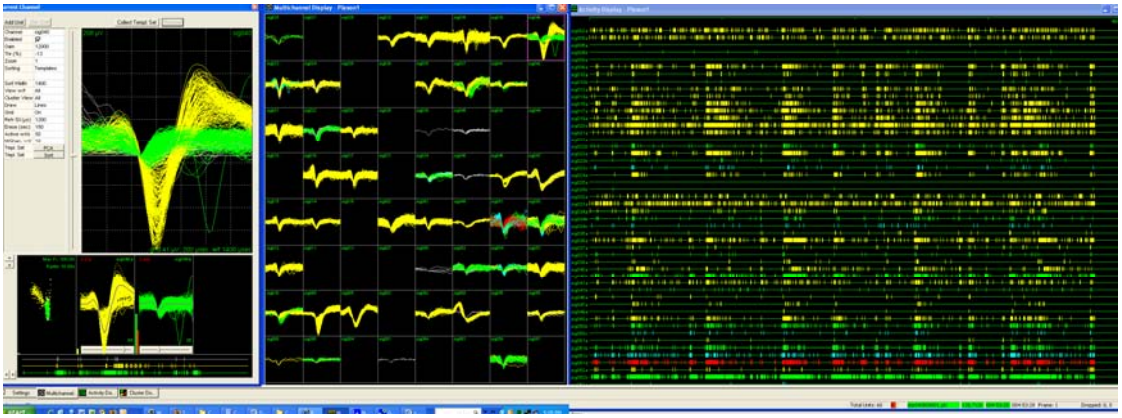

Fig. 4.8: Midbrain activity 35 minutes after the addition of 20 µM bicuculline. Time period shown in activity window: 40 seconds.

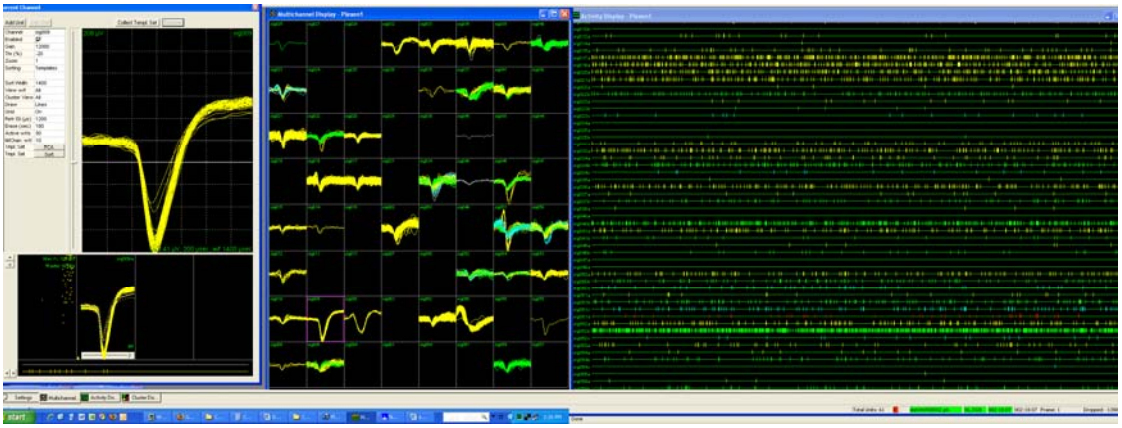

Fig. 4.9: Activity pattern and waveshapes of the same midbrain culture after wash-out of the bicuculline.

The activity response of the network to the addition of bicuculline can be analyzed in several different ways. Figure 4.10 shows the unedited spikes/min values of all the units for a period of 438 minutes with every one of the colored curves representing one unit. The activity rates range from 10 to 2,000 spikes/min during the reference activity period (minute 1-186), and from 10 to 5,000 during the time under bicuculline. After 186 minutes, bicuculline was added. For the next 36 minutes, the activity increased steadily, before leveling off at a value between the initial reference activity and the peak activity around minute 222. In Fig. 4.11, the spikes/min values

from all the units over 8 minutes (160-167) were plotted as a histogram with a bin size of 20 spikes/min. Most of the units display activity rates within two groups: 20-160 spikes/min (210 data points, or 56%) and 180-440 spikes/min (146 data points, or 39%), with a very low number of outliers around 1040 and 1320 spikes/min. The distributions among these groups are quite different, and it is obviously hard to determine a single value for the "network activity". The values deviate even more after 20 µM bicuculline were added: Fig. 4.12 shows that there are now 5 groups of neurons: 52% of the data points belong to the first group, 35% to the second one, and 9% to the third group. This makes it even more difficult to find one single value that could describe the network behavior. The curve fits in figures 4.11 and 4.12 are Lorentzian, which is a common method used to describe a distribution that is Gaussian in shape but with longer tails. The goodness-of-fit parameters R^2 are acceptable, but not excellent (0.69, 0.78, respectively). The median (blue line) and the mean (orange line) of the distributions vary by as much as 1 and 2 σ, and are located outside the peak of the fitted distribution. Therefore, they cannot be considered sufficiently accurate parameters that describe the network behavior.

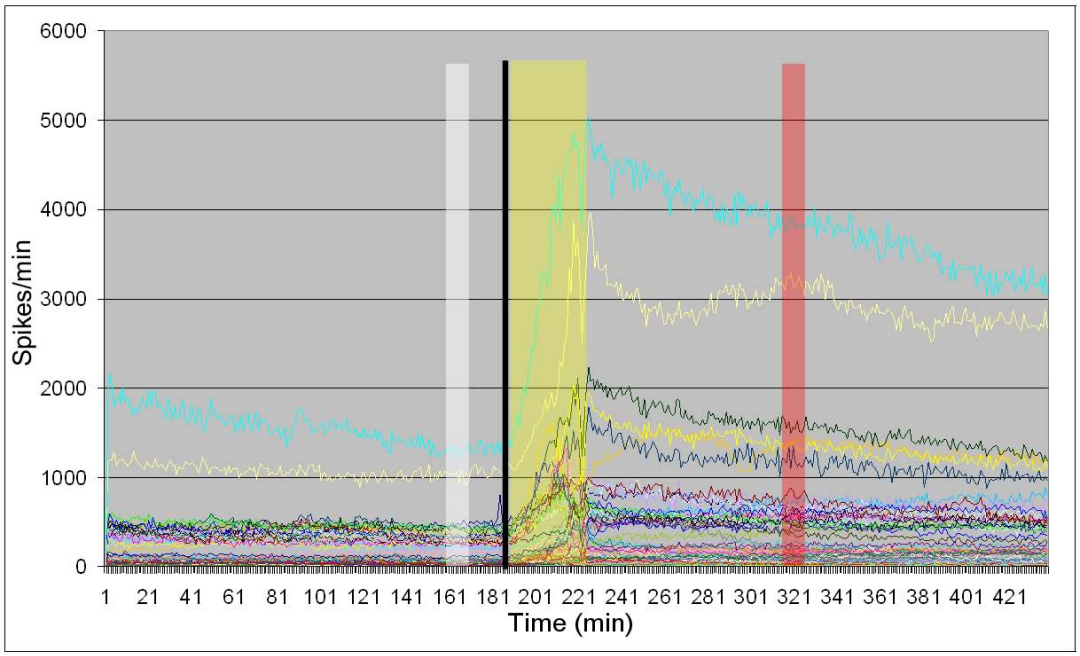

Fig. 4.10: Numbers of spikes/min (y-axis) of all the recorded units plotted as individual curves. Black bar: Addition of 20 µM bicuculline; yellow shaded area: time to maximum effect; white shaded area: reference time period for analysis in figure 4.11; red shaded area: time period for analysis in figure 4.12.

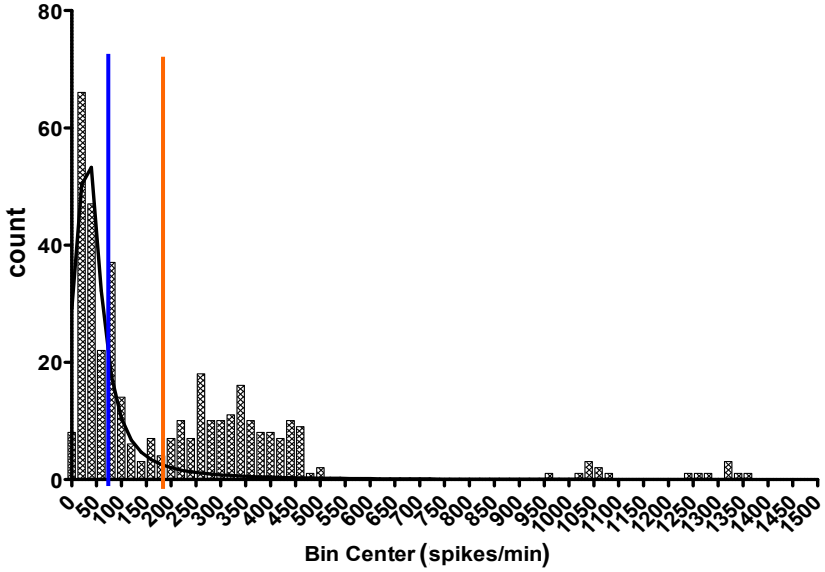

Fig. 4.11: Activity histograms of spikes/min values of all units, bin size: 20 sp/min, minutes 160-167. Blue line: median of distribution, orange line: mean of distribution. Curve fit: Lorentzian, $R^2 = 0.69$

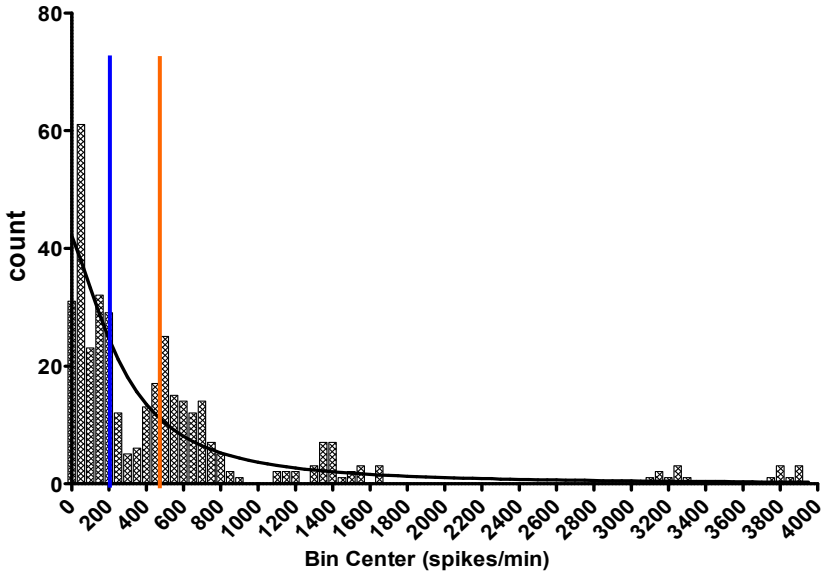

Fig. 4.12: Histograms of all recorded activity between minute 317 and 324, bin size: 50 sp/min. Blue line: median, orange line: mean; curve fit: Lorentzian, $R^2 = 0.78$

The same data can be analyzed differently by normalizing each unit's activity rate first, avoiding the automatic ranking of neurons by their absolute spike output values (figure 4.13). Here, all units were normalized by their respective average value of the first 15 minutes of activity. This way, the distribution of activity during the initial reference activity phase became more uniform (Fig. 4.14), and a single value representing the peak of the distribution, and thereby the network behavior, could be assigned. Since these distributions are hardly ever perfectly symmetrical, the median is mathematically best suited to describe where the distribution's majority of values lie. After the addition of bicuculline, the activity distribution looks neater, even though the

goodness-of-fit value of the curve fit is still not superb. However, 83% of the values are now located inside the major peak, and 14% in the second one, so that the network activity can now be reasonably well quantified with one value, the median (blue line), which is also located considerably closer to the peak of the fitted curve than the mean.

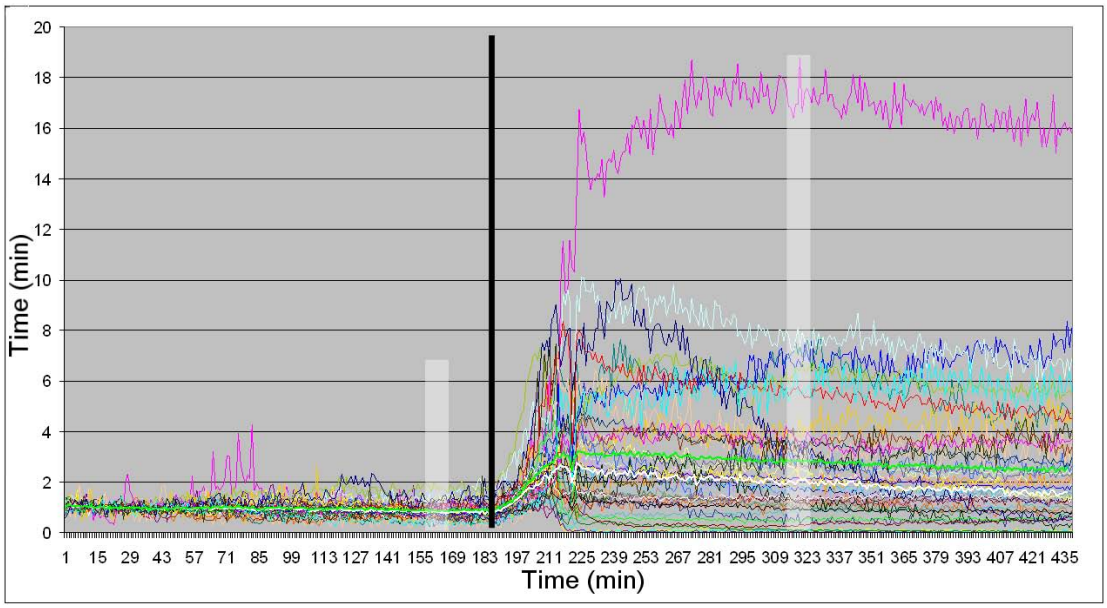

Fig. 4.13: The same data as in Fig. 4.10 after normalization with respect to the average spikes/min value of the first 10 min of the recording. Y-axis: standardized spikes/min. White shaded areas: time period data for histograms were taken from.

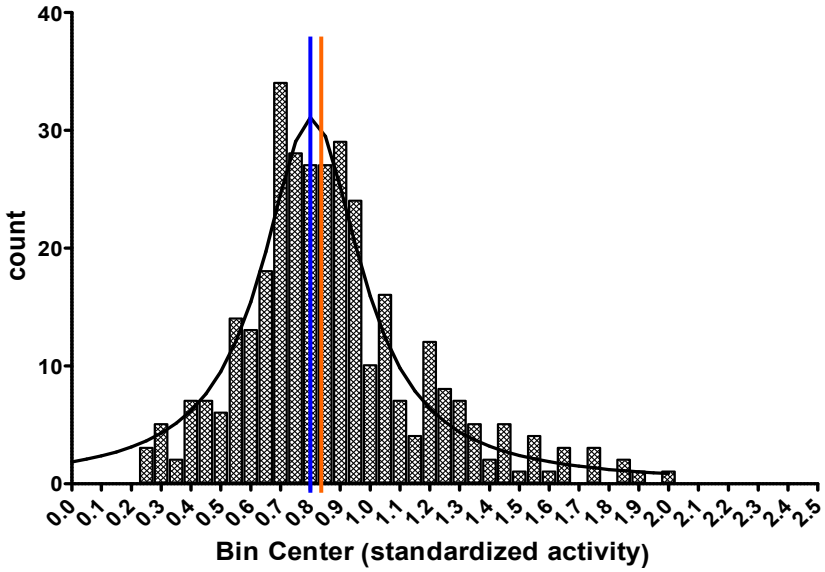

Fig. 4.14: Distribution of spikes/min during the reference activity period. Values standardized to each unit's respective initial activity levels. Bin size: 0.05. Blue line: median, orange line: mean. Curve fit: Lorentzian, $R^2 = 0.91$

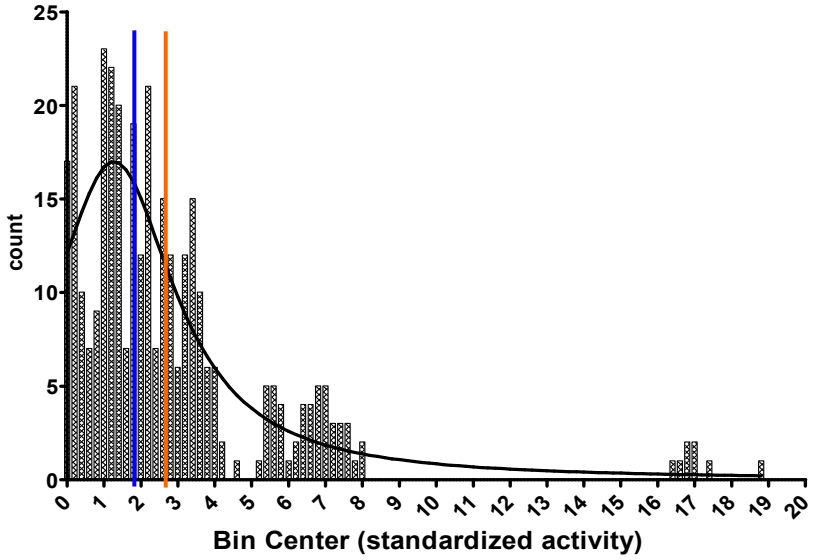

Fig. 4.15: Distribution of spikes/min values under 20 µM bicuculline. Bin size: 0.2. Blue line: median, orange line: mean. Curve fit: Lorentzian, $R^2 = 0.78$

In figure 4.16, the different analysis approaches are summarized. The white and black curves represent the median and the average of the activity values that were normalized first for each unit, respectively, while for the green (median) and light green (average) curves, the values were normalized after the median and mean were calculated from the actual spikes/min values. Depending on the type of analysis, the maximum rise in activity after the addition of 20 µM bicuculline was between 160% (average taken before normalization), and 310% (median taken before normalization). The median value taken after normalization yielded a maximum increase of 175%. The activity dynamics did not differ significantly, showing a time to maximum effect of 36 minutes.

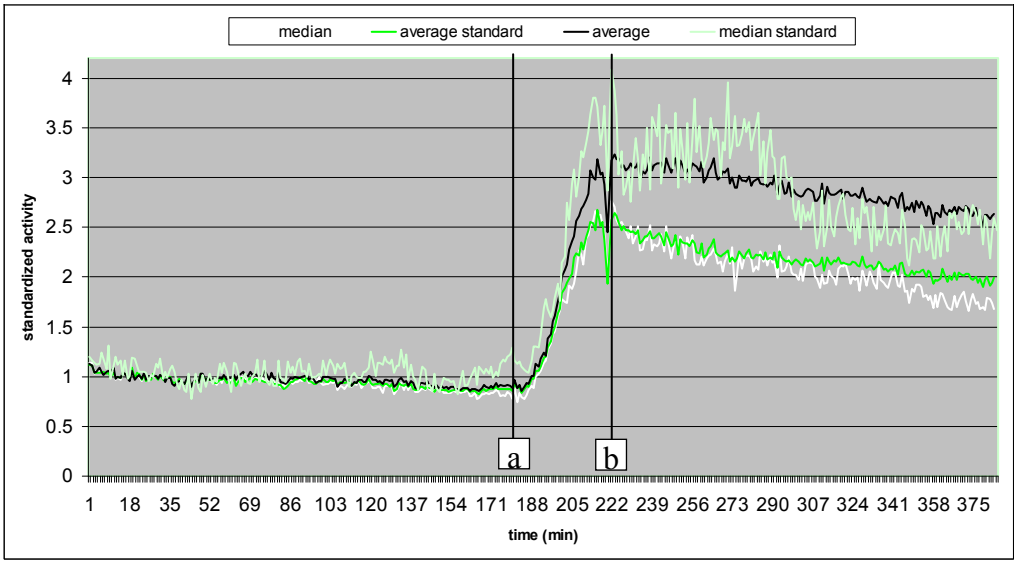

Fig. 4.16: Average (black curve) and median (white curve) spikes/min of the data with prior normalization of the individual units' activity values, and without such normalization (green, light green, respectively). A: Addition of bicuculline, b: time of maximum network response.

4.1.2 Frontal cortex networks under bicuculline

4.1.2.1 Example 1: Low number of units

In frontal cortex tissue, bicuculline has an excitatory effect on the activity as well. A major difference that was observed in comparison with midbrain cells is the short onset time of merely 1-2 minutes. In the following example, the data analysis of an experiment with a very low density culture is exemplified. First, the spikes/min values for all individual units as well as the average and the median are shown (Fig. 4.17), followed by the activity rate plot of the same data after normalization of every single individual unit with respect to their own initial reference activity.

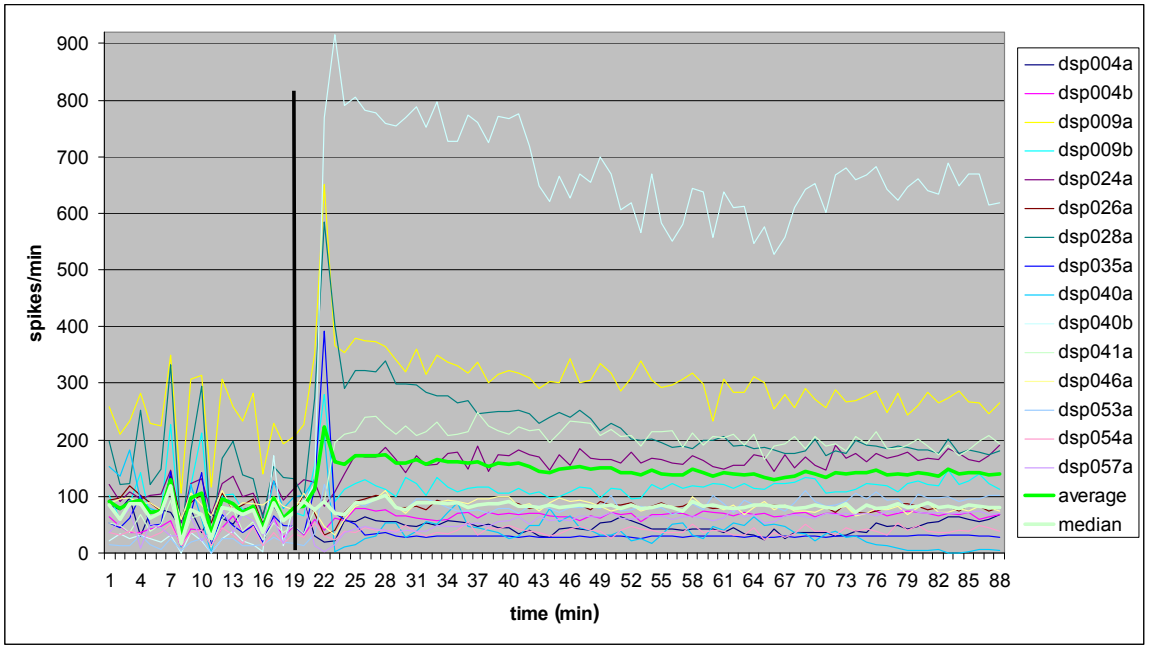

Fig. 4.17: Spikes/min values for all units over 88 minutes of recording. Black bar: addition of 50 µM bicuculline. Thick green line: average, thick light green line: median

A broad range of activity rates can be seen, which, in this case, is even more obvious after normalization of the data (Fig. 4.18). Fig. 4.19 summarizes the values resulting from the different analysis methods: average and median values before normalization, and average and median values after normalization. In this recording, the activity distributions of the reference period (minute 1-18) could be fitted almost equally well for both the unedited spikes/min data points (Fig. 4.20) and the unit-wise normalized activity values (Fig. 4.22) with R^2-values of 0.93 and 0.98, respectively. Under the influence of 50 µM bicuculline, however, the spikes/min values cannot be fitted satisfactorily anymore (Fig. 4.21: $R^2 = 0.58$). The average line is located outside the majority of the distribution, while the median still gives an acceptable indication of the peak of the distribution. Using the initial normalization for each individual unit provides a significantly tighter fit of the bell-shaped Lorentzian curve ($R^2 = 0.92$). The median describes the location of the distribution peak very well, while the average does not.

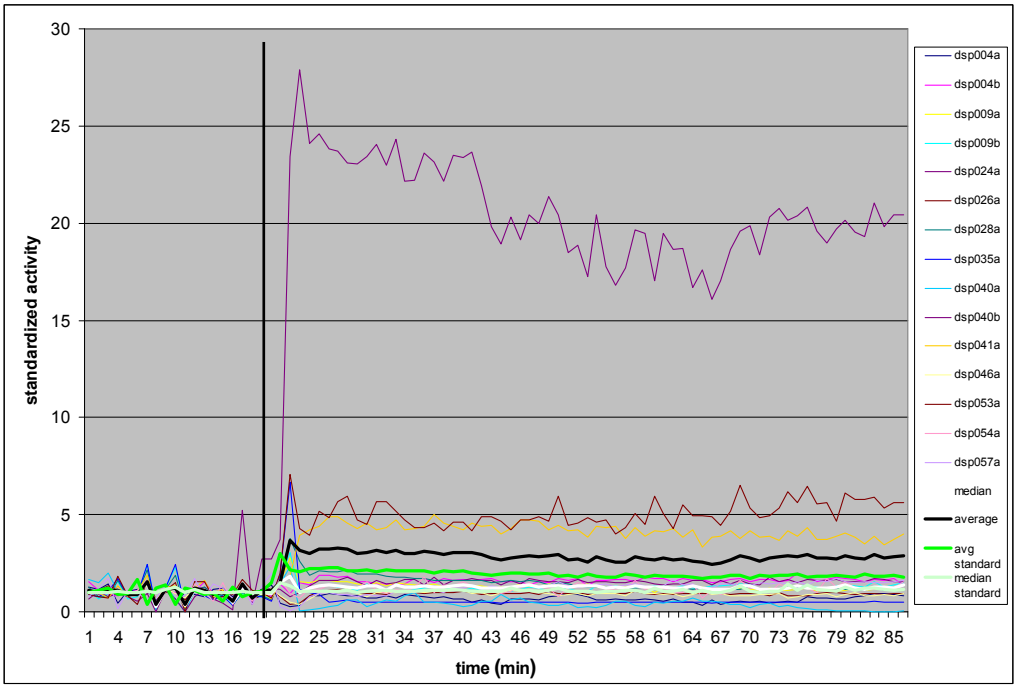

Fig. 4.18: Activity rates normalized by the initial average reference activity of each individual unit.

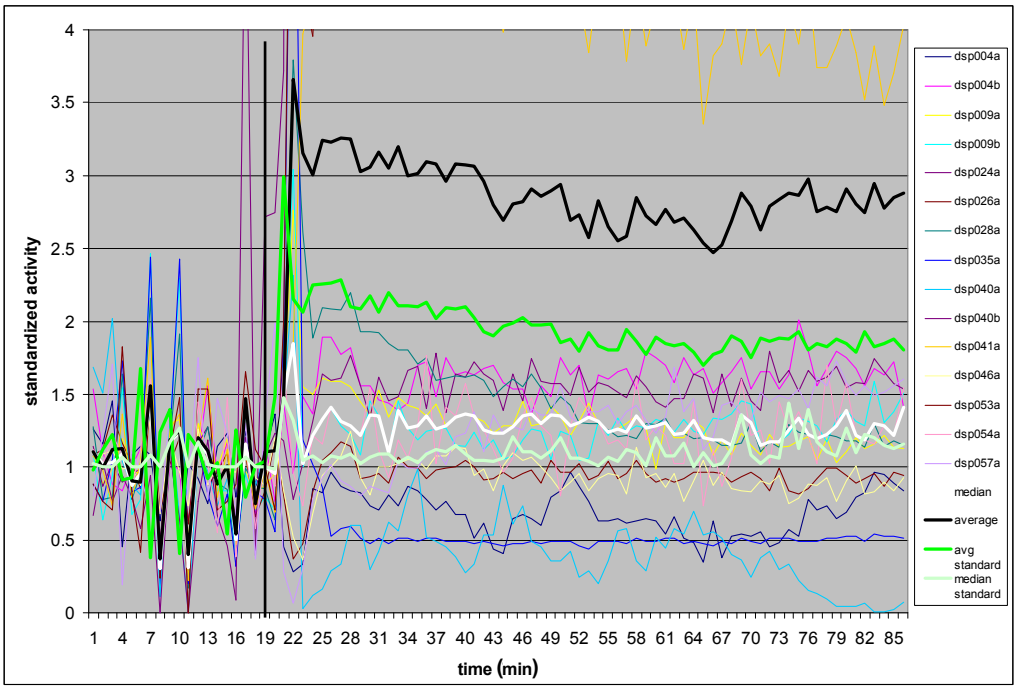

Fig. 4.19: The same data as in Fig. 4.18, zoomed in for better visibility of the average and median curves. Note the relatively high temporal fluctuations of the initial activity plateau when analyzed as the average value, both before (thick green curve) and after (thick black curve) normalization.

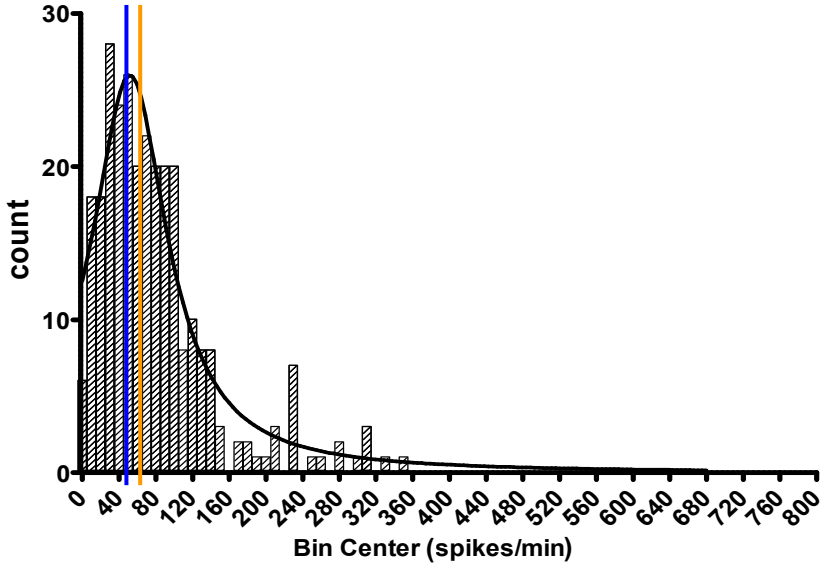

Fig. 4.20: Activity histogram of spikes/min values of all units, bin size: 20 sp/min, minutes 1-18. Blue line: median of distribution, orange line: mean of distribution. Curve fit: Lorentzian, $R^2 = 0.93$

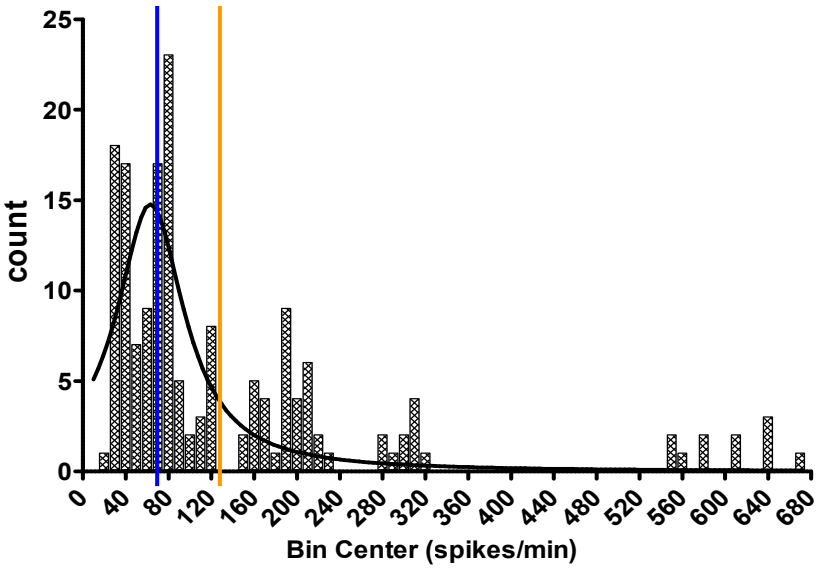

Fig. 4.21: Activity histogram of spikes/min values of all units, bin size: 10 sp/min, minutes 53-63. Blue line: median of distribution, orange line: mean of distribution. Curve fit: Lorentzian, $R^2 = 0.58$

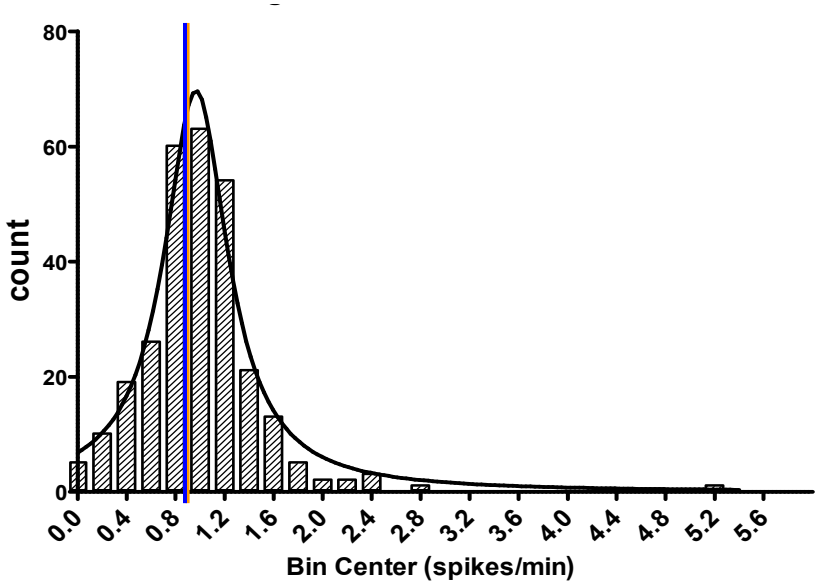

Fig. 4.22: Activity histogram of spikes/min values of all units, bin size: 0.2, minutes 1-18. Blue line: median of distribution, orange line: mean of distribution. Curve fit: Lorentzian, $R^2 = 0.98$

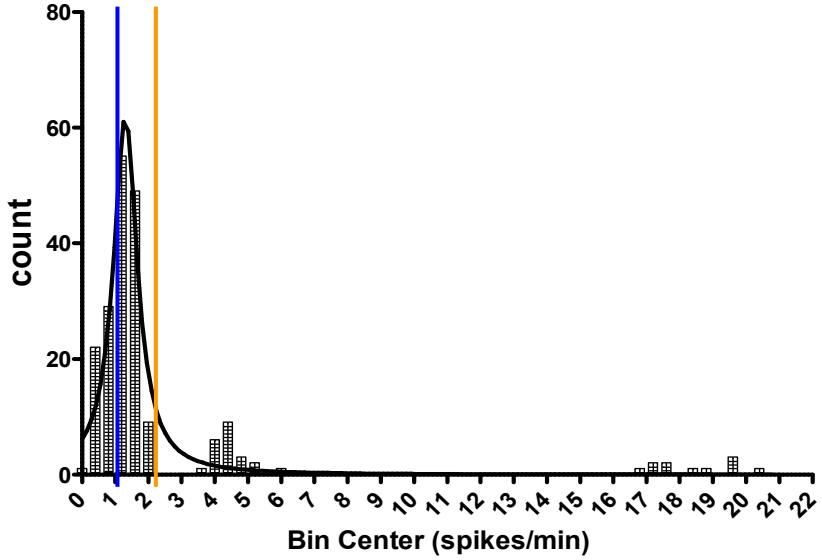

Fig. 4.23: Activity histogram of spikes/min values of all units, bin size: 0.4, minutes 53-63. Blue line: median of distribution, orange line: mean of distribution. Curve fit: Lorentzian, $R^2 = 0.92$

4.1.2.2 Example 2: High number of units

In the following recording, 80 units were identified and monitored. The FC cells were subjected to a very high concentration of bicuculline, 250 µM. Fig. 4.24 shows the largely deviating values for the different analysis types, as described above. The reason for this is illustrated in figures 4.25 to 4.28, which show the distributions of unit activity values during the reference period (4.25, 4.27), and while under the influence of bicuculline (4.26, 4.28): The histograms depicting the reference activity can both be fitted equally well with a Lorentzian curve. Then, under bicuculline, the network splits up into several subgroups, in terms of activity rates, which is most apparent in the raw spikes/min values in figure 4.26. Here, no single value for the network activity can be assigned because of the even distribution of values over a wide range. However, when normalized first, the values can be fitted reasonably well, and the median describes the network behavior.

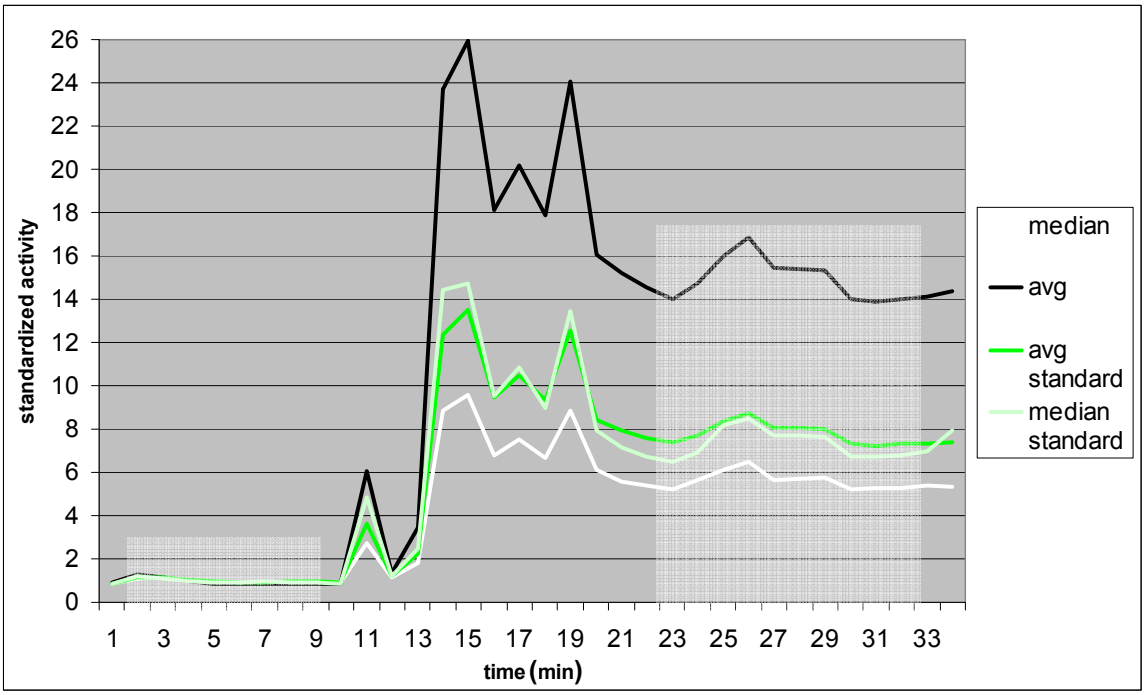

Fig. 4.24: Network activity rates before and after the addition of 250 µM bicuculline. White curve: median of unit activity rates after normalization; black curve: mean of unit activity rates after normalization; green curve: mean of unit activity rates calculated before normalization; light green curve: median of unit activity rates calculated before normalization. Shaded areas: Times during which values for the following histograms were taken.

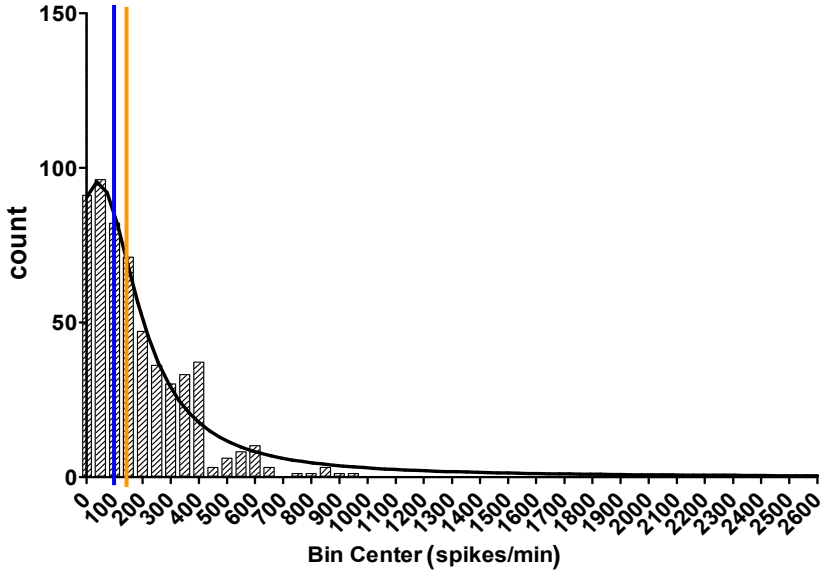

Fig. 4.25: Activity histogram of spikes/min values of all units, bin size: 50 sp/min, minutes 2-9. Blue line: median of distribution, orange line: mean of distribution. Curve fit: Lorentzian, $R^2 = 0.95$

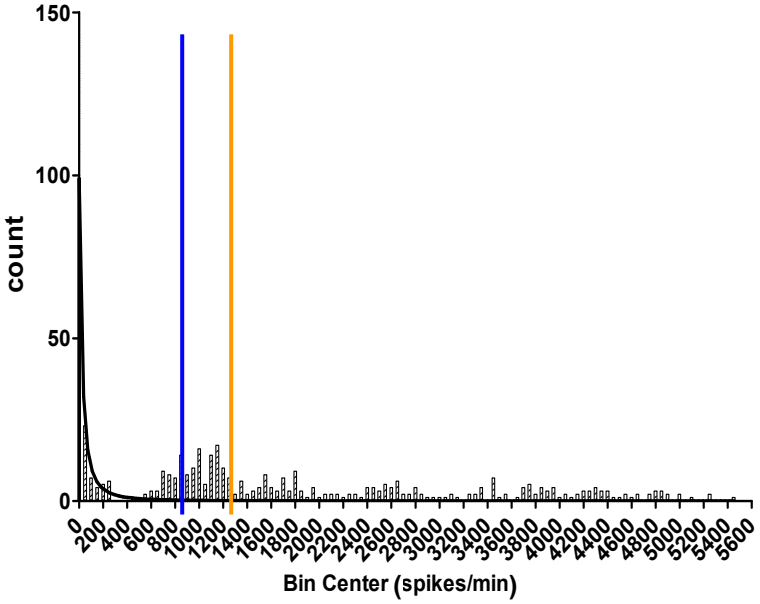

Fig. 4.26: Activity histogram of spikes/min values of all units, bin size: 50 sp/min, minutes 23-32. Blue line: median of distribution, orange line: mean of distribution. Curve fit: Lorentzian, $R^2 = 0.79$

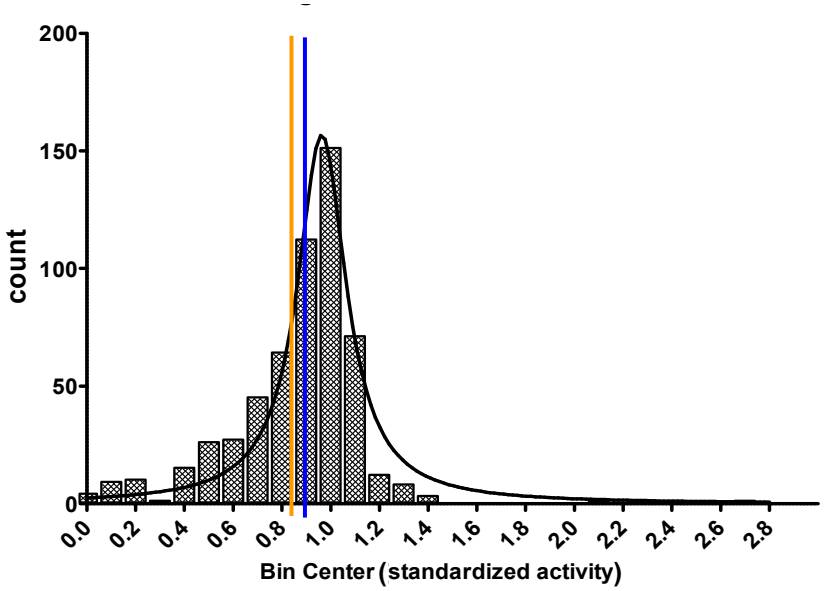

Fig. 4.27: Activity histogram of spikes/min values of all units, bin size: 0.1, minutes 2-9. Blue line: median of distribution, orange line: mean of distribution. Curve fit: Lorentzian, $R^2 = 0.95$

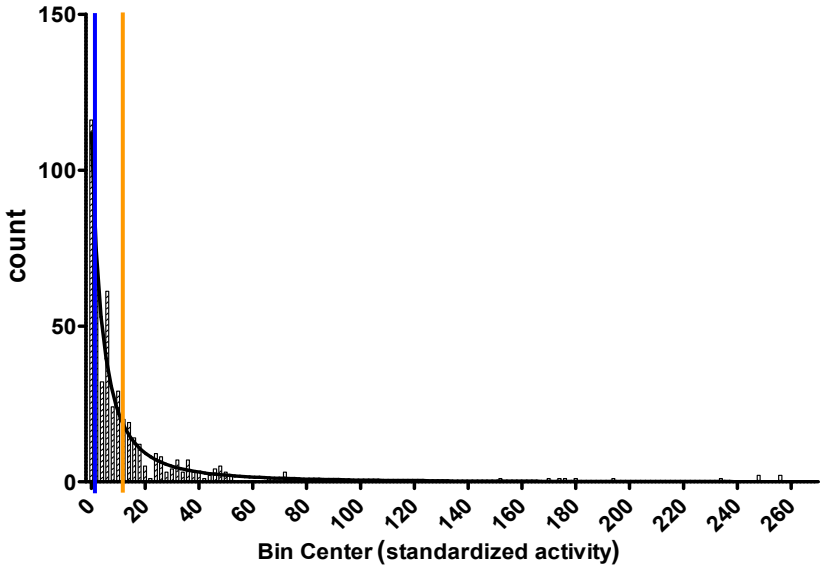

Fig. 4.28: Activity histogram of spikes/min values of all units, bin size: 2, minutes 23-32. Blue line: median of distribution, orange line: mean of distribution. Curve fit: Lorentzian, $R^2 = 0.95$

4.2 Midbrain responses to ethanol

4.2.1 Example recording

The acute neurotoxicity of pure ethanol has been studied extensively using a variety of animal and cell culture models, including cortical neuronal cultures grown on MEA plates [3]. The frontal cortex is the primary area of conscious decision-making, including prioritization, foresightedness, and inhibition or control of actions, which is why a glass of wine loosens us up. However, with diminished inhibition and control in the frontal cortex, more basic functions, such as motor control, are still mostly intact. Many of these functions are located in the midbrain, specifically in the substantia nigra, where the density of dopaminergic neurons is very high. Not many pharmacological studies have been focused on this part of the brain, especially using the MEA technology.

Fig. 4.29 shows an exemplary ethanol titration with five cumulative concentrations: 68.5, 137, 205.5, 342.5 and 411 mM, followed by a full medium exchange. Note the relatively long delay after each ethanol addition before the effect of the new concentration set in. Using the median as the measure for the network activity, the culture is almost entirely silent at 411 mM ethanol. The median must be used in this case, as shown in the histograms in Figs. 4.30 and 4.31.

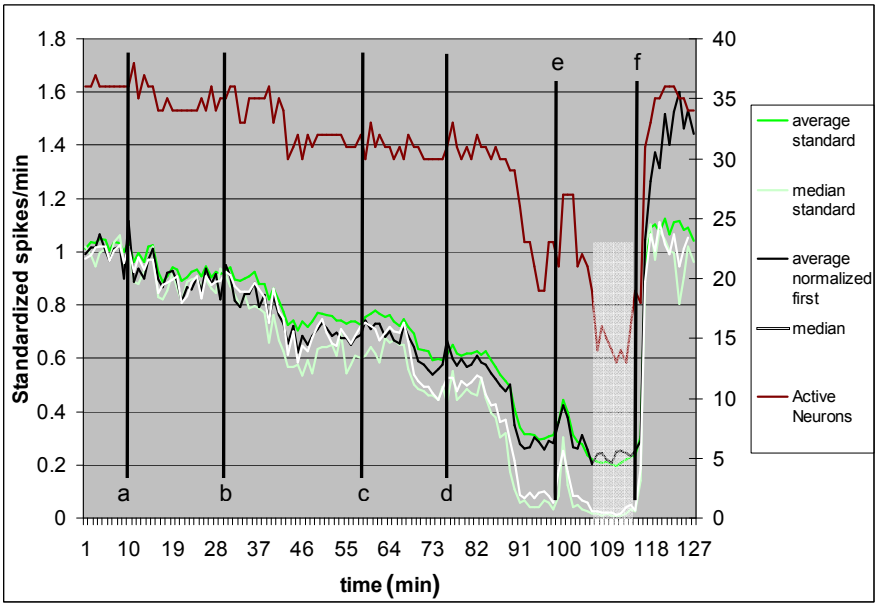

Fig. 4.29: Midbrain recording showing a step-wise reduction in activity resulting from administration of the following ethanol concentrations (in mM): a: 68.5, b: 137, c: 205.5, d: 342.5, e: 411. F: full medium change. White and black curves: data were normalized first (median, mean, respectively). Green and light green curves: average, median of data that were normalized afterwards. Dark red curve: Number of active units (on secondary y-axis). Shaded area: period analyzed in the following histograms.

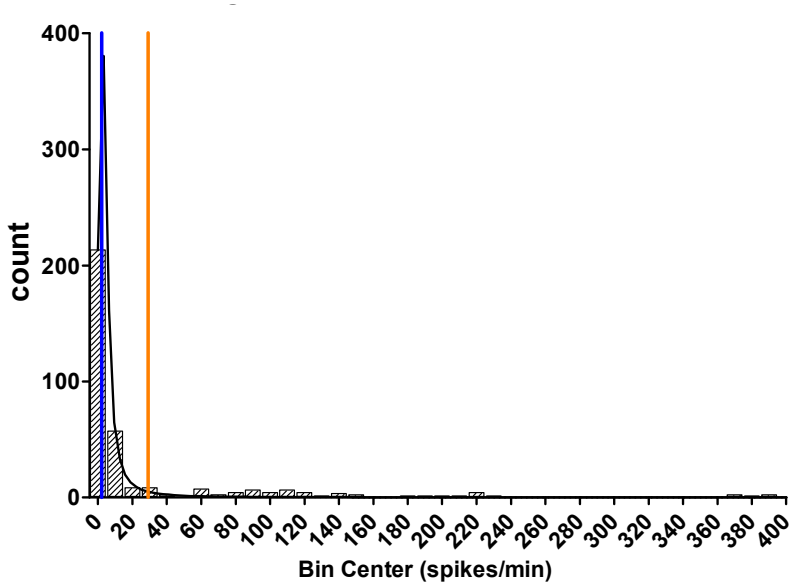

Fig. 4.30: Activity distribution under 411 mM ethanol, unedited spikes/min values, $R^2 = 1$

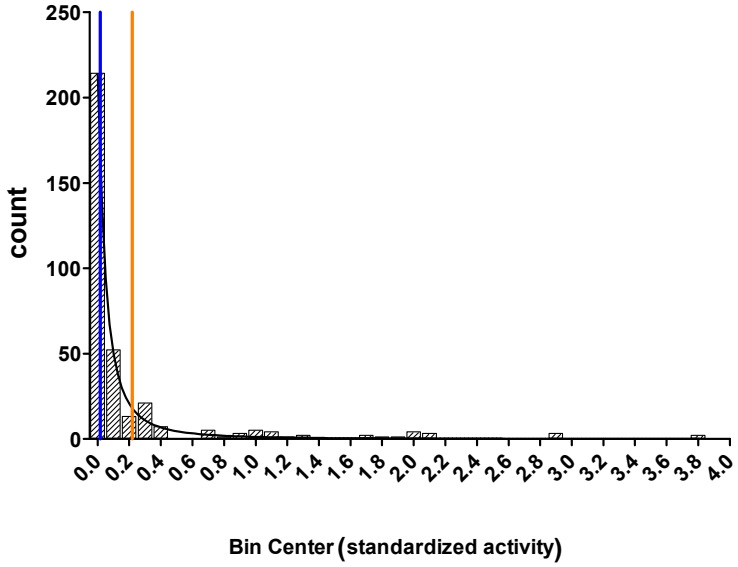

Fig. 4.31: Activity distribution under 411 mM ethanol, normalized spikes/min values, $R^2 = 0.99$

In previous tests conducted at the CNNS, cortical neurons had been shown to survive prolonged periods of exposure to high concentrations of ethanol (up to 160 mM), which would lead to coma and death in humans. Since this had not been attempted in a midbrain culture, the medium was replaced with fresh DMEM5 after the first titration of ethanol, and 548 mM were added 42 minutes later (Fig. 4.32). Another 79 minutes later, the medium was replaced again, and 20 minutes after that 40 µM bicuculline were added. The medium change resulted in a very strong reaction of one particular unit (fig. 4.33) that was up to 420 times as active as in its reference state after the addition of bicuculline and that dominated the network average after normalization (black curve in fig. 2.32). Fig. 2.34 shows that this particular unit was an extreme

outlier and that the majority of the active units were located around the median value (white curve in figs. 4.32 and 4.34. Figs. 4.35 and 4.36 verify this assumption: The blue lines depict the median in both graphs and give a more accurate indication of the distributions' peaks than the means (orange lines). In addition, the curve fit of the normalized data (R^2 = 0.99) is much better than the one using the original spikes/min values (R^2 = 0.85).

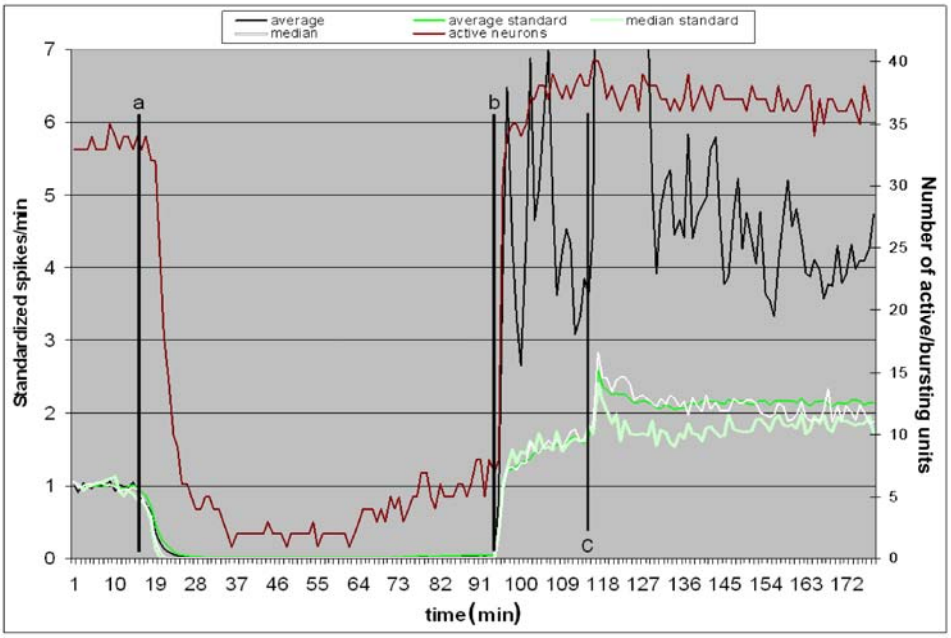

Fig. 4.32: Second part of the experiment after first medium wash. A: addition of 548 mM ethanol, b: full medium change, c: addition of 40 µM bicuculline. White and black curves: data were normalized first (median, mean, respectively). Green and light green curves: average, median of data that were normalized afterwards. Dark red curve: Number of active units (on secondary y-axis).

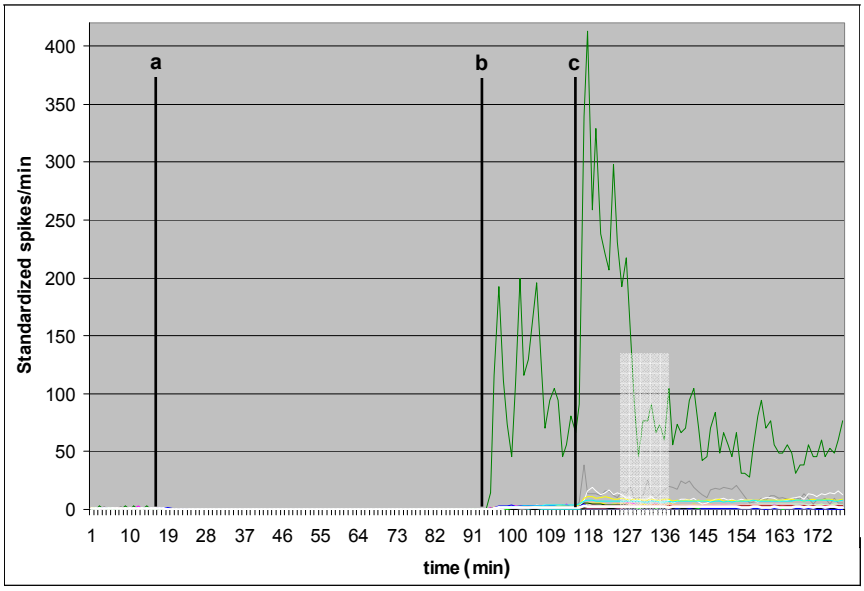

Fig. 4.33: Second part of the experiment after first medium wash: Normalized data of all individual units. Green curve: Unit that was up to 420 times more active after medium wash and addition of bicuculline.

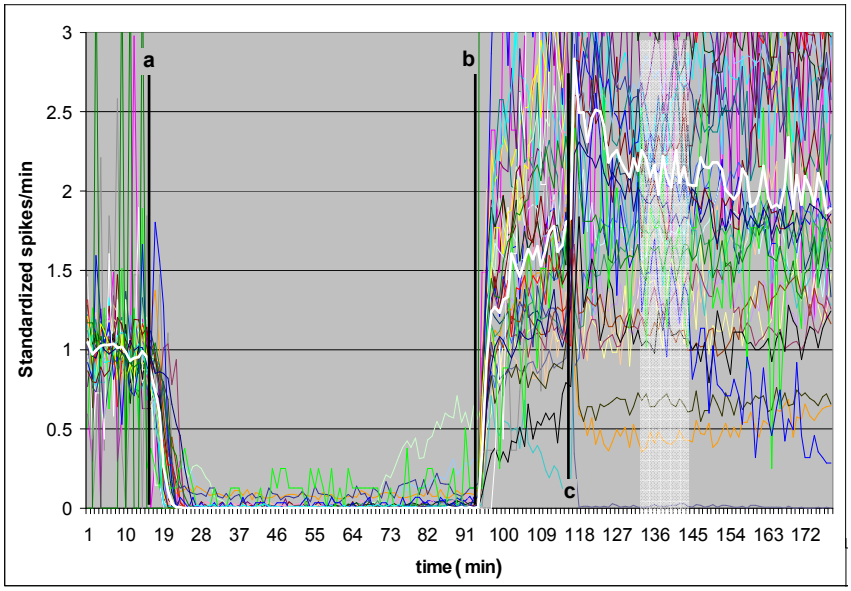

Fig. 4.34: Second part of the experiment after first medium wash: Normalized data of all individual units, zoomed in to visualize the majority of the units. White curve: median.

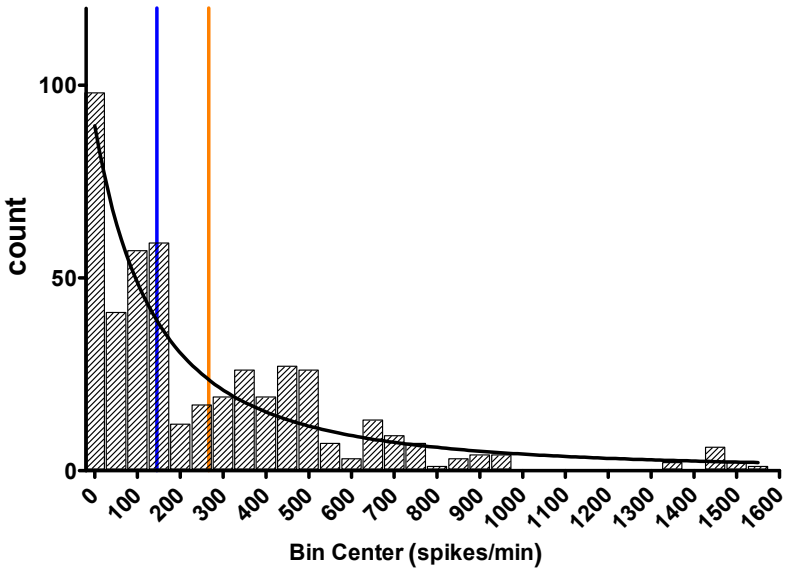

Fig. 4.35: Activity distribution under 411 mM ethanol, minutes 136-146, spikes/min values, $R^2 = 0.85$

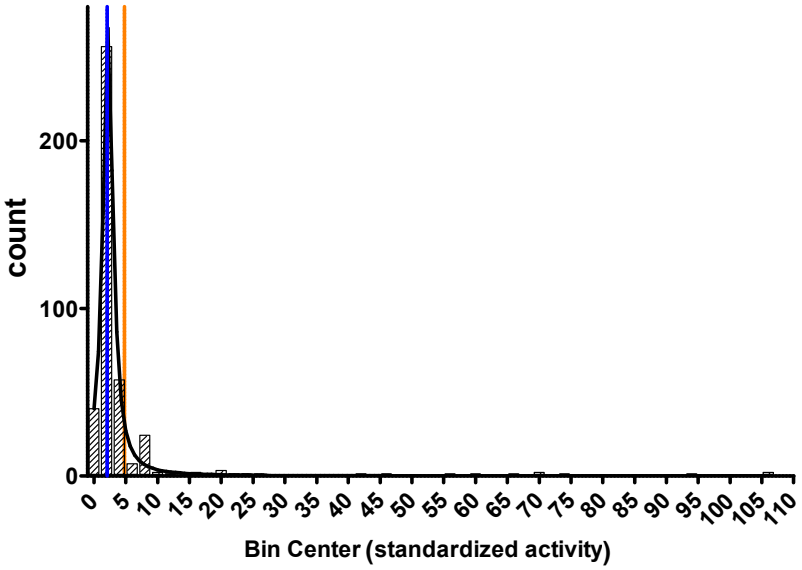

Fig. 4.36: Activity distribution under 411 mM ethanol, minutes 136-146, normalized spikes/min values, $R^2 = 0.99$

4.2.1.1 Summary of data from two networks

Combining the data points from two distinct networks, the dose-response relation in figure 4.37 can be constructed. The sigmoidal decay curve fit has a goodness-of-fit value of $R^2 = 0.98$. The IC50 calculated from this curve is 224 mM. This value is approximately 6 times as high as the average IC50 determined using cortical cultures on MEAs at the CNNS (fig. 4.38).

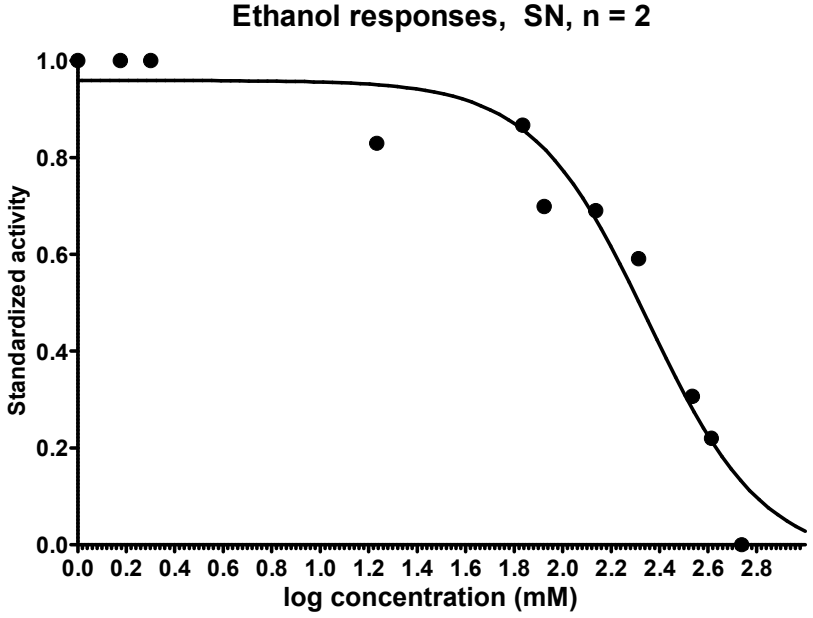

Fig. 4.37: Dose-response curve with data points from two different midbrain networks. R^2=0.974

The equation used for all dose-response curves shown here is:

$$y = \min + \frac{\max - \min}{1 + 10^{(\log EC50 - x)Hillslope}} \qquad \textbf{4-1}$$

Best-fit values		**Goodness of Fit**	
Bottom	-0.03226	Degrees of Freedom	11
Top	0.9591	R square	0.9740
LogIC50	2.351	Absolute Sum of Squares	0.06274
HillSlope	-1.826	Sy.x	0.07553
IC50	224.2	**Runs test**	
Span	0.9914	Points above curve	12
Std. Error		Points below curve	3
Bottom	0.04821	Number of runs	7
Top	0.03382	P value (runs test)	1.0000
LogIC50	0.05297	Deviation from Model	Not Significant
HillSlope	0.3356		
Span	0.06123		

Table 4.1: Analysis and fit parameters from the data used to generate the dose-response curve in fig. 4.37

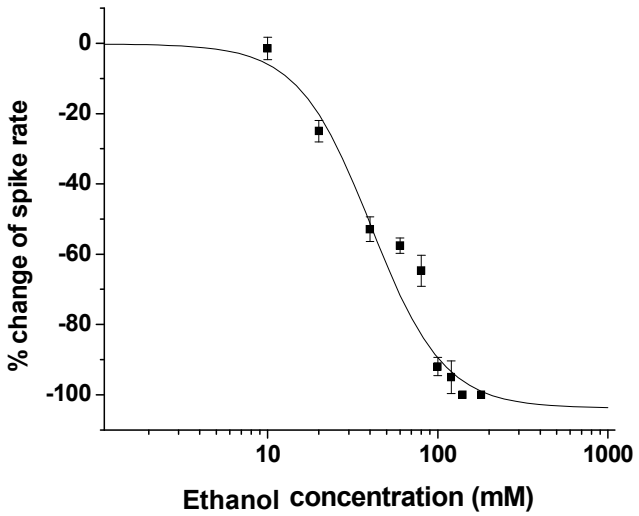

Fig. 4.38: Dose-response curve of frontal cortex responses to ethanol, source: [3]

4.3 Lidocaine experiments

4.3.1 Frontal cortex

4.3.1.1 Sample recording I

The first example of a culture treated with lidocaine is a good example for strictly coordinated bursting activity, as seen in figure 4.39: All units fired precisely in unison, except for two units, one of which produced far more APs per minute than the rest of the network. This unit fires tonically with increasing spike frequency before each network burst, except for a period of approximately 1.5 seconds after each burst, giving the impression that it is involved with their initiation. It is represented by the thick yellow curve in figure 4.40. Its average reference spike rate is around 1400 spikes/min, which is 23 times as high as the network's median reference spike rate. Hence the y-axis had to be scaled in a logarithmic fashion. This graph pictures the spikes/min values of all the units over 62 minutes, during which 3 doses of lidocaine were given: a: 1 µM, b: 2 µM, and c: 50 µM. Evidently, the majority of units fell silent after the addition of 50 µM lidocaine, except for the one extraordinarily active unit. The resulting average activity (thick green line) is strongly biased and does not reflect the behavior of the network's majority.
This problem is alleviated by normalizing every unit's individual activity progression with respect to their level of reference activity (Fig. 4.41), and using the median as the measure of the network activity. Figure 4.42 shows that, in this case, even the network average (thick black curve) provided a good estimate of the network's activity. Interestingly, the number of bursting and active units did decline all the way to zero, but intermittently, a portion of the units partially regained their function for a short period of time. This might suggest that a large dose of lidocaine initially causes an overreaction, inhibiting AP generation completely, followed by a recovery phase. The activity suppression was entirely reversible through two full medium changes in this recording. This was the case for all lidocaine experiments in this study.

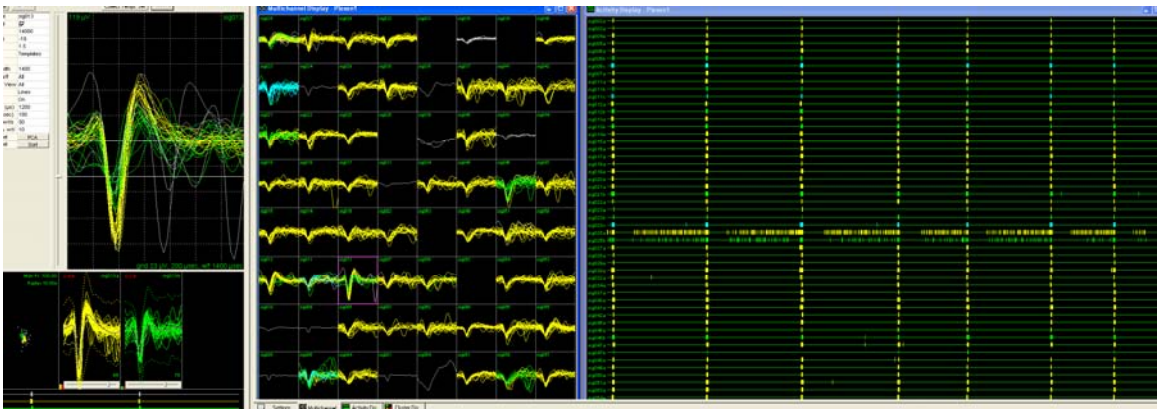

Fig. 4.39: Screenshot of the Plexon software showing frontal cortex reference activity: Single cell AP waveshapes (left window), multichannel window (middle), raster window: one row per unit, APs depicted as time stamps, 40 s time period shown (right).

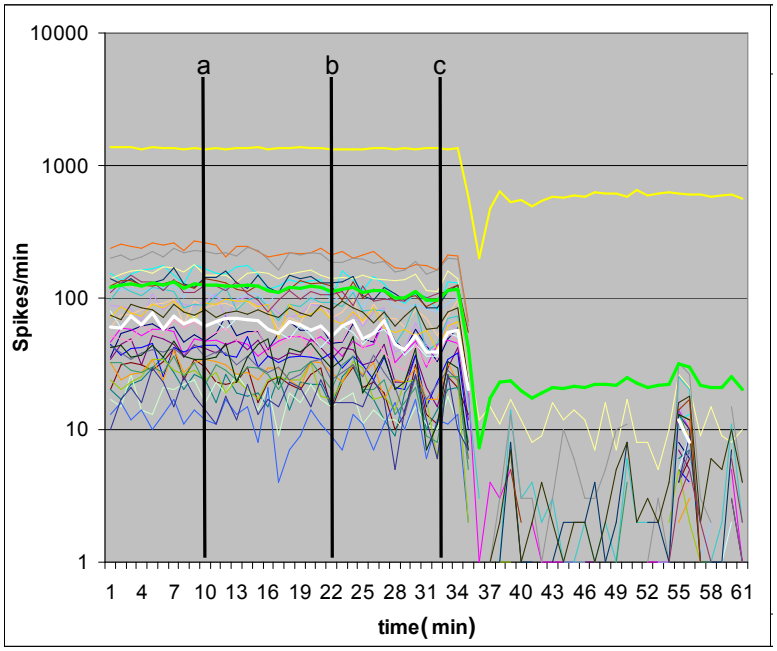

Fig. 4.40: Frontal cortex recording showing responses to three lidocaine additions: a: 1 µM, b: 2 µM, c: 50 µM. Thick yellow curve: highly active unit. Note the logarithmic scale on the y-axis.

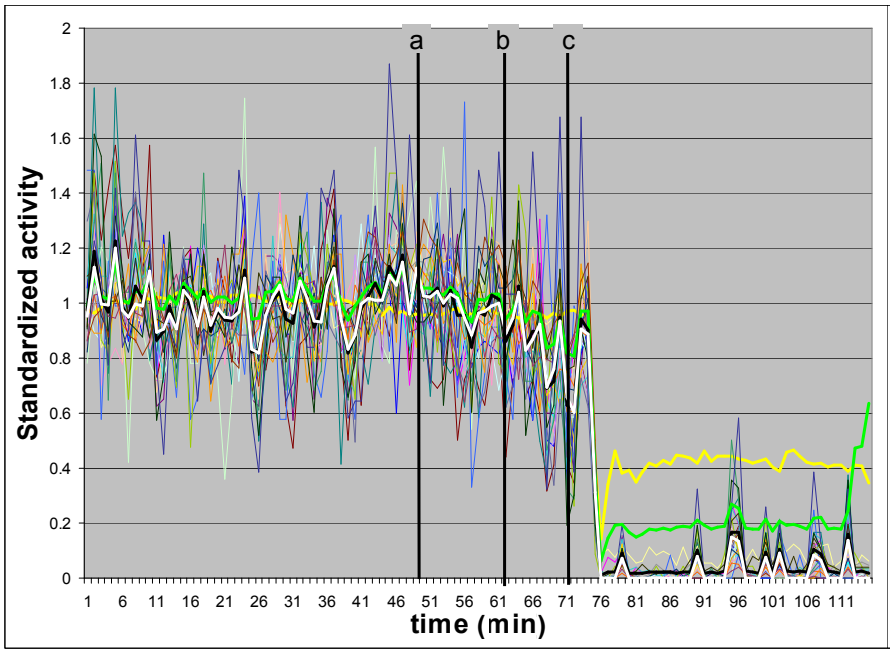

Fig. 4.41: Normalized activity values of all units recorded from, including the highly active one (thick yellow curve). Green curve: average values normalized after their calculation (same data as in figure 4.40)

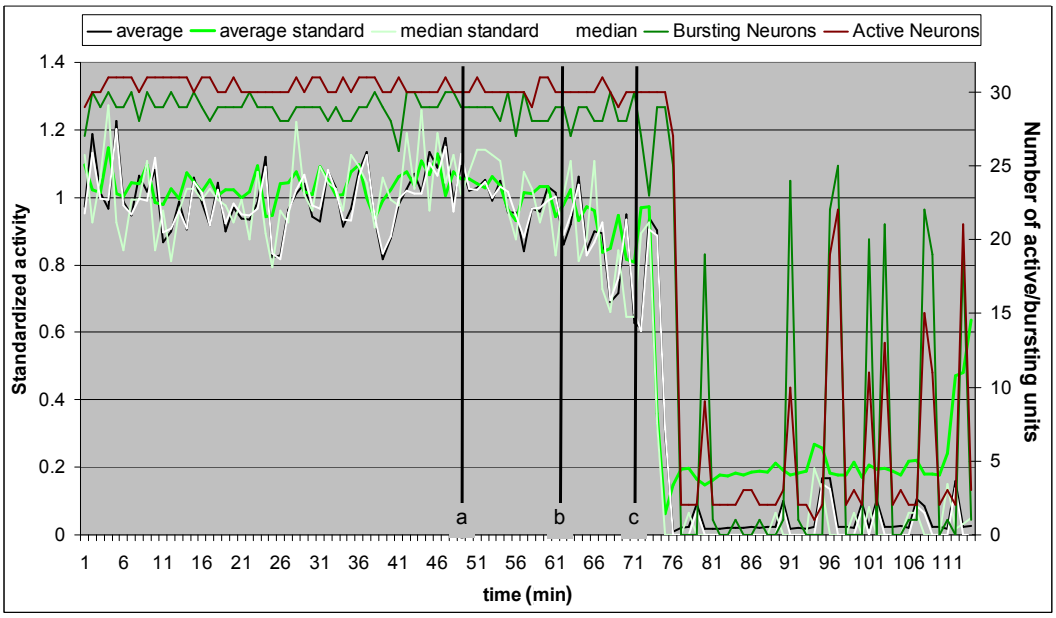

Fig. 4.42: Median and average activity graphs, both calculated before (light green, green) and after normalization (white and black curves, respectively).

4.3.1.2 Sample recording II

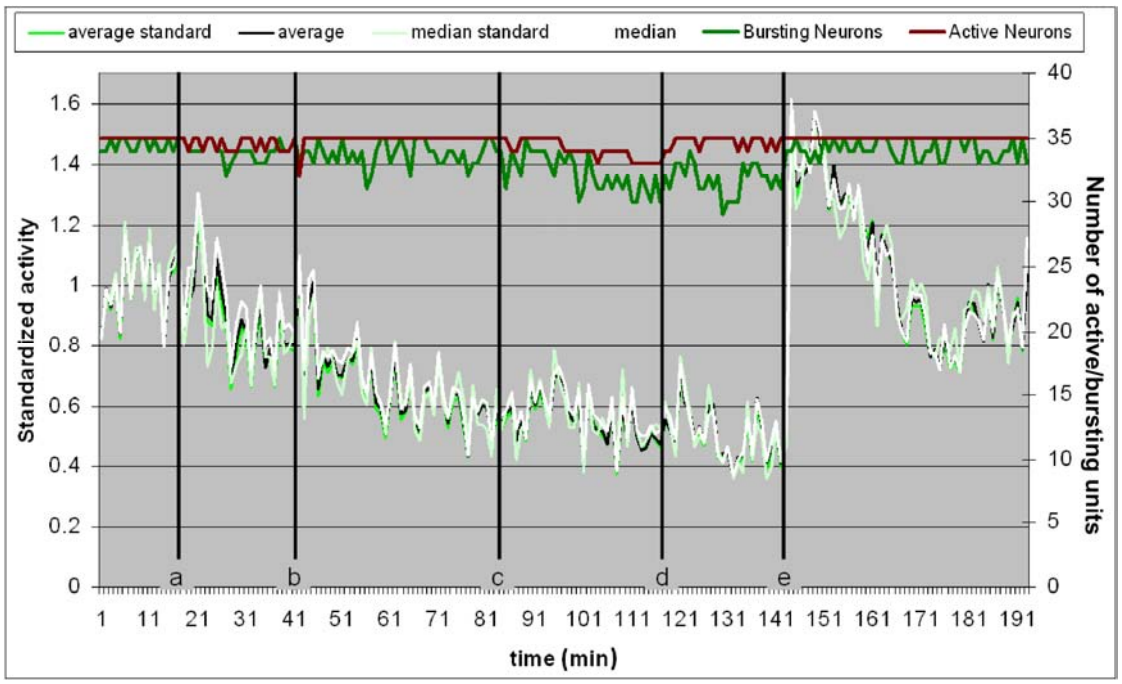

Fig. 4.43 a): Frontal cortex recording with lidocaine titration. Cumulative doses of lidocaine (in µM): a: 1, b: 3, c: 6, d: 14. e: full medium change.

In this second example of an FC recording under the influence of lidocaine, four different cumulative concentrations were evaluated (black vertical bars in figure 4.43 a): a: 1 µM, b: 3 µM, c: 6 µM, d: 14 µM. As evident in this particular recording, the average and median values, whether normalized first or after their calculation, can be almost identical in cultures whose neurons respond in a very uniform way to a particular compound. However, upon close inspection of the individual unit histograms of the same recording period (fig. 4.43 b), another interesting observation is made: Seven (red rectangles) out 35 units do not follow the trend of the rest of network, which is a gradual decrease in activity that follows the cumulative lidocaine concentration in magnitude. Instead, some of them respond the strongest to the first lidocaine addition, some to the second, and others to the third one.

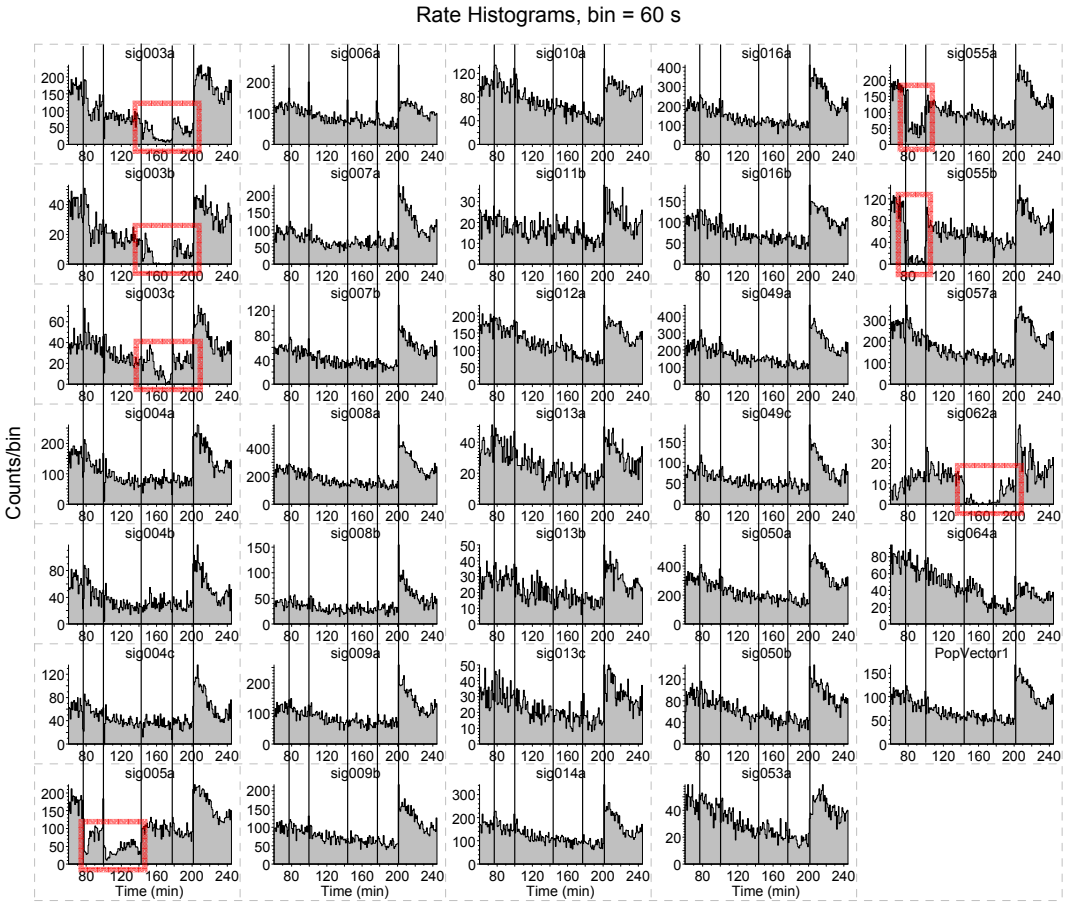

Fig. 4.43 b): Histograms of the individual units from the recording shown in fig. 4.43 a). Black vertical bars correspond to the ones in fig. 4.43 a). Time period shown: 190 minutes. Red rectangles: Units showing early maximum responses to lidocaine.

4.3.1.3 Summary of data from 11 networks

4.3.1.3.1 Dose response curve using network mean before normalization

The first analysis approach shown here is to use the mean spikes/min values and normalize with respect to the reference activity afterwards. The dose-response curve (figure 4.44) shows a high degree of variability. Lidocaine apparently causes slight differences in the networks to respond highly heterogeneously. Table 4.2 summarizes the important parameters associated with the curve fit used in this graph.

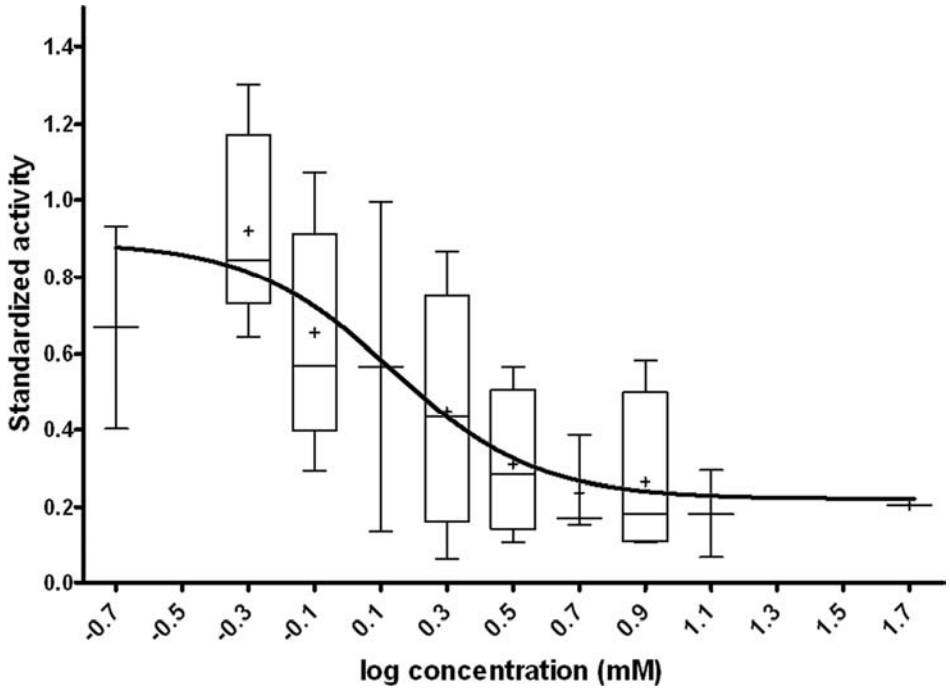

Fig. 4.44: Dose response curve generated with data from 11 recordings, IC50 = 1.374 ±1.48 μM, R^2 = 0.42

Best-fit values		**Goodness of Fit**	
Bottom	0.2203	Degrees of Freedom	39
Top	0.8886	R square	0.4180
LogIC50	0.1378	Absolute Sum of Squares	2.798
HillSlope	-1.999	Sy.x	0.2678
IC50	1.374	**Runs test**	
Span	0.6683	Points above curve	19
Std. Error		Points below curve	24
Bottom	0.1161	Number of runs	20
Top	0.1747	P value (runs test)	0.2970
LogIC50	0.1698	Deviation from Model	Not Significant
HillSlope	1.435	Number of points	
Span	0.2396	Analyzed	43

Table 4.2: Analysis and fit parameters from the data used to generate the dose-response curve in fig. 4.44

4.3.1.3.2 Dose response curve using initial normalization with subsequent calculation of the network median activity

Fig. 4.45 shows how the dose-response curve shifts when the same data are normalized unit-wise first, and the median is used as the measure of the network activity. The IC50 has not changed considerably (1.148 instead of 1.374 μM), but the distribution is fitted more easily to the logarithmic decay curve ($R^2 = 0.51$ instead of 0.4). The statistical parameters are summarized in table 4.3.

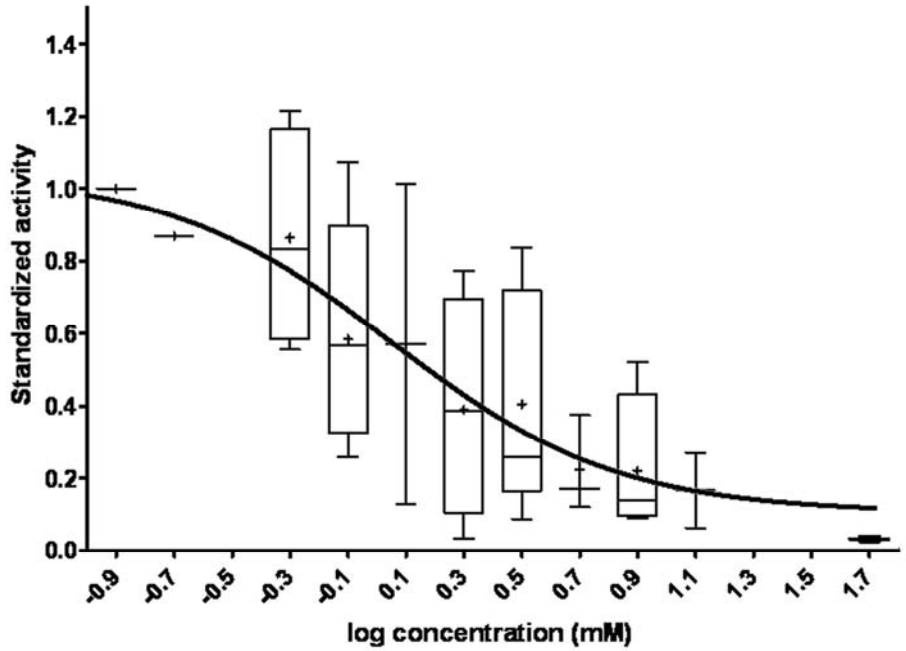

Fig. 4.45: Dose response curve generated using data from 11 recordings, IC50 = 1.148 ±1.661 μM, R^2 = 0.51

Best-fit values		**Goodness of Fit**		
Bottom	0.09914	Degrees of Freedom	41	
Top	1.036	R square	0.5142	
LogIC50	0.05992	Absolute Sum of Squares	2.797	
HillSlope	-1.115	Sy.x	0.2612	
IC50	1.148	**Runs test**		
Span	0.9369	Points above curve		15
Std. Error		Points below curve		30
Bottom	0.1569	Number of runs		27
Top	0.1477	P value (runs test)		0.9905
LogIC50	0.2063	Deviation from Model		Not Significant
HillSlope	0.5369	Number of points		
Span	0.2367	Analyzed		45

Table 4.3: Analysis and fit parameters from the data used to generate the dose-response curve in fig. 4.45

4.3.2 Midbrain

4.3.2.1 Sample recording I

The following graph (figure 4.46) shows a typical example of a long-term recording with a lidocaine titration leading to a step-wise reduction in electrical activity. Despite the relatively low number of units recorded from (17), the overall activity development follows the increasing lidocaine concentration with a steady decrease. The cumulative lidocaine concentrations applied were 20, 40, 60, 80, 100, 120 and 200 µM. The activity decrease is partially due to a complete dropout of some of the units (red curve in figure 4.46). However, the activity did almost vanish entirely at 200 µM, while up to four units were still (barely) active. This means that lidocaine did not just abruptly shut down the units one by one, but rather caused a general activity decrease in all of the units, with some of them dropping out completely earlier than others.
It is obvious that the different analysis methods yield results that deviate from each other significantly. For example, the median activity after the third lidocaine addition reads approximately 50% of the initial activity if it is calculated before normalizing it with respect to the initial reference value (light green curve in fig. 4.46), whereas it is as low as 30% if the normalization is carried out first. This discrepancy is explained by the following figures.

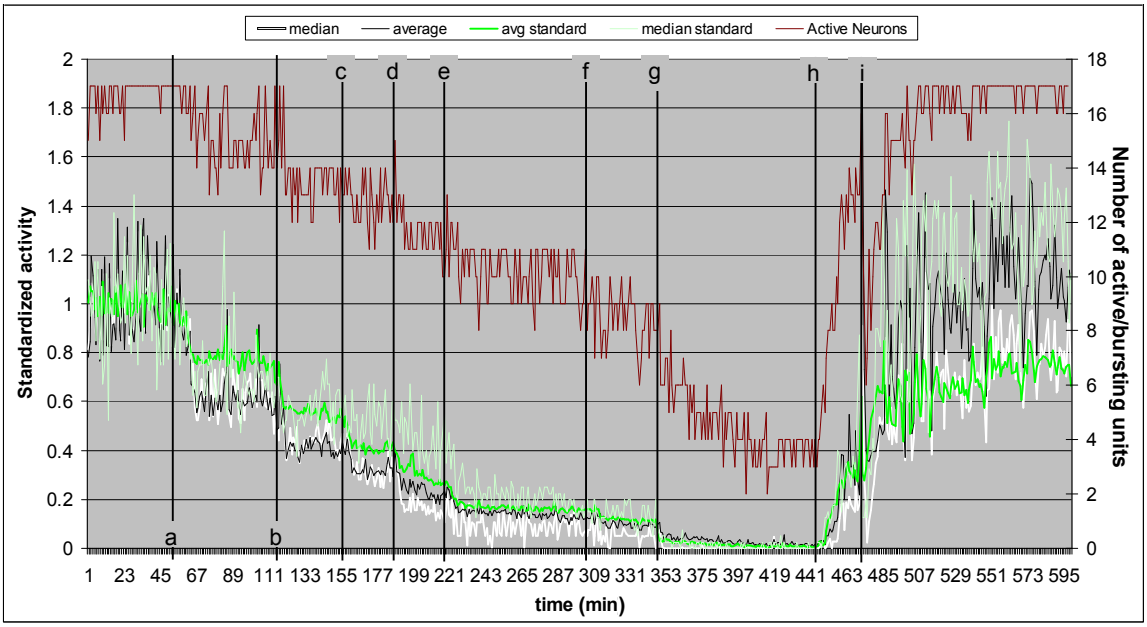

Fig. 4.46: Activity reduction caused by lidocaine in a midbrain culture. White, black curves: median, mean values after normalization, respectively; green, light green curves: mean, median values calculated before normalization, respectively. Dark red curve: number of active units (secondary y-axis). Vertical bars denote cumulative lidocaine concentrations (in µM): a: 20, b: 40, c: 60, d: 80, e: 100, f: 120, g: 200. h, i: medium changes.

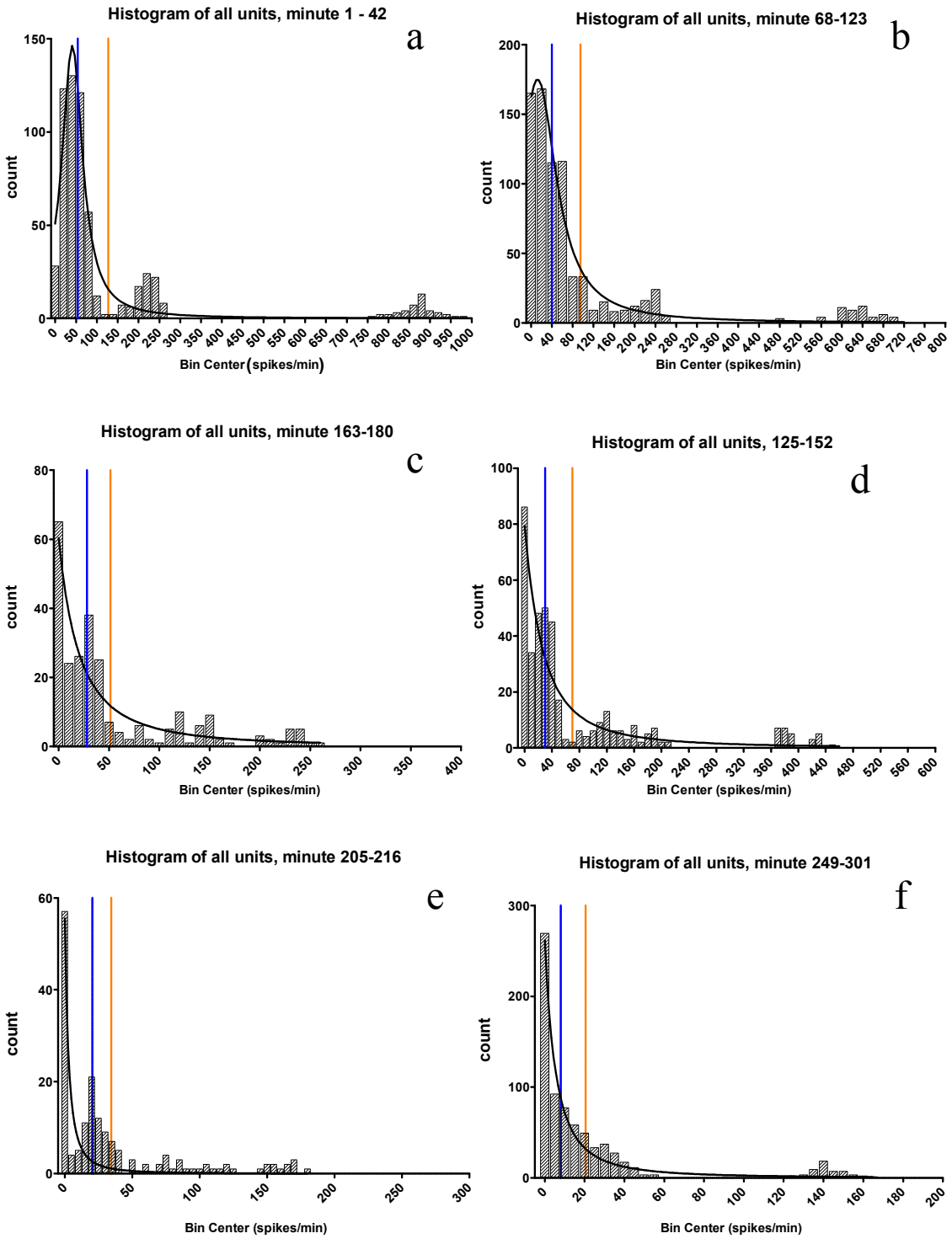
Histogram of all units, minute 1 - 42
a
count
Bin Center (spikes/min)
Histogram of all units, minute 68-123
b
count
Bin Center (spikes/min)
Histogram of all units, minute 163-180
c
count
Bin Center (spikes/min)
Histogram of all units, 125-152
d
count
Bin Center (spikes/min)
Histogram of all units, minute 205-216
e
count
Bin Center (spikes/min)
Histogram of all units, minute 249-301
f
count
Bin Center (spikes/min)

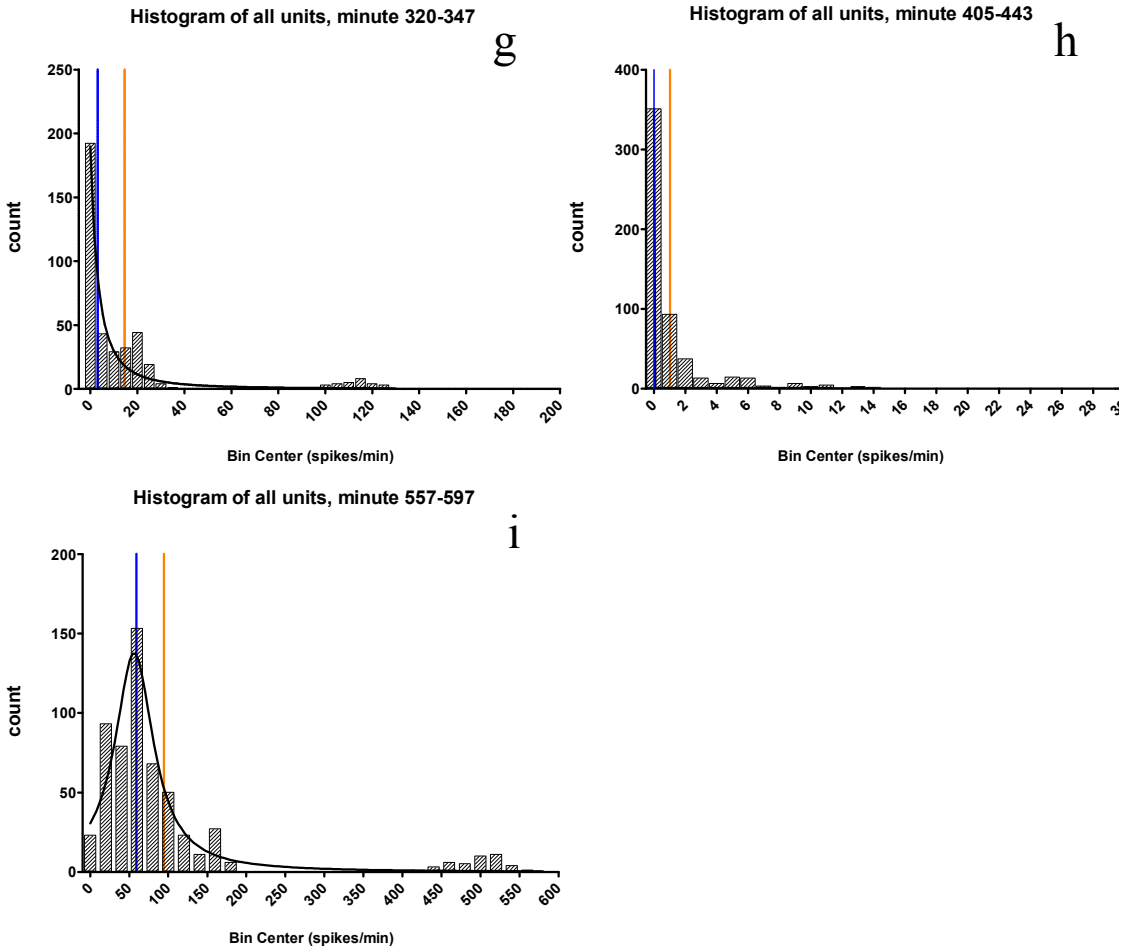

Fig. 4.47: Histograms depicting the distribution of activity during the reference period (a), and the subsequent activity plateaus induced by lidocaine (b-i). Blue vertical lines: medians of the distributions; orange vertical lines: means of the distributions. Note the varying scalings of the x-axes.

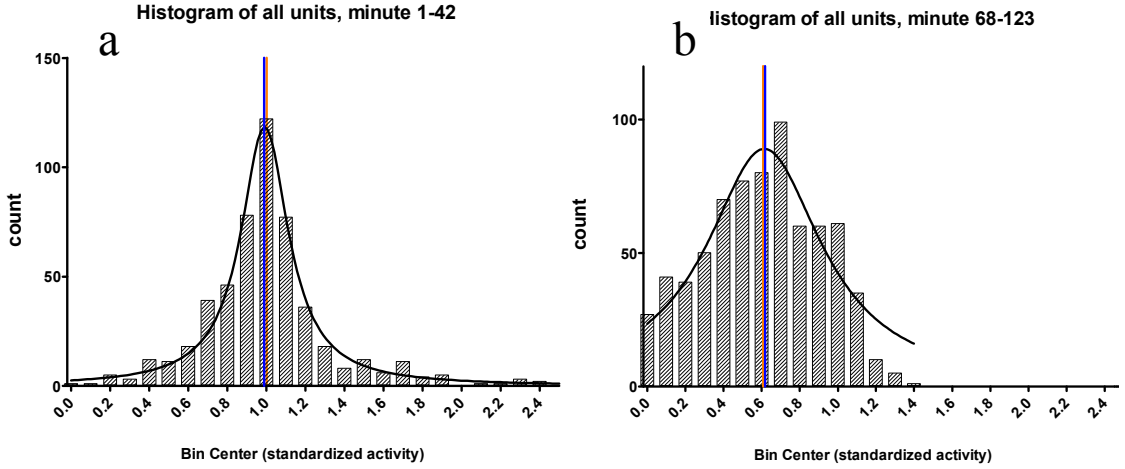

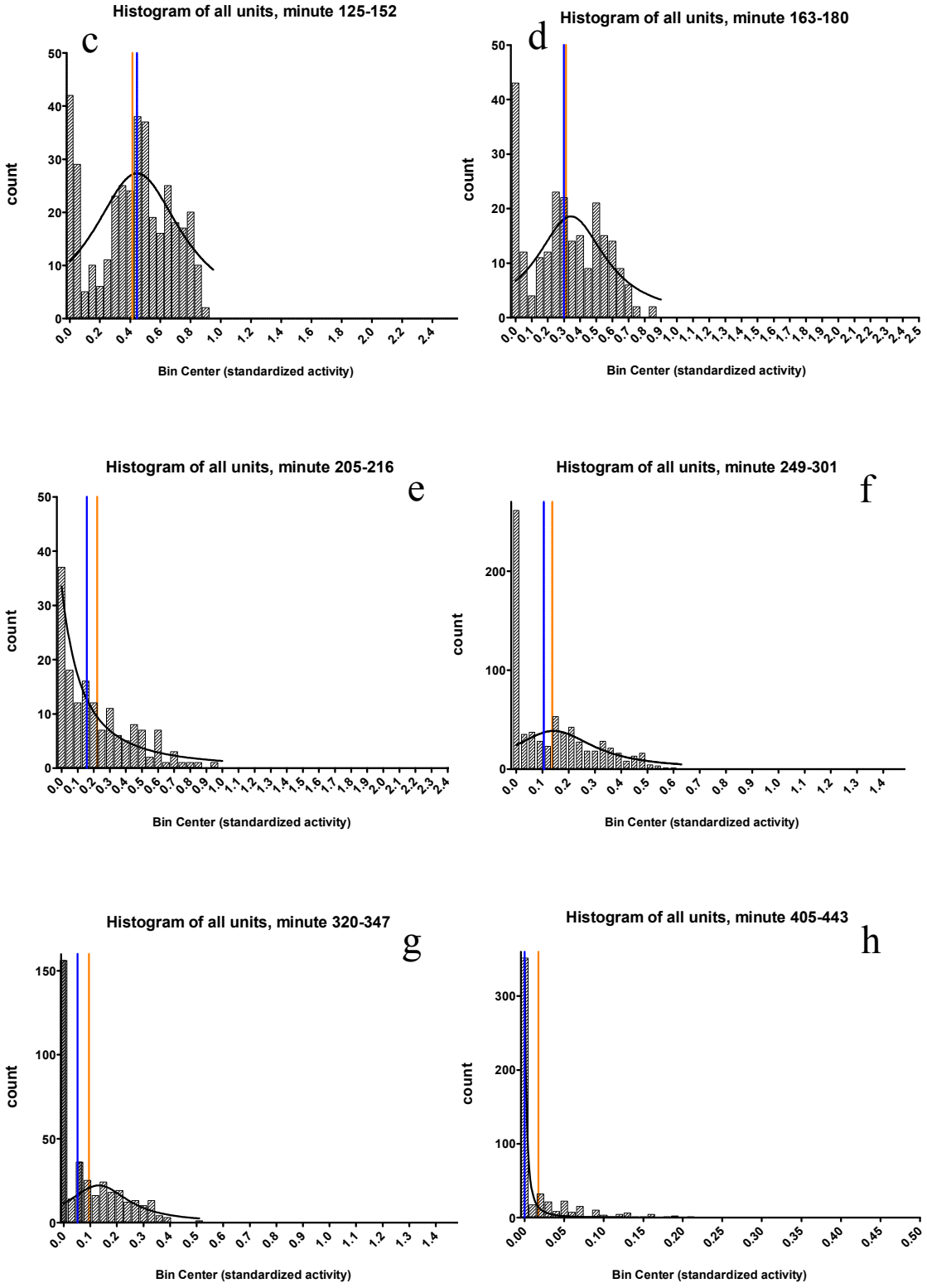
Histogram of all units, minute 125-152
c
count
Bin Center (standardized activity)
Histogram of all units, minute 163-180
d
count
Bin Center (standardized activity)
Histogram of all units, minute 205-216
e
count
Bin Center (standardized activity)
Histogram of all units, minute 249-301
f
count
Bin Center (standardized activity)
Histogram of all units, minute 320-347
g
count
Bin Center (standardized activity)
Histogram of all units, minute 405-443
h
count
Bin Center (standardized activity)

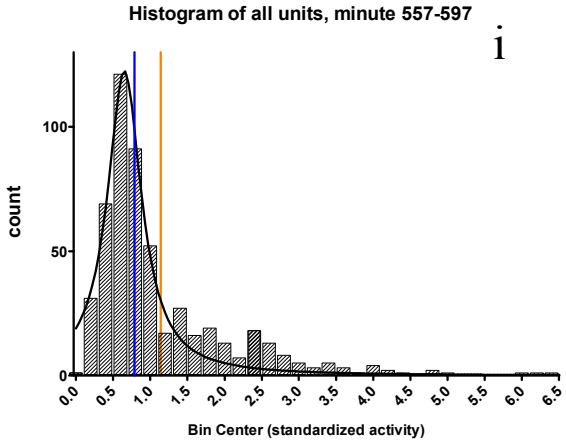

Fig. 4.48: Histograms depicting the distribution of activity during the reference period (a), and the subsequent activity plateaus induced by lidocaine (b-i). Blue vertical lines: medians of the distributions; orange vertical lines: means of the distributions. Note the varying scalings of the x-axes.

4.3.2.2 Sample recording II

Another example of a lidocaine titration in a midbrain culture indicates that dose-dependent activity plateaus are easily achievable using this substance (fig. 4.49). In this recording, the network overreacted to each lidocaine addition first (a: 83 µM, b: 96 µM, c: 192 µM). Not all the units quit producing APs when the median network activity reached its lower limit around minute 300, but the activity rates of these units were very low (between 5 and 20 spikes/min. After the medium wash at minute 320, another overreaction is observed: the activity rates and (especially) the number of active units return to almost their initial reference levels, only to drop back down by approximately 35% before climbing gradually towards their initial values. A second medium change brought the activity rate all the way back up to its reference value (not shown in this diagram).

The rather large discrepancy between the unit-wise normalized and non-normalized median curves (white, light green, respectively) is explained by the activity histograms in figure 4.50: In c), after the second addition of lidocaine, the distribution becomes skewed and three subgroups can be seen, with the one around 0.2 dominating. The one around 2.5 is so far away from the rest of the distribution, that its members make a significant contribution to the overall network mean value (orange line). Similarly, d) and e) exhibit subgroups as well, which make it difficult to assign one single value as the network activity, but in both cases the median is better suited to describe the network behavior.

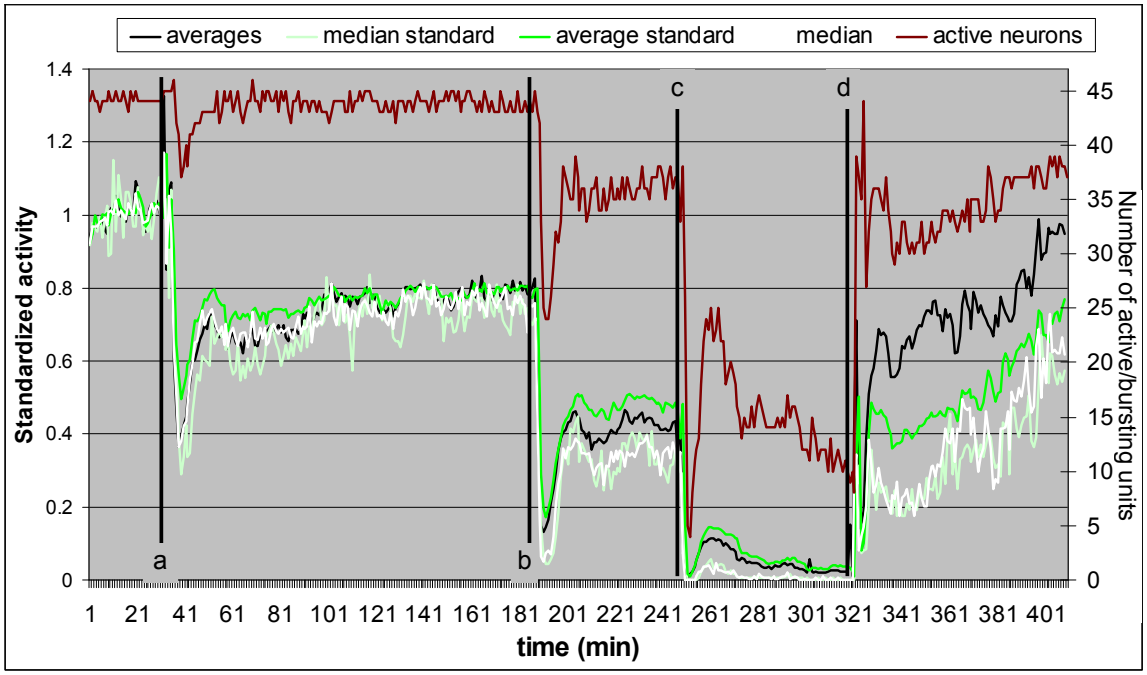

Fig. 4.49: Lidocaine titration in midbrain network. White and black curves: median, mean of unit-wise normalized data; light-green and green curves: median and mean calculated using the unedited data, then normalized. Dark red curve: number of active units.

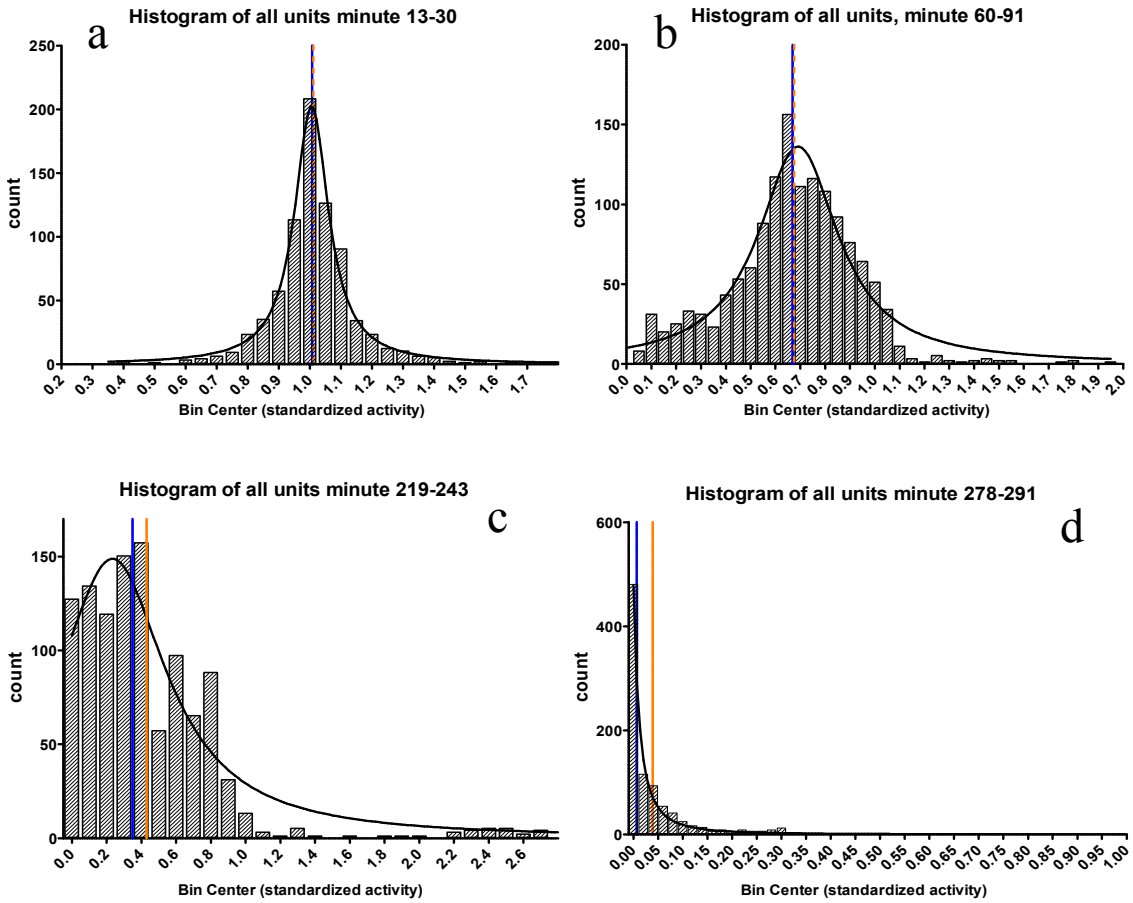

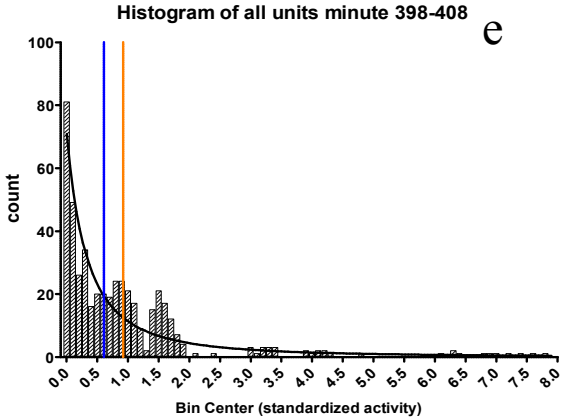

Fig. 4.50: Activity histograms of standardized spikes/min values of all units, bin size: 2, blue line: median of distribution, orange line: mean of distribution. Curve fit: Lorentzian, a: $R^2 = 0.99$, b: $R^2 = 0.94$, c: $R^2 = 0.9$, d: $R^2 = 0.99$, e: $R^2 = 0.88$.

4.3.2.3 Summary of data from seven networks

4.3.2.3.1 Dose-response curves generated with standard calculation of average:

A total of 40 data points from seven recordings were combined and analyzed by fitting them to the logarithmic decay function from equation 4-1. The result is shown in figure 4.51. This graph contains the average values that were computed before normalizing them, whereas figure 4.52 shows the median values that were calculated after the unit-wise normalization of the spikes/min values. While the unit-wise normalization and the use of the median caused a shift in the IC50 (27.5 instead of 40.7 µM), the goodness-of-fit parameter stayed almost the same (R^2 = 0.77, R^2 = 0.79, respectively).

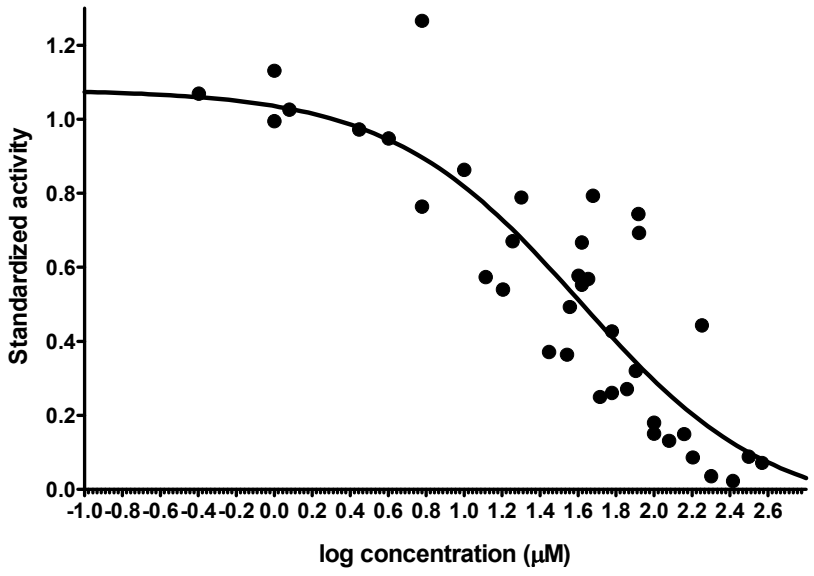

Fig. 4.51: Dose response curve generated using data from 11 recordings, IC50 = 40.7 ±1.5 µM, $R^2 = 0.79$

Best-fit values		**Goodness of Fit**	
Bottom	-0.06681	Degrees of Freedom	36
Top	1.080	R square	0.7927
LogIC50	1.610	Absolute Sum of Squares	1.028
HillSlope	-0.8663	Sy.x	0.1690
IC50	40.74	**Runs test**	
Span	1.147	Points above curve	16
Std. Error		Points below curve	24
Bottom	0.1621	Number of runs	20
Top	0.09519	P value (runs test)	0.5371
LogIC50	0.1711	Deviation from Model	Not Significant
HillSlope	0.2784	Number of points	
Span	0.2159	Analyzed	40

Table 4.4: Analysis and fit parameters from the data used to generate the dose-response curve in fig. 4.51

4.3.2.3.2 Dose-response curves generated with median of normalized data:

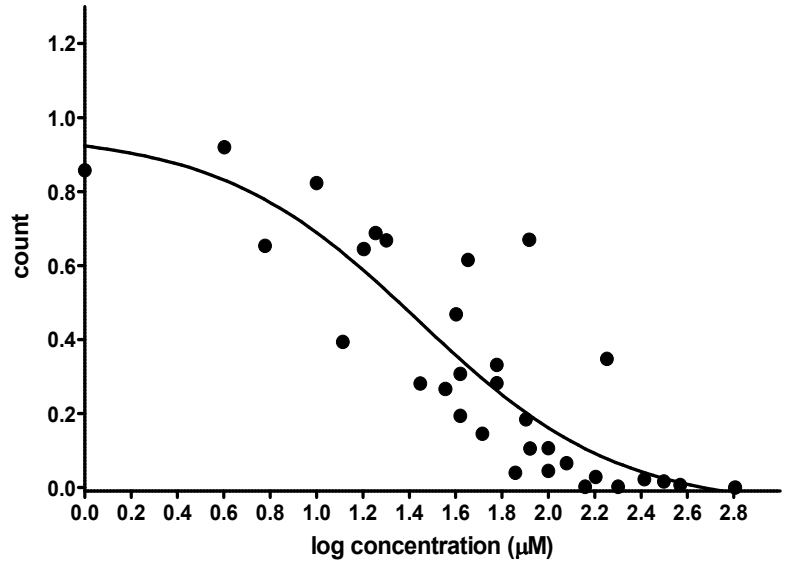

Fig. 4.52: Dose response curve generated using data from 11 recordings, IC50 = 27.5 ±1.46 μM, R^2 = 0.77

Best-fit values		**Goodness of Fit**	
Bottom	-0.05586	Degrees of Freedom	29
Top	0.9577	R square	0.7712
LogIC50	1.440	Absolute Sum of Squares	0.7128
HillSlope	-1.008	Sy.x	0.1568
IC50	27.52	**Runs test**	
Span	1.014	Points above curve	13

Std. Error		Points below curve	20
Bottom	0.1386	Number of runs	19
Top	0.1216	P value (runs test)	0.8465
LogIC50	0.1655	Deviation from Model	Not Significant
HillSlope	0.3876	Number of points	
Span	0.2145	Analyzed	33

Table 4.5: Analysis and fit parameters from the data used to generate the dose-response curve in fig. 4.52

4.4 Barbital-sodium experiments

4.4.1 Frontal cortex, data from three networks

4.4.1.1 Network averages calculated before normalization

Similarly to the lidocaine responses, the values from the barbital-sodium experiments were combined and fitted as shown in figure 4.53 and figure 4.54. Again, the first graph shows the average values that were calculated before normalization, and the second one shows the medians after normalization. The IC50 is now at 490 μM using the second method (567 μM using the first), and the curve fit is slightly better (R^2 = 0.84 instead of R^2 = 0.79.

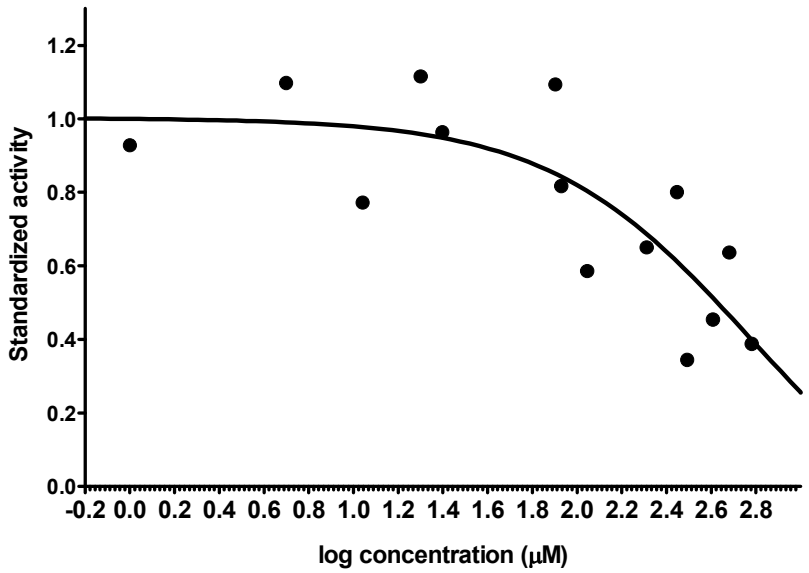

Fig. 4.53: Dose response curve generated using data from 3 recordings, IC50 = 567 ±1.7 μM, R^2 = 0.79

Best-fit values		**Goodness of Fit**	
Bottom	-0.1721	Degrees of Freedom	13
Top	0.9993	R square	0.7887
LogIC50	2.754	Absolute Sum of Squares	0.3187
IC50	566.9	Sy.x	0.1566
Span	1.171	Number of points	
Std. Error		Analyzed	16
Bottom	0.2547	**Runs test**	
Top	0.06473	Points above curve	6
LogIC50	0.2275	Points below curve	10
Span	0.2480	Number of runs	9
		P value (runs test)	0.7063
		Deviation from Model	Not Significant

Table 4.6: Analysis and fit parameters from the data used to generate the dose-response curve in fig. 4.53

4.4.1.2 Network median after normalization

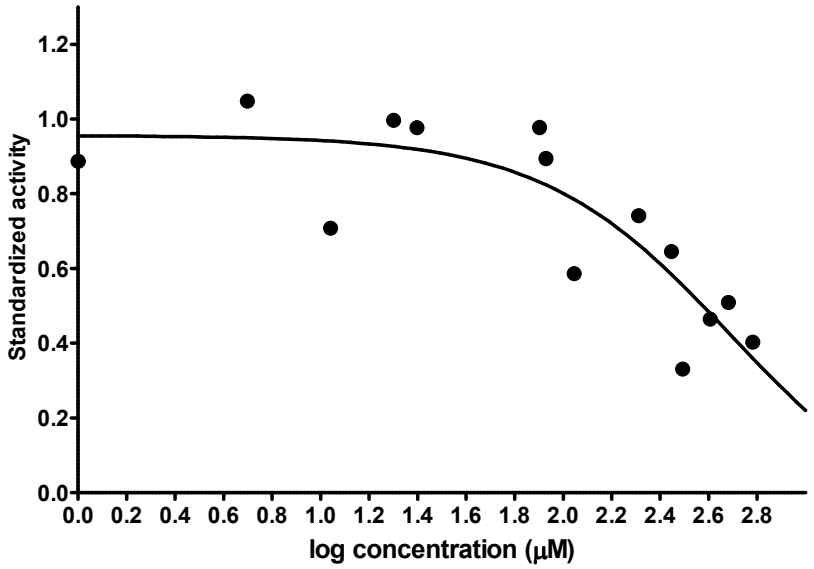

Fig. 4.54: Dose response curve generated using data from 3 recordings, IC50 = 490 ±1.82 μM, $R^2 = 0.84$

Best-fit values		**Goodness of Fit**	
Bottom	-0.1116	Degrees of Freedom	12
Top	0.9559	R square	0.8419
LogIC50	2.690	Absolute Sum of Squares	0.2133
HillSlope	-1.117	Sy.x	0.1333
IC50	490.1	**Runs test**	
Span	1.067	Points above curve	10
Std. Error		Points below curve	6
Bottom	0.2957	Number of runs	10
Top	0.06721	P value (runs test)	0.8636

LogIC50	0.2599	Deviation from Model	Not Significant
HillSlope	0.5593	Number of points	
Span	0.3265	Analyzed	16
		Outliers (not excluded, Q=1.0%)	0

Table 4.7: Analysis and fit parameters from the data used to generate the dose-response curve in fig. 4.54

4.4.2 Midbrain, data from two networks:

4.4.2.1 Network averages before normalization

Only two recordings using midbrain tissue could be made, but the analysis of this limited data set shows impressively how large the differences can be that the two analysis methods used here can produce. While there is hardly any chance of fitting the data when analyzed with the network average method without initial normalization (R^2 = 0.49, IC50 and other parameters not computable; figure 4.55, table 4.8, respectively), the fit is almost perfect when the median values are used and the spikes/min values are normalized first (R^2 = 0.99, IC50 = 1064 ±1.5 µM; fig. 4.56, table 4.9).

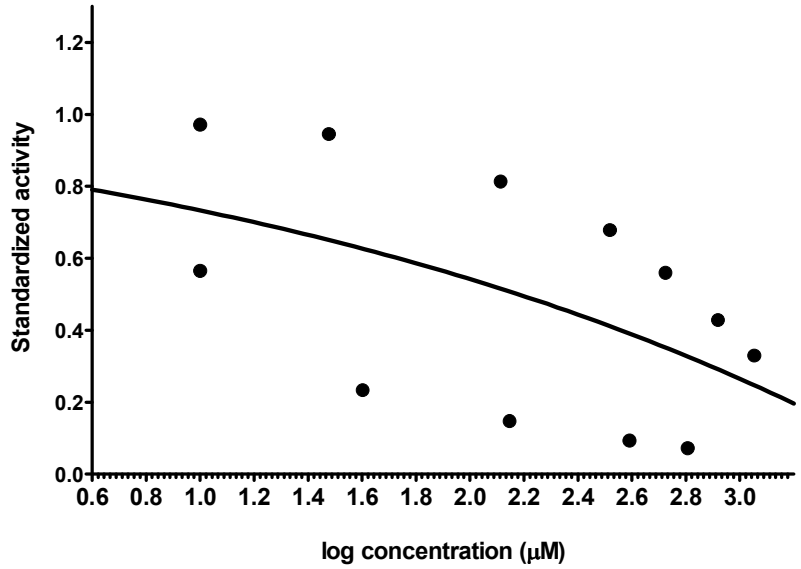

Fig. 4.55: Dose response curve generated using data from 2 recordings, IC50 = NA, R^2 = 0.49

Best-fit values		**Goodness of Fit**	
Bottom	~ -15.41	Degrees of Freedom	10
Top	1.130	R square	0.4858
LogIC50	~ 10.17	Absolute Sum of Squares	0.8404
HillSlope	~ -0.1755	Sy.x	0.2899

IC50	~ 1.478e+010	**Runs test**	
Span	~ 16.54	Points above curve	7
Std. Error		Points below curve	7
Bottom	~ 1387	Number of runs	11
Top	1.183	P value (runs test)	0.9749
LogIC50	~ 254.4	Deviation from Model	Not Significant
HillSlope	~ 0.9534	Number of points	
Span	~ 1388	Analyzed	14

Table 4.8: Analysis and fit parameters from the data used to generate the dose-response curve in fig. 4.55

4.4.2.2 Network median after normalization

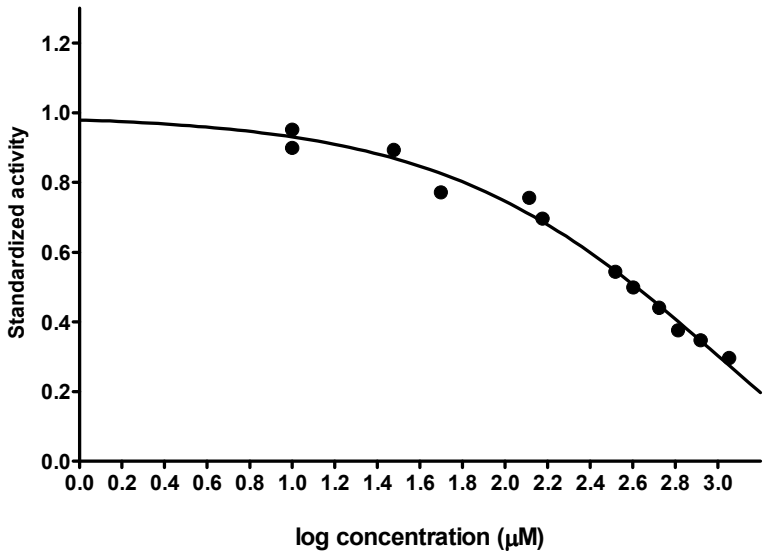

Fig. 4.56: Dose response curve generated using data from 2 recordings, IC50 = 1064 ±1.5 μM, $R^2 = 0.99$

Best-fit values		**Goodness of Fit**	
Bottom	-0.4164	Degrees of Freedom	10
Top	0.9943	R square	0.9925
LogIC50	3.027	Absolute Sum of Squares	0.008478
HillSlope	-0.6535	Sy.x	0.02912
IC50	1064	**Runs test**	
Span	1.411	Points above curve	7
Std. Error		Points below curve	7
Bottom	0.1869	Number of runs	8
Top	0.02544	P value (runs test)	0.6166
LogIC50	0.1774	Deviation from Model	Not Significant
HillSlope	0.08947	Number of points	
Span	0.2018	Analyzed	14
		Outliers (not excluded, Q=1.0%)	0

Table 4.9: Analysis and fit parameters from the data used to generate the dose-response curve in fig. 4.56

4.5 Cisplatin experiments

4.5.1 Frontal cortex responses

4.5.1.1 Sample recording

Cisplatin (CisPt) is a very common chemotherapeutic drug that has been associated with severe neurological side-effects. These effects have not been investigated satisfactorily on the cellular or network level. The exemplary recording in figure 4.57 shows that at low concentrations up to 10 µM, CisPt did not cause the spike rate to decrease substantially. At a cumulative concentration of 30 µM, the activity decreased by approximately 45%, and at 50 µM it was down to 20% of the original reference activity. At this point, up to 11 out of the 30 active units occasionally stopped firing in bursts, or altogether (dark green and red curves in figure 4.57). After a complete exchange of the culture medium, the spiking rate returned to its original value, indicating that the acute toxicity of cisplatin was reversible.

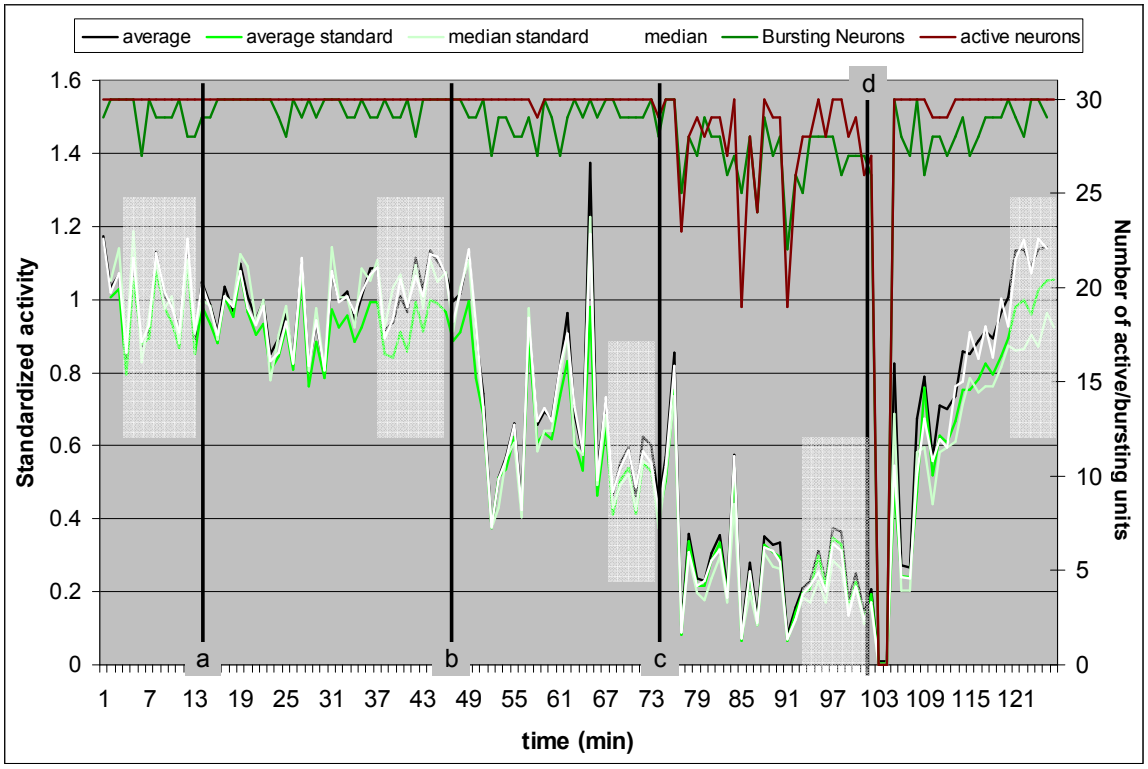

Fig. 4.57: FC recording with three cisplatin additions: a: +10 µM, b: +20 µM, c: +20 µM. d: full medium change. dark red curve: number of active units, dark green curve: number of bursting units. White shaded areas: time periods data for following histograms were taken from

The activity histograms (fig. 4.58) characterize the distribution of spike rates across all units beyond the mere quantification of activity levels as shown in figure 4.59. The network activity rate did not change significantly after the first addition of cisplatin (One-way-ANOVA, $p>0.05$). Neither differed distributions a and b from e

significantly, which means that the original reference activity was recovered adequately by washing out the cisplatin. However, the structures of the distributions in a, b and e were not entirely the same. All distributions resembled bell-shaped arrangements with varying degrees of skewness and were therefore fitted with a Lorentzian curve-fit. In a, the goodness-of-fit parameter was $R^2 = 0.88$, while it was 0.95 in b. This indicates a more synchronized activity behavior of the network units under 10 µM cisplatin than in plain culture medium. Following the subsequent cisplatin additions, the distributions were equally well fittable ($R^2 = 0.9$, 0,94 in c and d, respectively). After washing out the cisplatin, the median and the mean of the activity returned to the same level as during the reference period, but the spike production was distributed differently across the network. The curve fit is not as good ($R^2 = 0.75$), which means that the units did not follow the network trend homogenously, and it is much wider than before (span: 2.1, instead of 0.75), which also supports that interpretation.

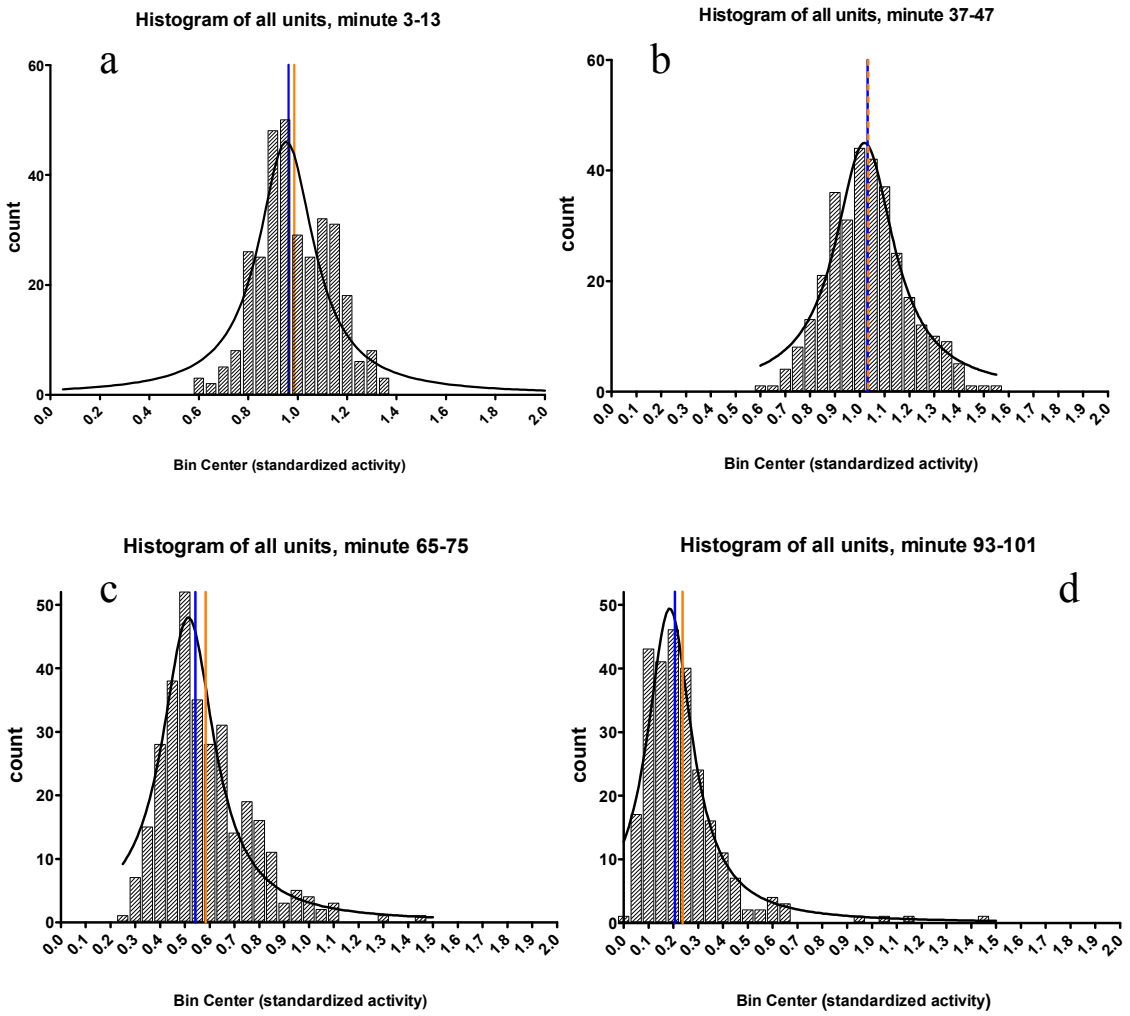

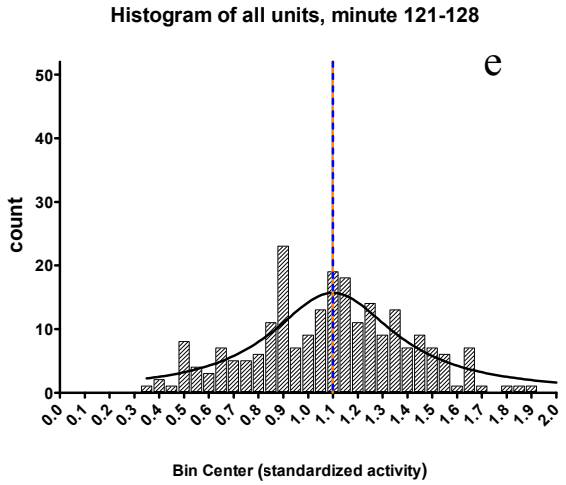

Fig. 4.58: Histograms of the minute median values from all units over the respective time periods indicated in figure 4.57. Blue vertical lines: medians; orange vertical lines: mean values. Goodness-of-fit parameters: a: $R^2 = 0.88$, b: $R^2 = 0.95$, c: $R^2 = 0.9$, d: $R^2 = 0.94$, e: $R^2 = 0.75$

Dunn's Multiple Comparison Test	Difference in rank sum	Significant? P < 0.05?
min 3-13 vs min 37-47	-68.93	No
min 3-13 vs min 65-75	515.9	Yes
min 3-13 vs min 93-101	974.3	Yes
min 3-13 vs min 121-128	-102.8	No
min 37-47 vs min 65-75	584.8	Yes
min 37-47 vs min 93-101	1043	Yes
min 37-47 vs min 121-128	-33.91	No
min 65-75 vs min 93-101	458.4	Yes
min 65-75 vs min 121-128	-618.7	Yes
min 93-101 vs min 121-128	-1077	Yes

Table 4.10: Results from one-way ANOVA with post-test comparing the activity distributions from figure 4.58 with each other. No significant differences between histogram a and b, a and e, and b and e (rows shaded grey).

4.5.1.2 Morphology of the neurons under CisPt

Before and after the MEA recording shown in figure 4.57, pictures of a portion of the neurons were taken. In figure 4.59, the neurons had not been subjected to cisplatin, whereas the picture in fig. 4.60 was taken while the cells were under the influence of 50 µM cisplatin. At this magnification (100x), no significant morphological changes were identified that would indicate any acutely cytotoxic properties of cisplatin.

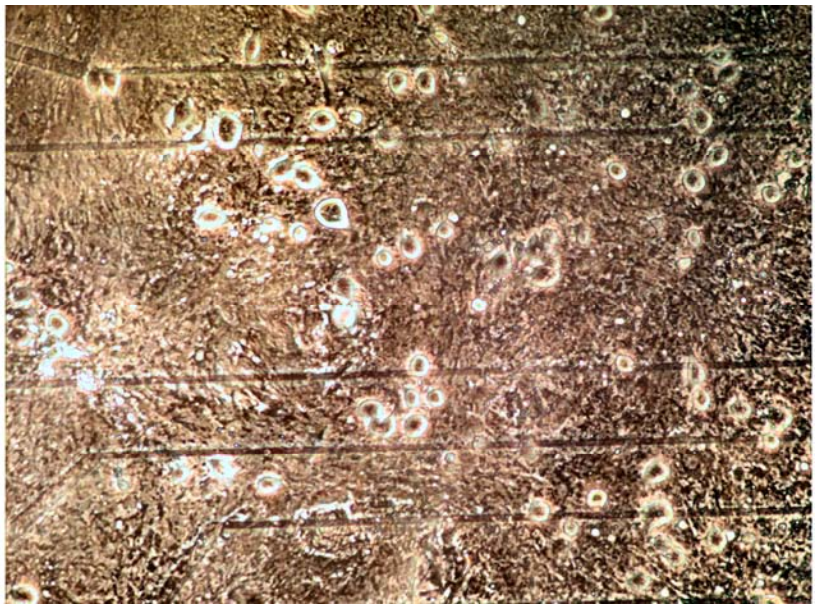

Fig. 4.59: Neurons and glia cells on the MEA plate used in the recording, before cisplatin was added.

Fig. 4.60: Neurons and glia cells on the MEA plate used in the recording, after addition of cisplatin.

4.5.1.3 Summary data from six networks

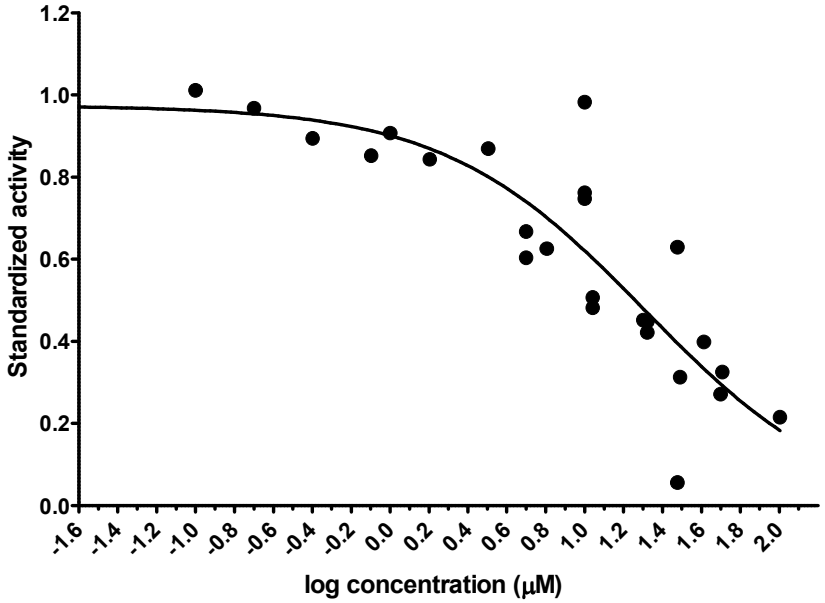

Fig. 4.61: Dose response curve generated with data from 6 recordings, IC50 = 20.5 ±3.45 μM, R^2 = 0.78

Best-fit values		**Goodness of Fit**	
Bottom	-0.02464	Degrees of Freedom	22
Top	0.9743	R square	0.7756
LogIC50	1.311	Absolute Sum of Squares	0.4209
HillSlope	-0.8393	Sy.x	0.1383
IC50	20.48	**Runs test**	
Span	0.9989	Points above curve	12
Std. Error		Points below curve	14
Bottom	0.5024	Number of runs	13
Top	0.08666	P value (runs test)	0.4296
LogIC50	0.5377	Deviation from Model	Not Significant
HillSlope	0.5155	Number of points	
Span	0.5525	Analyzed	26

Table 4.11: Analysis and fit parameters from the data used to generate the dose-response curve in fig. 4.61

4.5.2 Cisplatin responses after preincubation with 0.3 mM vitamin C

4.5.2.1 Data from 2 networks

In an attempt to protect the neurons from the acute cisplatin toxicity, two networks were pre-treated with 0.3 mM vitamin C, according to a clinical case study, in which this dose had proven useful (see introduction). As figure 4.62 shows, the network responses (medians) did indeed shift to the right, which means that the neurons were less susceptible to CisPt than the ones not treated with vitamin C. However,

concentrations above 100 μM in the culture medium could not be achieved with the cisplatin stock solution available. Therefore, the dose-response curve fit is not complete, and the IC50 value is only an estimate.

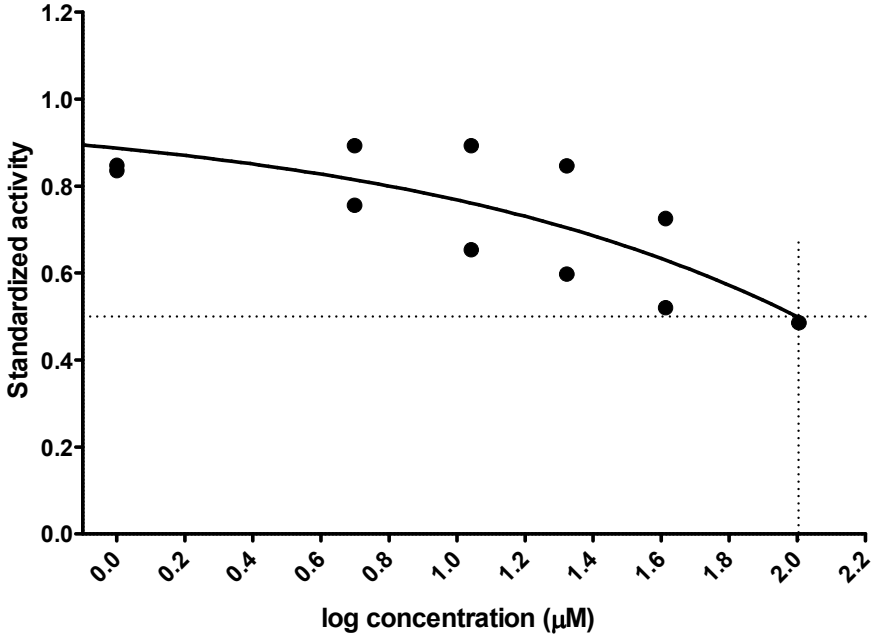

Fig. 4.62: Dose response curve generated using data from 11 recordings, IC50 ≈ 100 μM, $R^2 = 0.66$

4.5.3 Midbrain responses:

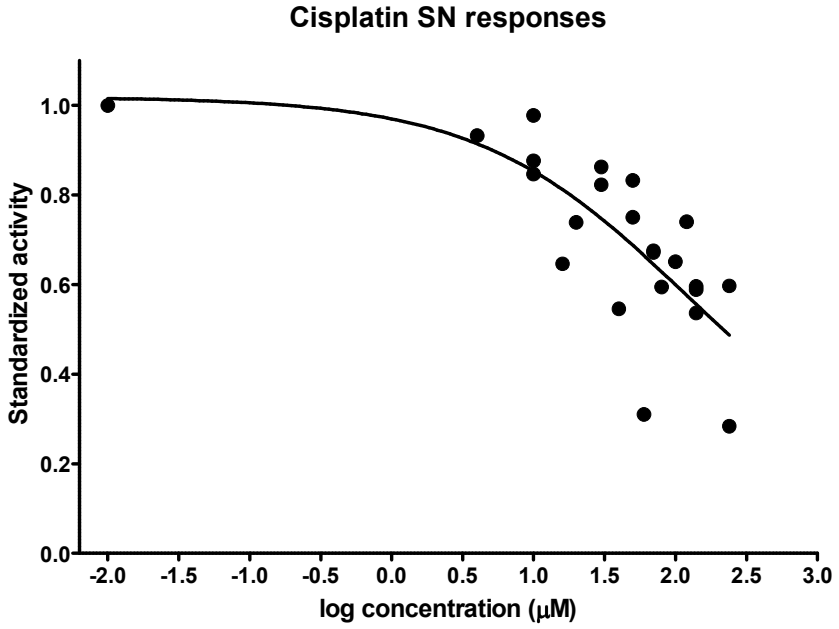

Fig. 4.63: Dose response curve generated using data from 6 recordings, IC50 = 114 ±103 μM, $R^2 = 0.56$

Midbrain cultures responded to cisplatin addition in a dose-dependent manner (fig. 4.63). However, complete inhibition of all activity was not caused at the doses applied (up to 400 μM). Higher concentrations could not be achieved since the concentration of the available, hypotonic stock solution would have required extensive volumes to be added. Thus the osmolarity of the recording medium would have been lowered significantly, which generally affects neuronal activity levels. The IC50 calculated from the midbrain recordings was 114 μM, 5.5-fold higher than for FC, supporting the notion that FC neurons are more sensitive to many different pharmacological substances than midbrain ones.

Best-fit values		Goodness of Fit	
Bottom	0.1468	Degrees of Freedom	19
Top	1.019	R square	0.5639
LogIC50	2.057	Absolute Sum of Squares	0.3339
HillSlope	-0.5959	Sy.x	0.1326
IC50	113.9	Runs test	
Span	0.8721	Points above curve	14
Std. Error		Points below curve	9
Bottom	1.234	Number of runs	14
Top	0.1427	P value (runs test)	0.8721
LogIC50	2.015	Deviation from Model	Not Significant
HillSlope	0.6907	Number of points	
Span	1.301	Analyzed	23

Table 4.12: Analysis and fit parameters from the data used to generate the dose-response curve in fig. 4.63

4.6 Chloroacetaldehyde experiments

4.6.1 Frontal cortex responses

CAA is the most prevalent and neurotoxic metabolite of Ifosfamide, a potent anti-neoplastic drug. Contrary to cisplatin, this compound proved to be highly neurotoxic, and its effects were not reversible through one or several consecutive medium changes.

Fig. 4.64 shows that 0.2 μM CAA sufficed to elevate the spike rate initially by 60% and then to reduce it by 70% over the following 20 minutes. Another 0.2 μM dose of CAA caused another initial, short activity increase. This increase was again approximately 60% in amplitude, measured based on the activity plateau that was generated by the first CAA dose. Over the subsequent 15 minutes, the activity decreased again, this time down to about 7% of the initial reference value. At the same time, the number of entirely inactive units rose to 50% of the original number. After the first CAA addition, 85% of the cells were still active. In contrast to the previous experiments using cisplatin, ethanol, lidocaine or barbital-sodium, a medium change was not sufficient to reverse the CAA effect permanently. After a very short 90%-recovery of the activity rate, the network activity declined again, this time until there was hardly any activity left, and 70% of the active units had fallen silent. This trend could not be stopped by a second medium change 37 minutes later, so that all activity was gone 190 minutes after the first addition of CAA.

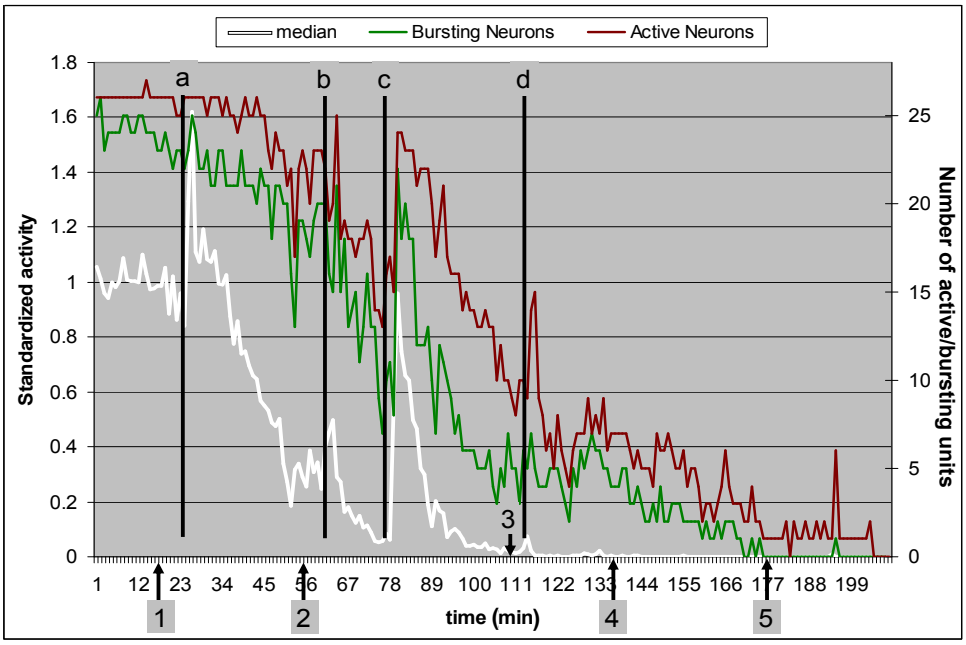

Fig. 4.64: CAA titration on FC tissue: a: +0.2 µM CAA; b: + 0.2 µM CAA; c, d: full medium change. Arrows: time points at which the pictures shown in figure 4.65 were taken.

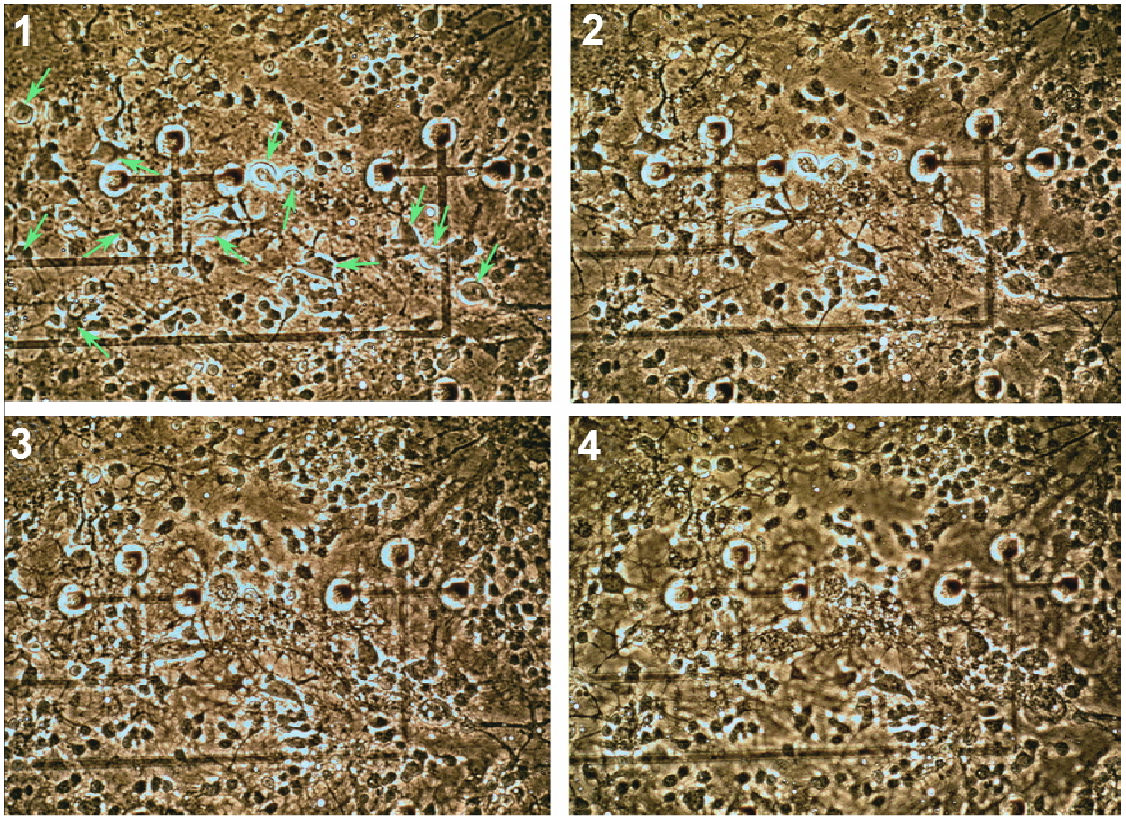

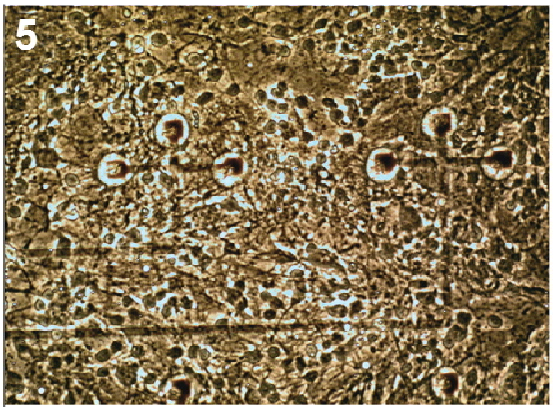

Fig. 4.65: Photographs of neurons taken at the time points denoted in fig. 4.64. Magnification: 100x. Green arrows in 1): Examples of neuronal cell bodies undergoing major cytoskeletal transformations throughout the CAA titration. Red arrows: electrode spots on MEA, ca. 15 µm diameter each.

An examination of the phase-contrast micrographs taken at the respective times denoted by arrows in figure 4.65 reveals dramatic morphological changes brought about by CAA. In 1), some of the neuronal somata are marked with green arrows for better orientation. The red arrows denote the recording electrodes. In this case, three de-insulated spots are located at the end of each conductor. By the time the activity had declined to almost zero (3), many of the cell bodies had become necrotic, and this transformation continued until hardly any phase-bright structures are visible in 5).

Another six CAA titrations are shown in figure 4.66. The following CAA concentrations were added to the respective cultures: a: 10 µM, then one medium change; b: 2 µM, then three medium changes; c: 6 µM, then one medium change; d: 30 µM, then three medium changes; e: 0.2 and 0.2 µM, then three medium changes; f: 5 and 20 µM, then one medium change. The recordings in e) and f) were interrupted due to technical problems, so that it is unclear whether the final activity plateau was reached before the end of the recording.

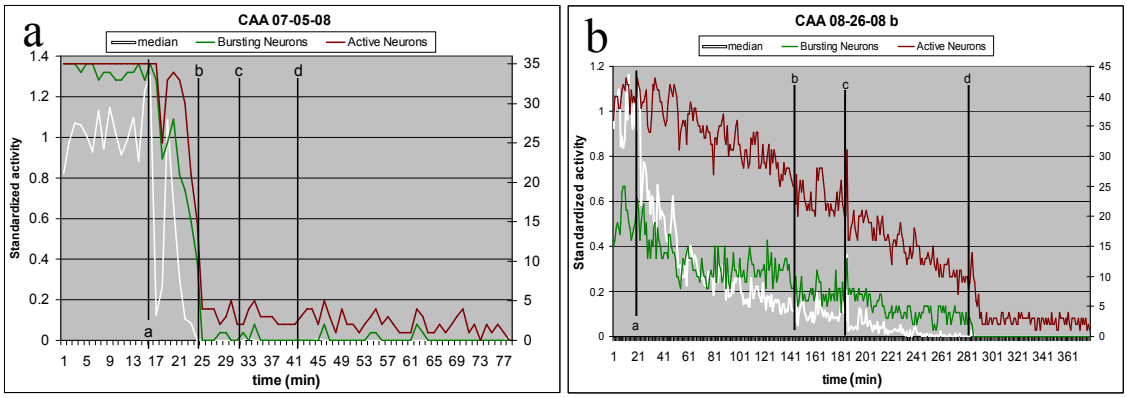

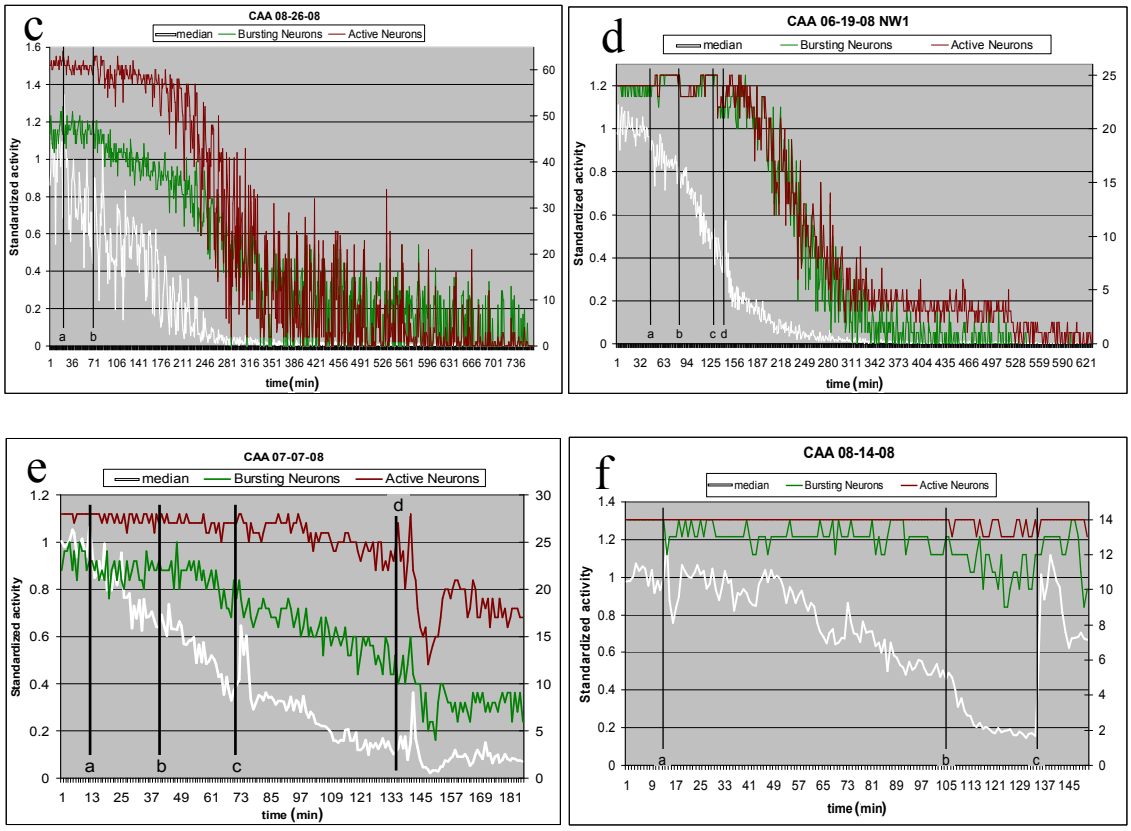

Fig. 4.66: Six independent recordings showing network responses (median, white curve) as well as number of participating units (active units: dark red curve; bursting units: dark green curve) resulting from CAA additions. Secondary y-axes: Number of active and bursting units.

4.6.2 Midbrain responses

Three cell cultures were used to evaluate the neurotoxicity of CAA on midbrain tissue. As it was the case for FC tissue, CAA caused irreversible activity suppressions, such as shown in fig. 4.67 a), where 20 µM CAA were added and a full medium change was administered only ten minutes later. After a short 160% increase in activity, the cells died very quickly. In b), 2 µM CAA caused the activity to decrease slowly.

Fig. 4.68 shows an attempt at protecting the cells from CAA using the antioxidant vitamin C. The result is in fact quite promising, as two additions of 1 µM CAA each did not cause a fatal activity decrease, and the activity recovered completely after a full medium change. Unfortunately, the recording could not be continued beyond the time period shown in the diagram because of a technical problem. This particular experiment should certainly be repeated in the future.

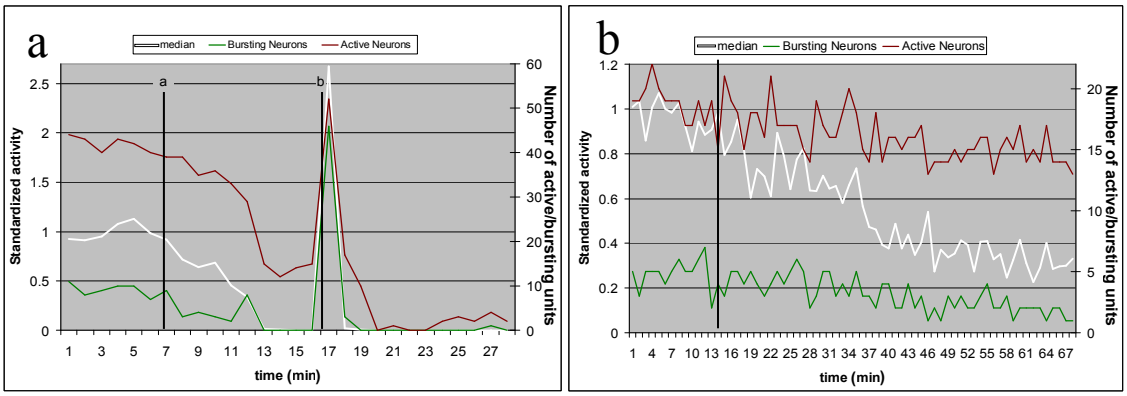

Fig. 4.67: a) +20 µM CAA, then one medium change; b) +2 µM CAA at black vertical bar. White curves: median network activity; green curves: bursting units, dark red curves: active units (both on secondary y-axis)

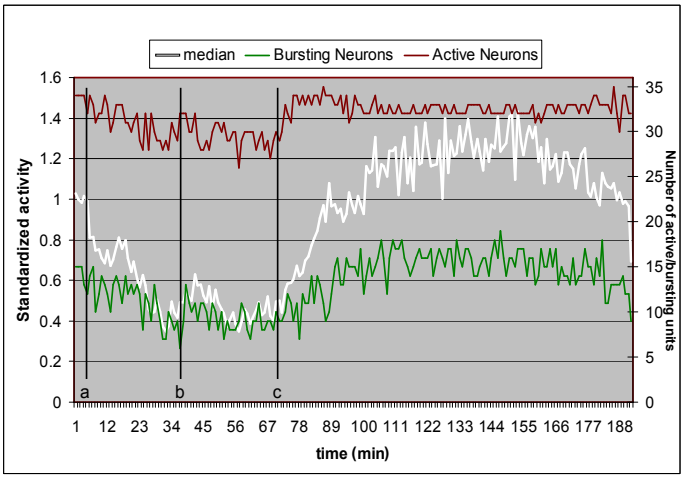

Fig. 4.68: Recording under 0.3 mM vitamin C. a, b: + 1 µM CAA, c: full medium change.

4.7 Amyloid-beta experiments

4.7.1.1 Analysis summary

Other than the compounds used in the investigations previously reported, beta-amyloid peptides are macromolecules which require more careful handling than ethanol, lidocaine, bicuculline or even cisplatin. Two main problems have to be addressed when using these peptides for actual titrations with cell cultures in order to make sure the cells actually experience the intended substance concentration. The first concern is whether the peptides interact with the culture medium, especially with the serum. Under conventional conditions, the cultures grow in culture medium that is supplemented with 5% horse serum, and that usually does not change during the recordings. The question whether the beta-amyloid peptides interact with or become inactivated by horse serum

could not be definitely answered before the first test runs. However, the weak and heterogeneous responses obtained during these first recordings (fig. 4.69) indicate that there is, in fact, a complex and significant interaction, which is not entirely digressive. Serum contains hundreds of different species of proteins, amino acids and other macromolecules that are well known to interact with each other.

On the other hand, it is equally important to maintain the functional integrity of the peptides *before* they are added to the culture medium. Since these substances react sensitively to changes in pH, they must be stored in appropriate buffer solutions that help avoid pH fluctuations. Serum-free recordings with a separate test of these buffer solutions were performed and are shown in fig. 4.70. Since two different types of beta-amyloid peptide were used here, and the stock concentrations were different with respect to the buffer molarities, several x-axes had to be plotted denoting the buffer concentration (black) and the amyloid-beta monomer/dimer concentrations (green/blue, respectively).

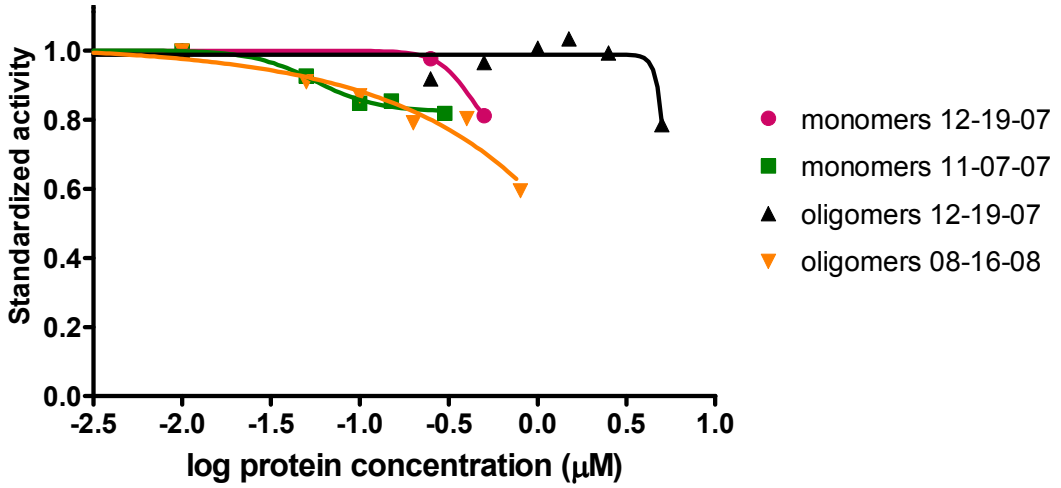

Fig. 4.69: Recordings in normal culture medium with 5 % horse serum (HS), showing inconclusive activity changes as a result of amyloid-beta monomer or oligomer additions.

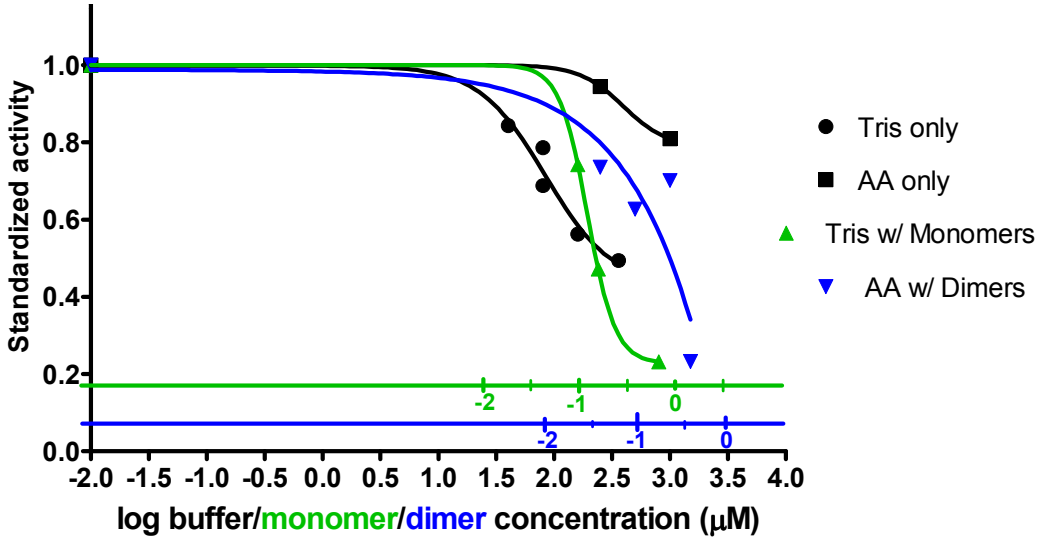

Fig. 4.70: Buffer tests (black) and monomer/dimer recordings (green/blue). The black x-axis quantifies the buffer concentrations tested, while the green and blue axes denote the monomer and dimer concentrations, respectively.

4.7.2 PH-buffer tests

4.7.2.1 Effects on activity levels

The beta-amyloid peptides used in this study are chains of 42 amino acids. This subtype of the amyloid-family is the dominating one found in human neurofibrillar plaques associated with AD. These peptides start out as single macromolecules (monomers) after they are cleaved by beta- and gamma-secretase, but they can quickly aggregate and form dimers, trimers, and so forth. After a long period of time, these oligomers can form even larger complexes, the fibrils, which in turn can clump together and precipitate as water-insoluble plaques in the brain, causing neuronal malfunction and death. However, recent findings have indicated that the smaller beta-amyloid aggregates may be acutely neurotoxic by interfering with the functions of cellular substructures, such as certain receptors or the cell membrane, directly. Available to us were small batches of monomers, dimers, and a mixture of oligomers (dimers, trimers, etc) without a precise description of the composition. Depending on the degree of aggregation, the peptides were stored in certain pH-buffers in order to maintain their functional integrity. Unfortunately, these buffer solutions, Tris and ammonium acetate (AA), were found to have certain neuroactive qualities of their own. Figure 4.71 shows that Tris buffer did suppress the spike production by as much as 50% at a concentration of 360 µM (around minute 145-160). In the second part of the experiment, a total concentration of 1 mM AA caused a 20% activity drop.

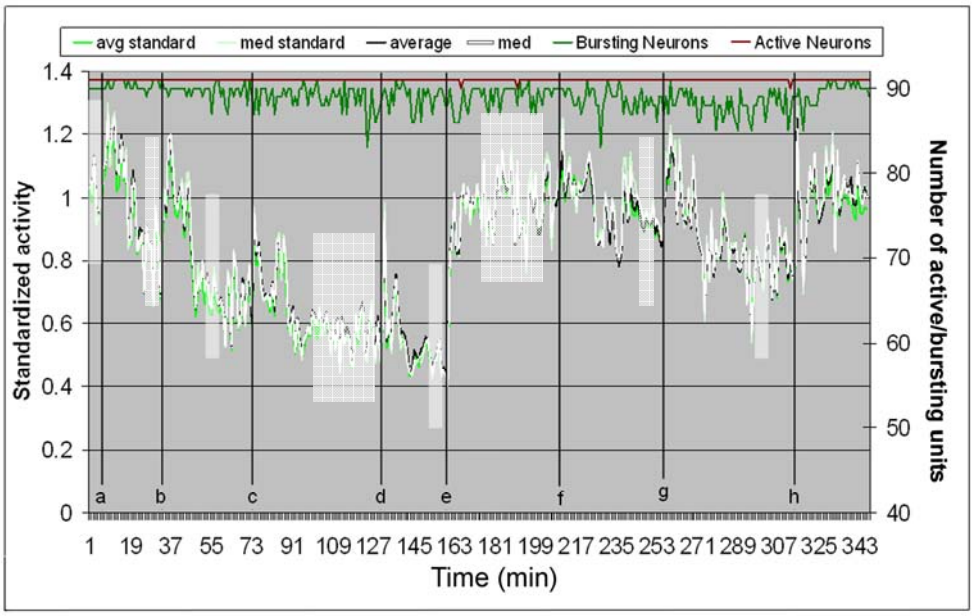

Fig. 4.71: Frontal cortex recording, 91 units total, culture: 48 days in vitro. a), b): +40 µM Tris; c): +80 µM Tris, d): +200 µM Tris, e): medium change, f): +250 µM Ammonium acetate (AA), g): +750 µM AA, h): medium change. White shaded areas: periods for analysis in the following histograms.

4.7.2.2 Burst parameter analysis

Since the buffer solutions did affect the activity rates by themselves, a quantification of the beta-amyloids' neuroactivity solely based on spike rate changes might prove difficult, even though a trend towards a stronger response to the buffer solutions with the peptides than to the buffers alone is visible (fig. 4.70). Therefore, a closer look at the internal structures of the activity dynamics is likely to be useful. As mentioned earlier, frontal cortex neurons always fire in unison, at least *in vitro*. By organizing the activity in short periods of concerted spiking, the so-called bursts, and relatively long periods of silence, a number of bursting parameters emerge that can be modulated. Fig. 4.72 shows what the burst pattern from the recording in figure 4.71 looked like, both in its reference state (a, b), and under 40 µM Tris (c, d). One important parameter is the burst period, which is a "network parameter", not a unit-specific parameter, given all the units always participate in every burst. Another important parameter is the spike frequency inside the bursts, which is unit-specific. This can be seen in b and d, which are detailed depictions of the bursts marked in a and c, respectively. The third basic parameter used to describe the burst pattern is the number of spikes in a burst, which is unit-specific, too.

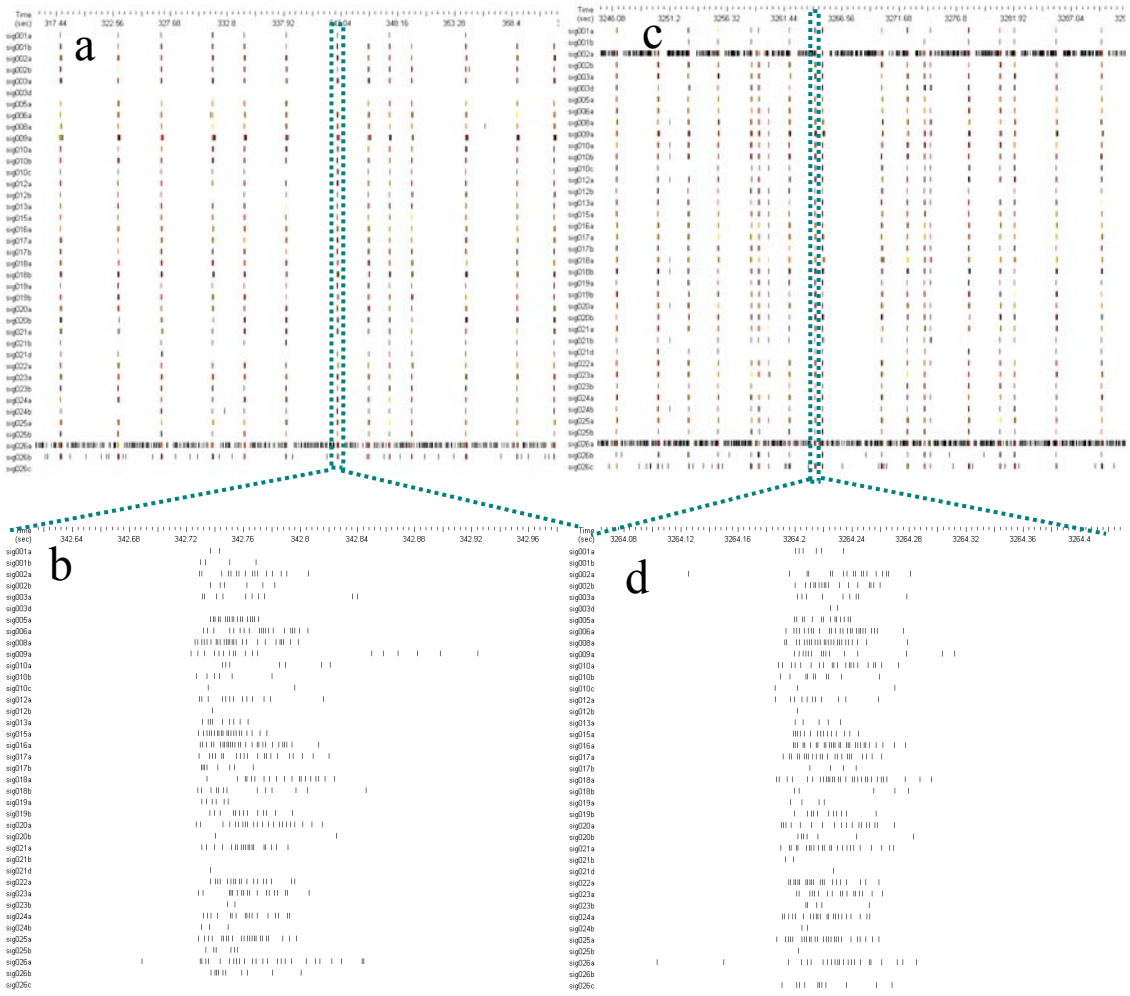

Fig. 4.72: Burst patterns taken from the recording in fig. 4.71, showing the activity pattern (a, c) and a detailed view of one burst each (b, d, respectively) Window widths: a, c: 47 seconds; b, d: 364 milliseconds.

The values for the burst period can be plotted as shown in figure 4.73. There is hardly any difference between the mean and the median burst period calculated from the individual unit values, which verifies the claim that it is a network parameter and requires no further in-depth analysis as to which way it should be quantified to yield the highest statistical precision and significance. In this case, 360 µM Tris elevated the burst period by 78%, while 1 mM AA raised it by only 14%.

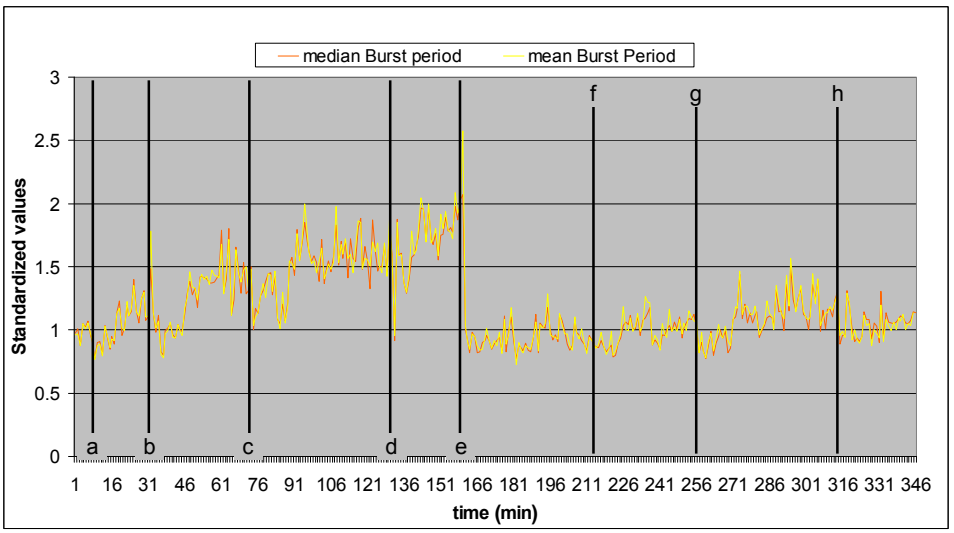

Fig. 4.73: Graph showing the evolution of the burst period over the entire recording. Yellow curve: Mean burst period.

In case of the spike frequency inside the bursts ("burst Hz") and the number of spikes per burst, the analysis is more complicated. Bursts are complex structures comprised by each participating units of a short chain of single events, the APs. Their distribution is highly dynamic and sometimes differs significantly from unit to unit, as we saw in fig. 4.72 b) and d). Just like the total number of spikes/min, which has been the main parameter for activity evaluation so far, there is a distribution of both the number of spikes per burst and the burst Hz, over all the active units. This means that before being able to quantify changes in those two parameters accurately, we have to investigate first which analysis approach is best suited, similar to what was done earlier with the spikes/min values. The key questions are again whether the data should be normalized first with respect to each unit's reference period, and whether it makes sense to use the median of all units' values as the one number describing the network behavior. Figures 4.74 and 4.75 reveal by how much the results vary depending on which method is chosen: In 4.74, the median and mean values of the burst Hz (dark blue and light blue lines, respectively) and of the spikes per burst (dark red and red lines, respectively) were calculated first and then normalized, while in 4.75 the process was carried out the other way around. The differences appear to be only marginal for the burst Hz graphs but major for the spikes per burst values.

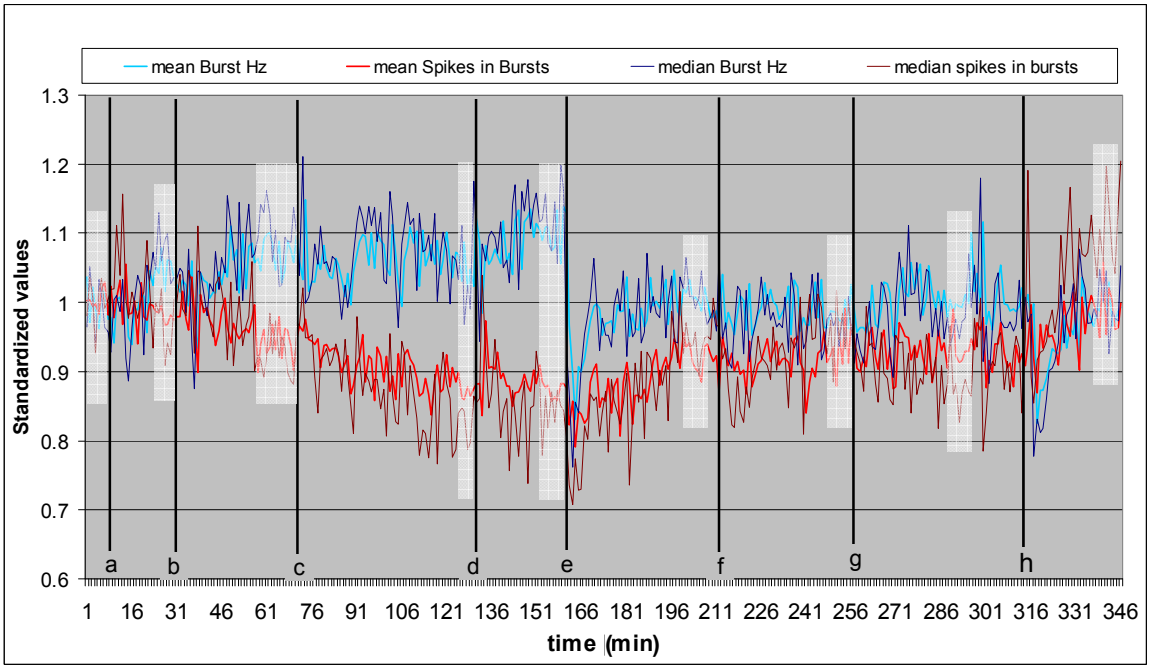

Fig. 4.74: Light blue and dark blue curves: mean and median values of the spike frequency inside the bursts ("burst Hz"), respectively; red and dark red curves: mean and median of the number of spikes per burst. All values were calculated before normalizing with respect to the initial reference activity period.

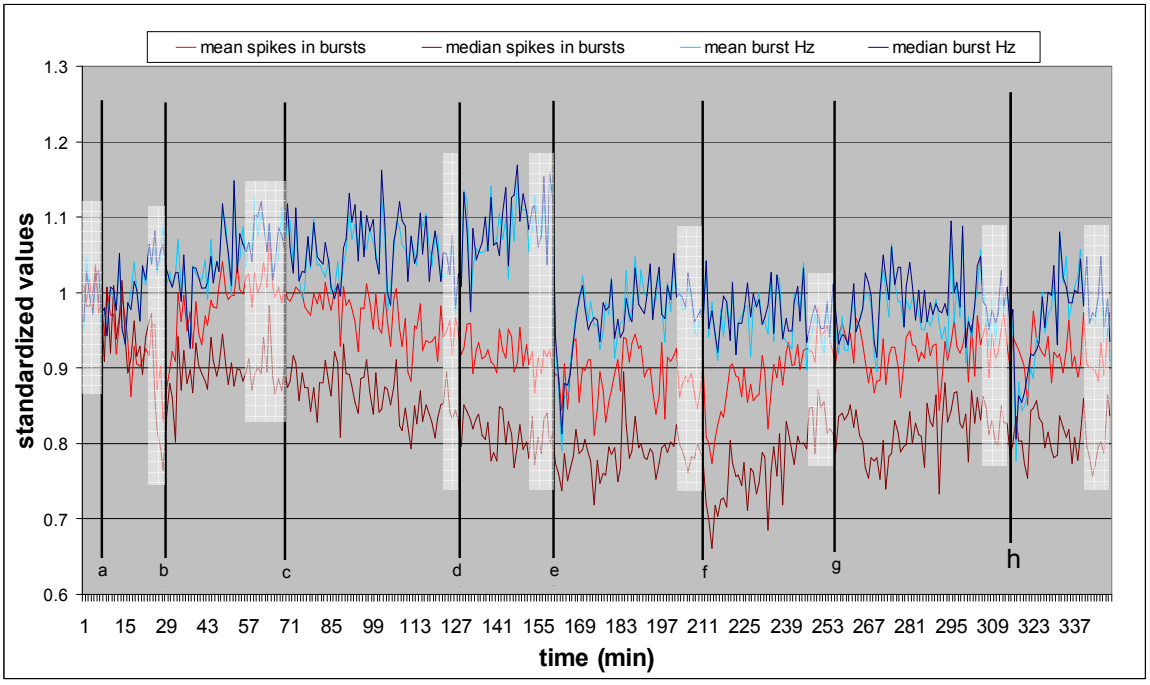

Fig. 4.75: Light blue and dark blue curves: mean and median values of the spike frequency inside the bursts ("burst Hz"), respectively; red and dark red curves: mean and median of the number of spikes per burst. All values were calculated after normalizing with respect to the initial reference activity period.

4.7.2.2.1 Detailed analysis: Number of spikes per burst

In order to quantify the discrepancies between the values resulting from the different analysis methods, histograms of the non-normalized spikes/burst values of all individual units over the time periods shown in figs. 4.74 and 4.75 were plotted (fig. 4.76, a)-i)). In addition, these data were combined in a multiple box plot (fig. 4.76 j) showing the 25th-75th percentile of the data as the box, the median as the line crossing it, the mean as a cross inside the box, with the whiskers representing the 1st-99th percentile and the black dots the outliers. Statistical analysis of these data reveals poor R^2-values of the Lorentzian curve fits performed on each of the histograms (between 0.488 and 0.817, see the legend of fig. 4.76). Additionally, a one-way ANOVA with a post-test comparing every histogram's median with each other's for significant differences was carried out (table 4.13). According to this evaluation, only ten out of the 36 possible comparisons were considered significantly different.

Normalizing each unit's values first before calculating the network mean or median provides a different picture: The distributions are not as obviously split up into several subgroups as before, and they follow their fitted curves much more rigorously (R^2-values 0.91 – 0.98, see the legend of fig. 4.77). The ANOVA-analysis (table 4.14) reveals that 21 out of 36 possible combinations yield significant differences now when compared with each other. This means that there is an increase in sensitivity towards changes in the number of spikes per burst when calculated after normalizing each unit's values first. Visual inspection of the histograms in fig. 4.77 also shows that the median values (blue vertical bars) either give a better indication of the location of the distribution's peak than, or the same as, the network mean which is labeled with an orange vertical line. In summary, the number of spikes per burst decreased by 8.4% as a response to 360 µM Tris, and by 6.8% under 1 mM AA.

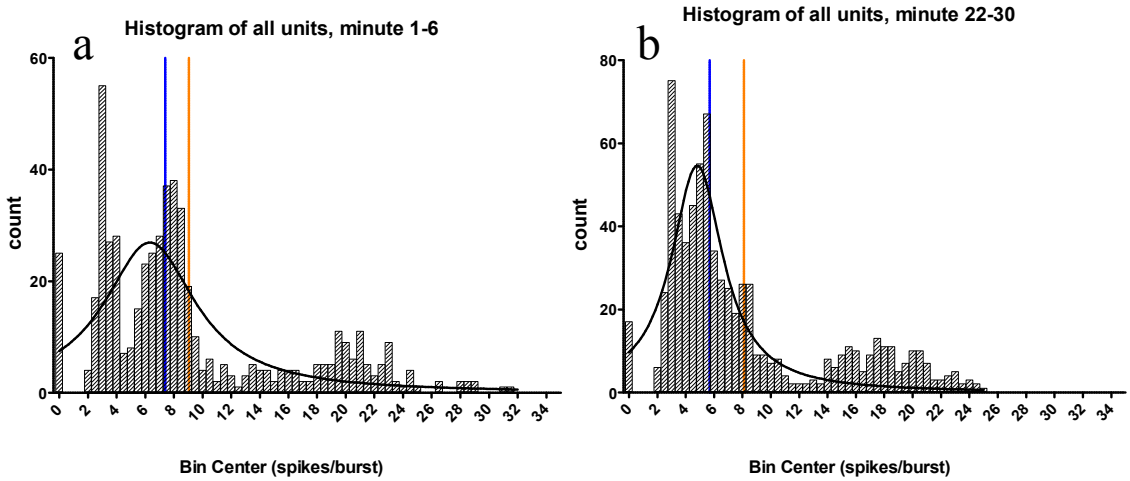

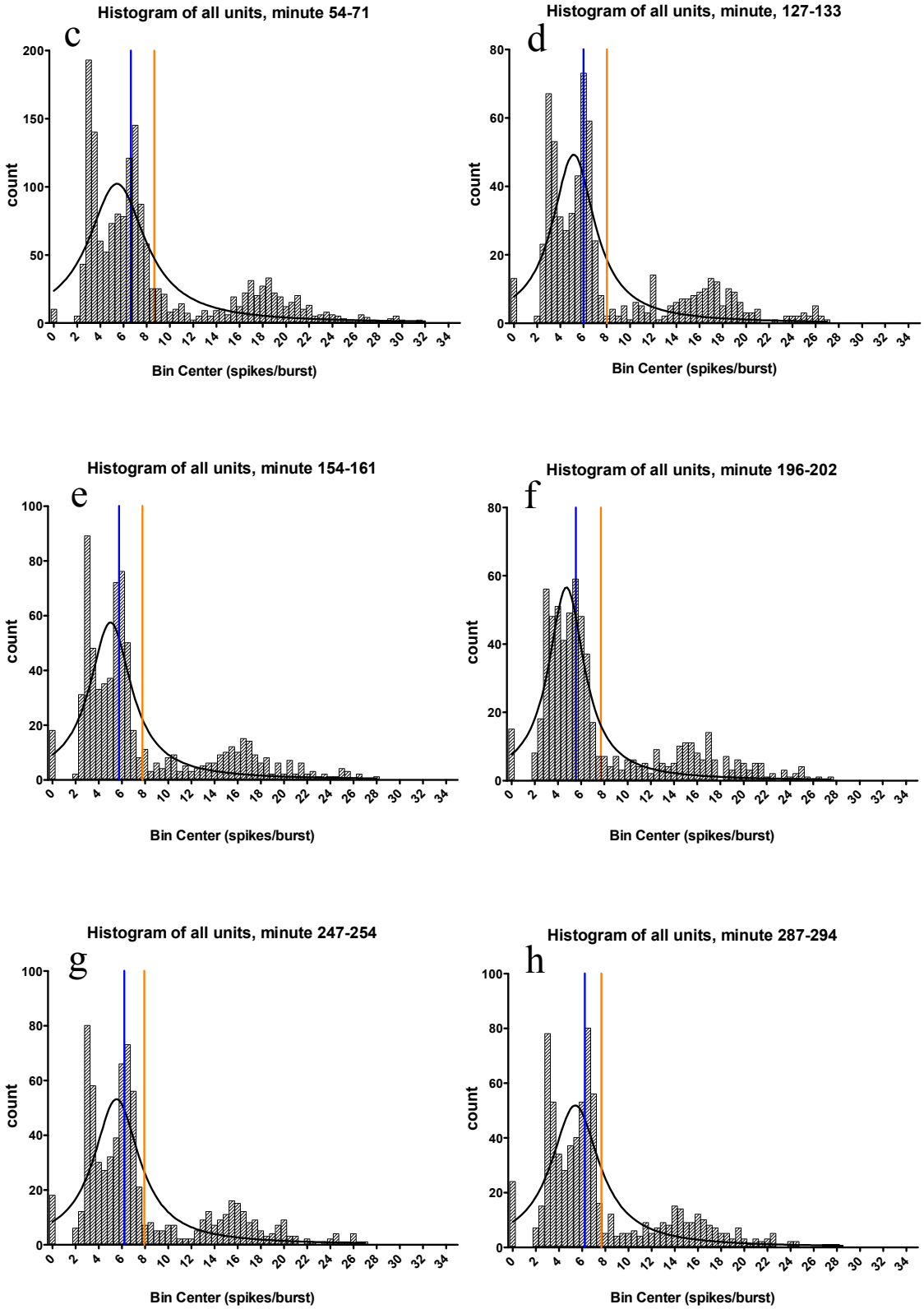
Histogram of all units, minute 54-71
c
count
Bin Center (spikes/burst)
Histogram of all units, minute, 127-133
d
count
Bin Center (spikes/burst)
Histogram of all units, minute 154-161
e
count
Bin Center (spikes/burst)
Histogram of all units, minute 196-202
f
count
Bin Center (spikes/burst)
Histogram of all units, minute 247-254
g
count
Bin Center (spikes/burst)
Histogram of all units, minute 287-294
h
count
Bin Center (spikes/burst)

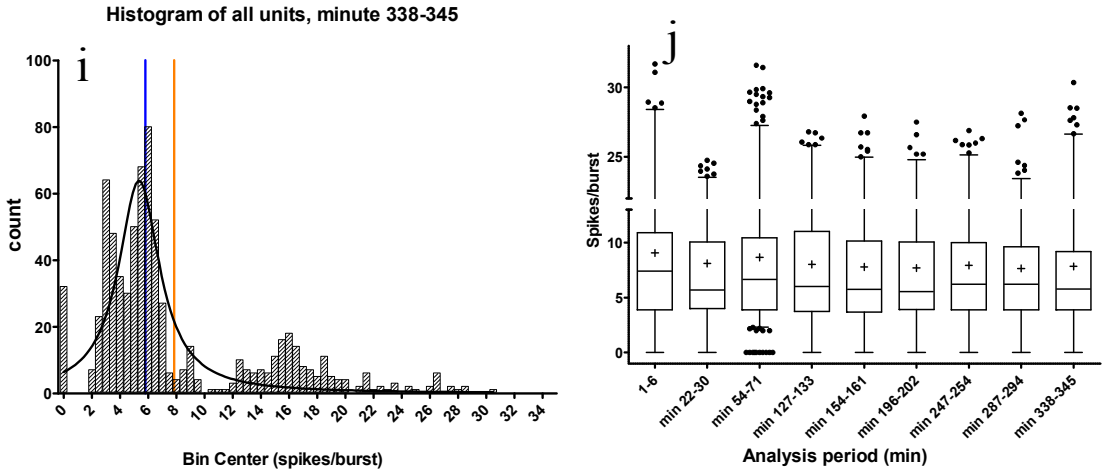

Fig. 4.76: a)– i): Spikes/burst histograms for all time periods indicated in fig. 4.71. R^2 values (a – i): 0.488, 0.736, 0.563, 0.617, 0.633, 0.817, 0.604, 0.619, 0.699. j): box plot summarizing the histograms

Dunn's Multiple Comparison Test	Difference in rank sum	Significant? P < 0.05?
1-6 vs 22-30	416.0	Yes
1-6 vs 54-71	175.2	No
1-6 vs 127-133	474.8	Yes
1-6 vs 154-161	579.7	Yes
1-6 vs 196-202	605.9	Yes
1-6 vs 247-254	381.7	Yes
1-6 vs 287-294	453.7	Yes
1-6 vs 338-345	555.4	Yes
22-30 vs 54-71	-240.8	No
22-30 vs 127-133	58.78	No
22-30 vs 154-161	163.7	No
22-30 vs 196-202	189.9	No
22-30 vs 247-254	-34.33	No
22-30 vs 287-294	37.69	No
22-30 vs 338-345	139.4	No
54-71 vs 127-133	299.6	No
54-71 vs 154-161	404.5	Yes
54-71 vs 196-202	430.8	Yes
54-71 vs 247-254	206.5	No
54-71 vs 287-294	278.5	No
54-71 vs 338-345	380.3	Yes
127-133 vs 154-161	104.9	No
127-133 vs 196-202	131.1	No
127-133 vs 247-254	-93.11	No
127-133 vs 287-294	-21.09	No
127-133 vs 338-345	80.65	No
154-161 vs 196-202	26.26	No
154-161 vs 247-254	-198.0	No
154-161 vs 287-294	-126.0	No
154-161 vs 338-345	-24.24	No
196-202 vs 247-254	-224.3	No
196-202 vs 287-294	-152.2	No
196-202 vs 338-345	-50.50	No
247-254 vs 287-294	72.02	No
247-254 vs 338-345	173.8	No
287-294 vs 338-345	101.7	No

Table 4.13: Results of a one-way ANOVA analysis with post-test comparing each histogram's data distribution from figure 4.76 j) with each other for significant differences in the medians.

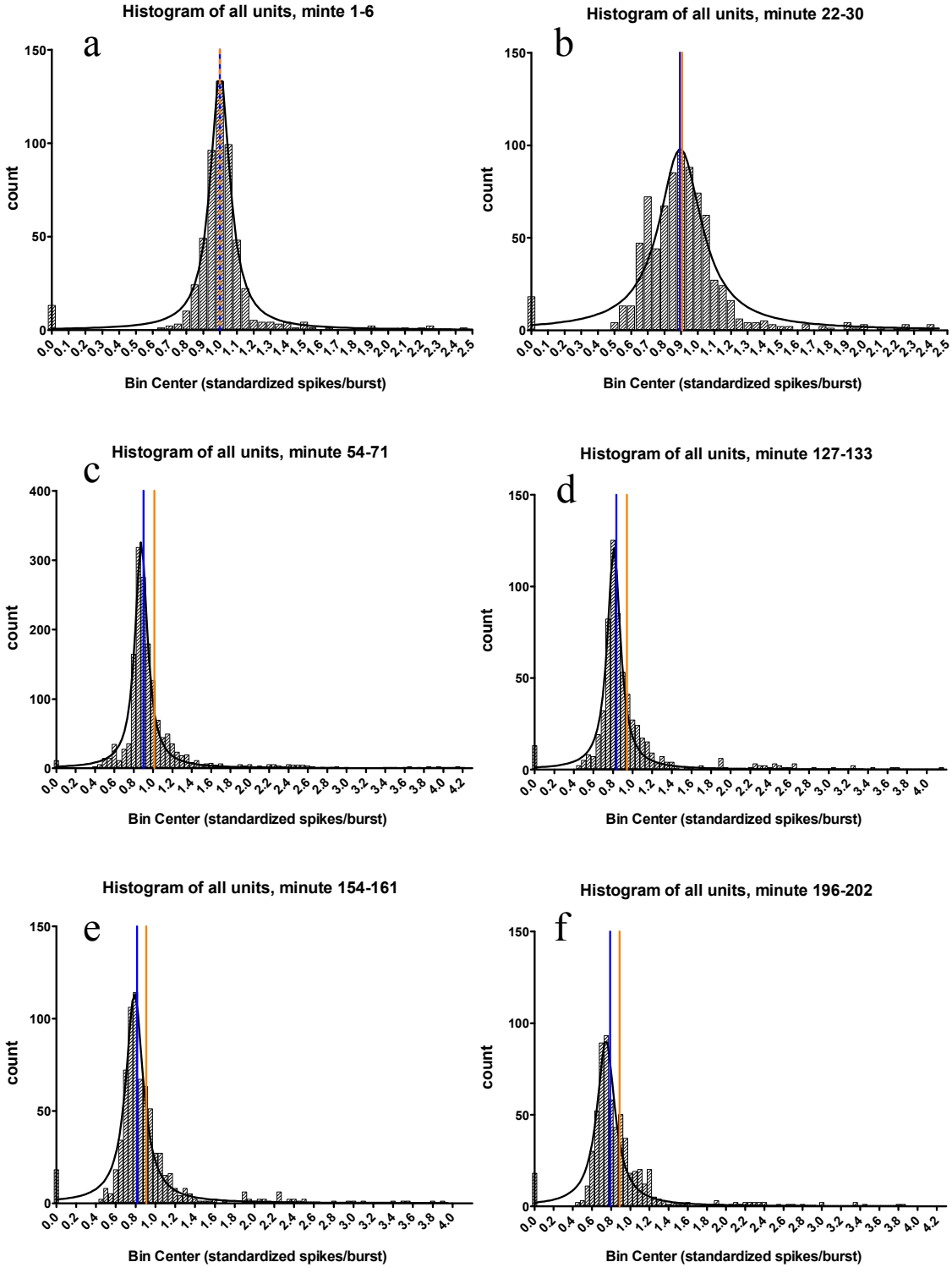
Histogram of all units, minte 1-6
a
count
Bin Center (standardized spikes/burst)
Histogram of all units, minute 22-30
b
count
Bin Center (standardized spikes/burst)
Histogram of all units, minute 54-71
c
count
Bin Center (standardized spikes/burst)
Histogram of all units, minute 127-133
d
count
Bin Center (standardized spikes/burst)
Histogram of all units, minute 154-161
e
count
Bin Center (standardized spikes/burst)
Histogram of all units, minute 196-202
f
count
Bin Center (standardized spikes/burst)

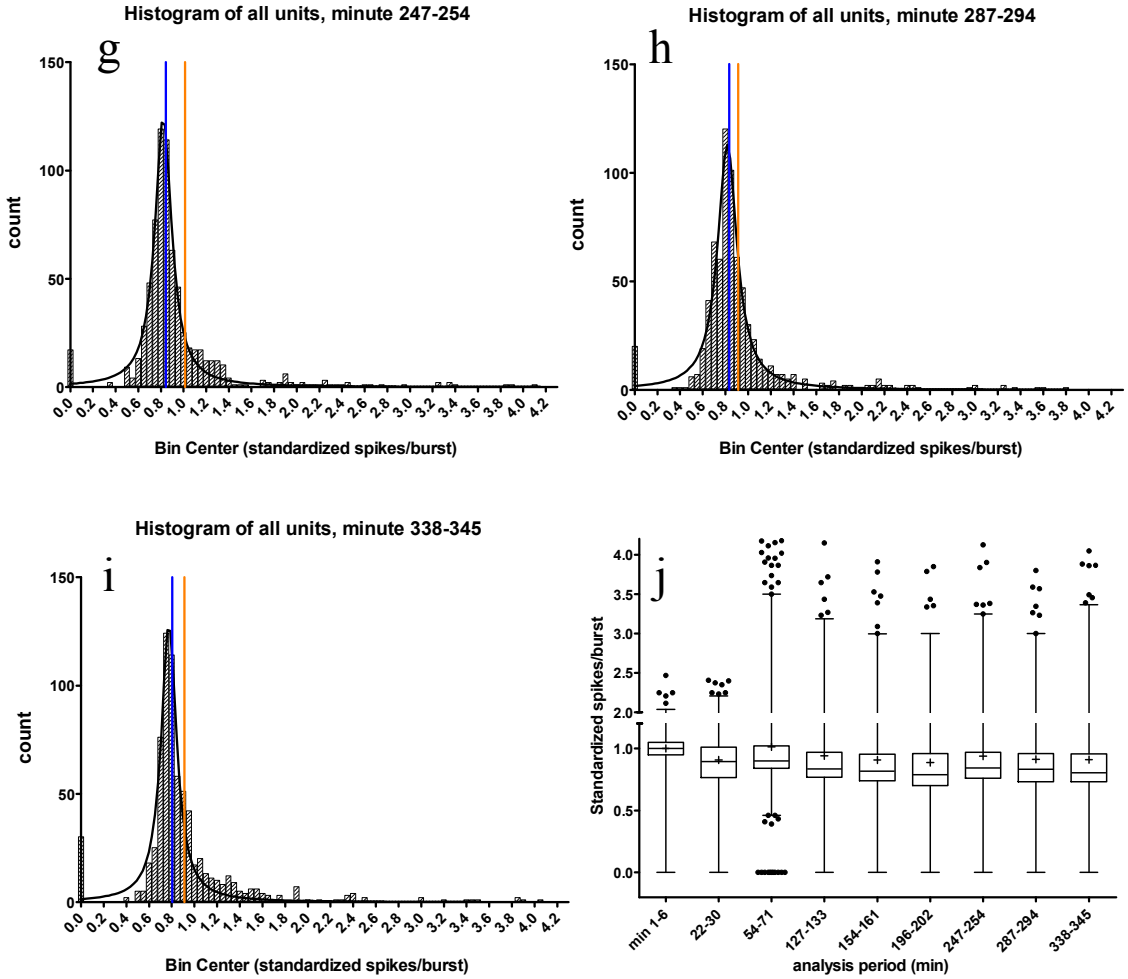

Fig. 4.77: a) – i): Spikes/burst histograms for all time periods indicated in fig. 4.71. R^2 values (a – i): 0.984, 0.928, 0.964, 0.964, 0.95, 0.912, 0.977, 0.954, 0.937. j): box plot summarizing the histograms

Dunn's Multiple Comparison Test	Difference in rank sum	Significant? P < 0.05?
min 1-6 vs 22-30	1383	Yes
min 1-6 vs 54-71	893.2	Yes
min 1-6 vs 127-133	1688	Yes
min 1-6 vs 154-161	1938	Yes
min 1-6 vs 196-202	2154	Yes
min 1-6 vs 247-254	1668	Yes
min 1-6 vs 287-294	1846	Yes
min 1-6 vs 338-345	1967	Yes
22-30 vs 54-71	-490.0	Yes
22-30 vs 127-133	305.2	No
22-30 vs 154-161	554.7	Yes
22-30 vs 196-202	770.9	Yes
22-30 vs 247-254	285.0	No
22-30 vs 287-294	463.0	Yes
22-30 vs 338-345	583.5	Yes
54-71 vs 196-202	1261	Yes
54-71 vs 247-254	775.1	Yes
54-71 vs 287-294	953.1	Yes
54-71 vs 338-345	1074	Yes
127-133 vs 154-161	249.5	No
127-133 vs 196-202	465.7	Yes
127-133 vs 247-254	-20.19	No
127-133 vs 287-294	157.8	No
127-133 vs 338-345	278.3	No
154-161 vs 196-202	216.2	No
154-161 vs 247-254	-269.7	No
154-161 vs 287-294	-91.66	No
154-161 vs 338-345	28.82	No
196-202 vs 247-254	-485.9	Yes
196-202 vs 287-294	-307.9	No
196-202 vs 338-345	-187.4	No

54-71 vs 127-133	795.2	Yes	247-254 vs 287-294	178.0	No
54-71 vs 154-161	1045	Yes	247-254 vs 338-345	298.5	No
			287-294 vs 338-345	120.5	No

Table 4.14: Results of a one-way ANOVA analysis with post-test comparing each histogram's data distribution with each other for significant differences in the medians.

4.7.2.2.2 Detailed analysis: Spike frequency inside bursts

The differences in the analysis of the burst Hz values are not as pronounced as it was the case for the spikes/burst distributions. Here, the R^2 values for the histogram curve fits lie within similar ranges: 0.89 – 0.96 for the distributions calculated from the raw values (fig. 4.78), as opposed to 0.94 – 0.99 for those calculated from normalized data (fig. 4.79). The ANOVA tests found 21 out of 36 combinations to be significantly different when analyzed using the raw data, but 28 out of 36 when the calculations were based on the normalized numbers. Therefore, the median values of the normalized data should be used here as well. As a result, the burst Hz increased by 8.7% under the influence of 360 µM Tris, whereas dropped by 2% after the addition of 1 mM AA.

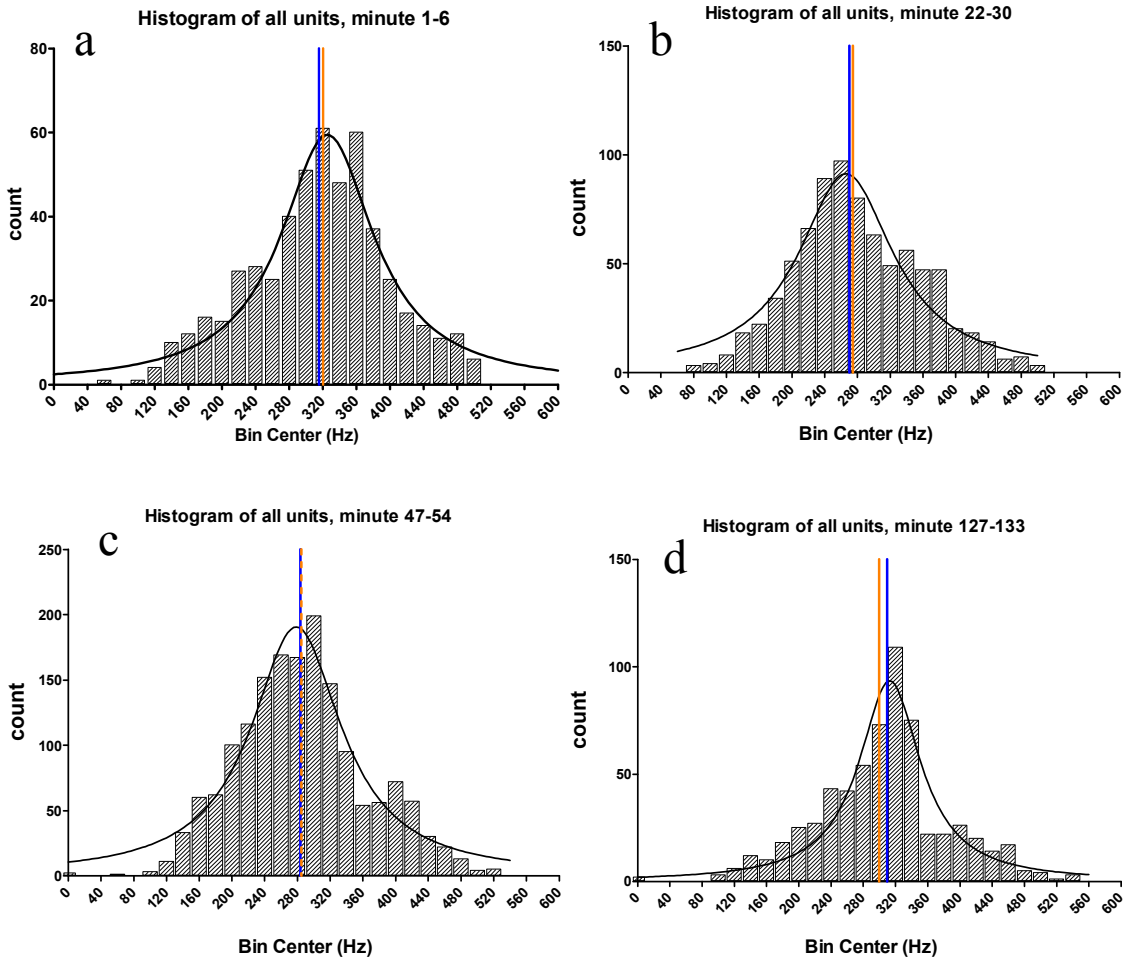

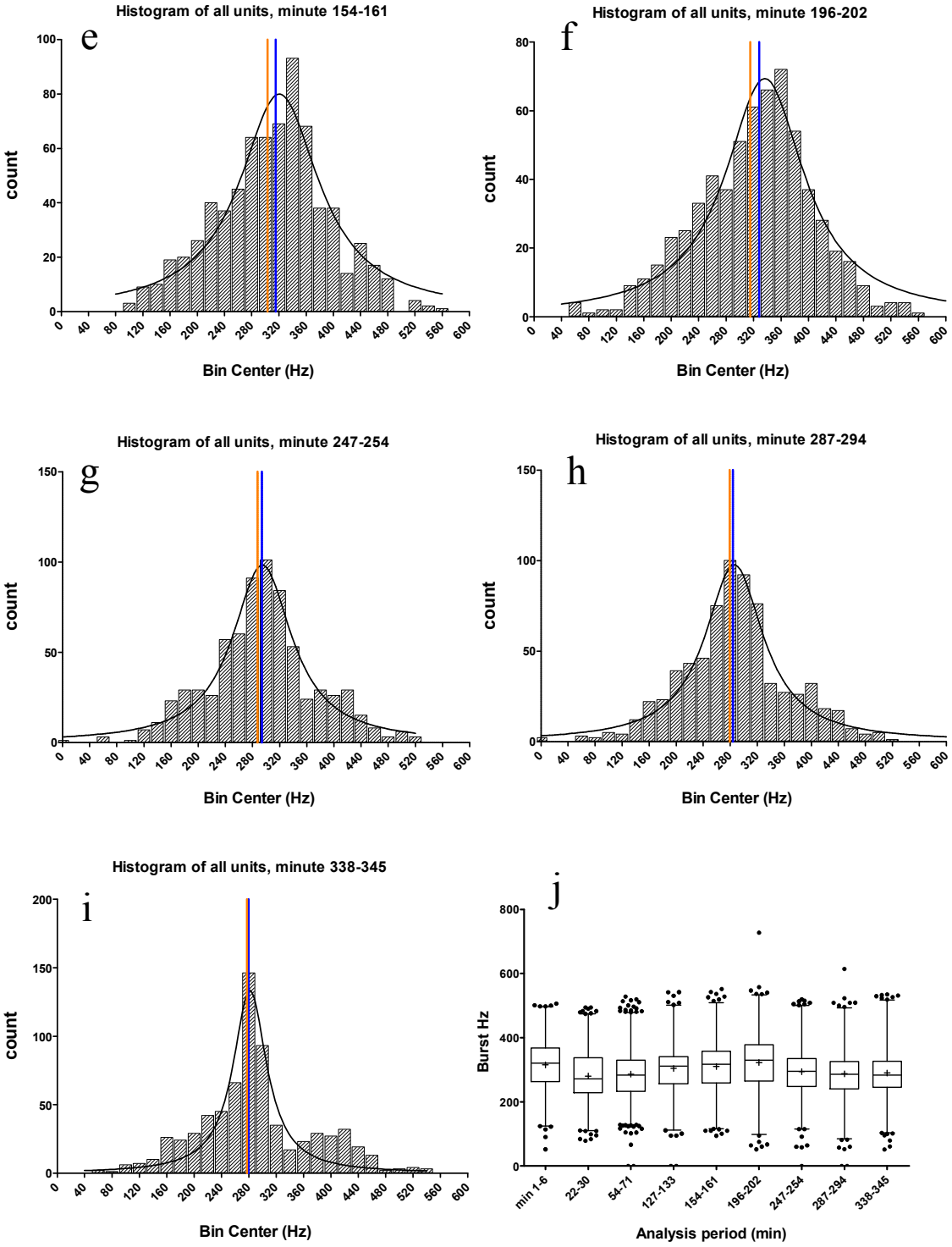

Fig. 4.78: a) – i): Spikes/burst histograms for all time periods indicated in fig. 4.71. R^2 values (a – i): 0.984, 0.928, 0.964, 0.964, 0.95, 0.912, 0.977, 0.954, 0.937. j): box plot summarizing the histograms

Dunn's Multiple Comparison Test	Difference in rank sum	Significant? P < 0.05?
min 1-6 vs 22-30	969.2	Yes
min 1-6 vs 54-71	825.5	Yes
min 1-6 vs 127-133	274.4	No
min 1-6 vs 154-161	134.6	No
min 1-6 vs 196-202	-161.9	No
min 1-6 vs 247-254	577.7	Yes
min 1-6 vs 287-294	757.2	Yes
min 1-6 vs 338-345	760.5	Yes
22-30 vs 54-71	-143.6	No
22-30 vs 127-133	-694.8	Yes
22-30 vs 154-161	-834.6	Yes
22-30 vs 196-202	-1131	Yes
127-133 vs 338-345	486.1	Yes
154-161 vs 196-202	-296.5	No
154-161 vs 247-254	443.1	Yes
154-161 vs 287-294	622.6	Yes
154-161 vs 338-345	625.9	Yes
22-30 vs 247-254	-391.5	Yes
22-30 vs 287-294	-211.9	No
22-30 vs 338-345	-208.7	No
54-71 vs 127-133	-551.2	Yes
54-71 vs 154-161	-690.9	Yes
54-71 vs 196-202	-987.4	Yes
54-71 vs 247-254	-247.8	No
54-71 vs 287-294	-68.29	No
54-71 vs 338-345	-65.05	No
127-133 vs 154-161	-139.8	No
127-133 vs 196-202	-436.2	Yes
127-133 vs 247-254	303.3	No
127-133 vs 287-294	482.9	Yes
196-202 vs 247-254	739.5	Yes
196-202 vs 287-294	919.1	Yes
196-202 vs 338-345	922.3	Yes
247-254 vs 287-294	179.6	No
247-254 vs 338-345	182.8	No
287-294 vs 338-345	3.238	No

Table 4.15: Results of a one-way ANOVA analysis with post-test comparing each histogram's data distribution with each other for significant differences in the medians.

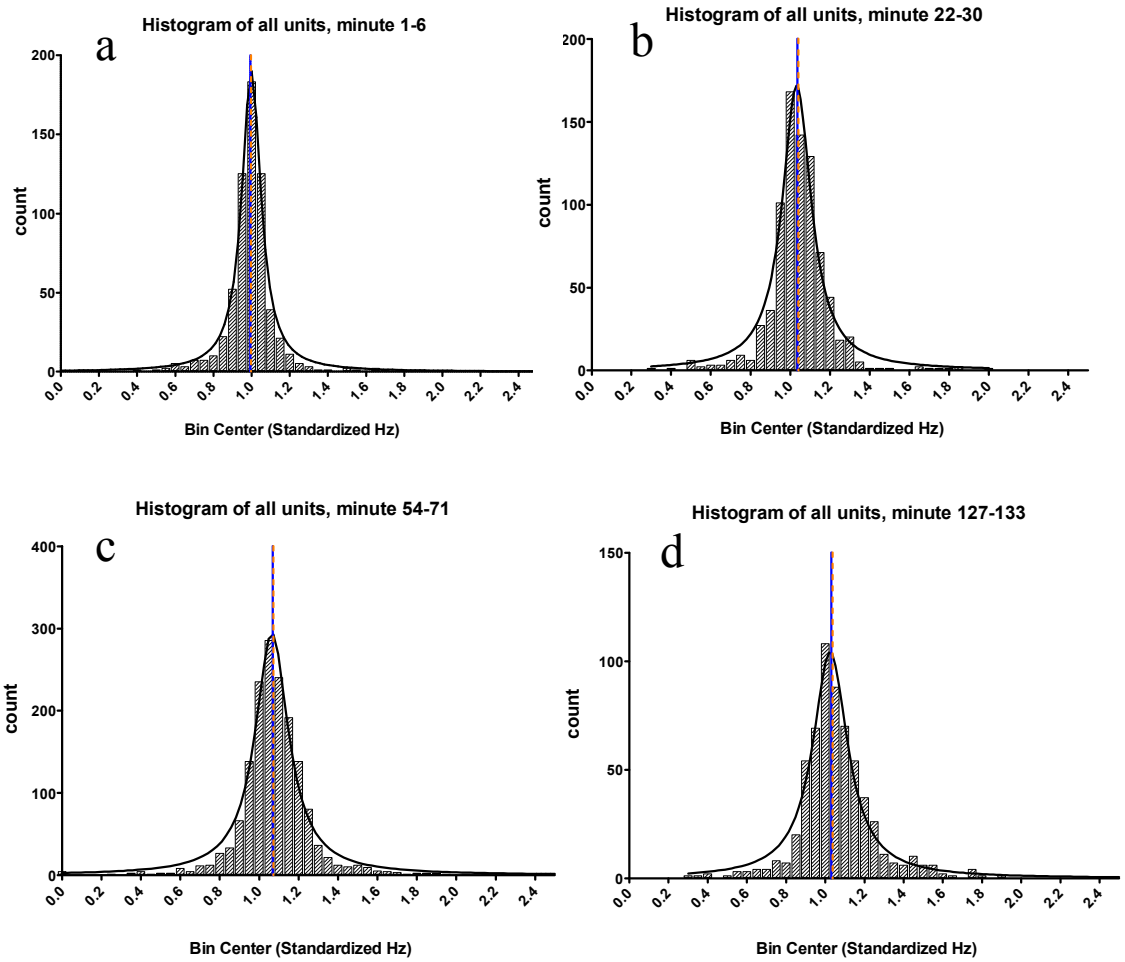

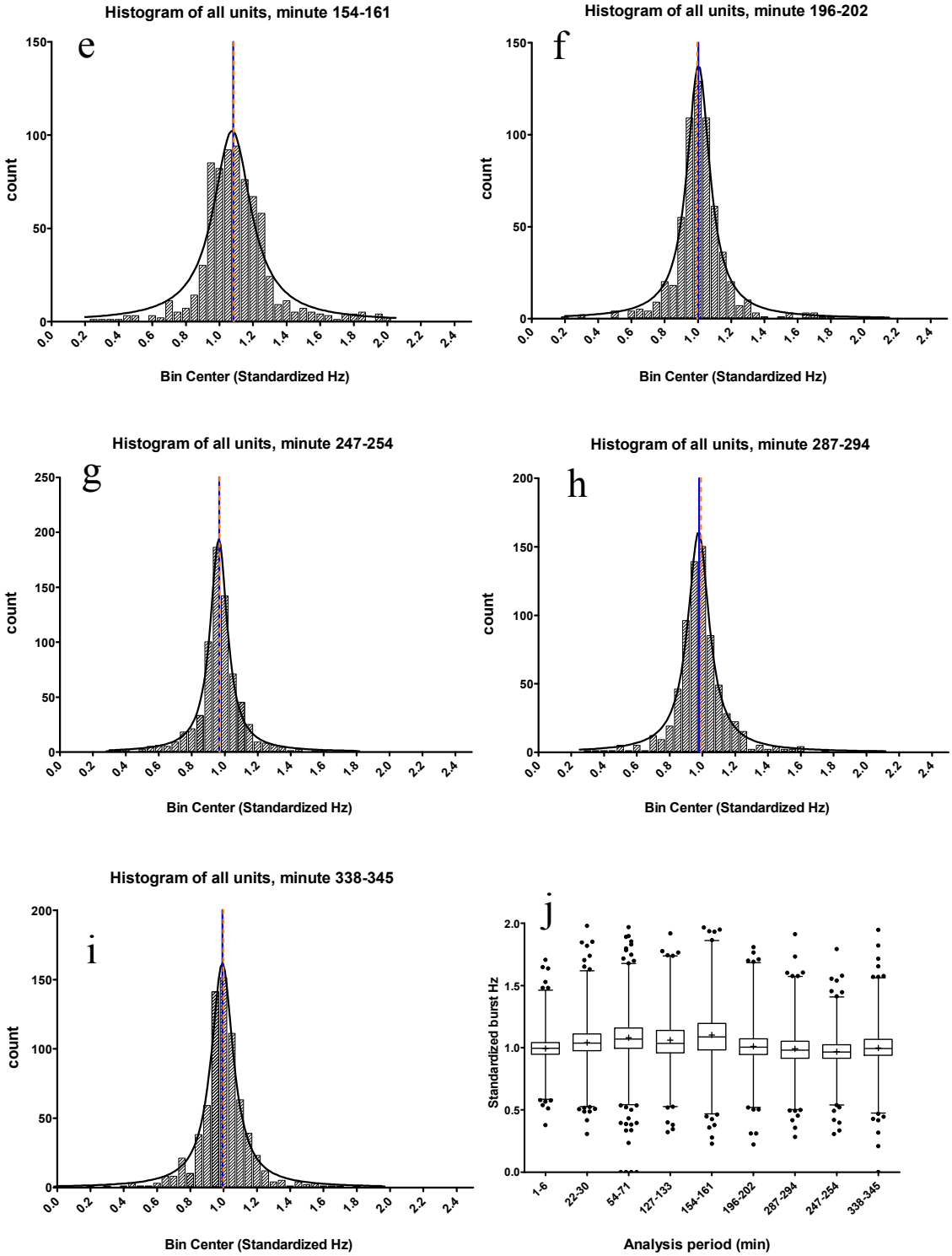

Fig. 4.79: a – i: Spikes/burst histograms for all time periods indicated in fig. 4.71. R^2 values (a – i): 0.989, 0.967, 0.98, 0.971, 0.939, 0.985, 0.994, 0.99, 0.985. j: box plot summarizing the histograms

Dunn's Multiple Comparison Test	Difference in rank sum	Significant? P < 0.05?			
1-6 vs 22-30	-857.3	Yes	54-71 vs 247-254	1781	Yes
1-6 vs 54-71	-1340	Yes	54-71 vs 287-294	1455	Yes
1-6 vs 127-133	-875.3	Yes	54-71 vs 338-345	1253	Yes

1-6 vs 154-161	-1430	Yes	127-133 vs 154-161	-554.2	Yes
1-6 vs 196-202	-274.5	No	127-133 vs 196-202	600.9	Yes
1-6 vs 247-254	440.8	Yes	127-133 vs 247-254	1316	Yes
1-6 vs 287-294	114.7	No	127-133 vs 287-294	990.0	Yes
1-6 vs 338-345	-87.24	No	127-133 vs 338-345	788.1	Yes
22-30 vs 54-71	-483.1	Yes	154-161 vs 196-202	1155	Yes
22-30 vs 127-133	-18.00	No	154-161 vs 247-254	1870	Yes
22-30 vs 154-161	-572.2	Yes	154-161 vs 287-294	1544	Yes
22-30 vs 196-202	582.9	Yes	154-161 vs 338-345	1342	Yes
22-30 vs 247-254	1298	Yes	196-202 vs 247-254	715.3	Yes
22-30 vs 287-294	972.0	Yes	196-202 vs 287-294	389.1	Yes
22-30 vs 338-345	770.1	Yes	196-202 vs 338-345	187.2	No
54-71 vs 127-133	465.1	Yes	247-254 vs 287-294	-326.1	No
54-71 vs 154-161	-89.10	No	247-254 vs 338-345	-528.0	Yes
54-71 vs 196-202	1066	Yes	287-294 vs 338-345	-201.9	No

Table 4.16: Results of a one-way ANOVA analysis with post-test comparing each histogram's data distribution with each other for significant differences in the medians.

4.7.3 A-beta monomers and oligomers

4.7.3.1 Example recording with monomers

The recording shown below (fig. 4.80) was analyzed with respect to its burst parameters the same way as the buffer test recording above. In summary, the final cumulative dose of 0.7 µM a-beta monomers caused the burst Hz to increase by 26%, the burst period by 270%, and the number of spikes per burst to decrease by 44%. The dashed vertical line in figure 4.85 denotes the respective final concentration of Tris from the buffer tests. Interpolating to that position, the burst Hz would have increased by 24%, the burst period by 60%, and the spikes/burst would have decreased by 28%.

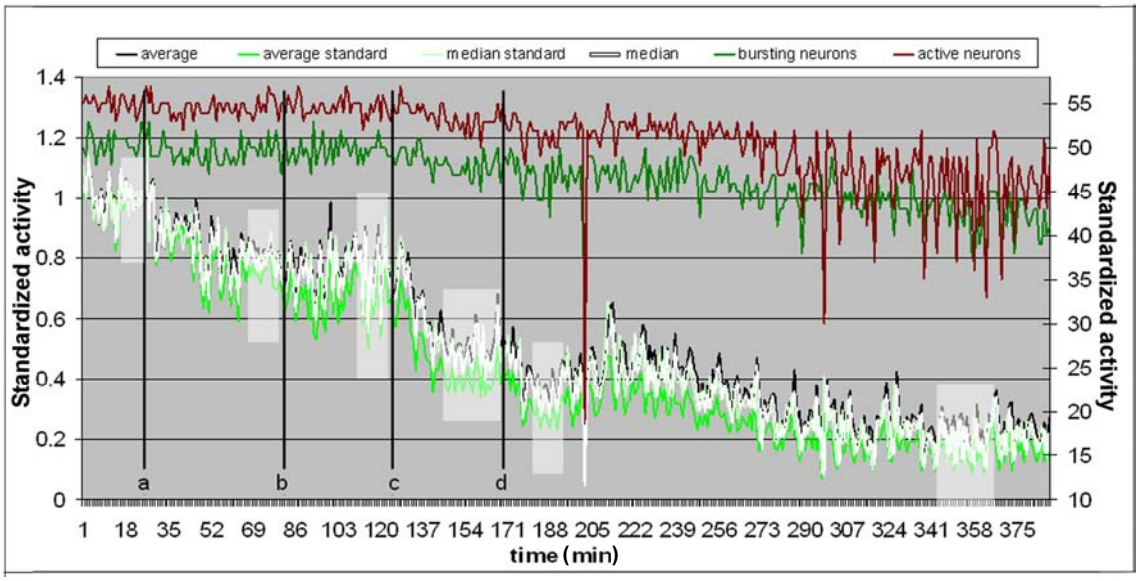

Fig. 4.80: a: +80 µM Tris buffer, b: +80 µM Tris +0.1 µM A-beta monomers, c: +80 µM Tris +0.1 µM A-beta monomers, d: +400 µM Tris + 0.5 µM A-beta monomers

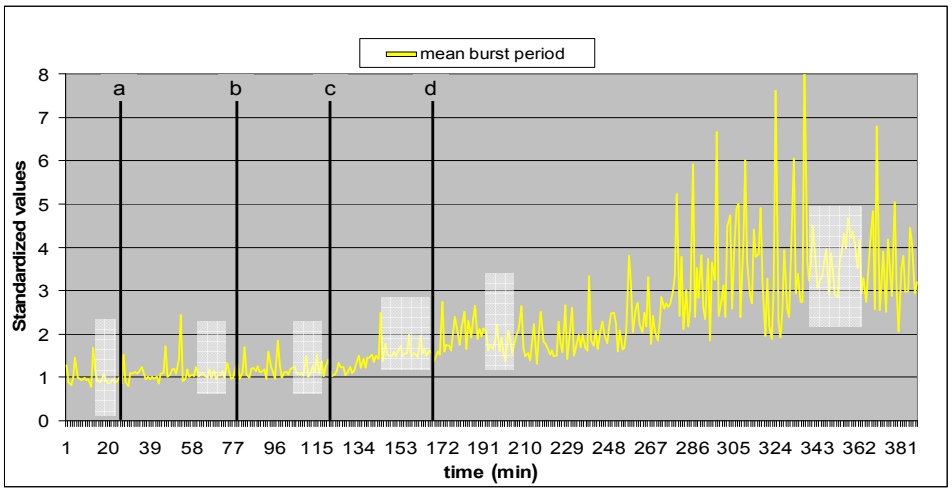

Fig. 4.81: Burst period evolution during the experiment shown in fig. 4.80

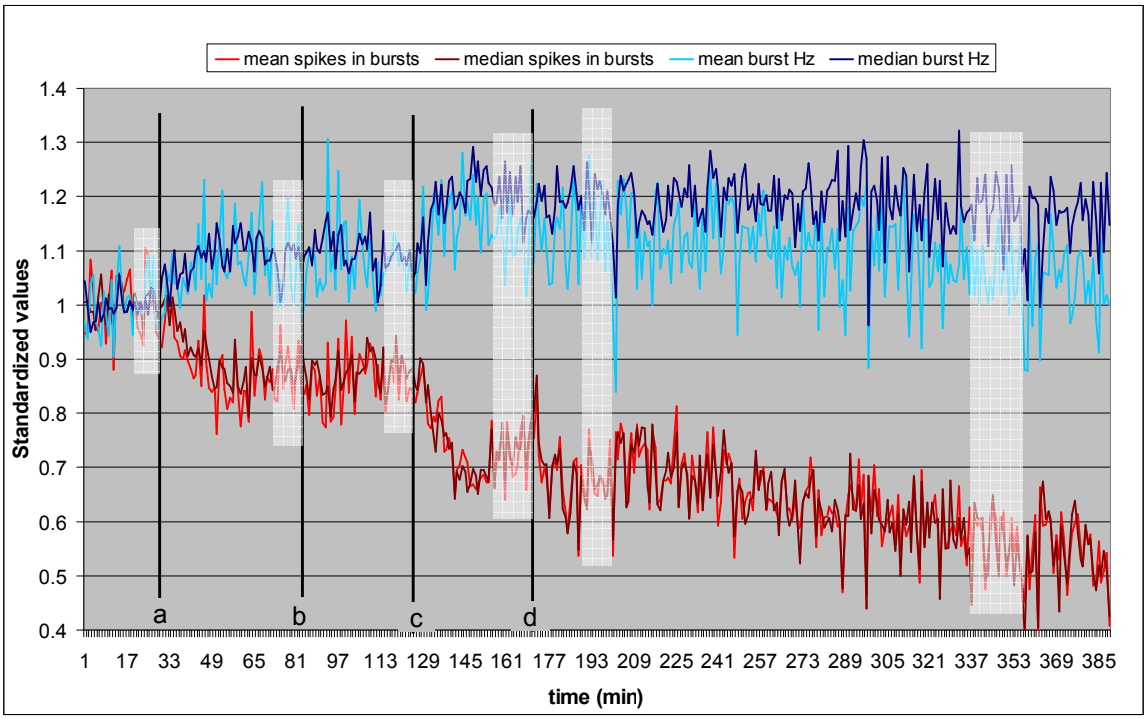

Fig. 4.82: Light blue and dark blue curves: mean and median values of the spike frequency inside the bursts ("burst Hz"), respectively; red and dark red curves: mean and median of the number of spikes per burst. All values were calculated after normalizing with respect to the initial reference activity period.

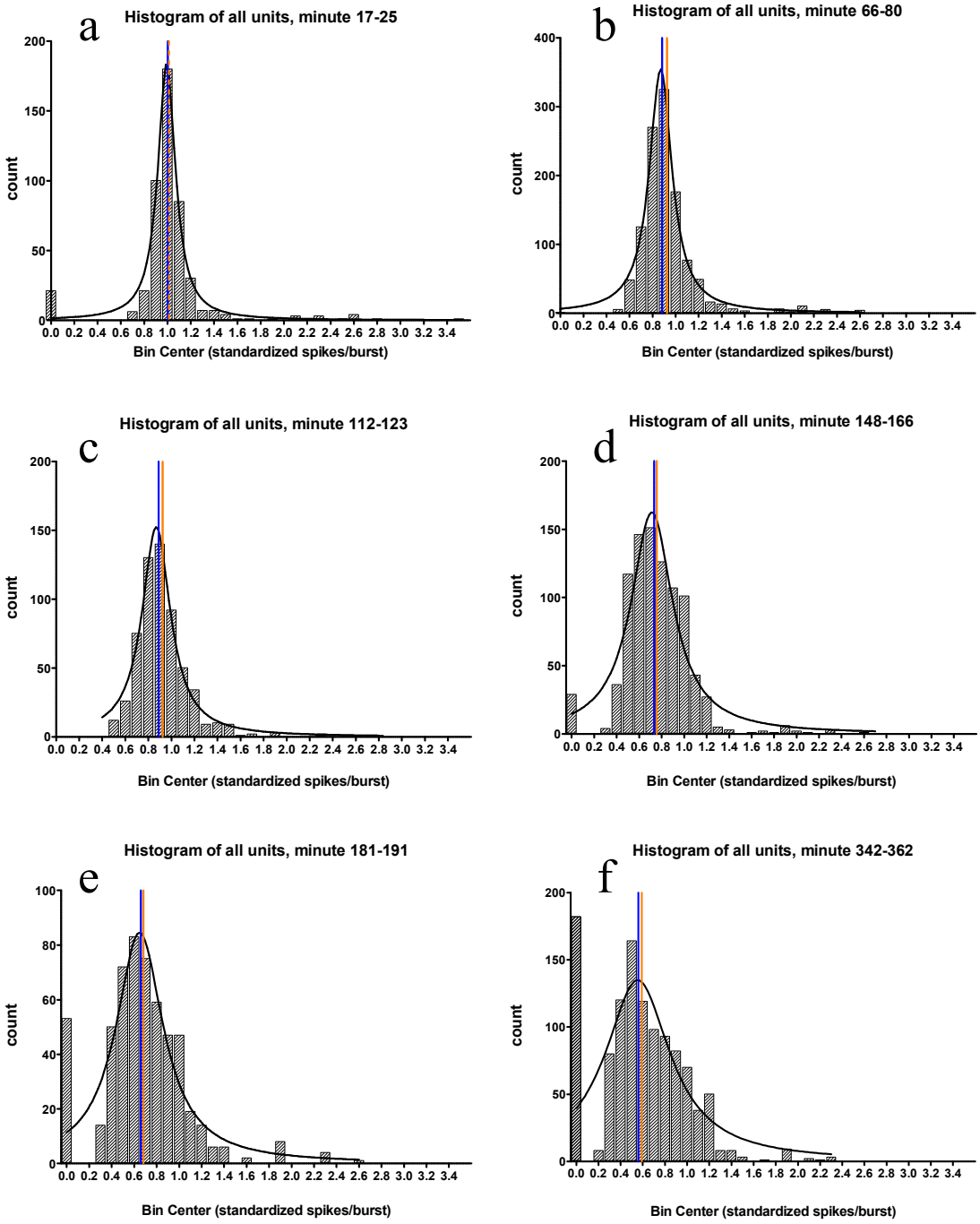
a
Histogram of all units, minute 17-25
count
Bin Center (standardized spikes/burst)
b
Histogram of all units, minute 66-80
count
Bin Center (standardized spikes/burst)
c
Histogram of all units, minute 112-123
count
Bin Center (standardized spikes/burst)
d
Histogram of all units, minute 148-166
count
Bin Center (standardized spikes/burst)
e
Histogram of all units, minute 181-191
count
Bin Center (standardized spikes/burst)
f
Histogram of all units, minute 342-362
count
Bin Center (standardized spikes/burst)

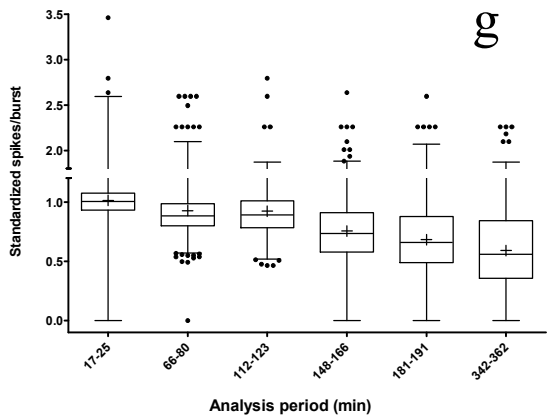

Fig. 4.83: a) – f): Spikes/burst histograms for all time periods indicated in fig. 4.80. g): box plot summarizing the histograms

Dunn's Multiple Comparison Test	Difference in rank sum	Significant? P < 0.05?			
17-25 vs 66-80	620.4	Yes	112-123 vs 148-166	835.3	Yes
66-80 vs 112-123	-6.477	No	148-166 vs 181-191	286.5	Yes
			181-191 vs 342-362	250.2	Yes

Table 4.17: Selection of ANOVA results comparing all distributions from fig. 4.83: Differences are significant from one analysis period to the next, except for the second to the third one.

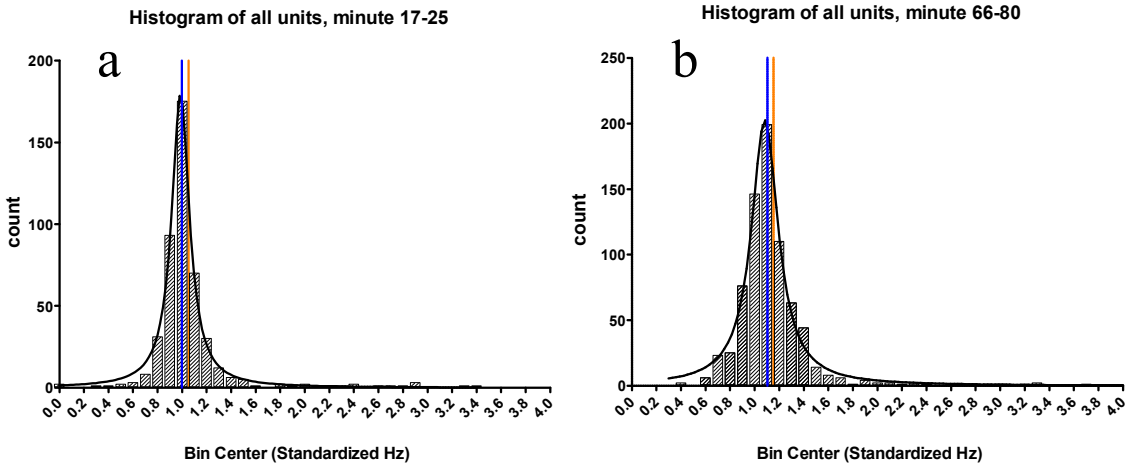

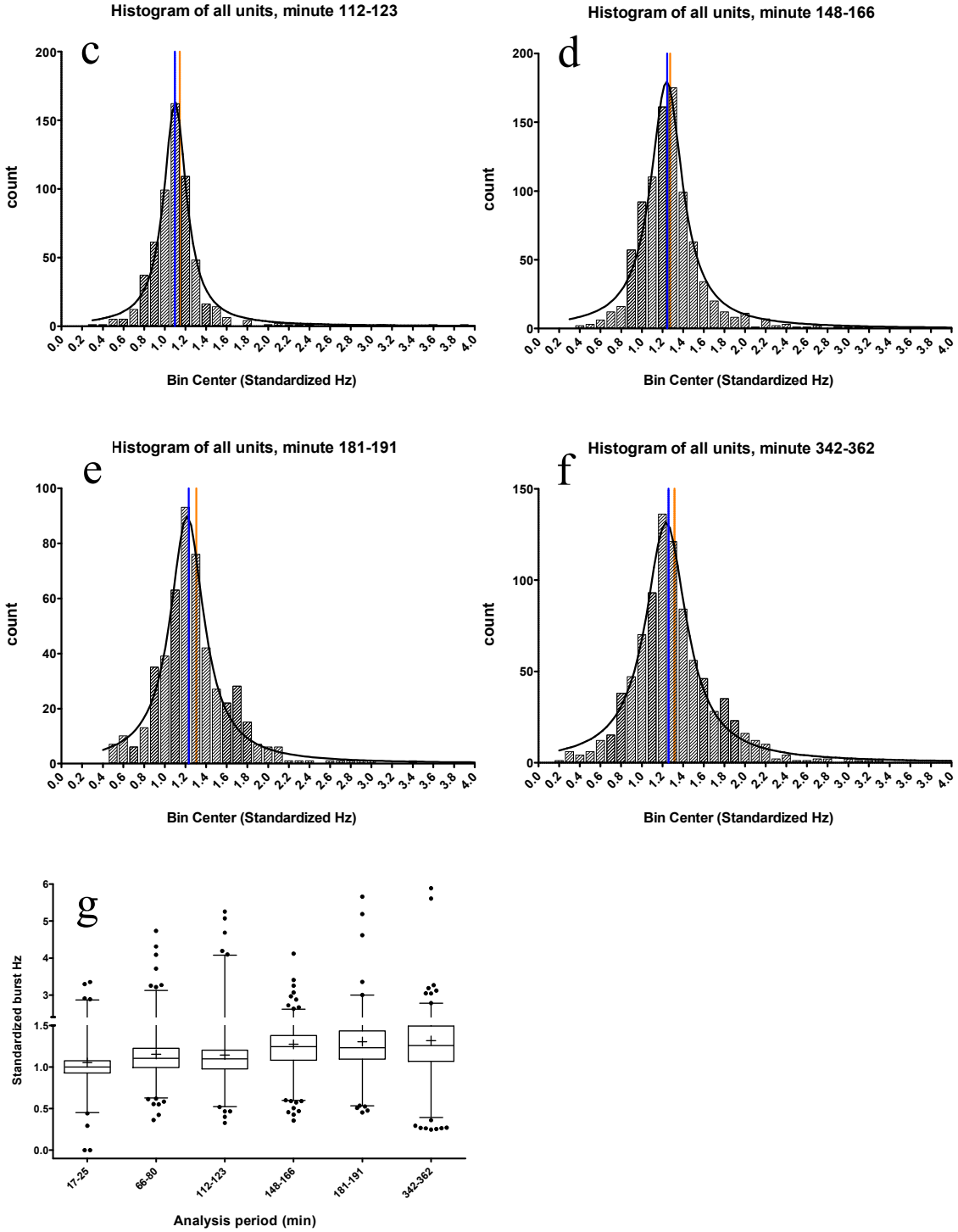

Fig. 4.84: a – f: Spikes/burst histograms for all time periods indicated in fig. 4.80. g: box plot summarizing the histograms

Dunn's Multiple Comparison Test	Difference in rank sum	Significant ? P < 0.05?			
17-25 vs 66-80	-546.5	Yes	112-123 vs 148-166	-711.0	Yes
66-80 vs 112-123	83.16	No	148-166 vs 181-191	-2.635	No
66-80 vs 148-166	-627.9	Yes	148-166 vs 342-362	-41.73	No
			181-191 vs 342-362	-39.10	No

Table 4.18: Selection of ANOVA results comparing all distributions from fig. 4.84: Differences are significant from one analysis period to the next only for the first to the second, the second to the fourth, and the third to the fourth.

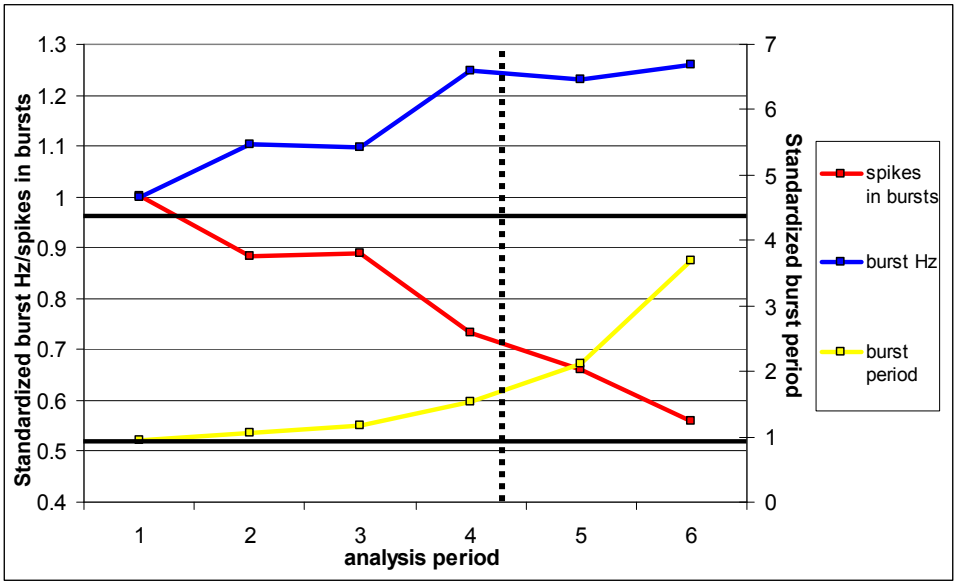

Fig. 4.85: Summary of burst parameter changes caused by the addition of a-beta monomers. Dashed vertical bar: Maximum Tris concentration in buffer tests. Burst period: on secondary y-axis

4.7.3.2 Example recording with dimers

This recording was analyzed the same way as the ones shown above. The results are summarized in figure 4.91. At a concentration of 0.3 µM a-beta dimers, which corresponds to 1 mM AA, the maximum concentration used in the buffer tests, the burst Hz were 17% above the reference level. The burst period was prolonged by 200%, and the number of spikes per burst declined by 60%.

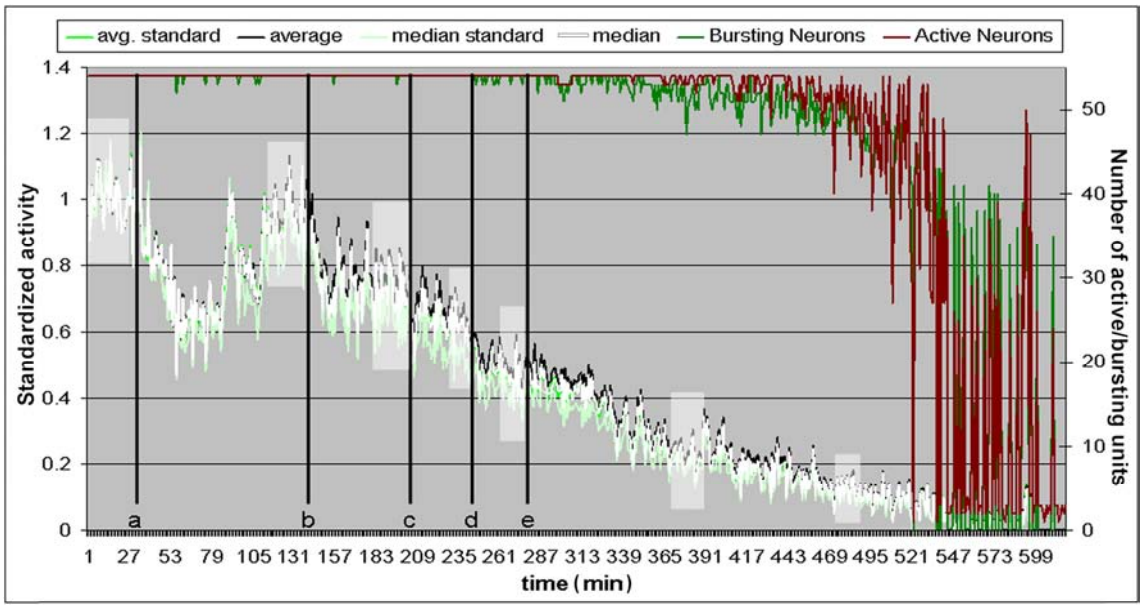

Fig. 4.86: a: +80 µM Tris buffer, b: +80 µM Tris +0.1 µM A-beta monomers, c: +80 µM Tris +0.1 µM A-beta monomers, d: +400 µM Tris + 0.5 µM A-beta monomers

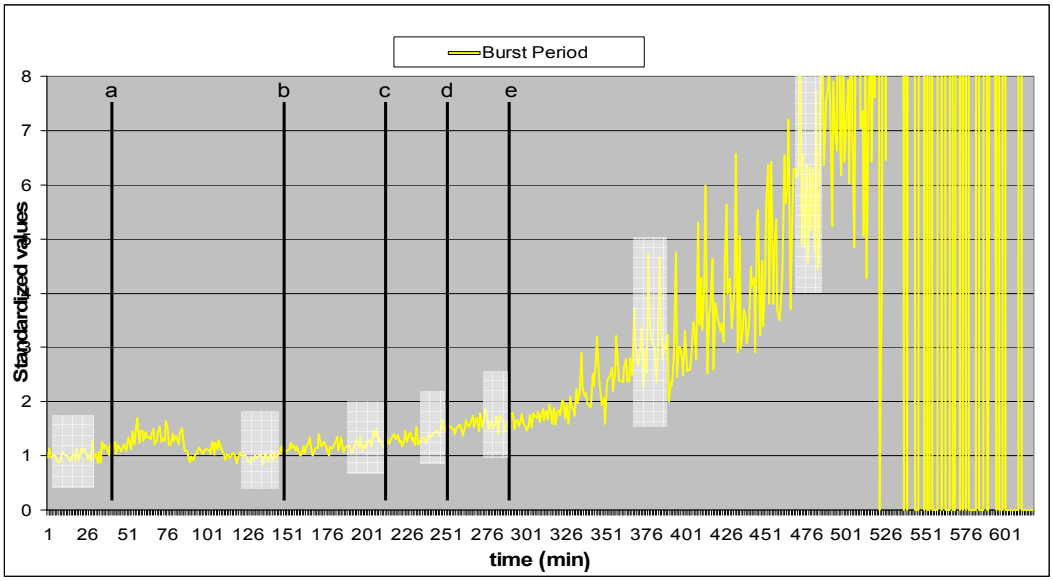

Fig. 4.87: Burst period evolution during the experiment shown in fig. 4.86.

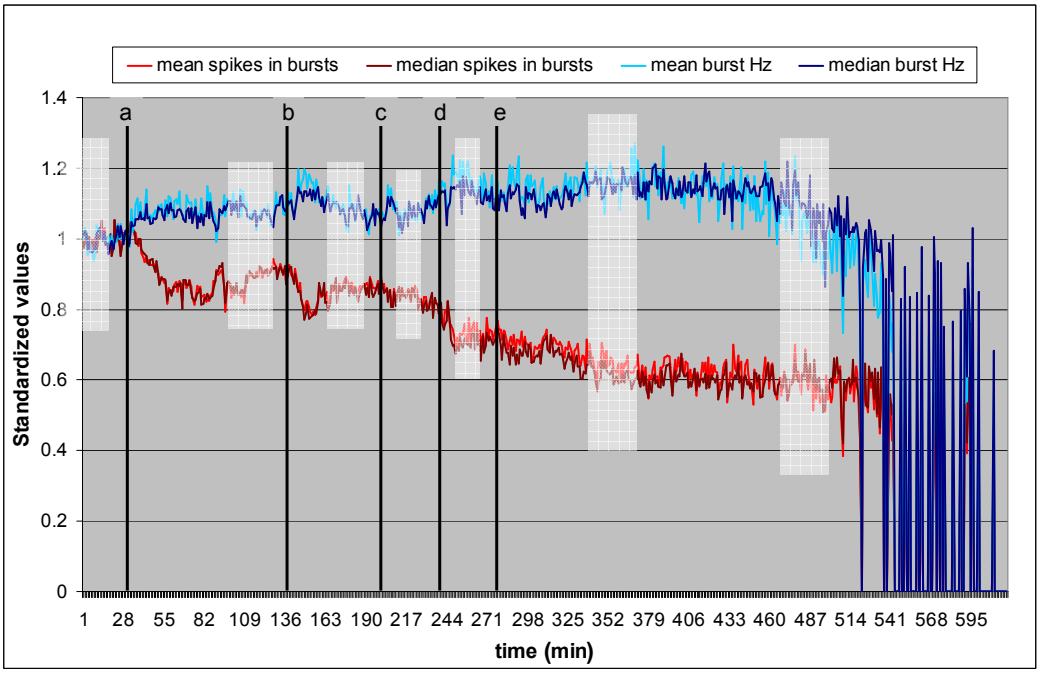

Fig. 4.88: Light blue and dark blue curves: mean and median values of the spike frequency inside the bursts ("burst Hz"), respectively; red and dark red curves: mean and median of the number of spikes per burst. All values calculated after normalizing with respect to the initial reference activity period.

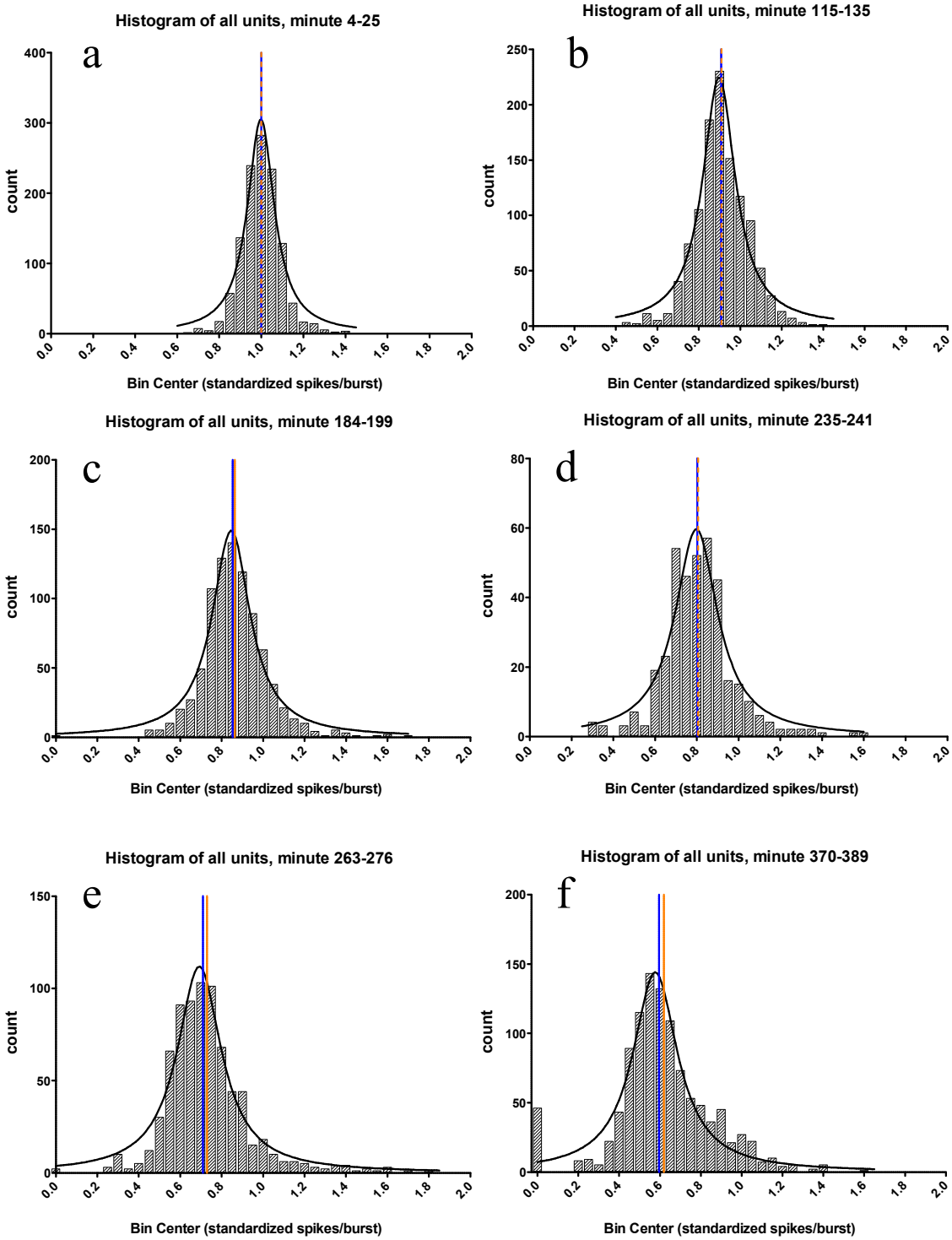
Histogram of all units, minute 4-25
a
count
Bin Center (standardized spikes/burst)
Histogram of all units, minute 115-135
b
count
Bin Center (standardized spikes/burst)
Histogram of all units, minute 184-199
c
count
Bin Center (standardized spikes/burst)
Histogram of all units, minute 235-241
d
count
Bin Center (standardized spikes/burst)
Histogram of all units, minute 263-276
e
count
Bin Center (standardized spikes/burst)
Histogram of all units, minute 370-389
f
count
Bin Center (standardized spikes/burst)

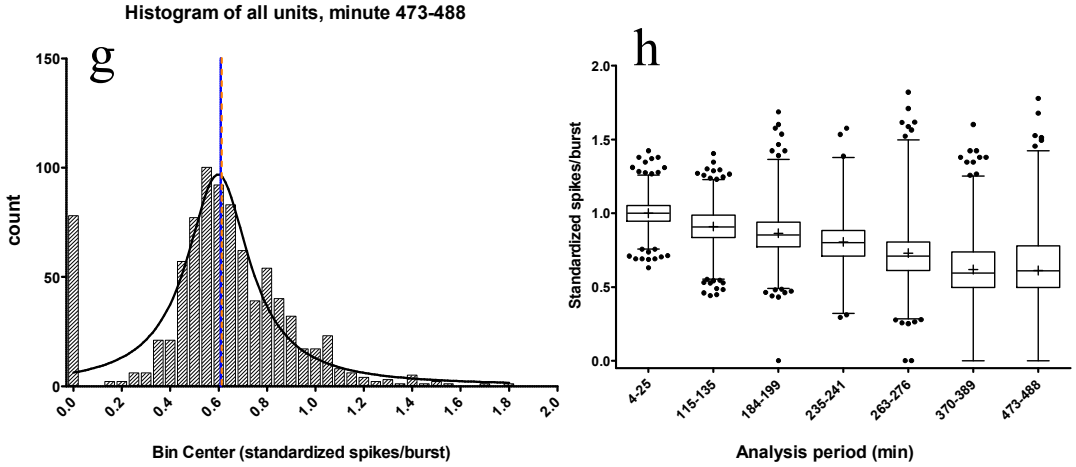

Fig. 4.89: a – f: Spikes/burst histograms computed from non-normalized data for all time periods indicated in fig. 4.86. g: box plot summarizing the histograms

Dunn's Multiple Comparison Test	Difference in rank sum	Significant? P < 0.05?			
4-25 vs 115-135	947.3	Yes	235-241 vs 263-276	663.1	Yes
115-135 vs 184-199	489.8	Yes	263-276 vs 370-389	600.4	Yes
184-199 vs 235-241	539.9	Yes	370-389 vs 473-488	-84.74	No

Table 4.19: of ANOVA results comparing all distributions from fig. 4.89 g).

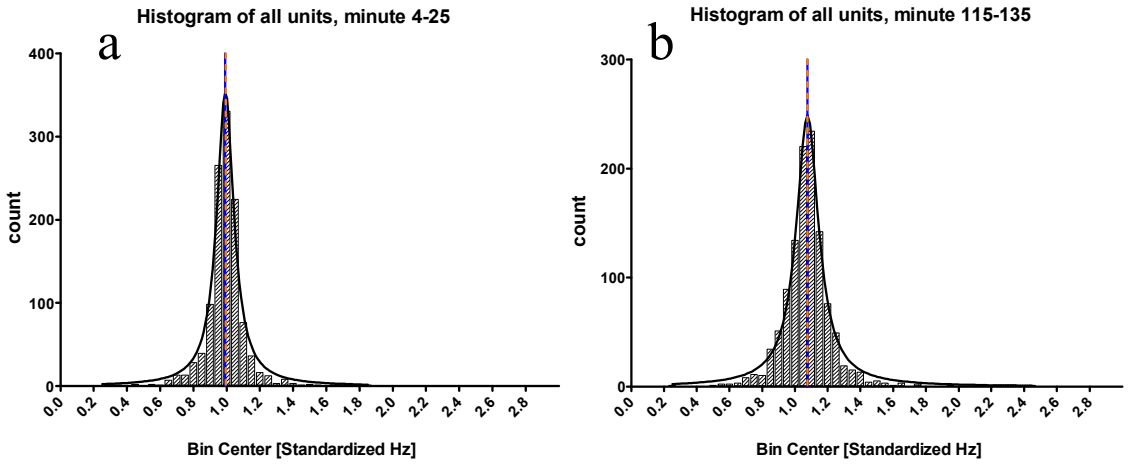

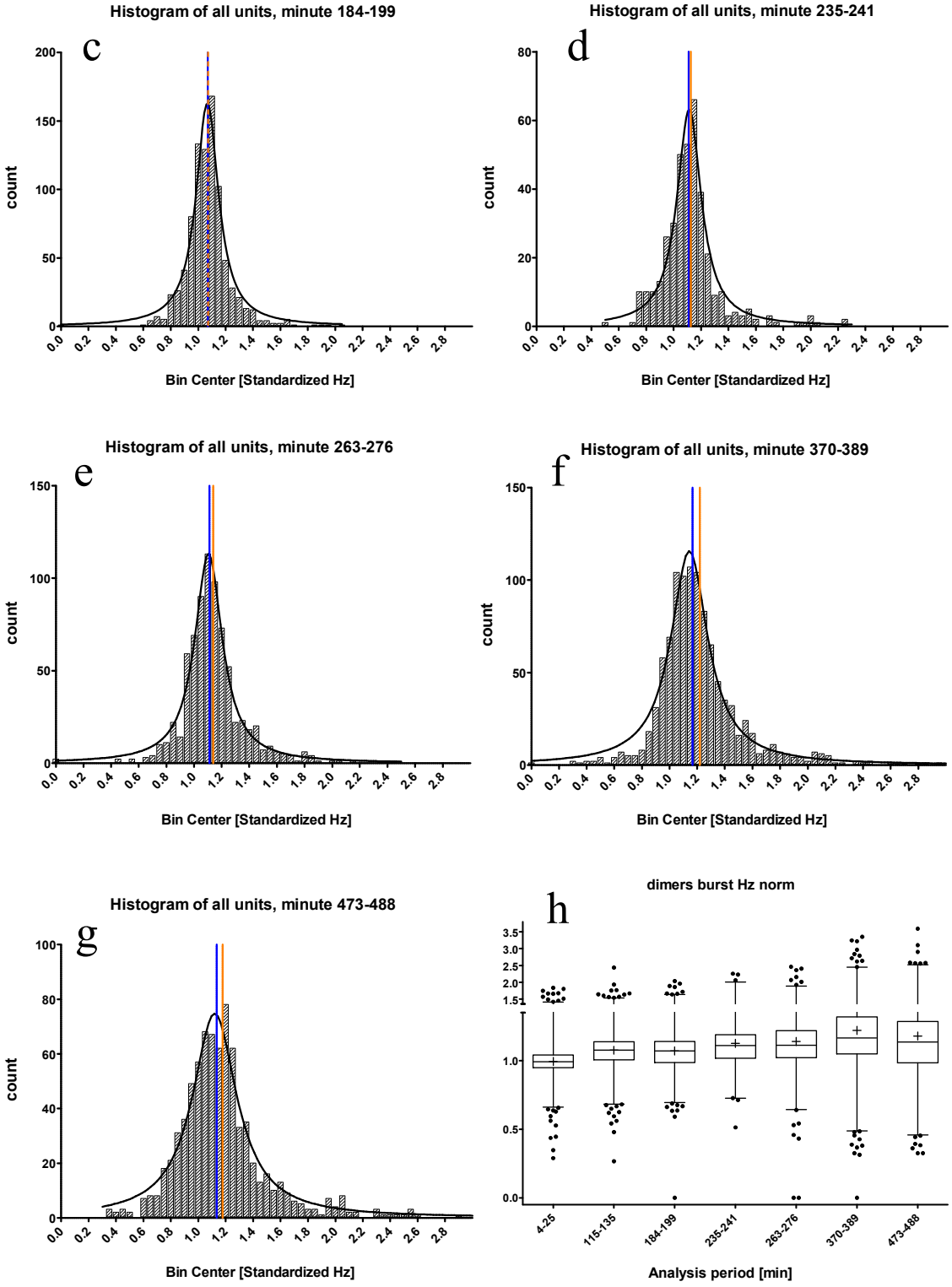

Fig. 4.90: a – f: Spikes/burst histograms computed from individually normalized data for all time periods indicated in fig. 4.86. g: box plot summarizing the histograms

Dunn's Multiple Comparison Test	**Difference in rank sum**	**Significant? P < 0.05?**
4-25 vs 115-135	-1098	Yes
115-135 vs 184-199	97.25	No

115-135 vs 235-241	-370.9	Yes
184-199 vs 235-241	-468.2	Yes
235-241 vs 263-276	-122.2	No
235-241 vs 370-389	-553.5	Yes
235-241 vs 473-488	-132.8	No
263-276 vs 370-389	-431.3	Yes
263-276 vs 473-488	-10.59	No
370-389 vs 473-488	420.8	Yes

Table 4.20: ANOVA results comparing all distributions from fig. 4.90 g)

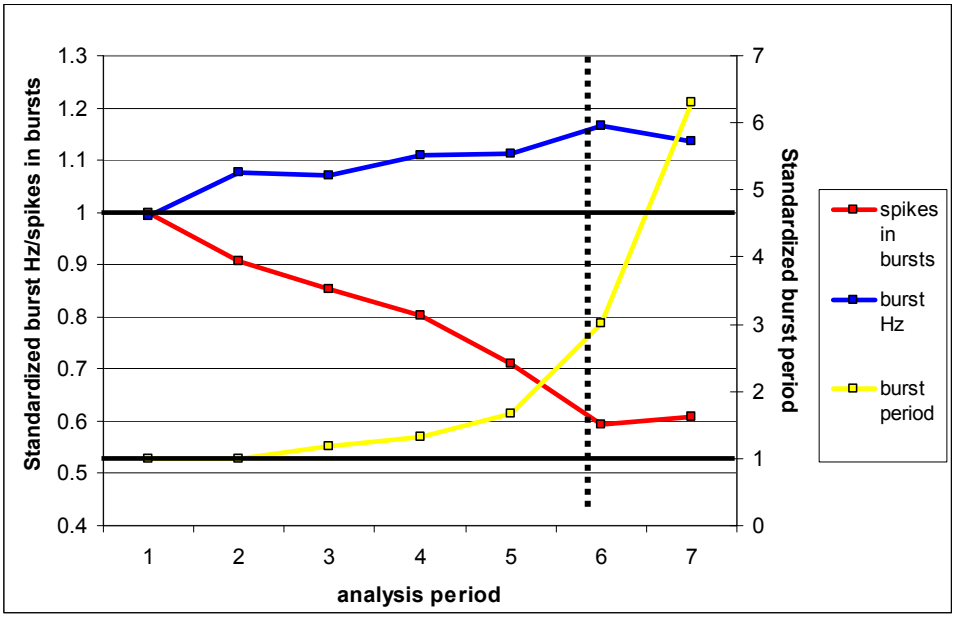

Fig. 4.91: Summary of burst parameter changes caused by the addition of a-beta monomers. Dashed vertical bar: Maximum AA concentration in buffer tests. Burst period: on secondary y-axis.

4.8 Multi-network titration of muscimol with a liquid handling robot

4.8.1 Simultaneous recording of eight networks:

The CNNS has been devoting a considerable portion of its resources to developing a high-throughput system that will allow users to perform a number of MEA-based recordings simultaneously. Obviously, this undertaking is accompanied by a plethora of new challenges and problems that need to be addressed in order for such a system to function reliably and in a practical way. One of the many challenges that have recently been worked on is the automatic addition of water for osmolarity control and of compounds for automated experiments. For the first time, an eight-site culture plate with eight separate, spontaneously active cortical cultures has been recorded from and subject to a fully automatic addition of bicuculline and muscimol (a GABA agonist), using a computer-controlled liquid handling system. While fig. 4.92 captures a moment in the live display of the recording, fig. 4.93 summarizes the response of the eight networks to the muscimol titration, after they had received 40 µM bicuculline each beforehand.

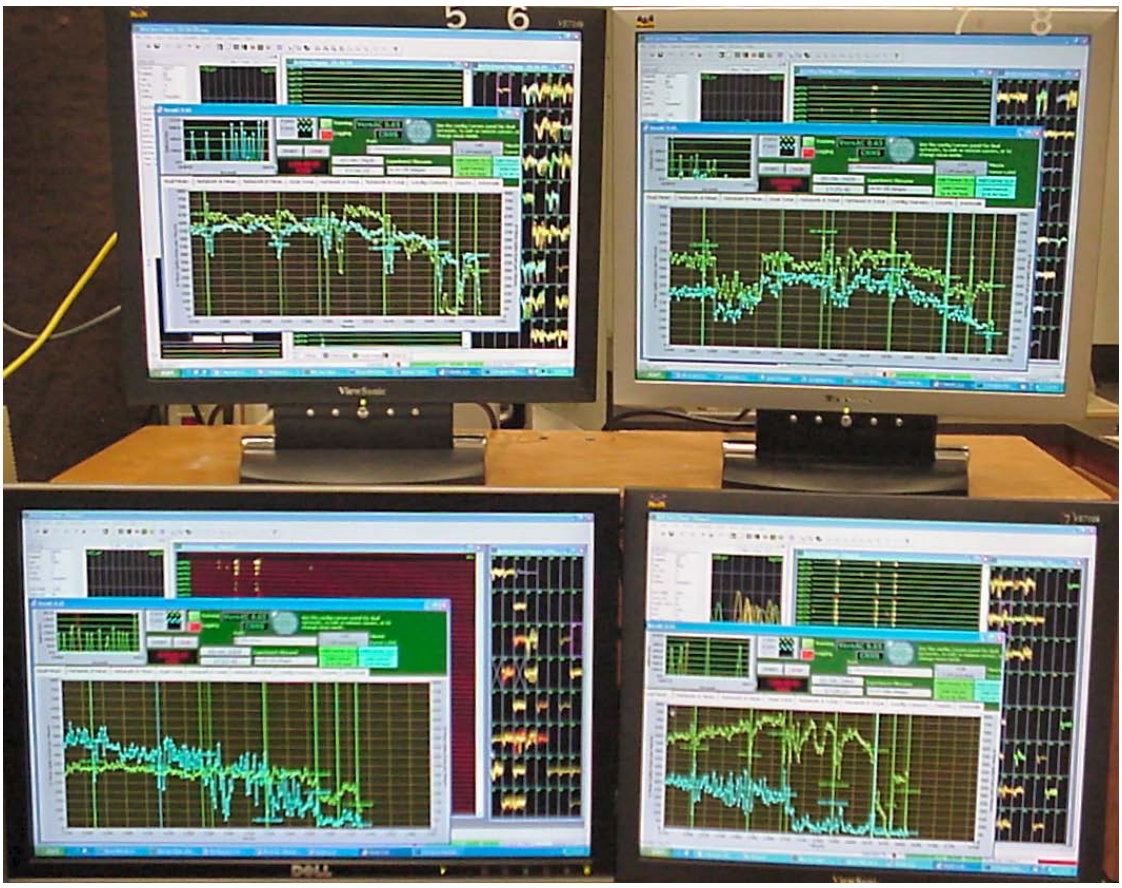

Fig. 4.92: Simultaneous recording of 8 separate networks using 4 PCs: Plexon Sortclient software, and CNNS custom made program "VernAC", based on LabView.

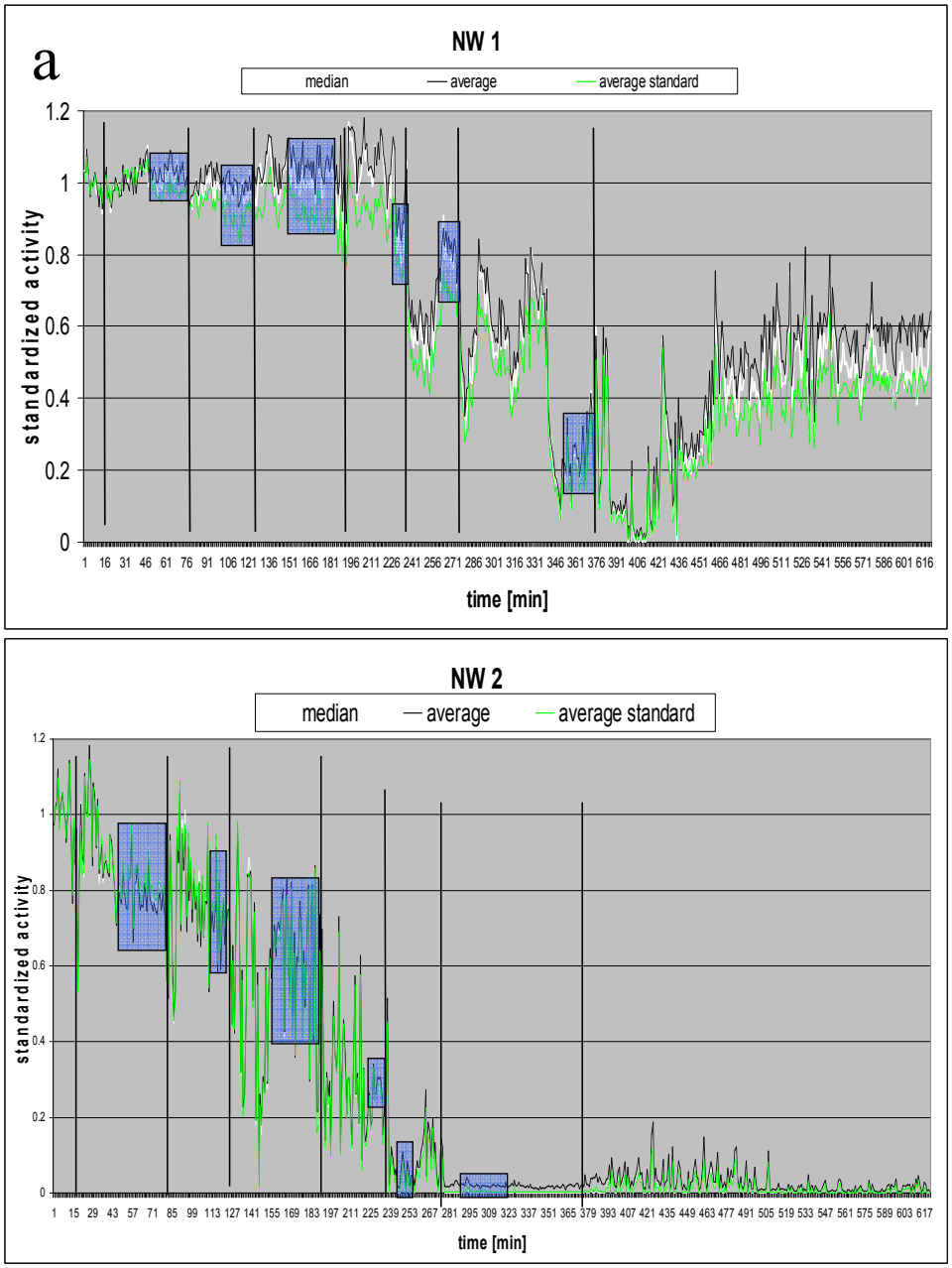
a
NW 1
median
average
average standard
standardized activity
time [min]
NW 2
median
average
average standard
standardized activity
time [min]

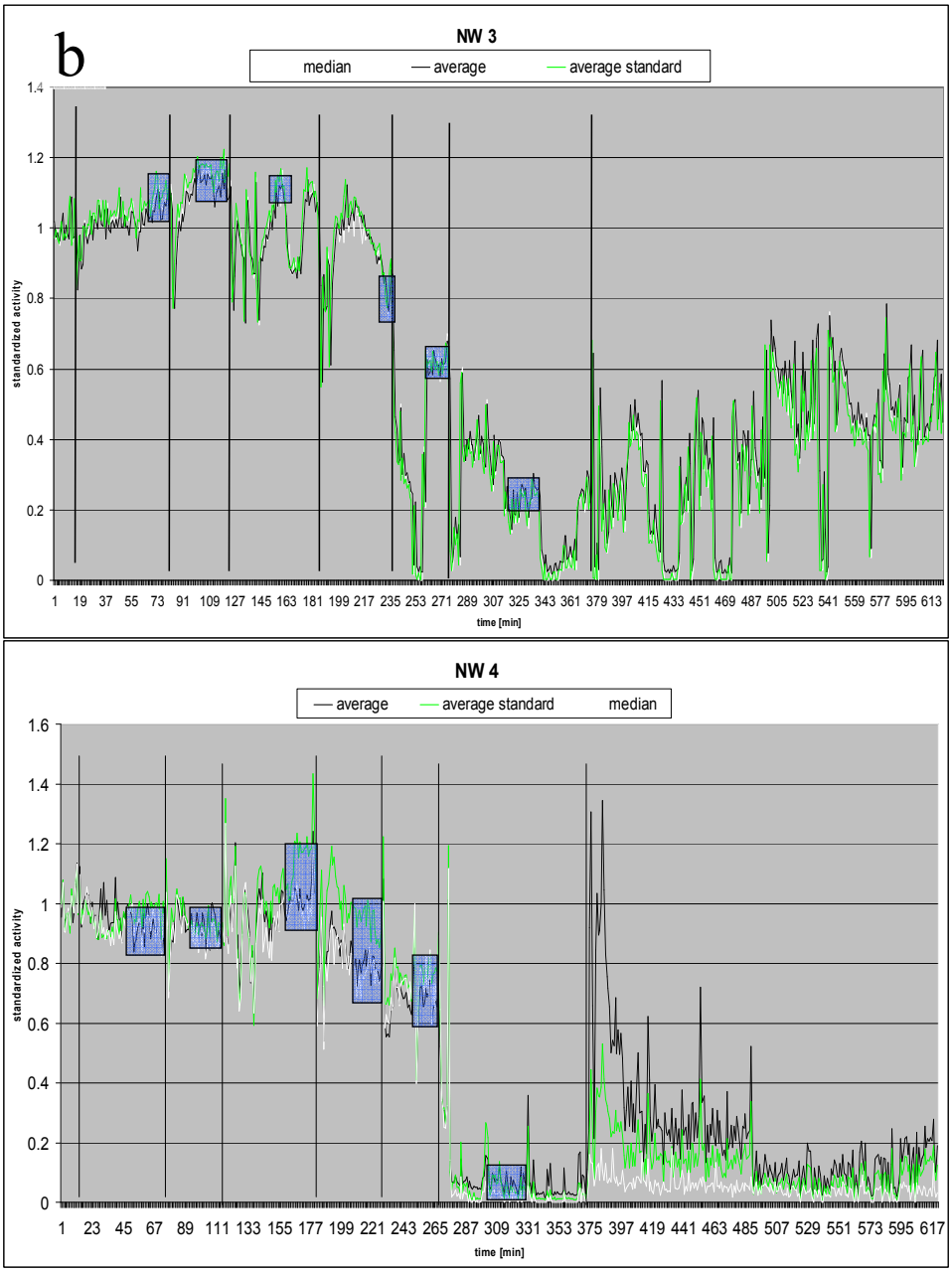
b
NW 3
median
average
average standard
standardized activity
time [min]
NW 4
average
average standard
median
standardized activity
time [min]

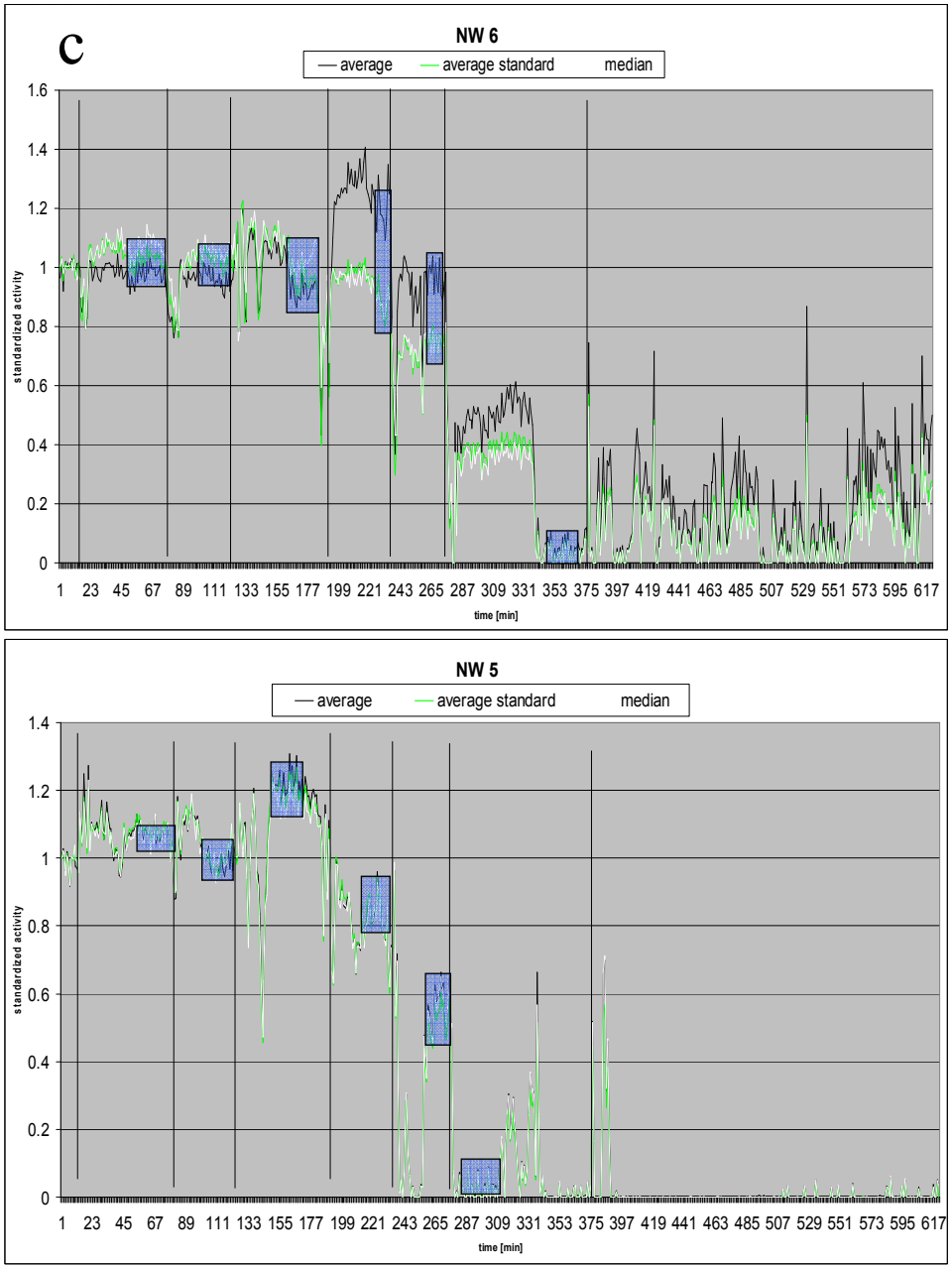
c
NW 6
average
average standard
median
standardized activity
time [min]
NW 5
average
average standard
median
standardized activity
time [min]

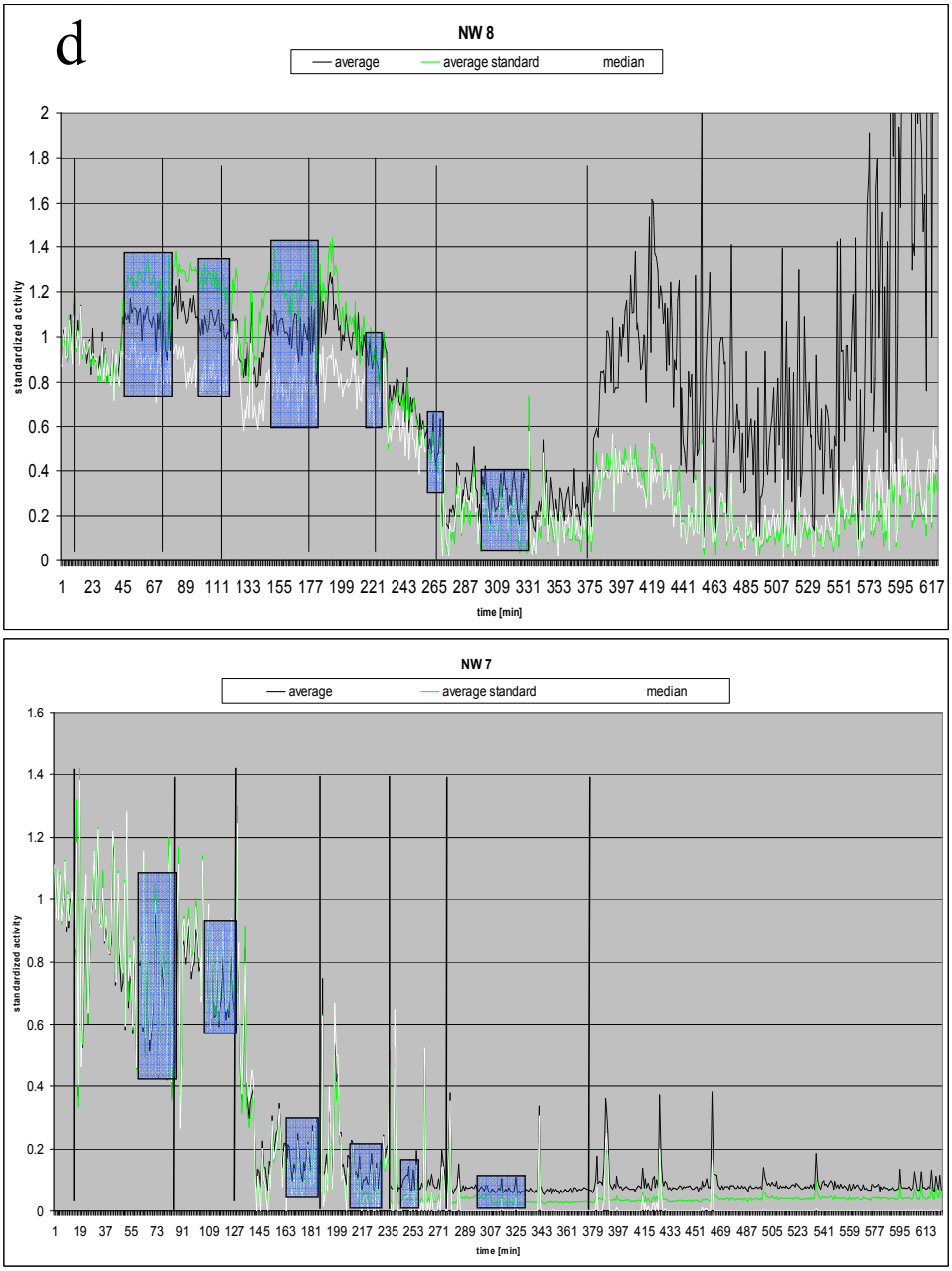

Fig. 4.93: Activity displays from all eight separate networks, analyzed both without unit-wise normalization (mean only, green curves) and after normalization (mean: black curves, median: white curves).

4.8.2 Analysis with initial normalization of individual units, using medians:

The 8-network data were analyzed in the two different ways described previously, in order to find out whether one or the other method would yield favorable results in this case. Calculating the median values after unit-wise normalization yielded the individual network dose-response curves in fig. 4.94 a), with most IC50 values around 4 µM. Two networks seemed to respond far more sensitively to muscimol, with IC50 values of approximately 1 µM and 0.5 µM (network 2 and 7, respectively). After combining the data points from all the networks into one dose-response relation, the box plot in figure 4.94 b) was generated. According to the subsequent ANOVA analysis (table 4.21), there were no significant differences between the reference activity and the activity after the first and second doses of muscimol, as well as between the first and the second, the second and the third, and between the third the fourth additions.

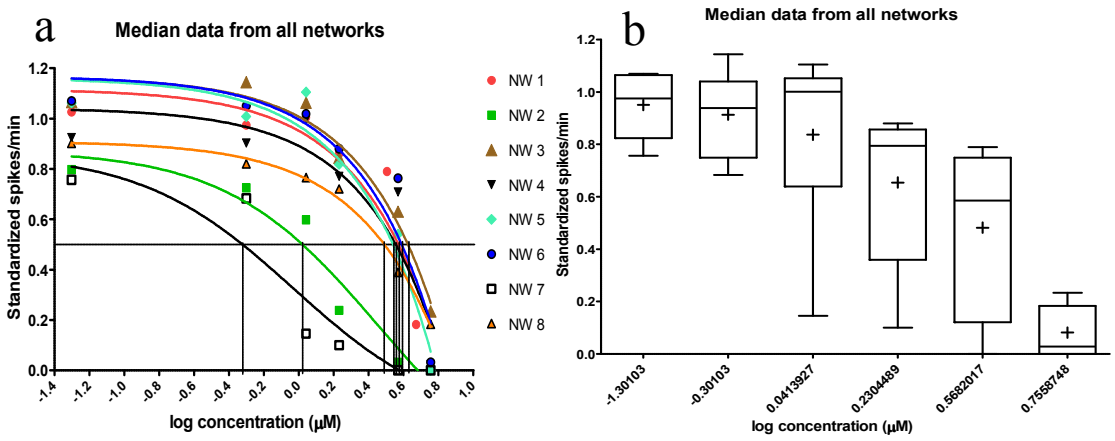

Fig. 4.94: Dose-response curves of the separate networks (a, error bars: standard deviation), and combined in one box plot (b, whiskers: min-max, cross: mean, bar: median).

Bonferroni's Multiple Comparison Test	Mean Diff.	t	Significant? P < 0.05?
-1.3 vs -0.3	0.03723	0.5333	No
-1.3 vs 0.041	0.1135	1.627	No
-1.3 vs 0.23	0.2967	4.251	Yes
-1.3 vs 0.568	0.4690	6.720	Yes
-1.3 vs 0.756	0.8688	12.45	Yes
-0.3 vs 0.041	0.07630	1.093	No
-0.3 vs 0.23	0.2595	3.717	Yes
-0.30 vs 0.568	0.4318	6.187	Yes
-0.3 vs 0.756	0.8316	11.91	Yes
0.041 vs 0.23	0.1832	2.624	No
0.041 vs 0.568	0.3555	5.093	Yes
0.041 vs 0.756	0.7553	10.82	Yes
0.23 vs 0.568	0.1723	2.469	No
0.23 vs 0.756	0.5721	8.198	Yes
0.568 vs 0.756	0.3998	5.728	Yes

Table 4.21: ANOVA test results comparing the distributions of data points from fig. 4.94 b) with each other.

Fig. 4.95 shows logarithmic decay curve fits of the medians (a, blue curve), and of the means (b, orange curve) from the box plot in fig. 4.94. The goodness-of fit parameters are both decent, but interquartile ranges (in a) and the standard deviations (in b) are very high, limiting the statistical value of these particular analyses.

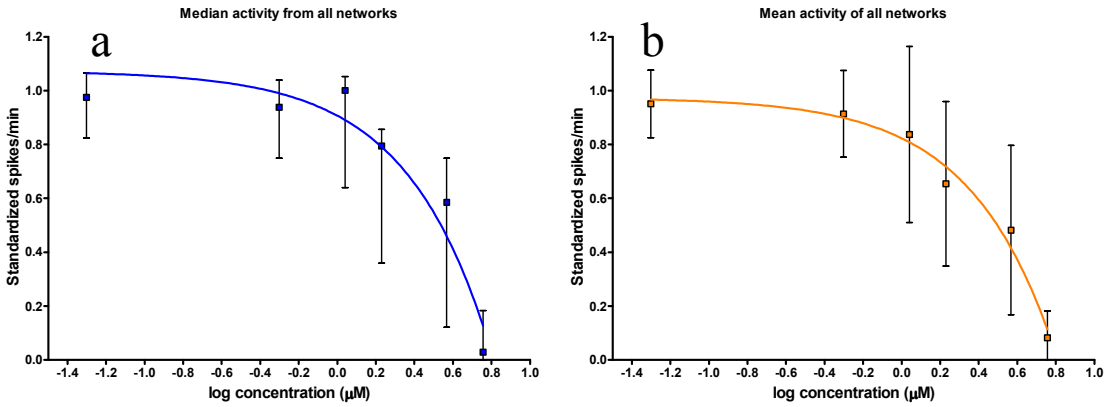

Fig. 4.95: Curve fits of the median (a) and mean (b) values from the box plot in fig. 4.94: Error bars in a: interquartile range, in b: standard deviation, IC50 (a) = 3.5, IC50 (b) = 3.1, R^2 (a) = 0.93, R^2 (b) = 0.98.

4.8.3 Calculation without initial normalization of individual units, network means:

Using the traditional way of determining the network activity values from the unedited spikes/min values prior to normalizing, we see that in this particular case the results are almost the same as with the normalization/median method. Both the ANOVA analysis and the curve fits of the combined data are virtually the same as in the analysis shown above.

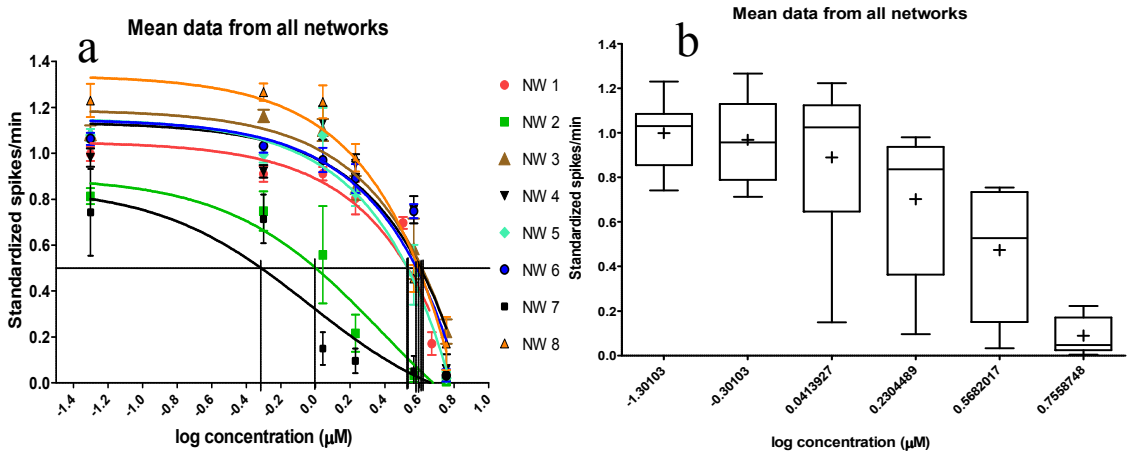

Fig. 4.96: Dose-response curves of the separate networks (a, error bars: standard deviation), and combined in one box plot (b, whiskers: min-max, cross: mean, bar: median).

Bonferroni's Multiple Comparison Test	Mean Diff.	t	Significant? P < 0.05?
-1.3 vs -0.3	0.03064	0.3978	No
-1.3 vs 0.041	0.1087	1.411	No
-1.3 vs 0.23	0.2973	3.860	Yes
-1.3 vs 0.568	0.5253	6.821	Yes
-1.3 vs 0.756	0.9097	11.81	Yes
-0.3 vs 0.041	0.07804	1.013	No
-0.3 vs 0.23	0.2666	3.462	Yes
-0.3 vs 0.568	0.4947	6.423	Yes
-0.3 vs 0.756	0.8790	11.41	Yes
0.041 vs 0.23	0.1886	2.449	No
0.041 vs 0.568	0.4167	5.410	Yes
0.041 vs 0.756	0.8010	10.40	Yes
0.23 vs 0.568	0.2281	2.961	No
0.23 vs 0.756	0.6124	7.952	Yes
0.568 vs 0.756	0.3843	4.990	Yes

Table 4.22: ANOVA (repeated measures) test comparing the distributions of data points from fig. 4.96 b) with each other.

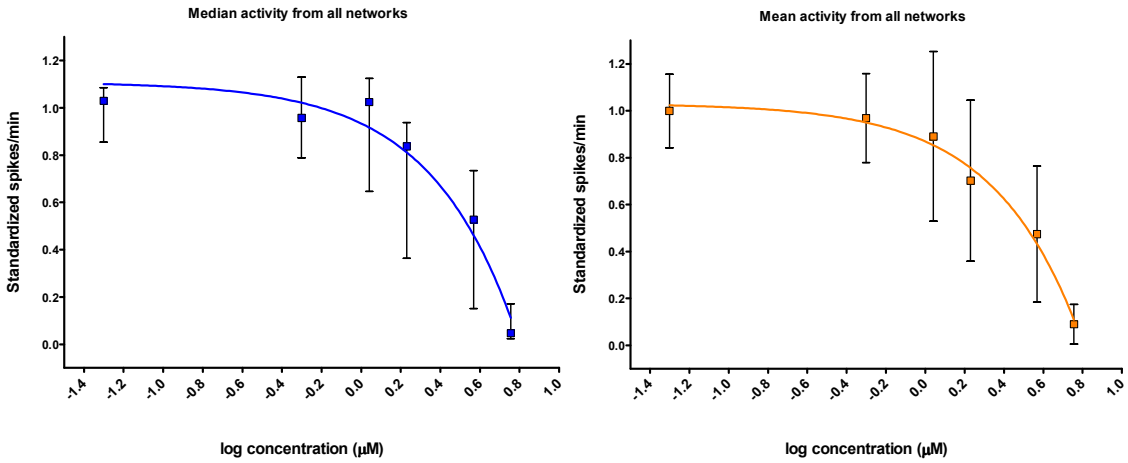

Fig. 4.97: Curve fits of the median (a) and mean (b) values from the box plot in fig. 4.96: Error bars in a: interquartile range, in b: standard deviation, IC50 (a) = 3.4, IC50 (b) = 3.5, R^2 (a) = 0.96, R^2 (b) = 0.98.

4.8.4 Excluding networks 2 and 7:

Since the poor separation of responses, in terms of significant activity changes from one muscimol dose to the next, was most likely due to the greatly enhanced sensitivity of networks 2 and 7, fig. 4.98 shows what happens when the data from these two networks are excluded from the analysis. The separation becomes much better, and tables 4.23 and 4.24 provide a quantification of these differences. Calculating the medians from the normalized values does improve the sensitivity in this case over using the raw data to calculate the means before normalization.

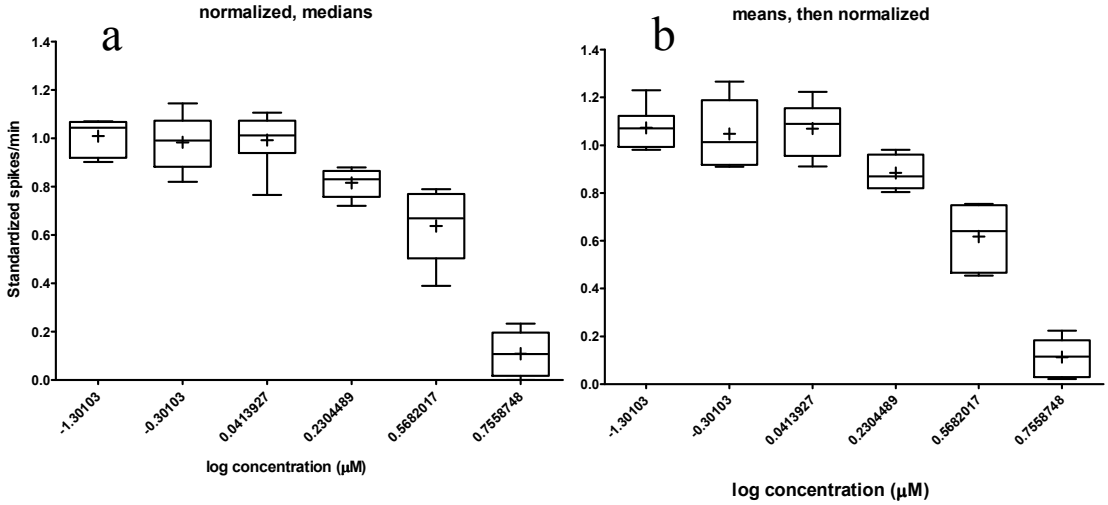

Fig. 4.98: Box plots showing the data from networks 1,3,4,5,6,8 and 9; a): normalized data, medians, b: non-normalized, means.

Bonferroni's Multiple Comparison Test	Mean Diff.	t	Significant? P < 0.05?
-1.3 vs -0.3	0.02515	0.5079	No
-1.3 vs 0.041	0.01612	0.3254	No
-1.3 vs 0.23	0.1930	3.897	Yes
-1.3 vs 0.568	0.3715	7.502	Yes
-1.3 vs 0.756	0.8993	18.16	Yes
-0.3 vs 0.041	-0.009033	0.1824	No
-0.3 vs 0.23	0.1678	3.389	Yes
-0.3 vs 0.568	0.3464	6.994	Yes
-0.3 vs 0.756	0.8741	17.65	Yes
0.041 vs 0.23	0.1769	3.571	Yes
0.041 vs 0.568	0.3554	7.177	Yes
0.041 vs 0.756	0.8832	17.83	Yes
0.23 vs 0.568	0.1786	3.606	Yes
0.23 vs 0.756	0.7063	14.26	Yes
0.568 vs 0.756	0.5278	10.66	Yes

Table 4.23: ANOVA analysis (repeated measures) results comparing the columns of data shown as box plots in fig. 4.98 a).

Bonferroni's Multiple Comparison Test	Mean Diff.	t	Significant? P < 0.05?
-1.3 vs -0.3	0.02536	0.4250	No
-1.3 vs 0.041	0.003557	0.0596 0	No
-1.3 vs 0.23	0.1891	3.169	No
-1.3 vs 0.568	0.4552	7.629	Yes
-1.3 vs 0.756	0.9600	16.09	Yes
-0.3 vs 0.041	-0.02180	0.3654	No
-0.3 vs 0.23	0.1638	2.744	No
-0.3 vs 0.568	0.4299	7.204	Yes
-0.3 vs 0.756	0.9346	15.66	Yes
0.041 vs 0.23	0.1856	3.110	No
0.041 vs 0.568	0.4517	7.569	Yes
0.041 vs 0.756	0.9564	16.03	Yes
0.23 vs 0.568	0.2661	4.459	Yes
0.23 vs 0.756	0.7708	12.92	Yes
0.568 vs 0.756	0.5047	8.458	Yes

Table 4.24: ANOVA (repeated measures) test results for the data from fig. 4.98 b).

4.9 Microchips for 24-network platform

4.9.1 Morphological assessment

In order to shed light on the biocompatibility of the new MEA-chips developed at the LME for a new 24-network recording system, cortical cultures were grown using a slightly modified version of the culture protocol. Fig. 4.99 shows good development of the glial cell monolayer at 6 days in vitro, as well as some emerging neurons with interconnections and smooth cell bodies.

The second picture (fig. 4.100) was taken one day later and shows that the neuronal cell bodies are now growing and the interconnections are becoming longer. Again, the cell health is good, and adhesion to the substrate seems to be unproblematic.

The last picture (fig. 4.101) taken from this particular chip shows the neuronal network on the entire electrode matrix after 10 days of development in the incubator. The network has now reached its final shape, and the cortical neurons usually start firing in coordinated bursts around this time.

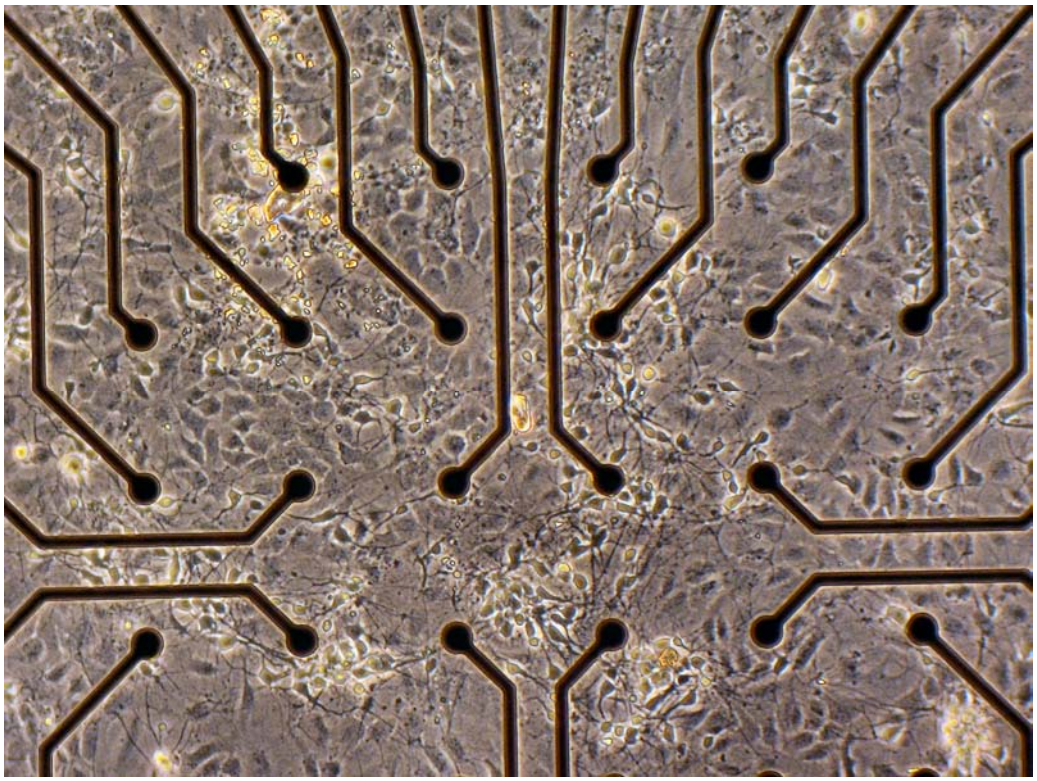

Fig. 4.99: Low density frontal cortex culture 6 days after seeding on a new 32-electrode microMEA chip.

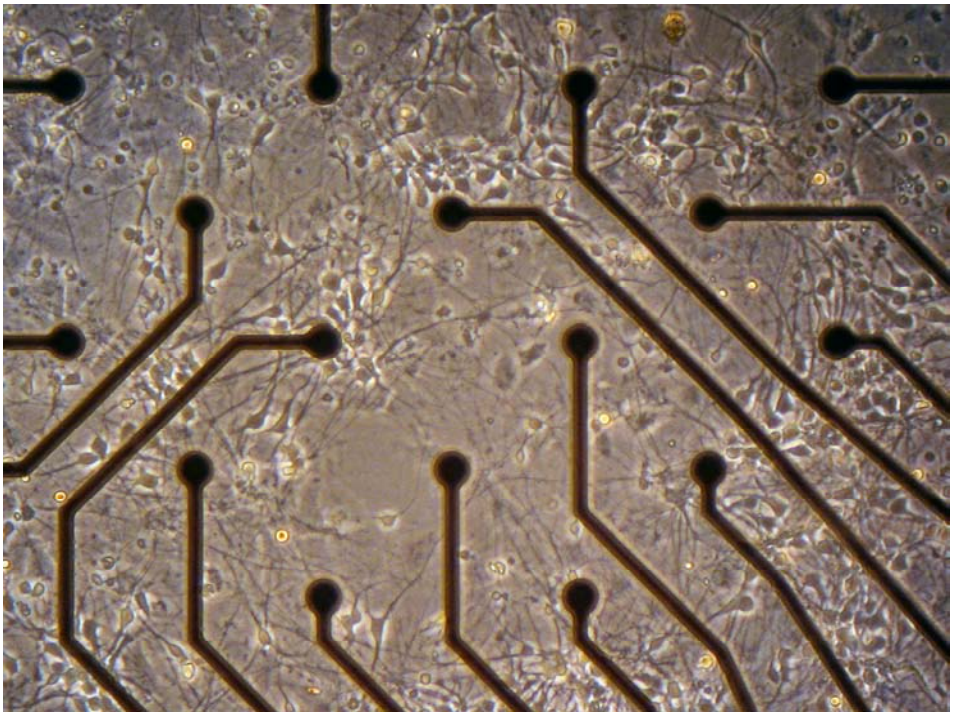

Fig. 4.100: Low density frontal cortex culture 7 days after seeding on a new 32-electrode microMEA chip.

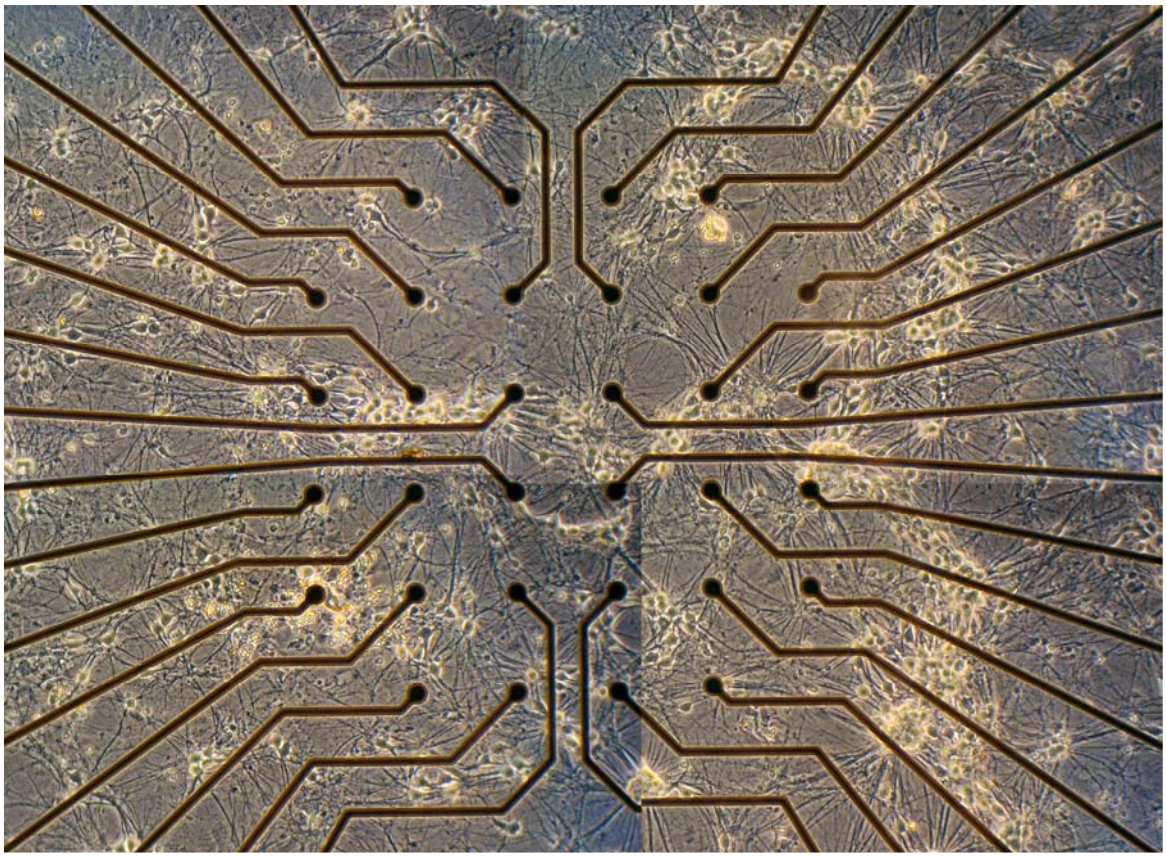

Fig. 4.101: Frontal cortex culture 10 days after seeding. The morphological development is nearly complete.

4.9.2 First recording

After mechanical difficulties with the adaptation of the new chips to the electronics that were available, electrical activity was recorded for the first time from cells grown on one of the newly developed MEA-microchips. Even though the cells were morphologically far from ideal (fig. 4.102), six cells were shown to be active (fig. 4.103). Figs. 4.104 and 4.105 reveal large differences in the spike rates among the individual units, as well as a strong, albeit very short, response to 20 µM bicuculline.

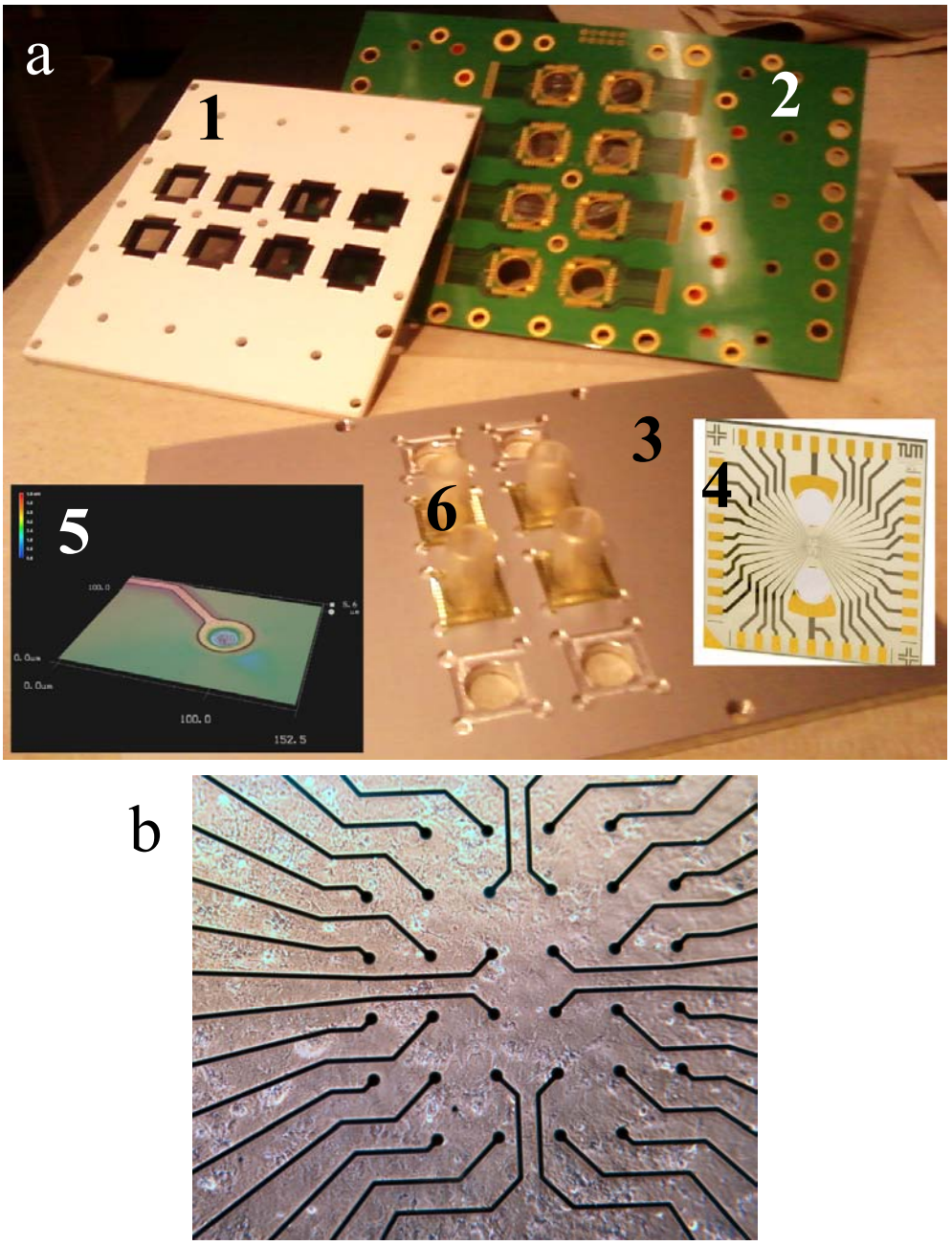

Fig. 4.102: a) Recording equipment: 1) Adapter with zebra strips for contacting MEA chips, 2) Bottom side of circuit board holding the pre-amplifiers, 3) Aluminum base plate, 4) microMEA chip without fluidics well, 5) 3D micrograph of electrode crater on microMEA chip, 6) microMEA chips with silicone medium well on top. b) Micrograph of the newly developed micro-MEA chip the activity shown in fig. 4.103 was recorded from (magnification: 100 x). Cell culture: FC, 48 days in vitro.

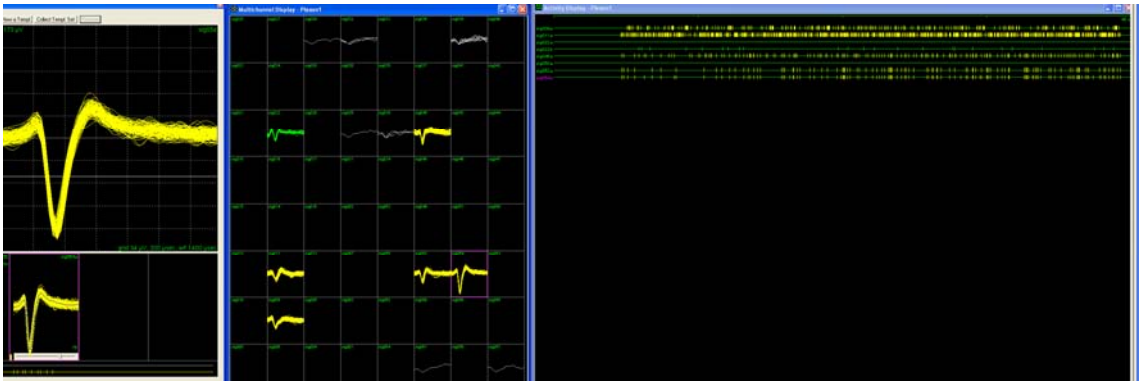

Fig. 4.103: Live screenshot of the recorded activity

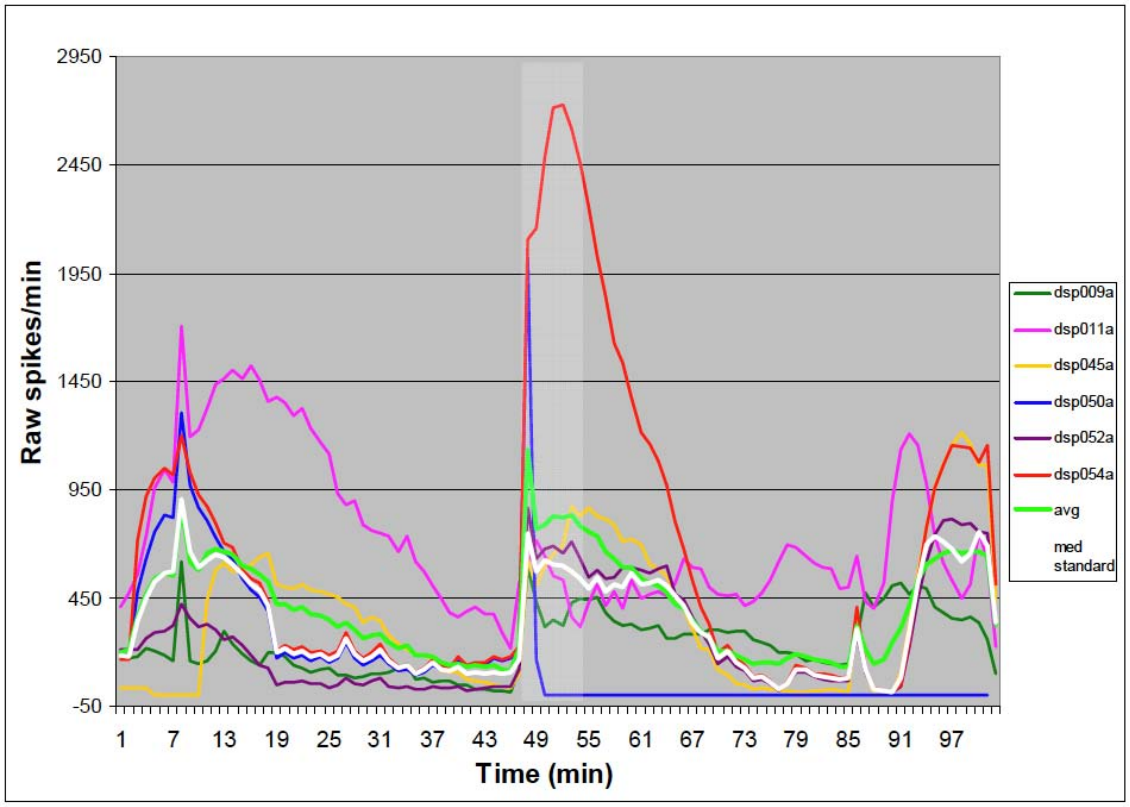

Fig. 4.104: Time course of recorded activity, raw data. Shaded area: Response to 20 µM bicuculline. Thick green line: mean values.

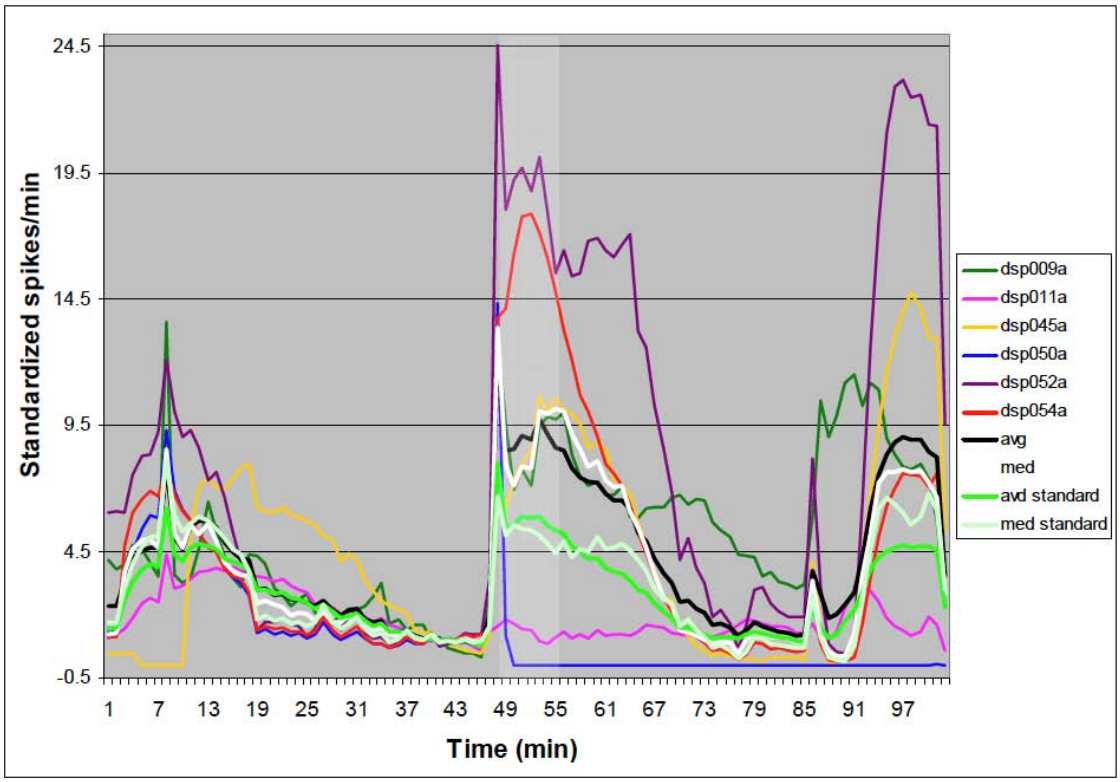

Fig. 4.105: Time course of recorded activity, normalized data. Shaded area: Response to 20 µM bicuculline. Median and mean values are shown as white and black curves, respectively. Median and mean values calculated without initial normalization are also shown (light green, green lines, respectively).

Chapter Five: Discussion

5.1 Electrical and magnetic inhibition of L929 cell proliferation

The rationale for this set of trials stems from a thesis first postulated by Cone and Tongier [134], and later by Binggeli and Weinstein, which state that mitotic activity might be functionally coupled with the TMP level and associated cellular ionic concentrations. Specifically, Binggeli and Weinstein showed that normal proliferating cells as well as uncontrollably dividing tumor cells always have a resting TMP less negative (i. e. higher) than -36 mV [10, 22]. They showed that other cells, which grow and cease growing in a controlled manner, reach more negative potentials and remain quiescent after one or two cell cycles in culture, whereas tumor cells are trapped at higher potentials and do not quit dividing. Since they point out that this relationship between membrane potential and proliferative activity may be causal in nature, we attempted to manipulate the growth rates of cells from a fibroblast cell line that had been treated to grow in a tumor cell-like fashion. We used different types of pulsed electrical fields with strengths ranging from 100 to 1350 V/m, which translates to 1.5 - 20.25 mV induced membrane potential change at the individual cells, according to equation 1-12. This, in turn, rendered the TMP more negative, as it is defined as the difference of the internal and the exterior potential. With the field application methods available, it is impossible to induce a uniform TMP shift in radial direction all over the cell surface. The field lines produced by our application geometries were approximately linear around the single cells and crossed them in one direction, polarizing the cell surface in accordance with figure 1.10. We used only positive stimulation pulses to make sure the surface potential not be shifted in both positive and negative directions, annihilating the desired effects. Applying the field in a DC mode would certainly have maximized the field exposure and polarization that one side of the cell membrane experiences. However, even with the inert platinum electrodes used here, electrochemical phenomena, but no hydrolysis (which occurs at 1.2 V), would eventually have been induced by the voltages we applied and affected the cells' viability. Therefore, pulsed fields with a duty cycle of 2.5% were chosen. To our knowledge, no cytotoxic electrochemical effects caused by these parameters have been reported.

In order to make sure the cells were merely inhibited but not directly killed by the voltages applied, treated and control cultures were stained with Trypan blue, a dye that only passes fatally disrupted cell membranes, thus selectively staining dead cells. No considerable differences between the treated and untreated cultures were observed. Another potential, artifactual cause of growth inhibition could be excessive heating induced by the electrical pulses. In a 21 hour test recording under realistic stimulation conditions, using Pt1000 sensors embedded on the glass chip, a temperature elevation of 0.8 °C was confirmed. However, no evidence from the literature was found suggesting that this amount of heating might inhibit cell proliferation. In fact, the opposite effect would have been more likely to occur. Finally, the cells were also photographed before, during and after each treatment, so that apparent morphological irregularities could be spotted. This, however, was not the case.

A limited number of studies suggest that electrical inhibition of cell growth is possible. For instance, the proliferation of endothelial cells was inhibited using a 200 V/m DC electric field for 24 hours [111]. In another study, L929 fibroblasts were

exposed to sine shaped electric fields at an amplitude of 100 V/m and various frequencies. Below 1 kHz, the cells were proliferating significantly slower, whereas above 1 kHz, the treatment induced an enhanced growth rate [63]. The author hypothesized that at low frequencies, the local ionic densities and dipoles could have been altered, and that mechanically sensitive and voltage-gated ion channels could have been influenced by the electric fields, leading to higher influx of calcium ions. At frequencies exceeding several kHz, the transport rates of cellular ionic pumps and exchangers was postulated to be the decisive factor of manipulation. Even higher frequencies were used in a study using a variety of human and rodent tumor cells [114]. At 100 – 300 kHz and field strength amplitudes of 200 V/m, proliferation was inhibited. The authors propose two mechanisms of action, the first one being the electric field forces orienting tubulin dimers in the direction of the field lines during early mitosis, the second one, at later stages of the cell cycle, interference with cytokinesis through polarization and movement of organelles. All of these studies indicate that electrical inhibition of cell proliferation is within the realm of possibilities, but they either gave an incomplete description of the stimulation parameters and no conclusion about which aspect of the field was the decisive one that actually caused the cell cycle arrest, or they showed results we were unable to reproduce. Some of them did not entirely clarify the field characteristics at the site of the cellular stimulation. Therefore, we made an effort to apply electrical energy to cell cultures in two distinct ways, comparing direct cell-electrode coupling with purely capacitive interaction using the same cell line and very similar incubation conditions. Field amplitudes and geometries were simulated using FEM methods, and calculations of the current densities at the cell layer level were performed as well. In the first phase of the inhibition trials, the cell cultures were treated electrically using a glass chip developed and fabricated at the LME with selectively deinsulated electrodes. In the second tier of the electrical stimulation experiments, we used a stimulation device that was designed to apply pulsed electric fields to industry-standard 6-well culture plates. The treatment parameters were chosen according to a comparison of the parameters from the literature and to practical considerations: For sufficient transmission of electrical energy, the fields should be pulsed, yet at the same time, there should be plateaus in each pulse that are long enough to actually polarize the cell. Using the glass chip with platinum stimulation electrodes developed at the LME, an effective current density of j_z = 10 A/m^2 at the site of the cells was calculated. We observed a significant cell number reduction of 30 % when the cells were counted right after the 21 hour stimulation period (independent of whether the treatment was administered 48 or 72 hours after seeding), and a reduction of 50 % in those cultures that were incubated for an additional 24 hours after the treatment. This indicates that the 21 hour generation time of the L929 cells may not be valid for all the cells in culture, and that the effect on those cells with a longer cell cycle may not have been observable right after the treatment period but after an additional incubation period. We conclude that the polarization induced by the electric field and currents sufficed to inhibit proliferation rates in a substantial way. The statistical significance of the differences between the treated cultures and the controls was confirmed by an ANOVA with multiple post test (Sidak-Holm, $p < 0.001$).

The capacitive stimulation device was designed to have adjustable voltage settings, so that field strengths between 0.6 kV/m and 2.2 kV/m at the level of the cells in the 6-well plate could be evaluated. The current densities experienced by the cells were between 10^{-6} and $6*10^{-6}$ A/m^2 and thus 6 – 7 orders of magnitude smaller than the ones produced on the glass chips. The data from several dozens of treatment cycles

demonstrate that these field strengths were not capable of inhibiting the proliferation rates in any significant way. Thus, a new stimulation board was designed featuring interdigital stimulation electrodes (IDES) of various dimensions which created a field gradient pattern as illustrated in fig. 2.16. The presence of a field gradient was proposed to be one potential reason for the greater inhibitory efficiency of the electrodes on the glass plates (fig. 2.6) over the 6-well stimulation board. Yet, a significant influence over the proliferation rates was not observed, which leads to the conclusion that the field gradient alone cannot be held accountable for the effects observed from the glass chip experiments.

A third method of external application of electrical energy involves the use of a stimulation coil that induces an electrical current inside the intra- and intercellular electrolytic fluids. Inductive coupling of electromagnetic energy with biological tissue has been used for several decades, partially with astonishing results. Transcranial magnetic stimulation, for example, has been used to treat symptoms of stroke, severe depression, epilepsy and other disorders of the central nervous system. The motor function-related symptoms of Parkinson's disease are greatly alleviated with electric deep brain stimulation, which could most likely be achieved non-invasively if stimulation coils were capable of penetrating the tissue deeply enough. However, the exact mechanisms of these (inter)actions on the cellular level remain elusive to date. Efforts have been made to stop cells from proliferating using magnetic stimulation in the past, but there are discrepancies between the results obtained by different laboratories. One study concludes that a 50 Hz, sine shaped magnetic fields of 1 mT flux can inhibit proliferation of lymphocytes [115], and another laboratory inhibited SV40-3T3 cell growth by 10 % using a 2 mT, 50 Hz field (60 min application, 300 minutes post-incubation time) [116], while a third group found no significant growth rate changes of tumor cells after exposure to alternating magnetic fields. They applied 50 and 60 Hz fields at 2, 20, 100 and 500 µT for 24 hours [117]. In a combined *in vitro* and *in vivo* study, artificially tumors were shrunk substantially by application of a 0.25 T (maximum amplitude) pulsed magnetic field in live mice. 1000 pulses were applied per day at a repetition rate of 25 Hz for 17 days, after which the tumors had reduced in weight by 70 %. The results indicated that the magnetic pulses activated the immune functions of the mice, thus causing the reduction in tumor size. However, the cell cultures used for the in vitro stimulations, which confirmed that the cell proliferation was not directly inhibited, only received a fraction of the number of pulses applied to the mice. Therefore, a convincing conclusion ruling out direct growth-inhibiting effects was missing.

The final portion of the inhibition tests was conducted using a magnetic stimulator. Initially, a miniaturized stimulation coil had been developed, but the actual field strengths, as measured using a Gauss meter, were not high enough to induce the currents needed. Therefore, a commercially available magnetic stimulation device was used. The stimulation parameters were chosen to resemble the ones used in the study that demonstrated tumor reductions in live mice. However, the pulses were given in a more evenly distributed way, so that a total amount of 40,000 pulses were given over a period of 17 hours. The current density at the site of the cells was $j_z = 11$ A/m^2, which was comparable in amplitude to the currents measured on the glass chips. The cultures were mounted in a custom made culture chamber with a closed-loop medium supply on a microscope stage for sterile, incubator-like life-support maintenance. For each treated culture, there were two controls that were kept under the same conditions during the stimulation period. The cell number of the treated cultures was between 30 % (n = 4)

and 50 % (n = 3) lower than in the controls, depending on the time of stimulation. In addition, two sham stimulations were conducted using approximately 5 % of the stimulation energy. The cultures did not respond to these weak fields, which provides further evidence that the effects were actually due to the applied fields.

In summary, we were unable to show a purely field-induced proliferation inhibition at the field strengths we provided. Higher field strengths are certainly possible. However, if one imagines an implant applying these fields inside a human body for treatment of a solid tumor, safety concerns do arise. At current densities of $6*10^{-6}$ A/m^2 at the cell level, no effects on the growth rates were induced. However, using deinsulated stimulation electrodes or a high-energy magnetic coil that induced eddy currents in the culture medium, the cells' proliferation rates were diminished significantly. Since a direct penetration of the interior of the cell is only possible at frequencies beyond 10^6 Hz, the results indicate that the outside of the cell membrane was sufficiently manipulated to slow down the cell cycle. The membrane potential is a likely candidate for a cellular mechanism, since it is directly affected by external fields and currents.

As shown in figure 1.8, the cellular mechanisms responsible for uncontrolled mitosis in cancer cells are manifold. Initially, a healthy cell is transformed into a tumorous one through a fatal mutation in the DNA, which causes the cell to lose control of the proper protein production parameters. While many cellular processes subsequently lose their balance, the most important change that influences mitotic behavior occurs at the plasma membrane where faulty transmembrane proteins no longer form gap junctions that ensure cell-to-cell adhesion and –communication. Furthermore, the inflow of sodium ions increases and the TMP becomes more positive, it depolarizes. The increased sodium levels stimulate DNA synthesis which, in turn, fuels the division of the cell, and the problems concerning the gap junctions and the membrane properties render the cell unable to repolarize (towards a more negative TMP) and to sense the neighboring cells. Thus, contact inhibition cannot be established and there is no feedback from the surrounding cells indicating the cell to stop dividing. This feedback may be the TMP itself, as some publications have pointed out [10, 22, 134]. Ultimately, this cycle cannot be stopped, and the cell divides irrepressibly. Breaking the cycle by artificially depolarizing the cell is not inconceivable. Of all the mechanisms keeping the uncontrolled division going, it may well be the one whose correction requires the least invasion and the one that would cause the least severe side-effects. After decades of searching for a cure for cancer in genetics and molecular biology, applying electromagnetic fields seems like an outdated approach. However, we believe that altering the membrane potential is a more global approach than trying to silence certain genes or to prohibit certain proteins from forming. Many of these gene manipulation approaches have failed in the past because most cells' signaling pathways are so immensely redundant that it is very difficult to completely shut the cells' activity down. From what was observed in this study, application of pulsed currents appears to have the potential for a new, alternative treatment strategy for certain tumor types. The most elegant, minimally invasive method is certainly the application of pulsed magnetic fields. However, currently available application devices are only capable of producing sufficient field strengths up to 3-5 cm away from the stimulation coil, which limits the application to certain tumor types that are in close proximity to the skin. New coil geometries and stimulation sources are currently under development at the Institut f. Medizintechnik (IMETUM) of the TUM. The use of these devices in future trials may substantiate the evidence for the anti-neoplastic potency of electromagnetic fields and

eventually lead to clinical trials for validation of this new experimental treatment method.

5.2 Neuronal network experiments

Recording electrical activity from electrically active – meaning AP producing – cells and tissues has continually gained popularity among researchers from many corners of biological science over the past decades. One core application that is emerging as more and more experience with the technology and the behavior of the cell cultures is gained is the screening of pharmacological and toxicological compounds using primary neuronal networks grown on MEAs. For commercialization of such a system in today's competitive world of medical research to become a success, certain characteristics will be crucial:

- Generation of a high number of data points in short periods of time
- Reliability of the system and repeatability of the results
- A high degree of automation for elimination of operator-induced errors
- Minimal training time for the experimenter
- Minimal training time for the cell culture technician
- Cost-efficiency of both the equipment and the consumables

In order to accomplish all of these objectives, Dipl.-Ing. Florian Ilchmann and other members of the Heinz Nixdorf-Lehrstuhl f. Med. Elektronik of the TUM have been developing a radically new concept that unites the latest engineering technologies with viable solutions for cell cultivation and maintenance for long-term stability. Following industry standard multi-well plate dimensions, a 24-network layout was chosen and named NeuroPlate. This will, on average, generate up to 24 dose-response relations with ~10 data points within one session. In comparison with the commercially available four- and eight-network systems (the MMEP8 is not commercially available), this will translate into an increase in throughput of 500% and 200%, respectively.

One important feature is the new MEA plate that is 12 x 12 x 0.5 mm in size and therefore well suited for concomitant high-resolution light microscopy. The silicon nitrite insulation layer's optical transmission characteristics are excellent. A silicon cylinder that is cast on top of the plate serves as the container for the culture medium during cultivation and recordings. This cylinder is easily accessible with a standard pipette tip. The small size of the individual plates will keep the production costs low enough for them to be disposable. This is a crucial advantage of the new system, as it will guarantee each plate to be in the exact same condition before cells are seeded on them. Re-use of MMEPs by means of cleaning and re-sterilizing is still quite common in most laboratories, but it is a major source of quality fluctuations of the culture quality. While the plates are situated in an anodized aluminum plate, an adapter containing zebra strips will connect the plates with the electronics board that sits on top of the plates. This board contains all the components required for amplification, filtering and digitization of the recorded APs. Using multiplexers now available at sufficient speeds, the signals from the 768 individual electrodes will be transmitted to a

workstation computer as a single, digital data stream. Real-time data acquisition and automated spike sorting will be performed by programs that are being developed. Efficient visualization of the temporal evolution of electrical activity is a particular challenge, since it is hard to keep track of 24 individual activity diagrams as shown in fig. 4.92 on a manageable number of computer displays. Plotting all the wave shapes gathered from 768 electrodes appears to be an overwhelming surge of data for one operator to handle. The solution to this could be that from an overview display that shows the current and past activity levels of all 24 networks, one can optionally move to a detailed display of up to four networks at a time to make sure all units are identified correctly. The reliability of the spike identification algorithms will be of utmost importance. As the result of each experiment, the program should generate a dose-response relation of the spike activity and all the desired spiking and/or bursting parameters, depending on the nature of the activity of the tissue type used. Sophisticated new statistical analysis methods will be incorporated. They will give a more detailed and comprehensive insight into the changes of the population- and subpopulation-dynamics evoked by the chemical stimuli of the compounds than currently available. An outline of promising approaches to a mathematically sound network activity analysis is discussed below.

At the start of each experiment, the automated data analysis program will have to make a decision as to when to apply the first dose of the compound under investigation. An initial reference – or equilibrium – period of several minutes is required for the statistical analysis of every single recording to be valid. Empirically, 15 – 20 minutes of steady activity have been agreed upon as being sufficient. Since most pharmacological responses quantified with this system are acute in nature and display onset times between a few seconds and a few minutes, a reference period exceeding 20 minutes would be unnecessary. The activity values usually oscillate temporally around a certain level at different time scales. While there are always variations from one minute to the next, there can also be inconsistencies at time constants of several minutes. Additionally, there is always a very slow activity drift due to nutrient depletion of the medium and buildup of metabolites, such as ammonia, that can be harmful to the neurons, but the slope of the mid-range fluctuations is in the main focus here. The stability of the reference activity is characterized by a slope of the mid-range variations that is ideally zero, while minute-to minute variations of a certain amplitude are acceptable. However, the culture should not be used – at least not at that particular time – if these fluctuations exceed a certain limit that reduces the sensitivity of the culture so much that small activity reductions induced by a compound could not be recognized in a statistically significant way. Therefore, one goal for an optimized experimental procedure is to minimize minute-to-minute fluctuations. This might be achieved biologically by automation of the seeding and culture maintenance process, or possibly by optimizing the mathematical data analysis methods. While it would be highly desirable to eliminate as much “operator-induced error” from the process, fully automated cell culture systems for primary neuronal cultures are not available, and the development of such a system would require a substantial amount of time and funding. The latter approach, however, may be relatively straightforward to be at least proven useful or aimless.

In pharmacological studies utilizing neuronal cultures on MEAs, changes in the electrical activity are mostly due to receptor-agonist (or -antagonist) interactions. However, other cellular mechanisms, such as energy production, necrosis, apoptosis etc., can be monitored by tracing the electrical activity as well. The rate of AP

production provides an immediate feedback of the cell's functional integrity, and many nuances of reversible and fatal neurotoxicity can be distinguished. However, the interpretation of activity changes is, to be honest, difficult. To date, there is no answer to the question, "What is the best representation of the network responses?" [129]. Unfortunately, it depends on the exact problem one is trying to investigate. One complication is the fundamental interaction of subpopulations which is highly non-linear and dynamic, both temporally and in terms of structural changes of the network connectivity. Yet, these challenges have received minimal attention in the past. On the path to high-throughput systems based on MEA technology, they need to be addressed. Several different types of data visualization and analysis may eventually co-exist, so that the user can choose from a set of statistical methods in order to always have the suitable approach at hand. A global population analysis and a subpopulation analysis should ultimately run side-by-side and be treated as independent parameters of the same network. For example, it is conceivable that steady network activity is possible even though subpopulations are highly dynamic. An automated program controlling the recording of several dozen cultures should also be capable of computing advanced statistical measurements, such as continuous variability control of EC50 values. Such information can then be used as important feedback for the cell cultivation.

The goal of a high-throughput system based on MEA technology is an efficient application of compounds and a productive data analysis in one program package that is based on the standard statistical methods tailored around the specific application. There is no standard selection of statistical analysis methods as found in many other scientific areas, where statistical methods have been established and are used the same way by the entire community. The significance of such a new set of statistical methods is to have an automated high-throughput system that delivers robust, trustworthy data that are in the best possible agreement with data from studies using other in vitro or in vivo techniques available in the literature. Decisions during the experiment or its analysis, such as "When should outliers be eliminated?", or "When should unstable networks be ignored?" are still made by the user. In a future, automated system, this should be made in a more reproducible manner by a program. As the reliability and automation of the high-throughput system are optimized, pharmacological studies investigating the neurotoxicity of chemicals may even emerge to be preferably carried out using this *in vitro* assay, rather than focusing on animal trials where compounds are metabolized and the interaction of the entire organism can complicate the evaluation of an effect on an individual organ, in this case the brain.

The CNNS and the group of Prof. Weiss of the University of Rostock have been using the mean values of the recorded spiking and bursting parameters as measures of the many facets of network activity in the past and have been obtaining good results that agree with most data from the literature. However, no systematic effort has been made to optimize the network analysis in terms of how the network activity should be described and quantified. A study performed at the CNNS showed that dissociation constants can be determined using the MEA system [113]. The values obtained from these recordings showed remarkable similarity with data from publications using different animal models. However, many "ill-behaved" networks could not be used in this study. Thus, an optimization of the experimental process is needed.

Recently, members of the CNNS have created new, Labview-based programs that are used as a display of the spike and burst production of the network. One version of this program uses the total number of units that were active at the beginning of the recording as a fixed denominator for calculation of the network average, another

approach in use is to update the number of active units from minute to minute and divide by that number. While the latter approach reflects more accurately the activity of those units still firing under a certain, externally induced chemical influence, it can also generate misleading numbers, especially when a lot of scarcely active units have quit firing, and only a few, but rather strong, units remain. The fact that groups of neurons react to a given compound more sensitively than others might indicate that one single value (per unit of time) might not be enough to provide a satisfying description of the behavior of the entire network. The network, even if comprised of a mere few dozens of neurons, is a highly dynamic, intricate system that owes its complexity mostly to the complicated architecture of the synapses, their interactions, and the sheer number of interconnections in the network.

The data shown in this study suggest that there is a large range of aspects along the statistical analysis process that hold potential for significant optimization. One of them is certainly to have separate analysis approaches for distinct activity pattern types generated by cells from different regions of the brain. Tissue from the frontal cortex typically generates coordinated bursting activity, as shown in the previous sections. Midbrain cultures with a high percentage of dopaminergic neurons are also spontaneously active, but in a – seemingly - more chaotic pattern. However, under certain conditions, the network can synchronize its activity through its interconnections, as shown in figure 4.3. This is an example for a response to a drug addition that was visible through changes in the internal pattern dynamics, but not by merely quantifying the AP output. It is obvious that only a portion of the neurons in that particular network responded significantly to the external stimulus, which leads to the suggestion that a subpopulation analysis might be a valid approach to quantify such changes.

Even a simple replacement of old culture medium with fresh solution can trigger heterogeneous, unit-specific responses, as fig. 4.7 reveals. In this case, analysis of the global activity would have concluded that the activity rose by a few percent as a response to the medium change. However, the array of histograms shows that some members of the network lost their activity entirely, while others' activity grew by more than 100%. It is certainly essential to incorporate this sort of information in future systems for a comprehensive description of the network dynamics.

A more drastic activity transformation can be seen in figures 4.8 and 4.9. Bicuculline, a $GABA_A$ antagonist, was used here to create a coordinated activity pattern out of a seemingly chaotic distribution of spikes. At first glance, this seems to be a uniform, global transformation, since the majority of units apparently switch from random chatter to orchestrated waves of activity. Yet, a closer look at the histograms in figs. 4.11/12 (showing the spikes/min values recorded throughout the respective periods) and 4.14/15 (the same data, but normalized by each unit's reference activity) changes one's realization quickly. During the reference period (no bicuculline), four groups of neurons with distinct firing rates are distinguishable easily, and in the normalized data set, it is of course only one, because the normalized data display changes with respect to the reference activity only. After the addition of bicuculline, however, the raw data now show five subgroups, while the normalized data go from one distribution to three. This means, on the one hand, that the bicuculline induced a shift and a splitting of subgroups, and on the other hand that normalizing the data unit-wise yields considerably different results from monitoring the absolute activity values: As opposed to the raw data, it shows how each unit's own activity evolves in relation to its own reference activity. Therefore, it shows relative changes. For the subsequent calculation of a value representing the network behavior, this means that normalizing

provides each unit with an equal weight, while without it, units with higher reference activity levels have a heavier weight in the calculation of the network value than those with weaker activity.

Another parameter that may be significant when investigating molecular mechanisms of substances is the temporal evolution of the activity during the transition time between the addition of the compound and the final activity level generated by it. In figures 4.10 and 4.13 we can see that, unlike in cortical tissue, the response to bicuculline by midbrain tissue is not apparent immediately, but it grows over a period of nearly 40 minutes. This in itself is interesting, as it might point towards different synaptic distributions of GABA- and other receptors. Additionally, the response kinetics are not uniform: some units reach their maximum activity after 20 minutes, while it takes twice as long for others. Onset kinetics are another variable that should be included in future sub-population analysis approaches.

Both recordings with a small number of units (figs. 4.17 – 4.23, 15 units) and those with a high sample number (figs. 4.24 – 4.28, 80 units) benefit from normalizing each unit's activity first and then using the median as the measure of network activity: Fig. 4.21 shows that under the influence of bicuculline, this FC network splits up into at least four subgroups. Therefore, it is almost impossible to mathematically describe the histogram as one distribution using a curve fit ($R^2 = 0.58$). This is even more apparent when a high number of units is available for recording (fig. 4.26). Normalizing the data first changes the shape of the distribution drastically. It creates a more pronounced peak that can be used to represent the network behavior. Normalizing also moves some of the outliers even further outward – especially those units that initially were weakly active and now increased their activity by a high factor (purple curve in fig. 4.18: up to 27.5 times as active as during initial period). Since these outliers have a strong influence over the mean (orange lines in all the histograms), the median is better suited to represent the behavior of the network's majority of units. One might argue that more active units have a greater influence on the network's activity because they usually have more synaptic connections than other members of the network. Hence, they should be granted stronger mathematical influence over the calculated network values as well. However, one does not always record from these types of cells. On a 64-electrode array with an electrode diameter of 10-15 µm, the limit of the effective radius around the electrode from which APs could be recorded was previously estimated to be 30-100 µm [132, 133]. Given the spacing of the electrodes is 150 µm, this translates into 8-100% coverage of the entire area of the square. However, the numerical simulations from [133] did not take into consideration many morphological parameters found in biological cell cultures, and the experiments from [132] were performed in acute brain slices, which obviously present a different geometric, and thus electric, tissue arrangement that changes the spreading and seal resistances considerably. From our own experience, these numbers seem like an unrealistically high estimate of the electrodes' reach. The sensitivities of the electrodes are highly variable and depend on numerous factors, such as glial overgrowth, stability and actual area of the gold plated crater, and the medium biochemistry, all of which are reflected in the spreading resistance and the seal impedance (fig. 1.26). Based on experience gathered at the CNNS from decades of recording from primary cultures, a 30-µm radius within which an electrode can sense an AP is an overestimation. The actual radius depends on the glia-neuron-electrode arrangement which can be 'neuron on top of electrode', 'neuron (including neuronal processes) on top of glia cell(s) on top of electrode', or 'glial cell(s) on top of neuron on top of electrode'. In this order, the sensitivity of the electrode

generally increases, meaning that in the first and second case, the neuron almost always has to be in direct contact with the electrode, and in the third case it may be several µm away and still be able to pick up signals. Considering the lucky case of having 64 electrodes with a "sensitivity radius" of 10 µm, the active area on the matrix would still be a mere 2.95%. In addition, the networks grown on the MMEPs usually spread out over 10-30 mm^2, so that the electrodes' coverage of the whole network is at least one order of magnitude smaller. Coming back to the problem of whether to normalize the units' individual activity or to give the highly active units more influence over the values representing the network state, it appears logical to assume that many neuronal networks have "outliers", highly active cells, but because of the sparseness of the electrode coverage, one will probably not always be able to record activity from them. Thus, when outliers are present, one should normalize their activity values and assign them the same weight as all the other members of the network. With larger, denser electrode arrays - possibly available in the future - that could cover a neuronal network more fully, this issue should be revisited.

An unexpectedly blatant example of tissue specificity is given in fig. 4.37, which shows data from two ethanol titrations in midbrain cultures. Just like in frontal cortex tissue, which has been extensively studied (fig. 4.38, courtesy of CNNS), high concentrations of ethanol stall the electrical activity of the network altogether. While this is achieved at approximately 150 mM in frontal cortex tissue, 500 mM were needed to stop all activity in midbrain cultures. Accordingly, the IC50 for midbrain tissue was 224 mM, while it is 30 mM in FC. This is a remarkable discrepancy, which needs to be explored further in future trials. When translating these results to in vivo phenomena, it may be valid to conclude that when mammals are under the influence of ethanol, cortical functions such as planning, inhibition and control of conscious actions are inhibited first, while tasks that are controlled by older brain areas, such as motor control in the midbrain, are still working satisfyingly. For a strikingly convincing display of this hypothesis, one might spend a day at the Oktoberfest in Munich.

The data presented in this work are not limited to midbrain recordings. Lidocaine was tested using seven midbrain cultures and eleven FC ones, and figure 4.39 provides a screenshot of an interesting FC recording with highly coordinated bursting and two units that do not follow the rest of the network's pattern, one of which (the yellow unit) is considerably more active than the other one. Their firing seems to lead up to each network burst, pauses for a few seconds and starts back up. This might indicate that it is a pacemaker cell that drives the network's bursting rhythm. Interestingly, this particular cell was not nearly as strongly affected by the high dose of lidocaine (50 µM) as the rest of the network. Note the logarithmic scale on the y-axis in fig. 4.40. This single unit had a considerable influence over the network mean (green curve in fig. 4.41), while the median, representing the majority of the network population, is at zero under that high lidocaine concentration (fig. 4.42). Pacemaker cells may generally be less sensitive to inhibitory compounds because their spiking may not be primarily triggered by the input from other neurons but by intrinsic mechanisms that are independent of synaptic input. In other words, while the "normal" neurons are rendered silent one by one with more and more of them dropping out, failing to provide input to the remaining ones, the pacemaker cells keep generating APs because that is what they were designed to do.

A high degree of variability in the responses to lidocaine was observed in the FC cultures in general. Fig. 4.43 b) points out a particularly unexpected observation: In this experiment, four incremental lidocaine doses were applied: 1, 2, 3, and 8 µM.

While the global network activity decreased steadily with increasing cumulative lidocaine concentration (fig. 4.43 a), some of the individual units displayed their strongest responses after the first, second or third application, and then recovered while more lidocaine was added. This type of nonlinearity in the pharmacological response eludes explanation at this point and will require more attention in future trials that incorporate subpopulation analysis.

The high inter-cultural variability is reflected in the large amount of variability in figs. 4.44 and 4.45. These graphs summarize the data from eleven networks. A sigmoidal curve fit was attempted, but the goodness-of-fit parameter is very poor (R^2 = 0.4) when the data points showing the network mean value before normalization were used, and still poor, but considerably better, when the data was derived using unit-wise normalization before calculating the network median values (R^2 = 0.51). The IC50s are in a range between 1.15 and 1.37 μM, but their standard errors are very high. These data may point towards an extremely selective mode of action of lidocaine that affects certain subtypes of cortical neurons differently than others. Since the primary cultures used here contain a mixture of neuronal cell types as present in the embryonic tissue they were isolated from, slight deviations in the proportion of these cell types may have major influences over the dose-response behavior.

The midbrain data show less variability, even though the curve fit is still not perfect. In this instance, using the medians of the normalized data did not improve the tightness of the fit (fig. 4.52), but it gives a lower value of 27.5 μM for the IC50 than the network mean (40.7 μM, fig. 4.51). However, both of these values are 20-35 times higher than the ones derived from FC tissue. This is a remarkable tissue specificity that may help pinpoint mechanisms of action in future studies.

A substantially higher concentration of the global anesthetic barbital-sodium is required to achieve activity suppression than of lidocaine. Data from three FC networks yielded IC50s of 567 μM and 490 μM, depending on the analysis method applied. The lower value was again yielded using the normalized medians, just as seen in the lidocaine data. The curve fit did not improve significantly either way.

A major improvement using the normalized median values was seen when the data from two midbrain recordings were combined. Using the means of the raw data, the data points could not be fitted to a sigmoidal curve (Fig. 4.55, table 4.8), whereas the fit was almost perfect for the normalized median data, and an IC50 of 1 mM could be assigned (fig. 4.56, table 4.9). Therefore, barbital-sodium did not induce such varying responses in the two tissue types as lidocaine or ethanol. The FC IC50s correspond very well with anesthesia-inducing values from the literature [85].

The chemotherapeutic drug cisplatin has been demonstrated to cause a broad range of cellular and biomolecular reactions, e. g. blockage of sodium and potassium current in myelinated axons, decrease of glutathione (an intracellular antioxidant) levels, reduction of calcium currents in small dorsal root ganglion (DRG) neurons, and cytotoxicity resulting from blockage of DNA replication and transcription [77, 78]. We saw that cisplatin did acutely reduce electrical activity with IC50s of 21 and 114 μM (FC and midbrain, respectively). Drastic morphological changes that would reflect fatal cytotoxicity were not seen (figs. 4.59, 4.60). Cytotoxicity would also have been recognized by the failure to reverse the activity suppression by replacing the culture media, which was not observed. However, a subtle shift in the activity distribution seen in an FC recording may indicate that there may be several coexisting mechanisms of action, or that there is only one that acts in various ways at different concentrations: Fig. 4.57 shows that there was no significant change in spike production after the first

addition of cisplatin. This is confirmed by the ANOVA that was performed over all the data groups that are plotted in the separate histograms (table 4.10). Meanwhile, the unit-specific and temporal distribution changed, as shown in fig. 4.58 a/b, form a somewhat bell-shaped distribution ($R^2 = 0.88$) to an almost perfect one ($R^2 = 0.95$). In addition, the median of the distribution is not significantly different from the reference activity after the medium change, but the shape of the distribution is. This might point towards a combination of mechanisms that act on different time-scales. While the acute effect was completely reversible, there may have been another one that just started unfolding at the end of the recording.

A very interesting observation was made when two FC cultures were pre-treated with 0.3 mM vitamin C, and 100 µM cisplatin were needed to reduce the activity by 50 %, as opposed to 21 µM without vitamin C. This approach had proven useful in a clinical case report [79], but no other studies on this particular issue were found in the literature. The search for compounds that have neuroprotective capacities will certainly become one of the most important application areas of a high-throughput MEA-screening system.

Unlike all the compounds discussed so far, CAA proved to be toxic in a way that was generally not reversible by simply washing it out of the culture medium, both for FC and midbrain cultures. At the range of concentrations tested, it would always cause the network to cease all electrical activity after a limited period of time. Interestingly, medium changes that were supposed to rescue the cells often seemed to facilitate the fatal loss of activity and viability instead. Fig. 4.64 exemplifies this process and shows, that even at a very concentration of 0.2 µM, the activity decayed drastically after an initial excitation phase, which might be important for the identification of mechanisms of action. After another dose of CAA and a subsequent medium change, all activity vanished within 2 hours. During that time, several pictures of the neurons were taken. They document the gradual neuronal cell death induced by the CAA.

Another type of study that will be carried out with the novel high-throughput system focuses on simulating neurodegenerative disease states *in vitro* on the culture plate. The most talked about neurodegenerative disease is certainly AD. It is widely accepted among researchers that AD builds up over long periods of time through the accumulation of amyloid-beta peptides, fragments of APP, a protein of unknown function which gets cleaved by other proteins and thus splits up into the beta-amyloid peptides that form polymers spontaneously. These water-insoluble proteins then become longer chains, later fibrils and eventually plaques that ultimately lead to the diagnosis Alzheimer's, which to date is only safely made post mortem. Recently, however, evidence that points towards acute neurotoxicity of the smaller peptide chains, such as single fragments, the monomers, or oligomers, has been collected [88-100]. We used both monomers, dimers and a general mixture of oligomers, which encompasses everything from two-peptide chains to several dozens of peptides. During the first trials, the results obtained remained inconclusive (fig. 4.69). Since all cultures are usually kept in medium containing 5 % horse serum, interaction of the proteins in the serum with the amyloid-beta peptides and interference with their functionality was a concern. Thus, two recordings with amyloid-beta monomers and dimers were done using serum-free medium. Since the conformational state of the peptides may influence their biological activity [131], they had to be stored in certain pH buffer solutions for stability, and thus the neuroactivity of these buffers had to be evaluated as well. As shown in fig. 4.71, the two buffer solutions, Tris and ammonium acetate (AA) were

indeed reversibly neurotoxic, so that the superposition of their effects and the amyloids' actions may have been hard to untangle, based on activity level changes alone. Thus, the effects on three different burst parameters were quantified in addition: the burst period, the spike frequency inside the bursts ("burst Hz"), and the number of spikes per burst. The burst period is a global network parameter, since all the units in an FC network usually follow the same bursting rhythm. The burst Hz and spikes per burst values, on the other hand, are unit-specific. Therefore, their distributions during the respective analysis periods were investigated. The spikes per burst distributions did prove to be non-uniform and dynamically changed at different buffer concentrations (fig. 4.76). Normalizing the data first (fig. 4.77) proved effective in achieving a better statistical separation of the data from the separate analysis periods. This was confirmed by a one-way ANOVA with a post test, comparing the medians of every group with each other (tables 4.13, 4.14). The burst Hz histograms revealed visible distribution changes in response to the buffer solutions as well. However, the subgroups that emerged, e. g. in fig. 4.78 d, g, or i, were much closer to the main peak of the distribution, indicating that the variations in spike frequency within the network were more subtle than the activity or spikes per burst variations. Again, an ANOVA test confirmed that the groups were separated more clearly when normalized value were used and the network median was taken instead of the mean. The analysis showed that at the maximum concentration of Tris, the burst Hz increased by 11 %, the burst period by 84 %, and the spikes per burst decreased by 19.5 %. AA caused a 15 % rise in burst period, but no considerable changes in burst Hz and spikes per burst (-2 %, +4 %, respectively). In contrast, the beta-amyloid dimers dissolved in AA buffer elevated the burst Hz by 17 %, the burst period by 200 %, and the number of spikes per minute declined by 60 %. The monomers caused significantly stronger responses than the Tris buffer alone as well (spikes/burst: - 28 %, burst Hz: + 24 %), except for the burst period (+ 60 %). Therefore, both monomers and dimers did alter the internal bursting pattern of the networks significantly, even though the activity changes alone (fig. 4.70) did not show an unambiguous difference between the responses to the buffers alone and the buffers with the proteins. This implies that the beta-amyloid peptides may not block ion channels or certain receptors directly, since this should reduce the overall activity levels in a direct, dose dependent manner, as it is the case with agents such as muscimol, a $GABA_A$ receptor agonist, or tetrodotoxin (TTX), the poison of the puffer fish, which inhibits neuronal and muscular AP production by blocking fast-type Na^+ channels. In contrast, changes in burst pattern dynamics can be caused by a large variety of interactions with receptors, slow-type ion channels, other membrane proteins and the membrane and its potential itself. At this point, it is impossible to say which specific mechanisms combine to cause the observed effects. However, the mechanisms proposed in recent publications involving NMDA receptors [89], mitochondria [90], or dendritic spines [97, 98], do not contradict the observations made in this study. In a study from the early 1990s [131], primary neuronal cultures were used and evaluated for neurotoxicity screening of amyloid beta peptides. Here, pre-incubation times of the proteins were much longer (between 12 hours and 14 days), and morphological changes were reported. It will be interesting to see in future experiments whether morphological changes can be correlated with activity changes, provided the neurons do not move away from the electrodes so that their signals are lost. Combining extracellular recordings on MMEPs with fluorescence-microscopic and biomolecular methods has the potential to become an invaluable tool in the investigation of acute and intermediate-term toxicity of beta-amyloid peptide.

It is important to point out that the experiments using neuronal cell cultures shown here served two purposes. One was to answer some important questions regarding the neuroactivity of a range of compounds previously not investigated: We were able to show that midbrain cultures are considerably less susceptible to lidocaine, ethanol, and cisplatin, but not to barbital-sodium. Pre-incubation with 0.3 mM vitamin C protected cortical cultures partially from the activity decrease induced by cisplatin, while it did not help protect the cells against chloroacetaldehyde, which was always irreversibly cytotoxic. Alzheimer-inducing beta amyloid peptides exhibited a more complex interaction with the electrical activity, as they did not reduce the number of generated spikes significantly, but caused changes in spike and burst patterns. The other purpose of these trials was to establish guidelines for the further development of an MEA-based high throughput system and to point out difficulties regarding reliability of cell culture behavior, recording stability and automated data acquisition and analysis. A new high-throughput cell-based screening system has to be developed both in the electronics and engineering laboratory and in the biological laboratory where the interaction of electronic circuits and live biological tissue can be evaluated and fed back into the development process. Practical aspects concerning the handling and integration of biological tissue, sterility, life-support and addition of compounds are crucial components of the final product. Those aspects will only be solved successfully if the whole system is extensively used and tested in its early stages with real cells in a real biological laboratory environment.

The CNNS has been accompanying its efforts in developing an eight-network MEA system with laboratory environment tests since the first prototypes were made. Over the years, a workstation for the MMEP8 experiments has emerged that is capable of providing long-term life-support for the neuronal cultures, so that recordings over periods of several weeks are now possible. In fact, one culture we recorded from was kept alive for 31 days. The workstation features a liquid handling robot which is installed inside a CO_2- and temperature-controlled, sterile glove box. The base of the robot holds the 8-network MMEP that was developed at the CNNS, as well as supplies and dump stations for water and compound additions. The pipetting robot is programmed by the user to maintain the osmolarity by regularly adding water, to replace culture medium and to add compounds. For the first time, we show an automatic compound addition, in this case one dose of bicuculline followed by a step-wise titration of muscimol, in an FC culture. Six of the eight active networks responded to the muscimol in a reasonably uniform way. The other two were far more sensitive and quit firing when the rest had merely lost 50 % of their activity (figs. 4.94, 4.96). This may indicate that on the eight-network MMEP, not all the cultures grew the exactly same way. The handling of the MMEP8 plates is still being optimized. The data also show that in this case, there were no outlier units within each culture, because no considerable difference between the two analysis methods “normalize data, then compute the median”, and “mean values of raw data, then normalize” were seen (figs. 4.95, 4.97, tables 4.21, 4.22). No cells with extremely high activity levels were recorded from in any of the networks. However, the separation between the plateau data groups does improve when the two “ill-behaved” networks are excluded (fig. 4.98, tables 4.23, 4.24). This may be a valid step in the analysis, if it is shown that the cells in these networks differed, physiologically and/or morphologically, from the rest. However, in a high-throughput setting, all the components of the system must function reliably. That includes MEA plates which, following a tailored cell cultivation protocol, yield >90% long-term viable cultures that are morphologically and physiologically as

similar to the parent tissue as possible. In summary, the automatic addition of water and compounds using a pipetting robot appears to be the most efficient one at the moment, but some substantial modifications will have to be made for the system to work reliably and to ensure a high sensitivity of the cultures to neuroactive compounds.

One problem that has not been addressed adequately in the past is the mixing of compounds in the culture medium without damaging the neurons. Since the pipetting robot concept only works in an open setup without a fluidic system providing continuous flow of medium in a closed chamber, and since the neurons do need a relatively large volume of culture medium to keep functioning properly, a compound that is added has to be mixed thoroughly with this large volume. Normal pipette tips eject their contents straight down towards the bottom of the well, where the neurons reside. This means that the cells will always experience a concentration of the compound that is much higher than what was intended, and that they are also mechanically stressed by the shear forces of the fluid stream exerted on them. The pipetting robot is capable of mixing the medium after the addition of a compound by aspirating and dispensing a pre-defined number of times while keeping the bottom of the pipette tip immersed in the medium. However, in a mixing test using phenol red as a dye, we saw that this pumping action did not homogenize the solution, but merely distributed the dye outward towards the perimeter of the well. This is most likely due to the large size of the wells in the MMEP8 chamber block (diameter: 15 mm, max. volume: 2.4 ml, max. mixing volume: 50 µl). In a 96-well plate, the type of mixing provided by the robot certainly works better. We modified some pipette tips by sealing the bottom hole with biocompatible silicone sealant and piercing four holes into the walls of the tips using a 28.5 gauge needle to allow passage of the medium sideways in all four directions (fig. 2.47). This approach did prove to be helpful, as in another dye test good swirling of the dye was observed, and when used on the neuronal cultures, much less artifactual activity disturbance was seen than with the normal tips. However, there were still some irregularities (see figure 4.93). The analysis of the onset time and the time needed to achieve the maximum effect of a certain compound is only meaningful if all the cells experience the correct final concentration within a very short time after the application. The kinetics of a drug's interaction with the cells after application may contain valuable information hinting at possible mechanisms of action. In the future, a new fluidics system for the high-throughput platform will have to be developed that might incorporate the sideways ejection of medium for enhanced mixing and mechanical protection of the neurons.

Another important aspect of the handling of cultures for the new 24-network system under development at the LME is the actual design of the MEA chips. Since the size of the MMEP8 does pose problems with the preparation and incubation of the cultures, we have tested prototypes of miniaturized, single MEA plates with 32 electrodes each. These plates will eventually be supplied pre-sterilized and disposable, so that the cleaning of the MMEPs, one major source of error in the culture preparation chain, will become obsolete. Figs. 4.99 – 4.102 show that neurons and glia grown on these silicon-nitrite insulated plates developed within the normal parameters. After 10 days, a morphologically proper network was photographed for fig. 4.101. A first attempt at recording from these chips is depicted in figs. 4.103 – 4.105. Although the number of cells was rather low, and the activity was not as well coordinated as expected, the cells did respond to 20 µM bicuculline. A large number of tests have yet to follow, but we feel confident that this new MEA design will ultimately play an important role in the overall system of the high-throughput platform.

References

[1] http://www.who.int/mediacentre/factsheets/fs310_2008.pdf

[2] P. Dames, B. Gleich, A. Flemmer, K. Hajek, N. Seidl, F. Wiekhorst, D. Eberbeck, I. Bittmann, C. Bergemann, T. Weyh, L. Trahms, J. Rosenecker, C. Rudolph, *Targeted delivery of magnetic aerosol droplets to the lung*. Nat Nanotechnol., vol. 2(8), 495-499, 2007

[3] Y. Xia, G. W. Gross, *Histiotypic electrophysiological responses of cultured neuronal networks to ethanol*. Alcohol, vol. 30: 167-174. 2003

[4] http://upload.wikimedia.org/wikipedia/commons/1/1a/Biological_cell.svg ({{Information |Description= |Source=own work created in Inkscape |Date=15.10.2006 |Author=MesserWoland |Permission=Own work, copyleft: Multi-license with GFDL and Creative Commons CC-BY-SA-2.5 and older versions (2.0 and 1.0) |other_)

[5] M. Strong, K. G. Chandy, G. A. Gutmany, *Molecular Evolution of Voltage-sensitive Ion Channel Genes: On the Origins of Electrical Excitability,* Mol. Biol. Evol., vol. 10(1):221-242, 1993

[6] T. Heida, J. B. M. Wagenaar, W. L. C. Rutten, E. Marani, *Investigating Membrane Breakdown of Neuronal Cells Exposed to Nonuniform Electric Fields by Finite-Element Modeling and Experiments*, IEEE Transactions on Biomedical Engineering, vol. 49(10), 1195-1203, 2002

[7] L.A. Pardo, C. Contreras-Jurado, M. Zientkowska, F. Alves, W. Stühmer, *Role of Voltage-gated Potassium Channels in Cancer,* J. Membrane Biol., vol. 205, 115–124, 2005

[8] L. Munaron, S. Antoniotti, D. Lovisolo, *Intracellular calcium signals and control of cell proliferation: how many mechanisms?*, J. Cell. Mol. Med., vol. 8 (2), 161-168, 2004

[9] K. Kunzelmann, *Ion Channels and Cancer*, J. Membrane Biol., vol. 205, 159–173, 2005

[10] R. Binggeli, R. C. Weinstein, *Membrane Potentials and Sodium Channels: Hypotheses for Growth Regulation and Cancer Formation Based on changes in Sodium Channels and Gap Junctions*, J. theor. Biol., vol. 123, 377-401, 1986

[11] M. Olivotto, A. Arcangeli, M. Carlà, E. Wanke, *Electric fields at the plasma membrane level: a neglected element in the mechanisms of cell signalling*, Bioessays, vol. 18(6):495-504, 1996

[12] C. Xu and L. M. Loew, *The Effect of Asymmetric Surface Potentials on the Intramembrane Electric Field Measured with Voltage-Sensitive Dyes*, Biophysical Journal, vol. 84, 2768–2780, 2003

[13] L. M. Mannuzzu, M. M. Moronne, E. Y. Isacoff**,** *Direct Physical Measure of Conformational Rearrangement Underlying Potassium Channel Gating***,** Science, vol. 271(5246), 213 – 216, 1996

[14] F. Bezanilla, *Voltage-Gated Ion Channels*, IEEE Transactions on Nanobioscience, vol. 4(1), 34-48, 2005

[15] R. Glaser, *Biophysik*. Gustav Fischer Verlag, Jena Stuttgart, Auflage 4, 1996

[16] J. I. Fiske, VP Fomin, ML Brown, RL Duncan, RA Sikes, *Voltage-sensitive ion channels and cancer*. Cancer Metastasis Rev, vol. 25, 493-500, 2006

[17] S.-Y. Lee, A. Lee, J. Chen, R. MacKinnon, Structure of the KvAP voltage-dependent K_ channel and its dependence on the lipid membrane Proc. Natl. Acad. Sci., vol. 102(43), 15441–15446, 2005

[18] O. Platoshyn, V. A. Golovina, C. L. Bailey, A. Limsuwan, S. Krick, M. Juhaszova, J. E. Seiden, L. J. Rubin, J. X.-J. Yuan, *Sustained membrane depolarization and pulmonary artery smooth muscle cell proliferation,* Am J Physiol Cell Physiol, vol. 279, C1540–C1549, 2000

[19] R. Schreiber, *Ca^{2+} Signaling, Intracellular pH and Cell Volume in Cell Proliferation*, J. Membrane Biol., vol. 205, 129–137 (2005)

[20] E. A. Mayer, A. Kodner, X. P. Sun, J. Wilkes, D. Scott, G. Sachs, *Spatial and temporal patterns of intracellular calcium in colonic smooth muscle*, Journal of Membrane Biology, vol. 125(2) 2, 107-118, 1992

[21] M. Mesnil, S. Crespin, J.-L. Avanzo, M.-L. Zaidan-Dagli, *Defective gap junctional intercellular communication in the carcinogenic process*, Biochimica et Biophysica Acta, vol. 1719, 125 – 145, 2005

[22] R. Binggeli, R. C. Weinstein, *Deficits in Elevating Membrane Potential of Rat Fibrosarcoma Cells after Cell Contact*, Cancer Research, vol. 45, 235-241, 1985

[23] C. A. Cain, *Biological effects of oscillating electric fields: Role of voltage-sensitive ion channels*, Bioelectromagnetics, vol. 2(1), 23 – 32, 1981

[24] V. E. Klepeis, A. Cornell-Bell, V. Trinkaus-Randall, *Growth factors but not gap junctions play a role in injury-induced Ca^{2+} waves in epithelial cells*, Journal of Cell Science, vol. 114(23), 4185-4195, 2001

[25] A. Okuda, K. Furuya, T. Kiyohara, *ATP-induced calcium oscillations and change of P2Y subtypes with culture conditions in HeLa cells*, Cell Biochem Funct, vol. 21, 61–68, 2003

[26] M. J. Berridge, *Unlocking the Secrets of Cell Signaling*, Annu. Rev. Physiol., vol. 67:1–21, 2005

[27] S. S. Stojilković, M. Kukuljan, T. Iida, E. Rojas, K. J. Catt, *Integration of cytoplasmic calcium and membrane potential oscillations maintains calcium signaling in pituitary gonadotrophs*, Proc. Natl. Acad. Sci. USA, vol. 89, 4081-4085, 1992

[28] R. Binggeli, R. C. Weinstein, D. Stevenson, *Calcium ion and the membrane potential of tumor cells*, Cancer Biochem Biophys., vol. 14(3), 201-210, 1994

[29] Y. Yokota, E. S. Anton, *Calcium waves rule and divide glia*, Neuron, vol. 43(5), 647-661, 2004

[30] L. Vodovnik, D. Miklavčič, G. Serša, *Modified cell proliferation due to electrical currents*, Medical and Biological Engineering and Computing, vol. 30(4), CE21-CE28, 1992

[31] J. Teissie, M. Golzio, M.P. Rols, *Mechanisms of cell membrane electropermeabilization: A minireview of our present (lack of ?) knowledge*, Biochimica et Biophysica Acta, vol. 1724, 270 – 280, 2005

[32] H. G. Sachs, P. J. Stambrook, J. D. Ebert, *Changes in membrane potential during the cell cycle*, Exp Cell Res., vol. 83(2), 362-366, 1974

[33] S. Chifflet, J. A. Hernández, S. Grasso, *A possible role for membrane depolarization in epithelial wound healing*, Am J Physiol Cell Physiol, vol. 288, 1420-1430, 2005

[34] D. Stevenson, R. Binggeli, R. C. Weinstein, J. G. Keck, M. C. Lai, M. J. Tong, *Relationship between cell membrane potential and natural killer cell cytolysis in human hepatocellular carcinoma cells*, Cancer Res., vol. 49(17), 4842-4845, 1989.

[35] E. Phez, C. Faurie, M. Golzio, J. Teissie, M.-P. Rols, *New insights in the visualization of membrane permeabilization and DNA/membrane interaction of cells submitted to electric pulses*, Biochimica et Biophysica Acta, vol. 1724, 248 – 254, 2005

[36] H. Sauer, R. Stanelle, J. Hescheler, M. Wartenberg, *The DC electrical-field-induced Ca^{2+} response and growth stimulation of multicellular tumor spheroids are mediated by ATP release and purinergic receptor stimulation,* Journal of Cell Science, vol. 115, 3265-3273, 2002

[37] W. Chen, *Evidence of electroconformational changes in membrane proteins: field-induced reductions in intra membrane nonlinear charge movement currents*, Bioelectrochemistry, vol. 63, 333– 335, 2004

[38] T. J. Goodwin, *Physiological and molecular genetic effects of time-varying electromagnetic fields on human neuronal cells*, NASA/TP-2003-212054, 2003

[39] Y. Eguchi, M. Ogiue-Ikeda, S. Ueno, *Control of orientation of rat Schwann cells using an 8-T static magnetic field*, Neuroscience Letters, vol. 351, 130 – 132, 2003

[40] S. Yamaguchi, M. Ogiue-Ikeda, M. Sekino, S. Ueno, *Effects of Pulsed Magnetic Stimulation on Tumor Development and Immune Functions in Mice*, Bioelectromagnetics, vol. 27, 64-72, 2006

[41] C. L. M. Baureus-Koch, M. Sommarin, B. R. R. Persson, L. G. Salford, J. L. Eberhardt, *Interaction Between Weak Low Frequency magnetic Fields and Cell Membranes*, Bioelectromagnetics, vol. 24, 395-402, 2003

[42] T. Ikehara, H. Yamaguchi, K. Hosokawa, H. Miyamoto, K. Aizawa, *Effects of ELF Magnetic Field on Membrane Protein Structure of Living HeLa Cells Studied by Fourier Transform Infrared Spectroscopy*, Bioelectromagnetics, vol. 24, 457-464, 2003

[43] T. Ikehara, K. H. Park, H. Yamaguchi, K. Hosokawa, H. Houchi, M. Azuma, K. Minakuchi, H. Kashimoto, M. Kitamura, Y. Kinouchi, K. Yoshizaki, H. Miyamoto, *Effects of a Time Varying Strong Magnetic Field on Release of Cytosolic Free Ca^{2+} From Intracellular Stores in Cultured Bovine Adrenal Chromaffin Cells*, Bioelectromagnetics, vol. 23, 505-515, 2003

[44] G. Stuart, N. Spruston, B. Sakmann, M. Häusser**,** *Action potential initiation and backpropagation in neurons of the mammalian CNS*, Trends in Neurosciences, vol. 20(3), 125-131, 1997

[45] N. Bauman, D. Pham-Dinh, *Biology of Oligodendrocyte and Myelin in the Mammalian Central Nervous System*, Physiol Rev, vol.81, 871-927, 2001

[46] L. Ranvier, *Traite technique d'histologie*, Paris: Savy, 1875

[47] E. R. Kandel, J. Schwartz, T. Jessell, *Principles of Neural Science*, Edition 4, Atlanta: McGraw-Hill Professional, 2000

[48] M. V. Orna, J. Stock, *Electrochemistry, past and present*. Columbus, OH: American Chemical Society, 1989, ISBN 0-8412-1572-3

[49] A. L. Hodgkin, A. F. Huxley, *A quantitative description of membrane current and its application to conduction and excitation in nerve*, J. Physiol., vol. 117, 500-544, 1952

[50] P. J. Basser, B. J. Roth, *Stimulation of a myelinated axon by Electromagnetic Induction*, Med & Biomed Eng & Comput., vol.29(3), 261-268, 1991

[51] A. L. Hodgkin, A. F. Huxley, *Resting and actions potential in single nerve fibres*, J. Physiol., vol. 104, 176-195, 1945

[52] A. F. Huxley, R. Stämpfli, *Evidence for saltatory conduction in peripheral myelinated nerve fibres*, J. Physiol, 315-339, vol. 108, 1949

[53] J. T. Rubinstein*, Analytical theory for extracellular electrical stimulation of nerve with focal electrodes*, Biophys. J, vol.60, 538-555, 1991

[54] J. D. Jackson, *Klassische Elektrodynamik*, Edition 3, Berlin, New York: Walter de Gruyter, 2002

[55] G. Müller, W. Schätzing, *FEM für Praktiker IV*, Elektrotechnik, Ed.1, Renningen- Malsheim: Expert-Verlag, 2002

[56] B. Hille, *Ion Channels of Excitable Membranes*, Edition 2, Sunderland, MA, USA: Sinauer Associates, 2001

[57] B. J. Roth, P. J. Basser, *A Model of Stimulation of a Nerve Fiber by Electromagnetic Induction*, IEEE Trans Biomed Eng., vol. 37(6), 588-597, 1990

[58] S. Y. Chiu, J. Ritchie, *A quantitative description of membrane currents in rabbit myelinated nerve*, London J. Physiol., vol. 292, 149-166, 1979

[59] S. Y. Chiu, J. Ritchie, *On the physiological role of internodal potassium channels and the security of conduction in myelinated nerve fibres*, Proc. R. Soc. Lond., vol. 220, 415-422, 1984

[60] E. W. Keefer, A. Gramowski, G. W. Gross, *NMDA Receptor-Dependent Periodic Oscillations in Cultured Spinal Cord Networks*, The Journal of Neurophysiology, vol. 86(6), 3030-3042, 2001

[61] K. Wendicke, *Optimierung von Stimulationsspulen für die induktive Nervenreizung*, Dissertation, Technische Universität München, 2007

[62] C. de Haro, C R. Mas, G. Abadal, J. Munoz, F. Perez-Murano, C. Domınguez, *Electrochemical platinum coatings for improving performance of implantable microelectrode arrays*, Biomaterials, vol. 32, 4515-4521, 2002

[63] B. Habel, *Elektrische Stimulation von Zellen und Geweben am besonderen Beispiel von Knochenzellen*, Dissertation, Humboldt-Universität Berlin, 2004

[64] G. Wrobel, Y. Zhang, H.-J. Krause, N. Wolters, F. Sommerhage, A. Offenhäusser, S. Ingebrandt*, Influence of the first amplifier stage in MEA systems on extracellular signal shapes*, Biosensors and Bioelectronics, vol. 22, 1092–1096, 2007

[65] H. J. Apell, B. Bersch, *Oxonol VI as an optical indicator for membrane potentials in lipid vesicles*, Biochim Biophys Acta, vol. 903, 480-494, 1987

[66] C. Wolff, B. Fuks, P. Chatelain, *Comparative study of membrane potential-sensitive fluorescent probes and their use in ion channel screening assays*, Journal of Biomolecular Screening, vol. 8(5), 533-543, 2003

[67] E. Neher, B. Sakmann, J. H. Steinbach, *The extracellular patch clamp: A method for resolving currents through individual open channels in biological membranes*, Pflügers Arch, vol. 375, 219-228, 1978

[68] G. W. Gross, E. Rieske, G. W. Kreutzberg, A. Meyer, *A new fixed-array multi-microelectrode system designed for long-term monitoring of extracellular single unit neuronal activity in vitro*, Neuroscience Letters, vol. 6, 101-105, 1977

[69] C. A. Thomas, P. A. Springer, G. E. Loeb, Y. Berwald-Netter, L. M. Okun, *A miniature microelectrode array to monitor the bioelectric activity of cultured cells*, *Exp Cell Res, vol. 74*, 61-66, 1972

[70] E. M. Izhikevich, *Dynamical Systems in Neuroscience: The Geometry of Excitability and Bursting ,* The MIT Press Cambridge, Massachusetts London, England, 2007, ISBN 978-0-262-09043-8

[71] A. F. Fercher, *Medizinische Physik, Edition 1*, Wien, NewYork: Springer Verlag, 1992

[72] M. Bove, M. Grattarola, S. Martinoia, G. Verreschi, *Interfacing cultured neurons to planar substrate microelectrodes: characterization of the neuron-to-microelectrode junction,* Bioelectrochemistry and bioenergetics, vol. 38, 255-265, 1995

[73] P. Fromherz, R. Weser, *Nanoelectronics and Information Technology*, Edition 1, 781-810, Berlin: Wiley-VCH, 2003

[74] M. Issing, *Messung der elektrischen Aktivität biologischer Zellen mit Feld-Effekt-Transistoren*, Diplomarbeit, Technische Universität Berlin, Institut für Mikroelektronik und Festkörperelektronik, 2000

[75] J. R. Buitenweg, W. L. C. Rutten, E. Marani, *Modeled Channel Distributions Explain Extracellular Recordings From Cultured Neurons Sealed to Microelectrodes*, IEEE Transactions on Biomedical Engineering, vol. 49(11), 1580-1590, 2002

[76] J. J. Pancrazio, S. A. Gray, Y. S. Shubin, N. Kulagina, D. S. Cuttino, K. M. Shaffer, K. Eisemann, A. Curran, B. Zim, G. W. Gross, T. J. O'Shaughnessy, *A portable microelectrode array recording system incorporating cultured neuronal networks for neurotoxin detection*, Biosensors and Bioelectronics, vol. 18, 1339-1347, 2003

[77] L. E. Ta, L. Espeset, J. Podratz, A. J. Windebank, "*Neurotoxicity of oxaliplatin and CisPt with platinum-DNA binding*, NeuroToxicology 27, 992-1002, 2006

[78] A. Tomaszewski, D. Buesselberg, *CisPt modulates voltage gated channel currents of dorsal root ganglion neurons of rats*, NeuroToxicology 28: 49-58, 2007

[79] R. C. Patra, D. Swarup, S. K. Dwivedi, *Antioxidant effects of α tocopherol, ascorbic acid and L-methionine on lead induced oxidative stress to the liver, kidney and brain in rats*, Toxicology 162, 81-88, 2001

[80] S. K. Brüggemann, K. Radike, K. Braasch, J. Hinrichs, J. Kisro, W. Hagenah, S. O. Peters, T. Wagner, *Chloroacetaldehyde: mode of antitumor action of the ifosfamide metabolite*, Cancer Chemother. Pharmacol. 57: 349-56, 2006

[81] T. Kerbusch, J. de Kraker, H. J. Keizer, J. W. G. van Putten, H. J. M. Groen, R. L. H. Jansen, J. H. M. Schellens, J. H. Beijnen, *Clinical pharmacokinetics and pharmacodynamics of ifosfamide and its metabolites*, Clin. Pharmacokinet., 40(1): 41-62, 2001

[82] N. Löfgren, *Xylocaine: a new synthetic drug*, Stockholm: Haeggstrom, 1948

[83] W. Zink, B. M. Graf, *Toxikologie der Lokalanästhetika. Pathomechanismen – Klinik – Therapie*, Anaesthesist 52, 1102-1123, 2003

[84] J. H. Ye, J. Ren, K. Krnjevic, P. L. Liu, J. J. McArdle, *Cocaine and lidocaine have additive inhibitory effects on the GABAA current of acutely dissociated hippocampal pyramidal neurons*, Brain Research 821, 26-32, 1999

[85] I. K. Ho, R. A. Harris, *Mechanism of action of barbiturates*, Ann. Rev. Pharmacol. Toxicol., 21, 83-111, 1981

[86] M. Bentahir, et al., *"Presenilin clinical mutations can affect gamma-secretase activity by different mechanisms*", J. Neurochem, vol. 96, 732-742, 2006

[87] G. B. Irvine, O. M. El-Agnaf, G. M. Shankar, D. M. Walsh, *Protein aggregation in the brain: the molecular basis for Alzheimer's and Parkinson's diseases*, Mol Med, vol. 14 (7-8), 451-464, 2008

[88] B. A. Yankner, L. K. Duffy, D. A. Kirschner, "*Neurotrophic and neurotoxic effects of β amyloid protein: Reversal by tachykinin neuropeptides*", Science, vol. 250, 279-282, 1990.

[89] Q. Wang, M. J. Rowan, R. Anwyl, *β-Amyloid-Mediated Inhibition of NMDA Receptor-Dependent Long-Term Potentiation Induction Involves Activation of Microglia and Stimulation of Inducible Nitric Oxide Synthase and Superoxide*, J. Neurosci., 24(27), 6049-56, 2004

[90] M. Manczak, T. S. Anekonda, E. Henson, B. S. Park, J. Quinn, P. H. Reddy, *Mitochondria are a direct site of Aß accumulation in Alzheimer's disease neurons: implications for free radical generation and oxidative damage in disease progression*, Hum. Mol. Genet., 15:1437-49, 2006

[91] D. L. Price, D. R. Borchelt, L. C. Walker, S. Sisodia, *Toxicity of synthetic Aβ peptides and modeling of Alzheimer's disease*, Neurobiology of Aging, vol. 13, 623-625, 1992.

[92] B. A. Yankner, *Commentary and perspective on studies of beta amyloid neurotoxicity*, Neurobiol. Aging, vol. 13, 615-616.

[93] D. M. Walsh et al., *Naturally secreted oligomers of amyloid beta protein potently inhibit hippocampal long-term potentiation in vivo*, Nature, vol. 416, 535-539, 2002

[94] Q. Walsh, D. M. Walsh, M. J. Rowan, D. J. Selkoe, R. Anwyl, *Block of long-term potentiation by naturally secreted and synthetic amyloid beta-peptide in hippocampal slices is mediated via activation of kinases c-jun N-terminal kinase, cyclin-dependent kinase 5, and p38 mitogen-activated protein kinase as well as metabotropic glutamate receptor type 5*, J. Neurosci, vol. 24, 3370-3378, 2004

[95] J. P. Cleary, D. M. Walsh, J. J. Hofmeister, G. M. Shankar, M. A. Kuskowski, D. J. Selkoe, K. H. Ashe, *Natural oligomers of the amyloid-beta protein specifically disrupt cognitive function*, Nat. Neurosci, vol. 8, 79-84, 2005

[96] B. Calabrese, G. M. Shaked, I. V. Tabarean, J. Braga, E. H. Koo, S. Helpain, *Rapid, concurrent alterations in pre- and postsynaptic structure induced by naturally-secreted amyloid-beta protein*, Mol. Cell. Neurosci., vol. 35, 183-193, 2007

[97] G. M. Shankar, B. L. Bloodgood, M. Townsend, D. M. Walsh, D. J. Selkoe, B. L. Sabatini, *Natural oligomers of the Alzheimer amyloid-beta protein induce reversible synapse loss by*

modulating an NMDA-type glutamate receptor-dependent signaling pathway, J. Neurosci, vol. 27, 2866-2875, 2007

[98] G. M. Shankar, S. Li, T. H. Mehta, A. Garcia-Munoz, N. E. Shepardson, I. Smith, F. M. Brett, M. A. Farrell, M. J. Rowan, C. A. Lemere, C. M. Regan, D. M. Walsh, B. L. Sabatini, D. J. Selkoe, *Amyloid-beta protein dimers isolated directly from Alzheimer's brains impair synaptic plasticity and memory,* Nat Med., 2008 Jun 22 [Epub ahead of print]

[99] J. Y. Koh, L. L. Yang, C. W. Cotman, *β-Amyloid protein increases the vulnerability of cultured cortical neurons to excitotoxic damage*, Brain Res. vol. 533, 315-320, 1990

[100] M. P. Mattson, B. Cheng, D. Davis, K. Bryant, I. Leieberburg, R. Rydel, *β-Amyloid peptides destabilize calcium homeostasis and render human cortical neurons vulnerable to excitotoxicity*, J Neurosci, vol. 12, 376-389, 1992

[101] L. Kirazov, E. Kirazov, L. Venkov, E. Vassileva, C. Naydenov, S. Stuewe, D. G. Weiss, *Comparison of the effect of different forms of the amyloidogenic peptide on the electrical activity of cultured neuronal networks*, Compt Ren Acad Bulg Sci, 55(5), 91-94, 2004

[102] F. Yang, G. P. Lim, A. N. Begum, O. J. Ubeda, M. R. Simmons, S. S: Ambegaokar, P. Chen, R. Kayed, C. G. Glabe, S. A. Frautschy, G. M. Cole, *Curcumin inhibits formation of amyloid ß oligomers and fibrils, binds plaques, and reduces amyloid in vivo,* J. Biol. Chem., 280(7), 5892-5901, 2005

[103] M. Necula, R. Kayed, S. Milton, C. G. Glabe, *Small molecule inhibitors of aggregation indicate that amyloid ß oligomerization and fibrillization pathways are independent and distinct,* J. Biol. Chem., 282(14), 10311-24, 2007

[104] D. G. Georganopoulou, L. Chang, J. M. Nam, C. S. Thaxton, E. J. Mufson, W. L. Klein, C. A. Mirkin, *Nanoparticle-based detection in cerebral spinal fluid of a soluble pathogenic biomarker for Alzheimer's disease*, Pro. Natl. Acad. Sci. U. S. A., vol. 102, 2273-2276, 2005

[105] Joint Commission on Accreditation of Healthcare Organizations (JCAHO). *Sentinel Event Alert* 6 Oct 2004;32. Sebel PS: *The incidence of awareness during anaesthesia: A multicenter United States study*. Anesth Analg 2004; 99:833-9 (online version)

[106] G. J. Stuart, L. M. Palmer, *Imaging membrane potential in dendrites and axons of single neurons*, Pflugers Arch – Eur J Physiol, 453, vol. 403-410, 2006

[107] L. M. Loew, *Potentiometric dyes: Imaging electrical activity of cell membranes*, Pure & Appl. Chem., vol. 68(7), 1405-1409, 1996

[108] K. R. Gee, K. A. Brown, W. -N. U. Chen, J. Bishop-Stewart, D. Gray, I. Johnson, "*Chemical and physiological characterization of fluo-4 Ca^{2+}-indicator dyes*", Cell Calcium, vol. 27(2), 97-106, 2000

[109] V. V. Martin, M. Beierlein, J. L. Morgan, A. Rothe, K. R. Gee, "*Novel fluo-4 analogs for fluorescent calcium measurements*", Cell Calcium, vol. 36, 509-514, 2004

[110] S. Ingebrandt, G. Wrobel, Y. Zhang, S. Meyburg, M. Schindler, F. Sommerhage, D. Borstlap, A. Offenhäusser, "*Investigation of extracellular signal shapes recorded by planar metal microelectrodes and field-effect transistors"*, Sensors, 2005 IEEE, Oct. 30 2005-Nov. 3 2005, 611-615

[111] E. Wang, Y. Yin, M. Zhao, J. V. Forrester, C. D. McCaig, "*Physiological electric fields control the G1/S phase cell cycle checkpoint to inhibit endothelial cell proliferation*", FASEB Journal, vol. 17 (3), 458-460, 2003

[112] R. Glaser, "*Biophysik*", Gustav Fischer Verlag, Jena Stuttgart, 4th Edition, 1996

[113] S. O. Rijal, G. W. Gross, "*Dissociation constants for $GABA_A$ receptor antagonists determined with neuronal networks on microelectrode arrays*", J. Neurosci Meth, vol. 173 (2), 18-192, 2008

[114] E. D. Kirson, Z. Gurvich, R. Schneiderman, E. Dekel, A. Itzhaki, Y. Wasserman, R. Schatzberger, Y. Palti, *"Disruption of Cancer Cell Replication by Alternating Electric Fields*", Cancer Research, vol. 64, 3288-3295, 2004.

[115] A. M. Khalil, W. Qassem, "*Cytogenetic effects of pulsing electromagnetic field on human lymphocytes in vitro: chromosome aberrations, sister-chromatid exchanges and cell kinetics*", Mutat. Res., vol. 247 (1), 141-146, 1991

[116] J. Schimmelpfeng, H. Dertinger, *"Action of a 50 Hz magnetic field on proliferation of cells in culture"*, Bioelectromagnetics, vol. 18, 177-183, 1997

[117] H. Yoshizawa H, T. Tsuchiya, H. Mizoe, H. Ozeki, S. Kanao, "*No effect of extremely low-frequency magnetic field observed on the cell growth or initial response of cell proliferation in human cancer cell lines*", Bioelectromagnetics, vol. 23, 355-368, 2002

[118] C. de Haro, R. Mas, G. Abadal, J. Muñoz, F. Perez-Muran and C. Domínguez, *"Electrochemical platinum coatings for improving performance of implantable microelectrode arrays"*, Biomaterials, vol. 23 (23), 4515 – 4521, 2002

[119] C. Alexiou, R. Jurgons, R. J. Schmid, C. Bergemann, J. Henke, W. Erhardt, E. Huenges, F. Parak, "*Magnetic Drug Targeting—Biodistribution of the Magnetic Carrier and the Chemotherapeutic agent Mitoxantrone after Locoregional Cancer Treatment*", Journal of Drug Targeting, vol. 11(3), 139-149, 2003

[120] G. E. Sosinsky, B. J. Nicholson, "*Structural organization of gap junction channels*", Biochim Biophys Acta, vol. 1711, 99-125, 2005

[121] https://wiki.brown.edu/confluence/display/BN0193S04/gap+junctions

[122] J. Bernhardt, H. Pauly, "*On the Generation of Potential Differences across the Membranes of Ellipsoidal Cells in an Alternating Electrical Field*", Biophysik, vol. 10, 89-98, 1973

[123] J. G. Nicholls, A. R. Martin, B. G. Wallace, P. A. Fuchs, "*From Neuron to Brain*", fourth edition; Sinauer Associates, Sunderland, Massachusetts, 2001 (ISBN 0-87893-439-1)

[124] N. A. Carlson, "*Foundations of Physiological Psychology"*. Needham Heights, Massachusetts: Simon & Schuster. pp. 53, 1992

[125] M. Nicoletti, "*Magnetic stimulation of organotypic neuronal cell cultures on multielectrode arrays*", Master thesis, Technische Universität München, Fakultät für Maschinenwesen, 2007

[126] F. Rattay, M. Aberham, "*Modeling Axon Membranes for Functional Electrical Stimulation*", IEEE Transactions on Biomedical Engineering, vol. 40(12), 1201-1209, 1993

[127] L. Hafner, "*Elektrische und Magnetische Wachstumsmanipulationen an Mausfibroblasten*", Master thesis, Fakultät für Maschinenwesen, Technische Universität München, 2009

[128] W. Humphrey, A. Dalke, K. Schulten, "*VMD – Visual Molecular Dynamics*", J. Molec. Graphics, 14(1), 33-38, 1996

[129] A. Stett, U. Egert, E. Guenther, F. Hofmann, T. Meyer, W. Nisch, H. Hämmerle, "*Biological application of microelectrode arrays in drug discovery and basic research*", Anal Bioanal Chem, 377, 486-495, 2003

[130] G. W. Gross, K. V. Gopal, "*Emerging histiotypic properties of cultured neuronal networks*", in: Advances in Network Electrophysiology using multi-electrode arrays, 193-214, M. Taketani, M. Baudry, eds., Springer US, ISBN 978-0-387-25857-7, 2006

[131] J. Busciglio, A. Lorenzo, B. Yankner, "*Methodological variables in the assessment of beta amyloid neurotoxicity*", Neurobiology of Aging, 13, 609-612, 1992

[132] U. Egert, D. Heck, A. Aertsen, "*Two-dimensional monitoring of spiking networks in acute brain slices"*, Exp Brain Res, 142, 268-274, 2002

[133] R. Lind, P. Connolly, C. D. W. Wilkinson, R. D. Thompson, "*Finite-element analysis applied to extracellular microelectrode design*", Sens Actuators B, 3, 23-30, 1991

[134] C. D. Cone Jr., M. Tongier Jr., "*Contact inhibition of Division: Involvement of the Electrical Transmembrane Potential*", J. Cell. Physiol., 82, 373-386, 1973

[135] B. Haider, D. A. McCormick, "*Rapid Neocortical Dynamics: Cellular and Network Mechanisms*", Neuron, 62, 171-189, 2009

[136] F. O. Morin, Y. Takamura, Eiichi Tamiya, "*Investigating Neuronal Activity with Planar Microelectrode Arrays: Achievements and New Perspectives*", J. Biosci. Bioeng., 100(2), 131-143, 2005

[137] D. Deamer, J. P. Dworkin, S. A. Sandford, M. P. Bernstein, L. J. Allamandola., "*The First Cell Membranes*", Astrobiology, 2(4): 371-381, 2002

[138] P. L. Luisi, P. Walde, M. Blocher, D. Liu, "*Research on the Origin of Life: Membrane-Assisted Polycondensations of Amino Acids and Peptides*", CHIMIA, 54 (1/2), 2000

[139] S. L. Miller, "*A Production of Amino Acids Under Possible Primitive Earth Conditions*", Science, 117, 528-529, 1953

[140] B. Wolf, M. Kraus, M. Brischwein, R. Ehret, W. Baumann, M. Lehmann, *"Biofunctional hybrid structures – cell-silicon hybrids for applications in biomedicine and bioinformatics"*, Bioelectrochem Bioenerg, 46, 215-225, 1998